

## ABSTRACT

Title of Document: EMBEDDED TWO-PHASE COOLING OF HIGH FLUX ELECTRONICS VIA MICRO-ENABLED SURFACES AND FLUID DELIVERY SYSTEM (FEEDS)

Raphael Kahat Mandel, Doctor of Philosophy, 2016

Directed By: Dr. Michael Ohadi  
Department of Mechanical Engineering

A novel cooler utilizing thin Film Evaporation on micro-Enabled surfaces and fluid Delivery System (FEEDS) is embedded into silicon die with the goal of achieving the metrics proposed by the Defense Advanced Research Project Agency's (DARPA) ICECool fundamentals program: a heat flux of  $1 \text{ kW/cm}^2$  at superheats below 30 K, vapor qualities above 90%, pressure drops below 10% of absolute pressure, and heat densities of  $1 \text{ kW/cm}^3$ . Preliminary models were used to investigate the various physical phenomena affecting two-phase flow in manifold-microchannels, including nucleate boiling, flow regime, annular film evaporation, void fraction, single-phase fully developed and developing forced convection, intra-microchannel flow distribution, and fin conduction. The various physical phenomena were then combined into a novel "2.5-D" microchannel model, which uses boundary layer assumptions and simplifications to model the 3-D domain with a 2-D mesh. The custom-coded microchannel model was first

validated by comparing single-phase thermal and hydrodynamic performance to a 3-D laminar flow simulation performed in ANSYS Fluent with errors of less than 5% as long as the flow remains two-dimensional. Two-phase validation was conducted by comparing past experimental data to model predictions, and found to provide heat transfer predictions that were qualitatively accurate and correct in order of magnitude, and pressure drop predictions accurate to within 30%. A parametric study was then performed in order to arrive at a baseline geometry for meeting the ICECool metrics.

A system level model was created to select the working fluid, and a manifold model was created to evaluate manifold flow configuration. A novel flow configuration capable of providing an even inter-microchannel flow distribution in two-phase mode was proposed, and a working manifold designed for the baseline geometry. Experiments with a press-fit FEEDS chip were then conducted, obtaining heat fluxes in excess of  $1 \text{ kW/cm}^2$  at 45% vapor quality. The volume of the FEEDS assembly was then reduced by bonding a chip directly to a FEEDS manifold. A bonding apparatus capable of providing a uniform and conformal clamping force was designed, fabricated, and used to hermetically bond the manifold to the chip. Three bonded chips were then tested, obtaining a maximum heat flux of  $700 \text{ W/cm}^2$  at vapor qualities approaching 30% and a heat density of  $220 \text{ W/cm}^3$ .

EMBEDDED TWO-PHASE COOLING OF HIGH FLUX ELECTRONICS VIA  
MICRO-ENABLED SURFACES AND FLUID DELIVERY SYSTEM (FEEDS)

By

Raphael Kahat Mandel

Dissertation submitted to the Faculty of the Graduate School of the  
University of Maryland, College Park, in partial fulfillment  
of the requirements for the degree of  
Doctor of Philosophy  
2016

Advisory Committee:

Professor Michael Ohadi, Chair

Professor Avram Bar-Cohen

Professor Marino diMarzo

Professor Amir Riaz

Professor Christopher Cadou, Dean's Representative

© Copyright by  
Raphael Kahat Mandel  
2016



## Acknowledgements

It is with my most sincere gratitude that I would like to acknowledge and thank those who have helped me achieve my academic accomplishments.

First and foremost, I would like to thank my adviser, Dr. Michael M. Ohadi for his unwavering support, guidance, and confidence in me, which has encouraged me to expand my capabilities and potential. I would like to express my gratitude to Dr. Serguei Dessiatoun for his technical guidance, encouragement, assistance, and support. Without him, I would not have been able to complete my Ph.D., and I will forever be grateful and appreciate the knowledge he imparted. I would also like to express my gratitude to Dr. Amir Shooshtari for his technical guidance, encouragement, assistance, and support. His ability to logically deconstruct a problem and formulate a rational approach is one I hope to be able to emulate.

I would like to thank my colleagues at the Smart and Small Thermal Systems Laboratory whom I have had the pleasure of working beside for providing a stimulating, productive, and peaceful environment. I would also like to thank others outside my laboratory for their assistance in their technical areas.

I would like to thank my parents, brothers, and their families for their support—both throughout the course of my Ph.D., as well as in the years leading up to it. And finally, I would like to thank Naomi Rosenblatt for her support, encouragement, and understanding in the final years of my Ph.D. To you, I dedicate my dissertation.

# Table of Contents

Acknowledgements.....	ii
Table of Contents .....	iii
List of Tables .....	v
List of Figures .....	vi
1 Introduction.....	1
1.1 Motivation.....	1
1.2 Embedded Cooling.....	3
1.3 Single-Phase vs. Two-Phase Cooling .....	5
1.4 Thin Film Evaporation vs. Nucleate Boiling .....	6
1.5 The Difficulty of Thin Film Evaporation.....	8
1.6 FEEDS Technology .....	12
1.7 ICECool Fundamentals .....	14
1.8 Objectives .....	16
1.9 Dissertation Outline .....	17
2 Literature Review.....	18
2.1 Manifold Microchannel Heat Exchangers .....	18
2.2 Embedded, Manifold-microchannel Cooling.....	19
2.3 Single-Phase High Flux Cooling .....	20
2.4 Two-Phase High Flux Cooling .....	21
2.5 Research Opportunities .....	29
3 Preliminary Microchannel Modeling .....	30
3.1 Preliminary Model Domains.....	30
3.2 Flow Boiling Correlations.....	35
3.3 Flow Regime Mapping .....	41
3.4 Annular Film Evaporation with Physics-Based Void Fraction Model.....	49
3.5 Single-Phase Forced Convection Model.....	61
3.6 Flow Tube “Streamline” Model.....	76
3.7 Preliminary Modeling Summary.....	95
4 2.5-D Microchannel Model.....	97
4.1 Model Domain .....	99
4.2 Model Assumptions .....	100
4.3 Model Equations .....	101
4.4 Model Validation .....	129
4.5 Discovery of Baseline Geometry & Parametric Study .....	145
4.6 2.5-D Microchannel Model Summary .....	149
5 Experimental Design.....	150
5.1 Working Fluid Selection .....	150
5.2 Manifold Model & Configuration Selection.....	155
5.3 Experimental Design Summary .....	176
6 Press-Fit FEEDS Experiment .....	177

6.1	Failed Experimental Designs .....	177
6.2	Experimental Design.....	181
6.3	Test Chip Soldering and Alignment .....	188
6.4	RTD Calibration.....	189
6.5	Data Analysis Equations .....	190
6.6	Uncertainty Propagation .....	194
6.7	SEM Images of the Microchannels and Manifold .....	196
6.8	Single-Phase Test Results .....	199
6.9	Two-Phase Test Results.....	206
6.10	Comparison to Model .....	210
6.11	Press-Fit FEEDS Summary.....	213
7	Bonded FEEDS Experiments.....	214
7.1	Header-Manifold.....	214
7.2	Solder Selection & Metalization.....	217
7.3	Preliminary Si-Si Bonding Work.....	221
7.4	Bonding Apparatus .....	223
7.5	Test Chip 1 .....	231
7.6	Test Chip 2.....	238
7.7	Test Chip 3.....	250
7.8	Comparison to Model .....	262
7.9	Bonded FEEDS Experiments Summary .....	264
8	Summary and Conclusions .....	266
8.1	Major Contributions.....	267
8.2	Opportunities for Future Work .....	268
9	Appendix A: Derivations of Equations Used in the Annular Film Evaporation with Physics-Based Void Fraction Model .....	272
9.1	Model Equations .....	272
9.2	Algebraic Solution for Friction Factor Source Term.....	283
9.3	Fully Developed Void Fraction .....	286
9.4	Fully Developed Friction Factor .....	288
10	Appendix B: Derivations of Equations Used in Microchannel Model .....	291
10.1	Conservation of Species.....	291
10.2	Conservation of Energy in the Mixture .....	292
	References.....	293

## List of Tables

Table 1.4.1: Comparison between flow boiling and thin film evaporation .....	8
Table 2.4.1: Summary of Two-Phase High Heat Flux Cooling Survey .....	23
Table 4.4.1: Summary of manifold and microchannel geometries .....	130
Table 4.4.2 Summary of various independent and mutually exclusive physics options, as well as corresponding equations.....	139
Table 4.5.1: Geometries tested to arrive at baseline manifold and microchannel geometry .....	147
Table 6.2.1 Summary of equipment specifications and uncertainties .....	186
Table 6.7.1 Comparison between nominal and actual values for microchannel and manifold dimensions of the press-fit test section.....	197
Table 7.3.1: Summary of tested heating methods, clamping mechanisms, and bond- testing apparatuses and methods.....	222
Table 7.6.1 Comparison between nominal and actual values for microchannel and manifold dimensions of bonded Chip 2 .....	239
Table 7.7.1: Comparison between nominal and actual values for microchannel and manifold dimensions of bonded chip 3 .....	252

## List of Figures

Fig. 1.1.1: History of Intel CPU trends. While number of transistors continues to grow exponentially (Moore's Law), the clock speed and power dissipation have peaked, in part, due to an inability to adequately cool electronic components, resulting in the recent trend of multicore processors [4].	2
Fig. 1.2.1: Conventional cooling paradigm: (a) diagram of a conventional silicon microchip; (b) accompanying thermal resistance diagram.	3
Fig. 1.2.2: Embedded cooling paradigm: (a) diagram of a silicon microchip with an embedded heat sink; (b) accompanying thermal resistance diagram in single-phase mode; and (c) thermal resistance diagram in two-phase mode.	4
Fig. 1.4.1: Schematic diagrams of (a) nucleate boiling vs. (b) thin film evaporation.	7
Fig. 1.5.1: Schematic diagram of spray cooling: (a) flow is too small such that large regions of dryout occur; (b) flow is too large such that a thick film of liquid forms resulting in nucleate boiling.	9
Fig. 1.5.2: Schematic diagram of capillary flow in a microgroove due to a heat flux at the base: (a) completely wetted grooved in absence of heat flux; (b) after the application of the heat flux.	10
Fig. 1.5.3: (a)-(f) Cross sections of capillary flow in a microgroove at various positions along the flow direction; (g) close-up of thin film profile near grooved wall.	11
Fig. 1.6.1: Schematic diagram of FEEDS system. A system of manifolds arranged perpendicular to a microgrooved surface is used to divide an array of long microchannels into a system of parallel ones, reducing pressure drop and pumping power and increasing heat transfer coefficient.	13
Fig. 1.6.2: (a) Geometric limit of film thickness in a microgroove; (b)-(c) use of FEEDS manifold pitch to control intra-microchannel flow distribution.	14
Fig. 1.7.1: Summary of metrics required by ICECool Fundamentals for the background heat flux. Table taken from DARPA-BAA-12-50 [1].	15
Fig. 2.4.1: Apparatus used by Cetegen et al. [10].	25
Fig. 2.4.2: Heat transfer coefficient vs. heat flux for various channel widths in order of decreasing channel width: (a) $60\ \mu m$ (b) $40\ \mu m$ (c) $20\ \mu m$ . Figure taken from [10].	27
Fig. 2.4.3: Comparison between experimental data and correlations for (a) high Reynolds numbers; and (b) low Reynolds numbers. Figures taken from [10].	28
Fig. 3.1.1: Unit cell of a manifold-microchannel system with geometric definitions.	31
Fig. 3.1.2: Domain of preliminary models, excluding the flow tube model.	32
Fig. 3.1.3: Summary of preliminary modeling effort, indicating the physical phenomena that each preliminary model attempted to probe.	34
Fig. 3.2.1: Comparison of experimental data in Cetegen et al. [10] to selected correlations.	39

Fig. 3.3.1: Flow regime map proposed by Taitel and Duckler [49].....	41
Fig. 3.3.2: Smooth stratified flow between parallel plates. ....	43
Fig. 3.3.3: Flow regime map proposed by Harirchian et al. [50].....	46
Fig. 3.3.4: Plotting of points from Cetegen [10] on flow regime map proposed by Harirchian et al. [50]. The data points tested by Harirchian are encompassed in the cyan parallelogram. The data points tested by Cetegen are shown in green, red, and yellow. The expected range to be tested in the present work is shown in blue.....	48
Fig. 3.4.1: Control volumes used for discretization in the annular film evaporation with physics-based void fraction model. ....	50
Fig. 3.4.2: Sample results from annular film evaporation with physics-based void fraction model with R245fa at 30°C in 10 $\mu\text{m}$ channel: (a) liquid and vapor mean velocities vs position; (b) liquid, vapor, and mixture pressures vs. position; (c) vapor quality, void fraction, and slip vs. position; (d) void fraction vs. vapor quality and comparison to Zivi and annular void fraction correlations.....	56
Fig. 3.4.3: Effect of mass flux on void fraction correlation for R245fa at 30°C in channels of various widths, corresponding to those tested by Cetegen et al.: (a) 60 $\mu\text{m}$ (surface #12), (b) 40 $\mu\text{m}$ (surface #17), (c) 20 $\mu\text{m}$ (surface #C), and (d) a new surface designed in the present work (surface #E). ....	59
Fig. 3.5.1: Control volumes for the forced convection model. ....	62
Fig. 3.5.2: Single-phase forced convection results for (a) 60 $\mu\text{m}$ , (b) 40 $\mu\text{m}$ , (c) 20 $\mu\text{m}$ -wide channel, corresponding to the geometries tested in Cetegen et al..	71
Fig. 3.5.3: (a)-(b) Temperature contours (not to scale) for the lowest and highest Reynolds number, respectively; (c)-(d) Wall heat flux profiles, corresponding to (a)-(b). ....	74
Fig. 3.6.1: Domain for flow tube (“streamline”) model. ....	77
Fig. 3.6.2: Sample mesh diagram with three flow-tubes shown for clarity. To obtain mesh-independent results, approximately 25 flow-tubes were found to be needed. (a) $i$ and $j$ coordinates (b) $n$ and $k$ coordinates.....	80
Fig. 3.6.3: Process flow diagram of the flow-tube model algorithm. ....	89
Fig. 3.6.4: Contours of vapor quality at various outlet vapor qualities: (a) 20% and (b) 50%. ....	91
Fig. 3.6.5: Void fraction vs. vapor quality from the Zivi void fraction correlation....	92
Fig. 3.6.6: Comparison of experimental results with those predicted by the model for various surfaces and working fluid combinations. Experiment design and surface design details are given in Cetegen [10]. ....	93
Fig. 4.1.1: Model domain and sample mesh for the 2.5-D microchannel model.....	100
Fig. 4.3.1: Control volumes for the continuity equation (pressure).....	102
Fig. 4.3.2: Control volumes for (a) x- and (b) y-momentum equations.....	104
Fig. 4.3.3: Comparison between pressure drop assuming homogenous and annular friction factor. ....	108

Fig. 4.3.4: Control volumes used to derive conservation equations for liquid species.	109
Fig. 4.3.5: Control volumes used to derive conservation of energy in the liquid domain.	113
Fig. 4.3.6: Control volumes used to derive conservation of energy in the solid domain.	116
Fig. 4.3.7: Boundary conditions for 2.5-D microchannel model.	123
Fig. 4.3.8: Boundary condition enforcement using fictitious cells.	123
Fig. 4.3.9: The SIMPLE Algorithm.	125
Fig. 4.4.1: Single phase fully developed comparison between 2.5-D to 3-D Model with (a) R245fa and (b) ethanol. Data points represent the 3-D CFD while lines represent the 2.5-D model.	132
Fig. 4.4.2: Single-phase developing flow comparison between 2.5-D to 3-D models with R245fa. Data points represent 3-D CFD, solid lines represent fully developed assumption using 2.5-D CFD, and dashed-lines represent developing flow assumption in the 2.5-D CFD model.	133
Fig. 4.4.3: Cross sectional cuts of velocity vectors for Surface #17: (a) $G=200 \text{ kg/m}^2\text{-s}$ , (b) $G=600 \text{ kg/m}^2\text{-s}$ , (c) $G=1400 \text{ kg/m}^2\text{-s}$ . As mass flux is increased, flow becomes increasingly three-dimensional.	134
Fig. 4.4.4: Accuracy of 2.5-D model in single-phase mode: (a) fully developed, and (b) developing.	135
Fig. 4.4.5: Effects of physics: (a)-(d) Liquid quality contours for various mass fluxes in surface #17 at 10% thermodynamic outlet vapor quality; (e) corresponding wall HTC vs. vapor quality graph; (f) wall HTC contours for thermally fully developed film evaporation with nucleate boiling turned off; (g) wall HTC contours for thermally fully developed film evaporation with nucleate boiling turned on.	140
Fig. 4.4.6: Effects of physics.	141
Fig. 4.4.7: Two-phase model validation; comparison to experimental results from Cetegen [10].	143
Fig. 4.4.8: Comparison between predicted and measured pressure drop for surfaces #12, #17, and #C.	144
Fig. 4.5.1: Arriving at a baseline geometry & parametric study.	148
Fig. 5.1.1: Working fluid selection. Fluids presented in order of increasing vapor pressure. Metrics are color coded with red signifying relatively inferior performance and green signifying relatively superior performance.	154
Fig. 5.2.1: Manifold flow configurations (a) Z-type and (b) C-type.	156
Fig. 5.2.2: Expected pressure drop distribution in inlet and outlet manifolds for (a) Z-type (b) C-type.	157
Fig. 5.2.3: Manifold model domain.	160
Fig. 5.2.4: Manifold model boundary conditions: (a) Z-type and (b) C-type.	161
Fig. 5.2.5: Control volumes used for conservation of mass for each manifold configuration: (a) Z-type and (b) C-type.	161

Fig. 5.2.6: Control volumes used for conservation of momentum for each manifold configuration: (a) Z-type and (b) C-type. ....	162
Fig. 5.2.7: Inlet and outlet pressure profiles for all three manifold configurations: (a) Z-type and (b) C-type. Both configurations have enormous pressure drops on the outlet due to the confined vapor and consequent large velocities, resulting in terrible flow distribution. ....	167
Fig. 5.2.8: L-type: (a) flow diagram, (b) boundary conditions, (c) control volume for continuity, (d) control volume for momentum, (e) inlet and outlet pressure profiles. L-type manifold maintains reasonable vapor-side velocities, and therefore achieves orders-of-magnitude better flow distribution than Z- and C-type manifolds. ....	170
Fig. 5.2.9: Flow maldistribution vs microchannel mass flux for R245fa and ethanol: (a) 250 $\mu\text{m}$ pitch and (b) 500 $\mu\text{m}$ pitch. ....	174
Fig. 6.1.1: 3-D printed alumina manifold design revisions: (a) first generation with wavy, non-parallel fins and (b) final generation with braces to prevent warping. ....	178
Fig. 6.1.2: Single-phase 3-D CFD simulation to determine the effect of a gap between the manifold and chip on heat transfer coefficient and pressure drop: (a) model geometry and (b) heat transfer coefficient (left) & pressure drop (right) vs. mass flow rate. ....	180
Fig. 6.1.3: Kapton tape to prevent electrical arcing: (a) suspected arcing location, (b) Kapton tape placement to prevent arcing locations, (c) soldered chip with Kapton tape in soldering alignment tool. ....	181
Fig. 6.2.1: Final test section design for press fit test section. ....	182
Fig. 6.2.2: Internal flow path through the (a) header and (b) manifold. ....	183
Fig. 6.2.3: (a) Thin-film platinum RTD-heater and (b) DRIE embedded heat sink. ....	184
Fig. 6.2.4: Test loop diagram. ....	185
Fig. 6.2.5: Voltage divider circuit for RTD measurement with DAQ. ....	187
Fig. 6.4.1: RTD calibration curve. ....	190
Fig. 6.7.1: SEM images of (a) microchannels, (b) cross-section of microchannels, (c) cross-section view of substrate, (d) angled view of microchannels with particulate clogging (e) manifold, and (f) manifold far view. ....	198
Fig. 6.8.1: Single-phase test results for press-fit test section before cleaning. ....	201
Fig. 6.8.2: Single-phase test results for press-fit test section after cleaning. ....	202
Fig. 6.8.3: Particle accumulation after opening up press-fit test section: (a)-(b) on tips of channels in manifold inlet region and (c)-(d) embedded into microchannels. ....	203
Fig. 6.9.1: Two-phase test results: (a) heat flux vs. RTD superheat; (b) base heat transfer coefficient vs. heat flux; (c) fin heat transfer coefficient vs. outlet vapor quality; (d) wall heat transfer coefficient vs. outlet vapor quality; (e) total pressure drop vs. outlet vapor quality; (f) total pressure drop vs. heat flux. ....	209



Fig. 6.10.1: Comparison between model and experimental results obtained here: (a) wall heat transfer coefficient vs. vapor quality, (b) pressure drop vs. vapor quality, and (c) comparison between predicted and measured pressure drop. ....	212
Fig. 7.1.1: CAD drawing of header-manifold test section: (a) chip bonded to header-manifold, (b) internal flow cavities and path, (c) sectioned isometric view, and (d) manifold unit-cell pattern. ....	217
Fig. 7.2.1: (a) Solder layer thicknesses, (b) solder atomic composition, and (c) Ag-Sn phase diagram [65]. ....	220
Fig. 7.2.2: SEM images of a working chip with solder on it: (a) before bonding and (b) after heating to 600°C in controlled environment. ....	221
Fig. 7.4.1: Advantages of uniform clamping pressure: (a) over point force clamping pressure; (b) uniform clamping pressure allows chip to conform around rounded manifold for hermetic bond without need for advanced lapping techniques. ....	224
Fig. 7.4.2: Bonding apparatus: (a) opened and (b) assembled. ....	225
Fig. 7.4.3: (a) 100 psi bonded chip and (b) profilometer scan results for 100 psig bonded chip. ....	227
Fig. 7.4.4: Summary of successful bonding results at various clamping pressures: (a) 15 psig, (b) 7.5 psig, (c) 5 psig, and (d) 3 psig. ....	229
Fig. 7.4.5: Bonding attempt of working chip at 7.5 psig: (a) before pressure test, (b) after pressure test, and (c) zoomed view of microchannels. ....	230
Fig. 7.5.1: Final wired test section for experimentation. ....	232
Fig. 7.5.2: Two-phase results with R245fa Chip 1: (a) heat flux vs. RTD superheat and (b) pressure drop vs. outlet vapor quality. ....	233
Fig. 7.5.3: Possible manifold-chip misalignments: (a) properly aligned, (b) direction perpendicular to the manifolds, and (c) direction parallel to the manifolds. ....	235
Fig. 7.5.4: Chip 1 after de-bonding: (a) lower manifold view, (b) upper manifold view, and (c) zoomed-out view near upper manifold. ....	236
Fig. 7.6.1: (a) Gas clamping method vs. (b) rope clamping method. ....	238
Fig. 7.6.2: SEM images of chip 2 and its corresponding manifold after testing and de-bonding: (a) cross-section of microchannels, (b) cross-section of chip substrate, (c) manifold measurements, (d) far view of manifold, (e) angled view of microchannel wall, and (f) far view of microchannels. ....	241
Fig. 7.6.3: Calibration curve for chip 2. ....	243
Fig. 7.6.4: Single-phase results for chip 2. ....	244
Fig. 7.6.5: Hot spots on chip 2 in single-phase mode: (a) temperature near center of chip and (b) temperature near hotspot. ....	246
Fig. 7.6.6: Hot spots on chip 2 in two-phase mode: (a) temperature near center of chip and (b) temperature near hotspot. ....	247
Fig. 7.6.7: Two-phase results for chip 2: (a) heat flux vs. RTD superheat, (b) base heat transfer coefficient vs. heat flux, (c) fin heat transfer coefficient vs. outlet vapor quality, (d) wall heat transfer coefficient vs. outlet vapor quality, (e)	

total pressure drop vs. outlet vapor quality, and (f) total pressure drop vs. heat flux. ....	249
Fig. 7.7.1: Hybrid clamping method. ....	251
Fig. 7.7.2: SEM images of chip 3 and its corresponding manifold after testing and de-bonding: (a) microchannels in manifold gap, (b) microchannels bonded to manifold wall, (c) angled view of microchannel wall, (d) close up view of microchannel walls, (e) particulate clogging, and (f) edge of microchannels. ....	254
Fig. 7.7.3: Calibration curve for chip 3. ....	254
Fig. 7.7.4: Single-phase results for chip 3. ....	255
Fig. 7.7.5: (a) Hotspots visible to the naked eye; (b) heat flux vs. RTD superheat; and (c) wall heat transfer coefficient vs. outlet vapor quality. ....	257
Fig. 7.7.6: Chip 3 with patched heater. ....	258
Fig. 7.7.7: Single-phase results for chip 3 after fixing the heater. ....	259
Fig. 7.7.8: Two-phase results for chip 3: (a) heat flux vs. RTD superheat, (b) base heat transfer coefficient vs. heat flux, (c) fin heat transfer coefficient vs. outlet vapor quality, (d) wall heat transfer coefficient vs. outlet vapor quality, (e) total pressure drop vs. outlet vapor quality, and (f) total pressure drop vs. heat flux. ....	261
Fig. 7.8.1: Test chip 3 two-phase results comparison to model: (a) wall heat transfer coefficient vs. vapor quality, (b) total pressure drop vs. vapor quality, and (c) comparison between predicted and measured pressure drop. ....	264
Fig. 9.1.1: Control volumes used for discretization in the annular film evaporation with physics-based void fraction model. ....	272
Fig. 9.2.1: Assumed velocity profiles. ....	283
Fig. 9.3.1: Control volumes to derive pressure drops per unit length for the liquid and vapor phases. ....	286

# 1 Introduction

## 1.1 Motivation

For the past 50 years, the famous prediction of the co-founder of Intel, Dr. Gordon E. Moore—that the number of transistors on integrated circuits will double every two years—has held true, increasing from 1000 transistors in the early 70’s to the billions we are familiar with today. However, as the number of transistors increases, the total power dissipation does as well, leading to an unprecedented increase in heat flux and heat density in electronic systems. Heat fluxes in power amplifiers and laser diodes already have surpassed  $1 \text{ kW/cm}^2$ , prompting new research initiatives, such as the DARPA ICECool program [1], and, in fact, heat fluxes in Gallium Nitride (GaN) High-Electron Mobile Transistors (HEMT) can theoretically approach heat fluxes in excess of  $300 \text{ kW/cm}^2$  [2]. Since the operational temperature of these devices is often limited to minimize thermomechanical stresses and maximize reliability, more efficient heat removal systems are needed to cope with the ever-increasing power densities.

The governing equation of heat transfer is given by Newton’s law of cooling [3]:

$$Q = U A \Delta T \quad (1.1.1)$$

where  $Q$  is the dissipated heat,  $U$  is the overall heat transfer coefficient,  $A$  is the area undergoing heat transfer, and  $\Delta T$  is the effective temperature difference. Since  $Q$  has been increasing,  $A$  has been decreasing, and  $\Delta T$  has remained constant, significant increases to the overall heat transfer coefficient,  $U$ , are required.

However, recently, a new trend towards parallel processing with GPU’s and multicore CPU’s has commenced. This is in part due to an inability to obtain heat transfer

coefficients large enough to sufficiently cool the electronic components operating at increasingly faster clock speeds. Thus, even while the total number of transistors continues to increase, the clock speed and dissipated power has peaked at around 4 GHz and 100 W, respectively (see Fig. 1.1.1) [4].

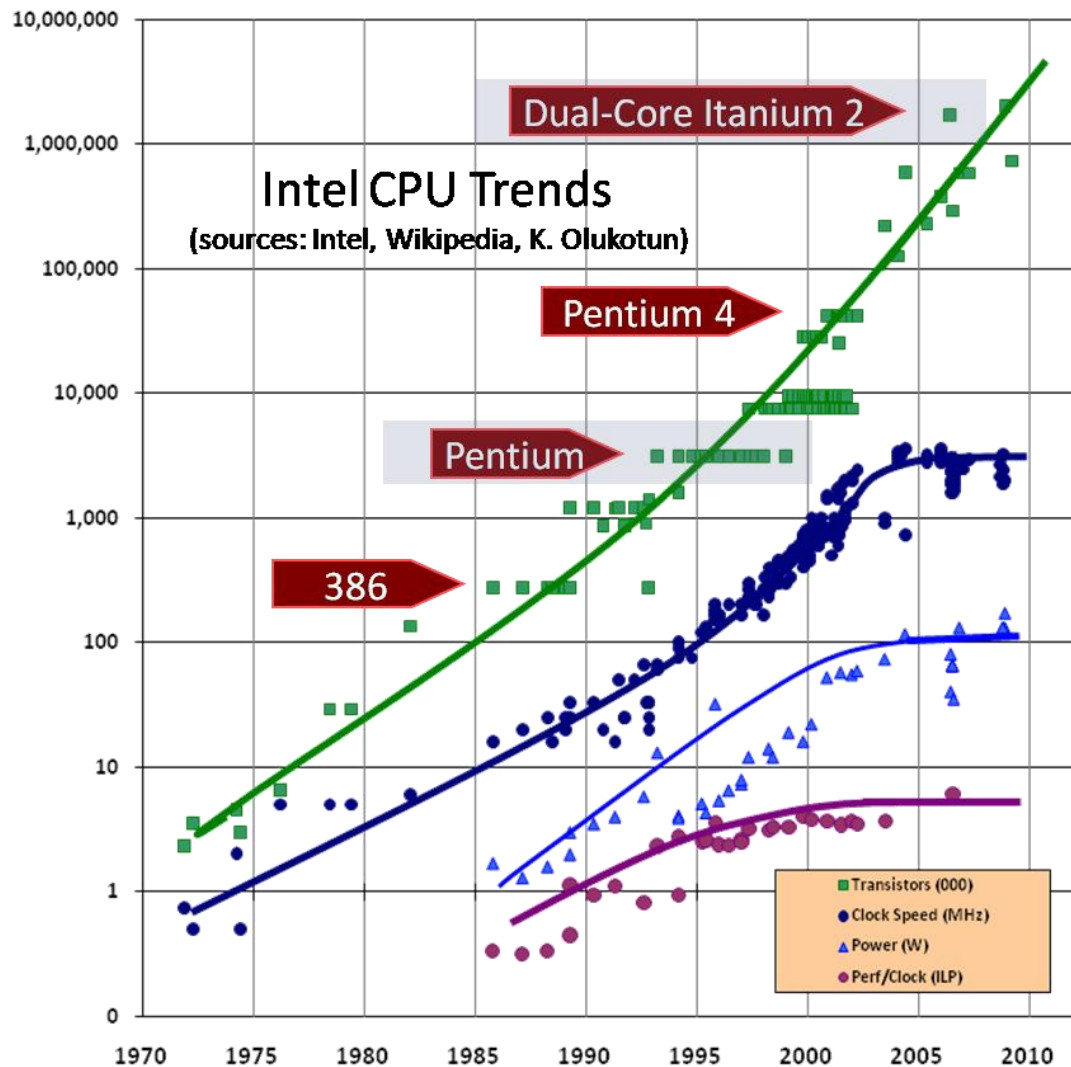


**Fig. 1.1.1: History of Intel CPU trends. While number of transistors continues to grow exponentially (Moore's Law), the clock speed and power dissipation have peaked, in part, due to an inability to adequately cool electronic components, resulting in the recent trend of multicore processors [4].**

## 1.2 Embedded Cooling

Increasing the overall heat transfer coefficient is not a simple task due to the presence of additional thermal resistances in the system. The chip package consists of several layers—the silicon active surface, where the integrated circuits are placed, the chip package (die base), a thermal interface material to join the chip package to the heat spreader, a heat spreader, a second thermal interface material to join the heat spreader to the heat sink, and the heat sink itself (see Fig. 1.2.1(a)). From the heat sink, two additional thermal resistances remain: the convective heat transfer coefficient between the fluid and the walls of the heat sink, and the bulk (caloric) thermal resistance due to the changing temperature of the fluid. The thermal resistance network is shown in Fig. 1.2.1(b). The convective heat transfer coefficient,  $h$ , is therefore just one of the many serial thermal resistances obstructing heat flow from the active surface (junction).

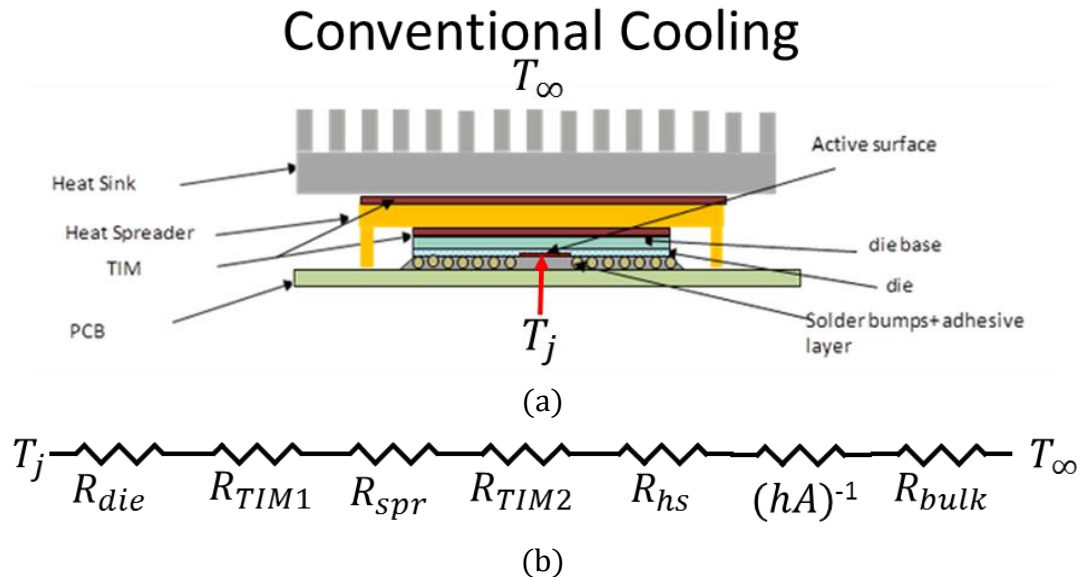


**Fig. 1.2.1: Conventional cooling paradigm: (a) diagram of a conventional silicon microchip; (b) accompanying thermal resistance diagram.**

To effectively reduce the overall thermal resistance, the thermal resistance of each component should be reduced or eliminated. One way to significantly reduce thermal resistance is to embed the heat sink directly in the silicon die (see Fig. 1.2.2(a)), thereby removing the heat spreader and the need for thermal interface materials (TIMs), which can account for a significant portion of overall thermal resistance. The thermal resistance would then contain three terms: the thermal resistance of the die itself, the thermal resistance of convection, and the bulk (caloric) thermal resistance of the fluid, as shown in Fig. 1.2.2(b).

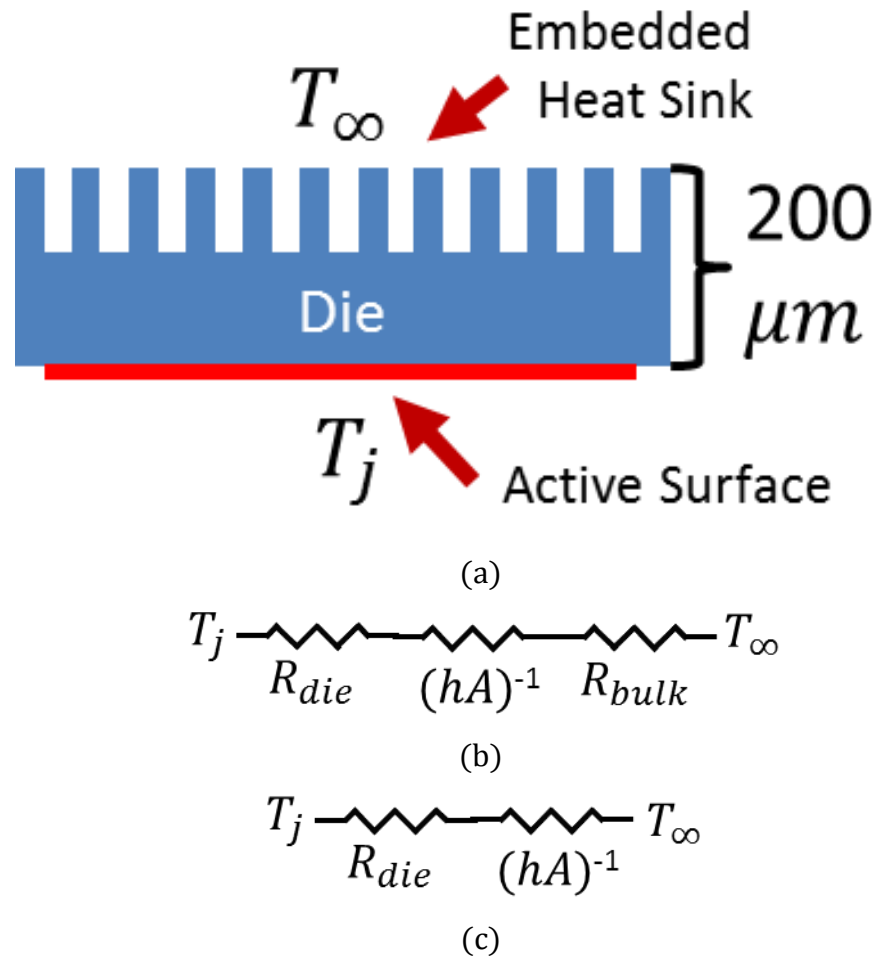


**Fig. 1.2.2: Embedded cooling paradigm: (a) diagram of a silicon microchip with an embedded heat sink; (b) accompanying thermal resistance diagram in single-phase mode; and (c) thermal resistance diagram in two-phase mode.**

### ***1.3 Single-Phase vs. Two-Phase Cooling***

For air-cooled integrated circuits, the thermal resistance of convection would be too large to make embedded cooling of integrated circuits desirable. One alternative is liquid cooling, where water or a dielectric fluid is used to capture and reject the heat. Due to the higher thermal conductivities and specific heat densities of liquids over air, liquid cooling produces higher convective heat transfer coefficients, lower bulk resistances, and reduced pumping power than air cooling. However, there is an intrinsic limitation on single-phase operation: all of the heat must be removed by an increase in the fluid temperature. This has a few important effects. First, it serves as an additional thermal resistance—known as a bulk thermal resistance—in the thermal resistance network (see Fig. 1.2.2(b)). In addition, at moderate to high heat fluxes, single-phase cooling requires a large mass flow rate to keep the surface temperature uniform, resulting in large pressure drops and pumping powers, reduced COP, and high liquid jet velocities, which could lead to surface erosion and reduced reliability. These problems are further exacerbated in applications where only dielectric liquids may be considered, due to the reduced specific heat densities of these fluids compared to water.

Two-phase cooling, on the other hand, has a few advantages over single-phase cooling. First, for low relative pressure drops, saturation temperature remains constant, allowing for more surface temperature uniformity, thereby improving reliability. In addition, reduced liquid velocities, mass flow rates and pumping powers can be expected—even for dielectric liquids—due to the use of the latent heat of evaporation to transport energy. Finally, reduced thermal resistance can be expected due to two independent effects: the elimination of the bulk thermal resistance, simplifying the

thermal resistance network to that shown in Fig. 1.2.2(c), and an increase in the convective heat transfer coefficient due to the presence of nucleate boiling and thin film evaporation, the latter of which is can provide order-of-magnitude higher heat transfer coefficients than the state of the art.

#### **1.4 *Thin Film Evaporation vs. Nucleate Boiling***

A further discussion of the advantages of thin film evaporation is warranted. Fundamental studies of phase change mechanisms reveal a substantial potential to increase heat transfer coefficients by switching from nucleate boiling to thin film evaporation. Nucleate boiling occurs on superheated surfaces that are submerged in a sub-cooled or saturated liquid [3]. Microscopic cracks—or nucleation sites—along the superheated surface trap vapor, creating a liquid-vapor interface where evaporation occurs. Evaporation drives bubble formation, expansion, and departure in a cyclical process, but requires a significant superheat to enable the bubble to overcome the capillary and/or static pressures suppressing bubble growth [3]. A schematic diagram of nucleate boiling appears in Fig. 1.4.1(a).

Rather than evaporate into a bubble—which must grow against capillary and static pressure and must rely on buoyancy or a flow field to detach the bubble and carry it into the vapor bulk [5]—it would be more efficient to evaporate directly into the vapor bulk. However, in practice, this will not occur unless the thermal resistance from direct conduction through the liquid bulk is less than the thermal resistance from nucleate boiling. Since thermal resistance is proportional to conduction length, as the liquid film thickness decreases to the scale of the nucleation sites, its thermal resistance will become



less than the thermal resistance from nucleate boiling, resulting in direct evaporation into the vapor bulk. This is known as thin film evaporation. A schematic diagram of thin film evaporation appears in Fig. 1.4.1(b).

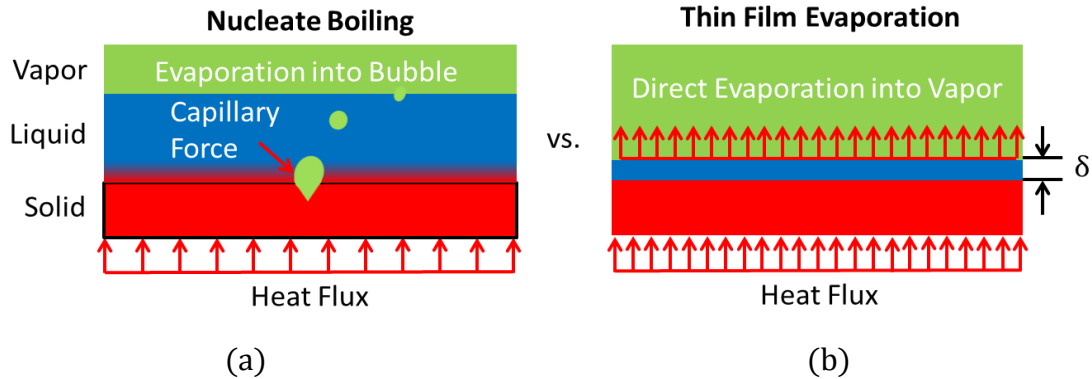


**Fig. 1.4.1: Schematic diagrams of (a) nucleate boiling vs. (b) thin film evaporation.**

Thus, flow boiling is, in essence, thin film evaporation into a bubble, and accordingly, is less efficient than thin film evaporation directly into the vapor bulk. Moreover, whereas thermal resistance in flow boiling is a complex phenomenon governed by many parameters—such as superheat, vapor quality, pressure, Reynolds number, and Prandtl number [3]—thermal resistance in thin film evaporation is relatively simple: it is directly proportional to the film thickness. As such, thin film evaporation is easier to understand and model, and provides the potential to increase heat transfer coefficients by orders of magnitude, since thermal resistance drops to zero with film thickness. A summary of the advantages of thin film evaporation over nucleate boiling is given in Table 1.4.1.

**Table 1.4.1: Comparison between flow boiling and thin film evaporation**

Category	Flow Boiling	Thin Film Evaporation
Evaporation	Into bubble	Directly into vapor
Effect of subcooling	Bubbles collapse	Longer developing length
Minimum superheat	Large	Small
Heat transfer coefficient	$h_{fb} = f(\Delta T, X, P_{sat}, Re, Pr)$	$h_{tfe} \cong k_l / \delta$

## 1.5 *The Difficulty of Thin Film Evaporation*

While thin film evaporation might be more efficient than nucleate boiling, it is difficult to realize in practice, due to the complexity of maintaining and organizing a thin film on a superheat surface. There are two main approaches that utilize thin film evaporation: spray cooling and capillary flow.

### 1.5.1 Spray Cooling

Spray cooling utilizes an atomizer to spray micron-sized droplets directly on top of superheated components in hopes of achieving a thin film for superior cooling [6]. However, in practice, this is often difficult. For instance, if too little flow for the given power level is supplied, large regions of dryout will form next to evaporating droplets, creating large thermal gradients on the surface (see Fig. 1.5.1(a)). Conversely, if too much flow is supplied to the surface, the droplets will coalesce into a thick film of liquid, resulting in nucleate boiling and subsequently, reduced heat transfer coefficients and elevated surface temperatures (see Fig. 1.5.1(b)). The challenge, therefore, is to carefully monitor the film thickness and properly control the flow rate in order to achieve a thin film [6]. As expected, this is often more difficult in practice, especially if the superheat

surface possesses surface area enhancements, such as pins or fins, which have been shown to improve heat transfer performance in spray cooling. Thus, in practice, often a combination of thin film evaporation and nucleate boiling is present in spray cooling systems.

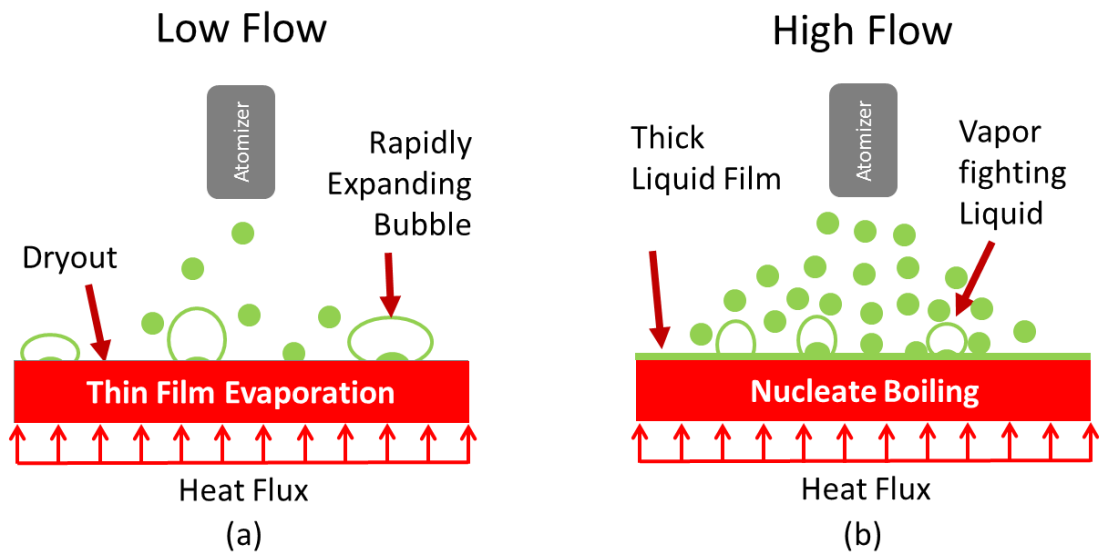


**Fig. 1.5.1: Schematic diagram of spray cooling: (a) flow is too small such that large regions of dryout occur; (b) flow is too large such that a thick film of liquid forms resulting in nucleate boiling.**

Moreover, spray cooling possesses a few additional undesirable qualities: first, increasing the flow will not always reduce the surface temperature—such as in jet impingement—due to the transfer of thin film evaporation dominated regime (high heat transfer coefficient) to nucleate boiling dominated regime (low heat transfer coefficient) via the increase in flow; second, the liquid supply arrives in discrete droplets, leading to an unsteady and unstable liquid film which can rapidly dry out; third, the liquid and vapor lack clear paths, and often impinge on one another, leading to increased liquid maldistribution and increased pressure drops; and finally, the maximum surface heat flux is limited by the critical heat flux, due to the use of nucleate boiling [6].

## 1.5.2 Capillary Flow

Capillary flow occurs in channels smaller than the characteristic capillary length and relies on a combination of liquid wall adhesion and the surface tension of the liquid to wick liquid toward the liquid-vapor interface, where thin film evaporation occurs [5, 7]. Initially, a wetting liquid fills a groove, as shown in Fig. 1.5.2(a). Upon application of a heat flux, the liquid meniscus begins to recede into the microgroove, at which point capillary action wicks fluid toward the heat flux to replace the evaporated fluid as shown in Fig. 1.5.2(b). Eventually, a steady-state meniscus profile is reached based on the particular balance of capillary forces and frictional pressure losses [8].

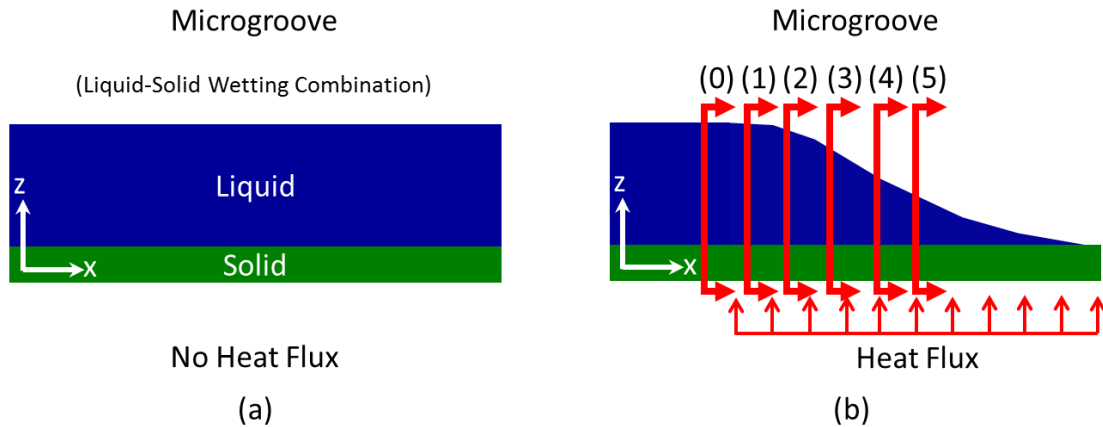


**Fig. 1.5.2: Schematic diagram of capillary flow in a microgroove due to a heat flux at the base: (a) completely wetted groove in absence of heat flux; (b) after the application of the heat flux.**

Upon examining the microgroove cross section, the trend appearing in Fig. 1.5.3 is observed: far from the heat flux, the liquid completely fills the groove, corresponding to an infinite meniscus radius (Fig. 1.5.3(a)); as the meniscus begins to recede, the radius decreases while remaining attached to the top of the groove wall (Fig. 1.5.3(b)-(d)); eventually, the meniscus detaches from the top of the groove wall and recedes into the groove at constant radius (Fig. 1.5.3(d)-(f)) [8]. Thus, capillary flow is very well

organized—especially when compared to spray cooling. Due to it this, a stable thin film naturally forms along the interline between the liquid-vapor interface and the solid wall [5, 7, 9].

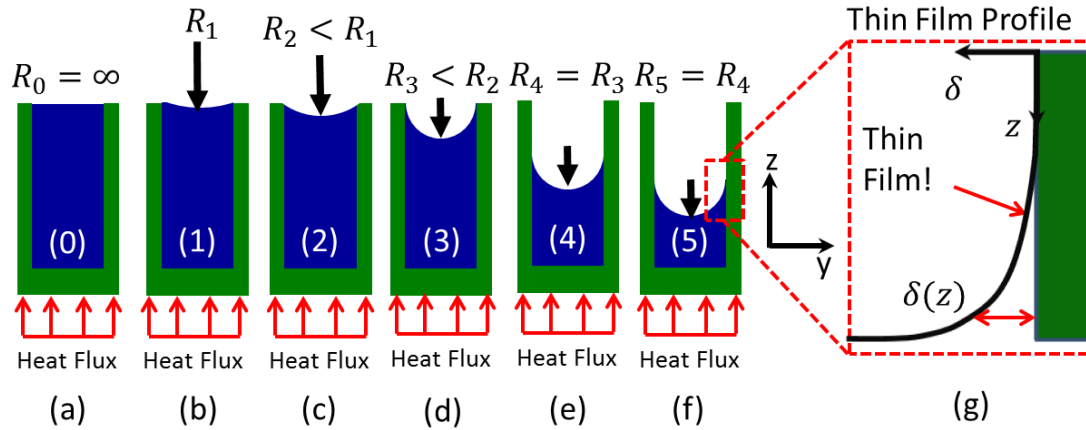


**Fig. 1.5.3: (a)-(f) Cross sections of capillary flow in a microgroove at various positions along the flow direction; (g) close-up of thin film profile near grooved wall.**

However, while capillary flow naturally forms a thin film, the fraction of total area undergoing thin film evaporation relative to the total heat transfer area is usually small, diluting any benefit from the order-of-magnitude larger heat transfer coefficients in the thin film region. Accordingly, capillary flow does not directly benefit from surface area enhancement, since the thin film area does not increase with microchannel aspect ratio. Finally, capillary flow is also subject to the capillary limit [5, 7]—the upper limit to the dissipated heat beyond which the meniscus will fully recede. Thus, the heat flux and/or heat capacity of such systems is intrinsically limited.

## 1.6 FEEDS Technology

One way to avoid the drawbacks of spray cooling and capillary flow is a new technology called “FEEDS:” Film Evaporation on micro-Enabled surface and fluid Delivery System. A schematic diagram of a FEEDS system is shown in Fig. 1.6.1. FEEDS utilizes an array of manifolds oriented perpendicular to a microgrooved surface to convert an array of long microgrooves into a system of short, parallel microchannels. It has been shown analytically in Cetegen et al. [10] that single-phase FEEDS has the potential to reduce pressure drop and pumping power by a factor of  $n^2$ —where  $n$  is the number of divisions—due to the simultaneous reduction of flow rate and flow length, both of which are linearly correlated with pressure drop and pumping power. Meanwhile, reduced flow length enhances heat transfer by taking advantage of the higher heat transfer coefficients present in thermally developing flow.

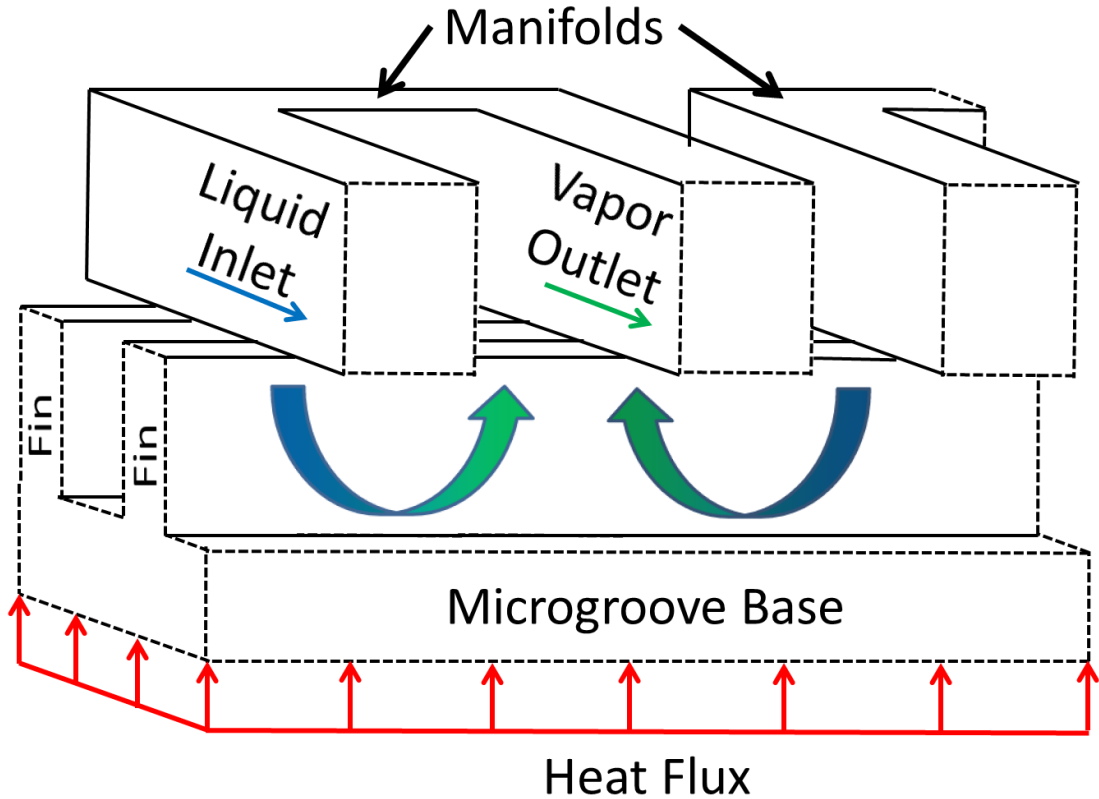


**Fig. 1.6.1: Schematic diagram of FEEDS system. A system of manifolds arranged perpendicular to a microgrooved surface is used to divide an array of long microchannels into a system of parallel ones, reducing pressure drop and pumping power and increasing heat transfer coefficient.**

In two-phase flow, FEEDS possesses additional benefits. Rather than rely on careful monitoring and controlling of film thickness to create a thin film, the thin gaps between the fins can be used to directly create a thin film, since the upper limit of the film thickness is geometrically limited by the channel width (gap), as shown in Fig. 1.6.2(a). Moreover, the manifold pitch can be used to guide the fluid distribution such that sufficient wetting occurs, as shown in Fig. 1.6.2(b)-(c). Furthermore, high aspect ratio microchannels can be used to enhance surface area and further reduce thermal resistance. Since liquid feed channels and vapor venting channels are separate, liquid and vapor do not impinge on each other and have clear paths, reducing flow maldistribution

and decreasing pressure drops. Finally, since thin film evaporation is used rather than nucleate boiling, the heat flux is not limited by critical heat flux, and due to the use of an active pump, the system is not limited by the capillary limit. Thus, FEEDS technology possesses numerous advantages over other means of obtaining thin film evaporation.

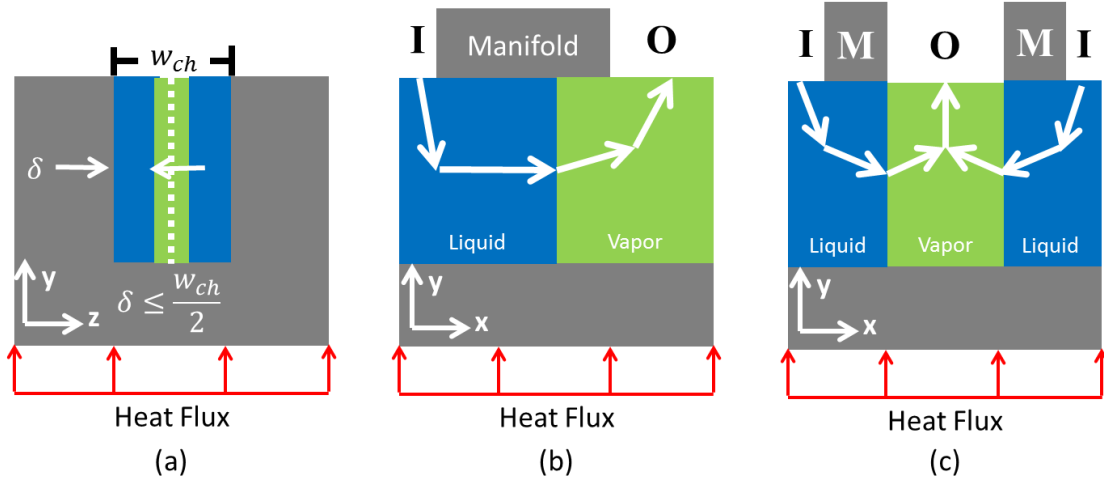


**Fig. 1.6.2: (a) Geometric limit of film thickness in a microgroove; (b)-(c) use of FEEDS manifold pitch to control intra-microchannel flow distribution.**

Using FEEDS technology, previous researchers [10] were able to obtain  $1.2 \text{ kW/cm}^2$  heat flux, and total base conductances as high as  $330 \text{ kW/m}^2\text{-K}$  at moderate pressure drops ( $< 100 \text{ kPa}$ ) and low vapor qualities (10-20%).

## 1.7 ICECool Fundamentals

Recently, the Defense Advanced Research Project Agency (DARPA) launched a new initiative entitled “ICECool Fundamentals” to study fundamentals of two-phase high heat flux heat transfer in embedded microchannels. In particular, DARPA laid out strict objectives that are summarized in the table of metrics, below [1]:



Category	Parameter	Metric	Units
Evaporative Cooling	Coolant details		
	Quality <sub>inlet</sub> and Quality <sub>outlet</sub>	Proposer defined (inlet) > 90 % (outlet)	% of mass flow in vapor
	$\Delta P_{(\text{inlet-outlet})}$ pressure drop	$< 0.1 P_{\text{sat}}$	kPa
	Coolant flow rate	Proposer defined	cm <sup>3</sup> /s
	Heat removed		
	Heat flux (removed)	> 1	kW/cm <sup>2</sup>
	Heat density (removed)	> 1	kW/cm <sup>3</sup>
	Total heat (removed)	Proposer defined	W
	$\Delta T$ across heated chip	$\Delta T < 10$	K
	Temperature rise above inlet	$\Delta T < 30$	K
Flow Manifold	Manifold and connector details		
	Hermetic connector leakage	< 1%	% per year
	Power Considerations		
	Pumping power (consumed)	Proposer defined	W
	Thermofluid CoP	$\geq 30$	-
Hot Spot Mitigation	Hot spot details		
	Hot spot flux	$\geq 5$	kW/cm <sup>2</sup>
	Temperature rise of hot spot	$\Delta T < 5$	K
Reliability	Physics of failure	Induced functional failures in chip	description
	Erosion and corrosion	Proposer defined	μm per year
	Lifetime		
	Design for reliability (MTTF)	10 <sup>4</sup>	hours
	Demo of thermal components	10 <sup>3</sup>	on/off cycles
	Demo of thermal system	10 <sup>2</sup>	hours

**Fig. 1.7.1: Summary of metrics required by ICECool Fundamentals for the background heat flux. Table taken from DARPA-BAA-12-50 [1].**

Thus, while heat fluxes in excess of the 1 kW/cm<sup>2</sup> required by the program have already been achieved with FEEDS microchannels, the corresponding vapor qualities did not meet the requirements; similarly, while heat transfer coefficients on the order of 333 kW/m<sup>2</sup>-K were achieved in the past, the corresponding vapor quality and heat flux were not on par with the ICECool metrics. Accordingly, more work is required to achieve all of these metrics simultaneously. In addition, it is worth noting that in addition to specifying heat flux, ICECool has strict requirements for power density. As the reader will see later on, (see Fig. 2.4.1), the experimental apparatus in the previous work would not meet these objectives, since the manifold is orders of magnitude larger than chip

being tested. Accordingly, further work is required to reduce the manifold size without sacrificing performance in order to meet the ICECool metrics and allow integration of a FEEDS system into a real-world system.

Finally, it is worth noting that in addition to requirements for thermal and hydrodynamic performance of the embedded cooler, ICECool also lays out requirements for hotspot mitigation and reliability. However, while a multidisciplinary team was established and collaborated with to ensure those requirements were met, they are beyond the scope of this work and will not be explicitly discussed.

## **1.8 Objectives**

Thus, the objectives of this project are:

- (1) To understand and model the governing physics dictating the observed FEEDS trends;
- (2) To assemble those physics into a comprehensive model in order to design a system to meet ICECool requirements;
- (3) To design a system with a form-factor compatible with ICECool requirements, without sacrificing flow distribution and while still cooling a full  $1\text{cm} \times 1\text{cm}$  chip;
- (4) To experimentally test the designed FEEDS embedded cooler and validate the model.

## **1.9 *Dissertation Outline***

The dissertation continues with Chapter 2, which provides a review of recent works in manifold-microchannels, embedded cooling, and single-phase and two-phase high flux cooling. Chapter 3 presents preliminary modeling used to understand the various physical phenomena that are thought to contribute to two-phase FEEDS thermal performance, while Chapter 4 details a custom-coded 2.5-D microchannel model which combines all of the preliminary models into one master model. Chapter 5 discusses experimental design, and details a system level model to aid in evaluating fluids for working fluid selection, and a 1-D manifold model used to select manifold flow configuration and design. Chapter 6 details the experimental test loop and the experiments performed with a press-fit FEEDS test section, while Chapter 7 details the experiments performed with bonded FEEDS test sections. The dissertation concludes with Chapter 8, which summarizes the work conducted in this dissertation, highlights the major contributions, and provides recommendations for future work.

## 2 Literature Review

This chapter will review relevant literature pertaining to single-phase and two-phase manifold-microchannels, embedded cooling, and single-phase and two-phase high flux cooling.

### 2.1 *Manifold Microchannel Heat Exchangers*

Single-phase manifold-microchannels have been extensively studied in the literature. Manifold-microchannels began with Harpole and Eninger [11] as a 2-D analytical model assuming fully developed flow and Nusselt numbers. The authors demonstrated cooling of  $1 \text{ kW/cm}^2$  using water as a coolant. Next, Copeland et al. [12] used 3-D Computational Fluid Dynamics (CFD) to parametrically analyze the effects of the various geometric variables associated with manifold-microchannels. The authors neglected the effects of conjugate conduction (i.e. the solid domain), assuming instead an isothermal or isoflux boundary condition on the solid-liquid interface. Since then, numerous numerical [13-15] and experimental [15, 16] studies have been conducted with water [14, 15], air [16], and nanofluids [17], including the effects of nanoparticle diameter and volume fraction on Nusselt number, pumping power, and entropy generation.

In particular, our research group has extensively studied manifold-microchannels, conducting both multi-objective optimization and experimental validation for single-phase flows. Cetegen et al. [10] conducted multi-objective optimization on single-phase manifold-microchannel heat sinks, and experimentally validated select test points. More recently, Arie et al. [18, 19] conducted numerical modeling and optimization for a single-

phase liquid plate heat exchanger. Optimization work was also performed using air as a working fluid [20]. Moreover, optimization has been performed for an air-to-air heat exchanger fabricated using 3-D printing [21].

Work has also been conducted using manifold-microchannels operating in two-phase mode. Jha et al. [22, 23] experimentally tested and characterized a manifold-microchannel tubular evaporator. Boyea et al. [24] tested and characterized a manifold-microchannel tubular condenser.

## ***2.2 Embedded, Manifold-microchannel Cooling***

Embedded manifold-microchannel cooling has become increasingly popular in recent years. Kermani et al. [25, 26] tested the applicability of embedded manifold-microchannel coolers for concentrated solar cells. Manifolds and microchannels were etched using DRIE in silicon wafers, and bonded together using Ag-Sn solder. Heat fluxes of  $75 \text{ W/cm}^2$  were obtained using water as a working fluid.

Similarly, Boteler et al. [27] investigated the potential of manifold-microchannels to cool power electronics. Manifolds and microchannels were etched from Si wafers using deep reactive ion etching (DRIE), and bonded together using Au-Sn solder. In a separate work, the authors also conducted a numerical analysis on the effects of various geometric and operational parameters [28].

Escher et al. [29] experimentally investigated manifold-microchannel coolers for liquid-cooled chips. They tested six different geometric designs and characterized pressure drop and thermal resistance response to changing flow rate, achieving  $0.09 \text{ cm}^2 \text{ K/W}$  with a pressure drop of 0.22 bar on a  $2 \times 2 \text{ cm}^2$  chip.

### ***2.3 Single-Phase High Flux Cooling***

High flux cooling began with Tuckerman and Pease [30], who were the first to propose utilizing microchannels. A high aspect ratio microchannel device was designed and tested, achieving  $790 \text{ W/cm}^2$  with a corresponding thermal resistance of  $0.0898 \text{ }^\circ\text{C/W}$ , and the results compared to a model, with good agreement.

Zhang et al. [31] tested single-phase water and galinstan—a liquid metal eutectic alloy of gallium, indium, and tin. Microchannels were utilized for water and minichannels were utilized for galinstan, due to the order-of-magnitude higher thermal conductivity of galinstan over water. A heat flux of  $835 \text{ W/cm}^2$  was obtained with water at a thermal resistance of  $0.09 \text{ }^\circ\text{C/W}$ . After optimization via a first-order model, a heat flux of  $1003 \text{ W/cm}^2$  was obtained with a thermal resistance of  $0.071 \text{ }^\circ\text{C/W}$ . A peak thermal resistance of  $0.077 \text{ }^\circ\text{C/W}$  was obtained at a heat flux of  $1214 \text{ W/cm}^2$  at a 209 kPa pressure drop. A peak heat flux of  $1504 \text{ W/cm}^2$  was achieved.

Ditri et al. [32] tested distributed microfluidic impingement jets utilizing 40% propylene glycol/60% water mixture. The design was first simulated and then manufactured using an additive photolithographic process. A peak heat flux of  $1000 \text{ W/cm}^2$  was obtained at  $0.0031 \text{ cm}^2\text{-K/W}$  at 765 kPa pressure drop.

Altman et al. [33] modeled and micro-fabricated an intra-chip cooling structure composed of GaN-on-diamond with integral manifold-microchannels fed using an Si manifold. High aspect ratio microchannels were micro-fabricated into a CVD diamond substrate with a width of  $25 \text{ }\mu\text{m}$  and a depth of  $191 \text{ }\mu\text{m}$ . Heat fluxes in excess of  $1 \text{ kW/cm}^2$  were obtained by a monolithic microwave integrated circuit (MMIC) while simultaneously, heat fluxes in excess of  $30 \text{ kW/cm}^2$  were obtained by a high electron

mobility transistor (HEMT), all while operating below the required peak junction temperature.

Finally, Campbell et al. [34] conducted simulations for single-phase embedded cooling of GaN-on-diamond MMIC's with heat loads up to  $30 \text{ kW/cm}^2$  and average heat fluxes of  $1 \text{ kW/cm}^2$  using 50EGW as a working fluid. Their work optimized manifold-microchannel design, and, unlike most other references, considered non-Cartesian microchannel form-factors. They experimentally verified their work, and were able to obtain thermal resistances of  $0.0224 \text{ cm}^2\text{-K/W}$  at 124 kPa pressure drop.

## ***2.4 Two-Phase High Flux Cooling***

Much experimental work has been conducted in the field of two-phase high flux cooling. Adera et al. [35] etched  $84 \text{ }\mu\text{m}$  tall,  $8 \text{ }\mu\text{m}$  diameter pin-fins into a silicon substrate over a  $1 \text{ cm}^2$  area. The pin-fins were capillary-fed, and heat fluxes up to  $20 \text{ W/cm}^2$  were obtained at 100% thermodynamic outlet vapor quality, and 0 W pumping power, due to the use of capillary flow.

Palko et al. [36] utilized a diamond heat sink with laser-micromachined triangular grooves approximately  $500 \text{ }\mu\text{m}$  deep and  $250 \text{ }\mu\text{m}$  wide, and coated in a conformal  $5 \text{ }\mu\text{m}$  copper porous wick structure. Fluid was supplied via a manifold fabricated from polyimide layers, which was designed to vent the vapor flow. A peak heat flux of  $1340 \text{ W/cm}^2$  was obtained with subcooled water at approximately 0% thermodynamic outlet vapor quality (due to extreme sub-cooling) and 42 kPa pressure drop.

Kanlikar et al. [37], and more recently, Kalani et al. [38] tested  $200 \text{ }\mu\text{m}$  wide,  $200 \text{ }\mu\text{m}$  deep microchannels with a 6% tapered gap manifold. The gap between the manifold

and the microchannels allows vapor to escape from the microchannels, while the inertia of the flow due to the high mass fluxes ( $2300\text{--}5000\text{ kg/m}^2\text{-s}$ ), ensures the liquid enters and stays in the microchannel. A peak heat flux of  $1070\text{ W/cm}^2$  was obtained using water at 14% thermodynamic outlet vapor quality, and 30 kPa pressure drop.

Houshmand et al. [39] utilized microtubes of diameters ranging between  $150\text{--}265\text{ }\mu\text{m}$  to test saturated and subcooled flow boiling. Mass fluxes between  $2000\text{--}7100\text{ kg/m}^2\text{-s}$  were tested at qualities ranging from  $-4\text{--}14\%$  thermodynamic vapor quality. A peak heat flux of  $1000\text{ W/cm}^2$  was obtained using methanol at  $-4\%$  thermodynamic outlet vapor quality.

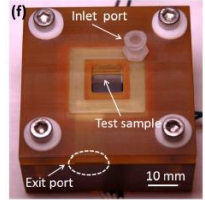
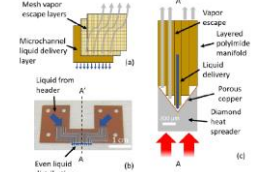
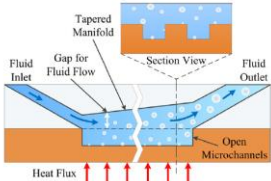
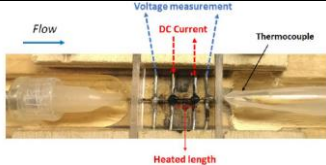
Li et al. [40] tested  $300\text{ }\mu\text{m}$  wide by  $1000\text{ }\mu\text{m}$  deep pin fins in spray cooling over a  $9\text{ cm}^2$  area. Mass fluxes ranging from  $22\text{--}41\text{ kg/m}^2\text{-s}$  were tested at thermodynamic outlet vapor qualities ranging from  $14\text{--}34\%$ . A peak heat flux of  $326\text{ W/cm}^2$  was obtained using R134a at 16% thermodynamic outlet vapor quality.

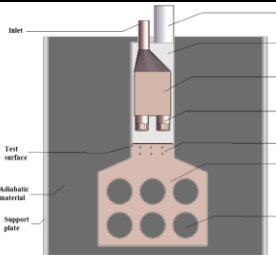
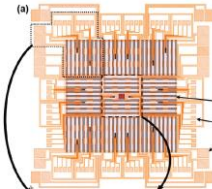
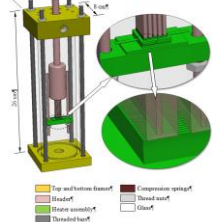
Drummond et al. [41] tested a manifold-microchannel array of  $300\text{ }\mu\text{m}$  deep and  $30\text{ }\mu\text{m}$  wide microchannels. Mass fluxes ranging between  $600\text{--}2070\text{ kg/m}^2\text{-s}$  and thermodynamic outlet vapor qualities between  $-7\text{--}25\%$  were tested. A peak heat flux of  $500\text{ W/cm}^2$  was obtained using HFE7100 at 5% thermodynamic outlet vapor quality and 70 kPa pressure drop.

Table 2.4.1 summarizes the two-phase high flux cooling survey.



**Table 2.4.1: Summary of Two-Phase High Heat Flux Cooling Survey**

Author(s)	Fluid	Mass Fluxes [kg/m <sup>2</sup> -s]	Channel Width/ Height [μm/μm]	Sub-Cooling [°C]	Vapor Quality Range [%]	Optimal Vapor Qualities [%]	Performance at Max Heat Flux	Picture of Test Section
Adera et al. [35]	Water	1.15-2.3	14/84	0	100	n/a	20 W/cm <sup>2</sup> @ 100%, & 0 kPa (capillary-fed)	
Palko et al. [36]	Water	14-43	500/500	75	-13-13	n/a	1342 W/cm <sup>2</sup> @ ~0%, & 42 kPa	
Kandlikar et al. [37] & Kalani et al. [38]	Water	2300-5000	200/200	10	0-14%	14	1070 W/cm <sup>2</sup> @ 14%, & 30 kPa	
Houshmand et al. [39]	Methanol	2000-7100	150-265 / (n/a)	6-42	-4-14	n/a	1000 W/cm <sup>2</sup> @ -4%	

Author(s)	Fluid	Mass Fluxes [kg/m <sup>2</sup> -s]	Channel Width/ Height [μm/μm]	Sub-Cooling [°C]	Vapor Quality Range [%]	Optimal Vapor Qualities [%]	Performance at Max Heat Flux	Picture of Test Section
Li et al. [40]	R134a	22-41	300/1000	<4	14-34	n/a	326 W/cm <sup>2</sup> @ 16%	
Drummond et al. [41]	HFE-7100	600-2070	33/318	5	-7-25	2-11	500 W/cm <sup>2</sup> @ 5% & 70 kPa	
Cetegen et al. [10]	R245fa	200-1400	22-60/ 406-483	0-13	0-70	10-30	1200 W/cm <sup>2</sup> @ 20%, 36 kW/m <sup>2</sup> -K, & 62 kPa	

Finally, Cetegen et al. [10] conducted experimental testing of two-phase manifold-microchannel coolers, obtaining impressive results. The apparatus used to obtain these results is shown in Fig. 2.4.1.

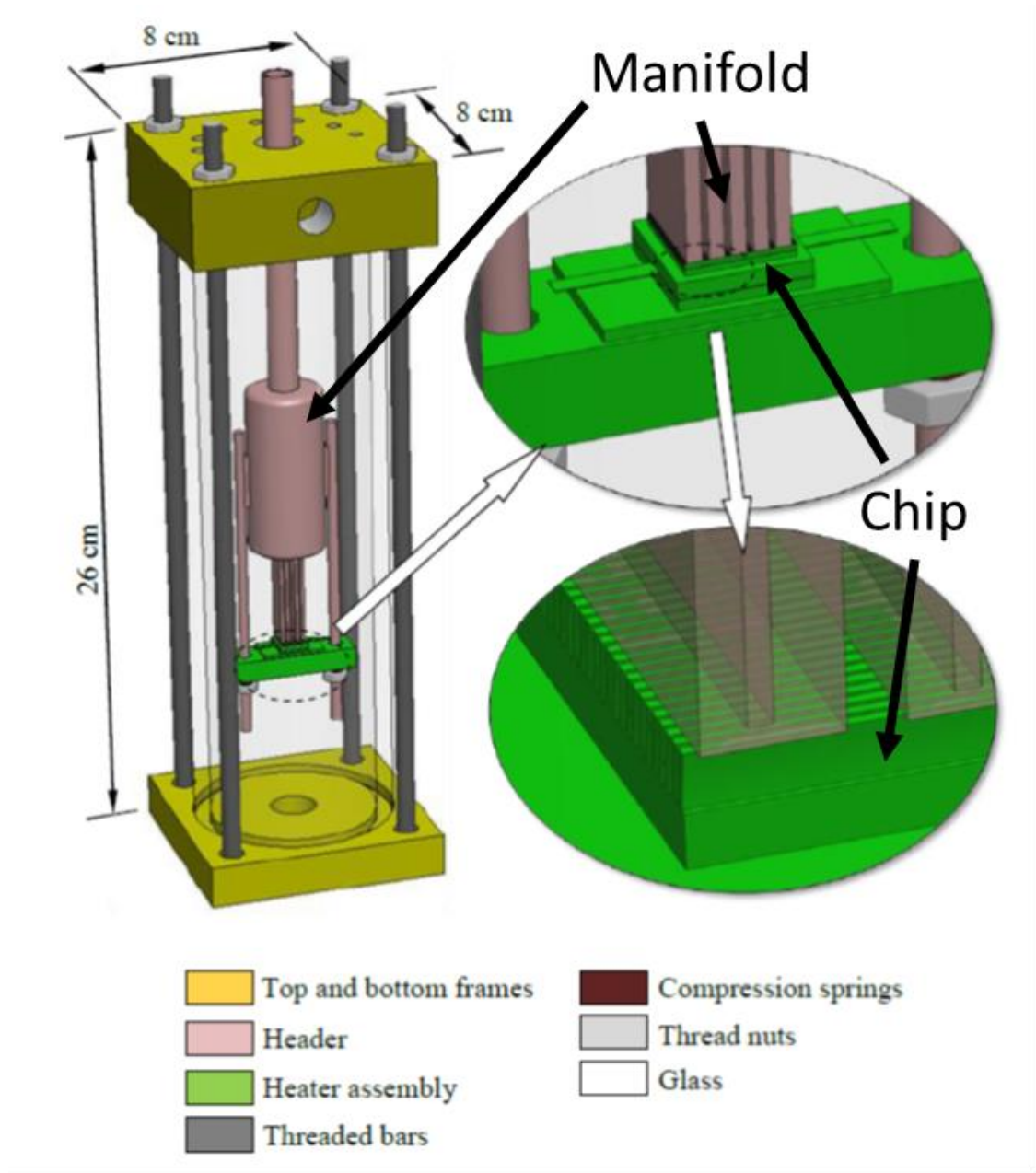
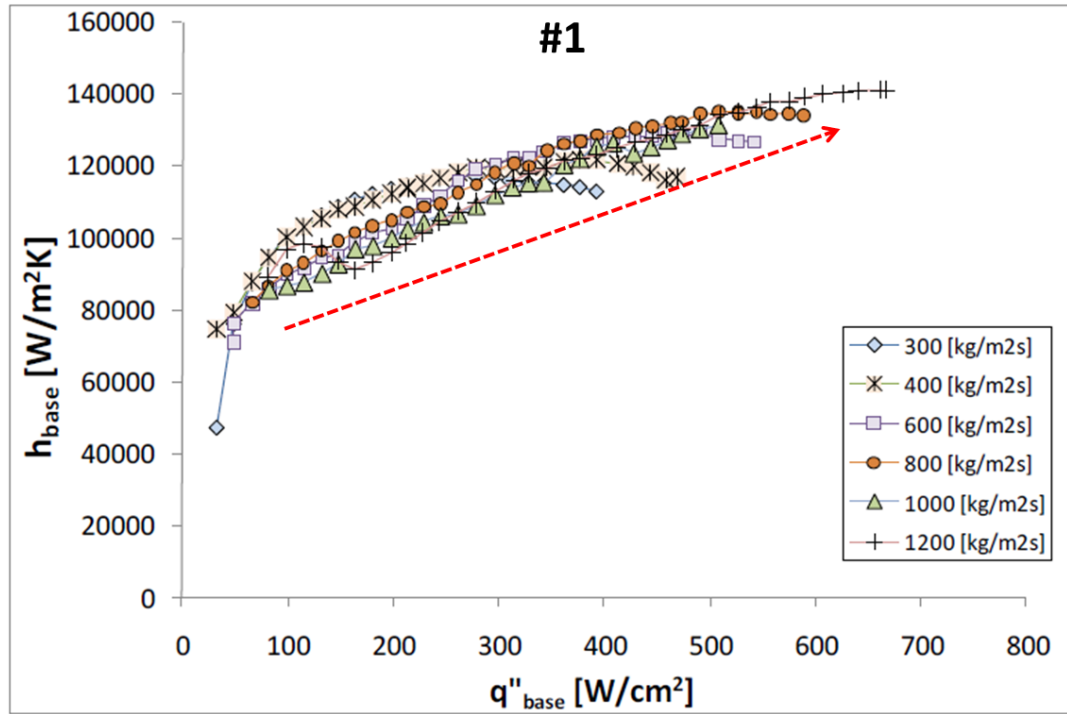


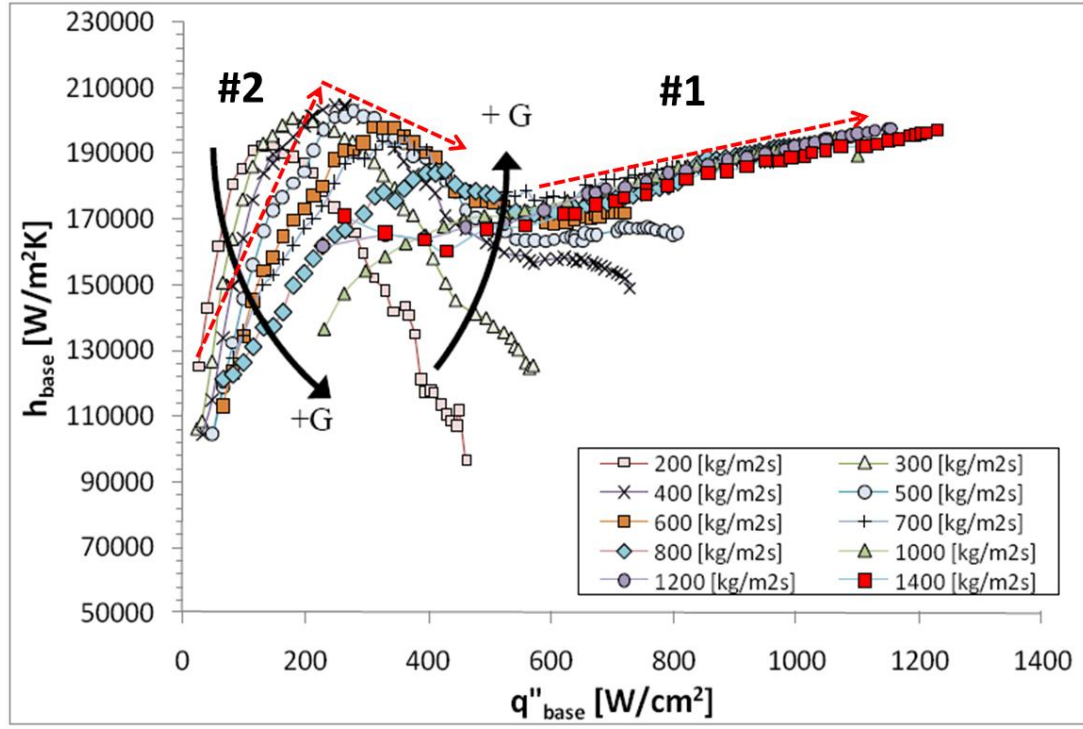
**Fig. 2.4.1: Apparatus used by Cetegen et al. [10].**

Heat transfer coefficients as high as  $330 \text{ W/m}^2\text{-K}$  and heat fluxes above  $1.2 \text{ kW/cm}^2$  were achieved at moderate pressure drops and low vapor qualities [10]. For wide

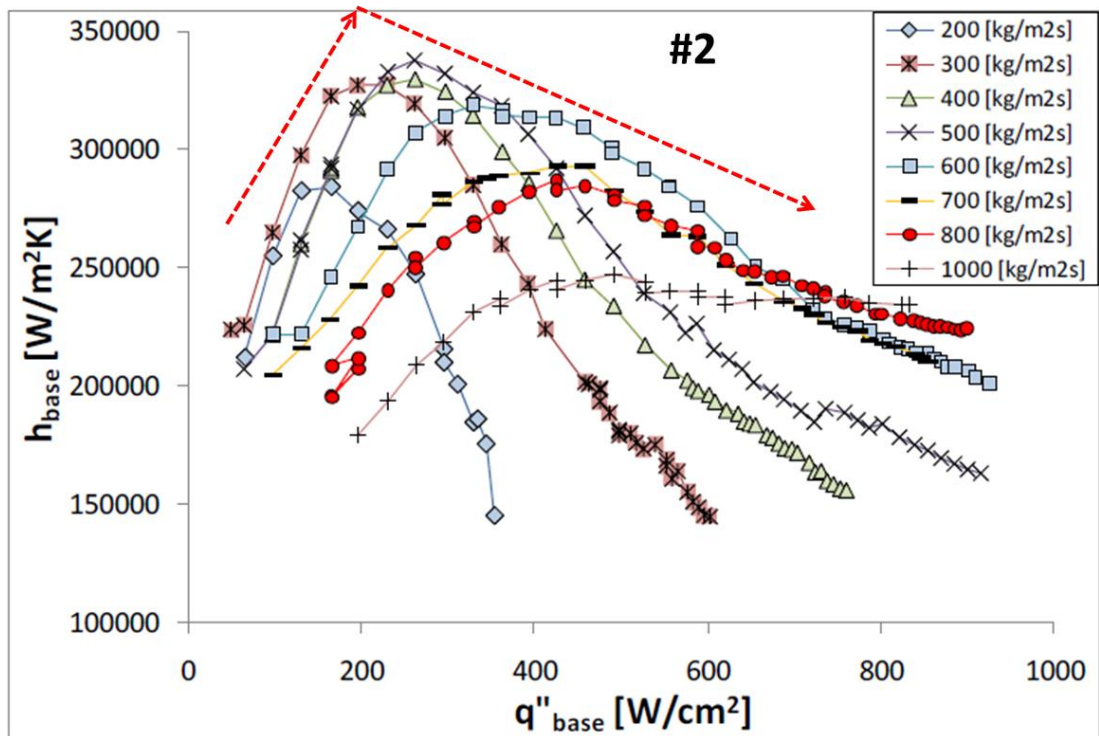
channels ( $60\ \mu\text{m}$ ), heat transfer coefficient was found to increase monotonically with heat flux regardless of mass flow rate, as shown in Fig. 2.4.2(a). For small channels ( $20\ \mu\text{m}$ ), an optimum heat flux was observed to produce a maximum heat transfer coefficient and was found to be dependent on mass flux, as shown in Fig. 2.4.2(c). Meanwhile, for moderate channel widths ( $40\ \mu\text{m}$ ), the former trend was observed for higher flow rates while the latter trend was observed for reduced flow rates, as shown in Fig. 2.4.2(b).



(a)



(b)



(c)

Fig. 2.4.2: Heat transfer coefficient vs. heat flux for various channel widths in order of decreasing channel width: (a) 60  $\mu\text{m}$  (b) 40  $\mu\text{m}$  (c) 20  $\mu\text{m}$ . Figure taken from [10].

In addition, the data were compared to the available correlations, and a quantitative lack of agreement was found for high Reynolds numbers, and a qualitative and quantitative lack of agreement was found for low Reynolds' numbers, as shown in Fig. 2.4.3(a) and Fig. 2.4.3(b), respectively. Despite the available correlations being slightly out of range with respect to hydraulic diameter and formulated for a standard microchannel flow configuration (rather than FEEDS), this qualitative and/or quantitative lack of agreement suggests some new physics are at play—due to the smaller hydraulic diameters and the FEEDS flow configuration—which are not included in the available standard feed correlations. Accordingly, correlations cannot be used in FEEDS design, and novel modeling work is required to understand and arrive at improved FEEDS designs.

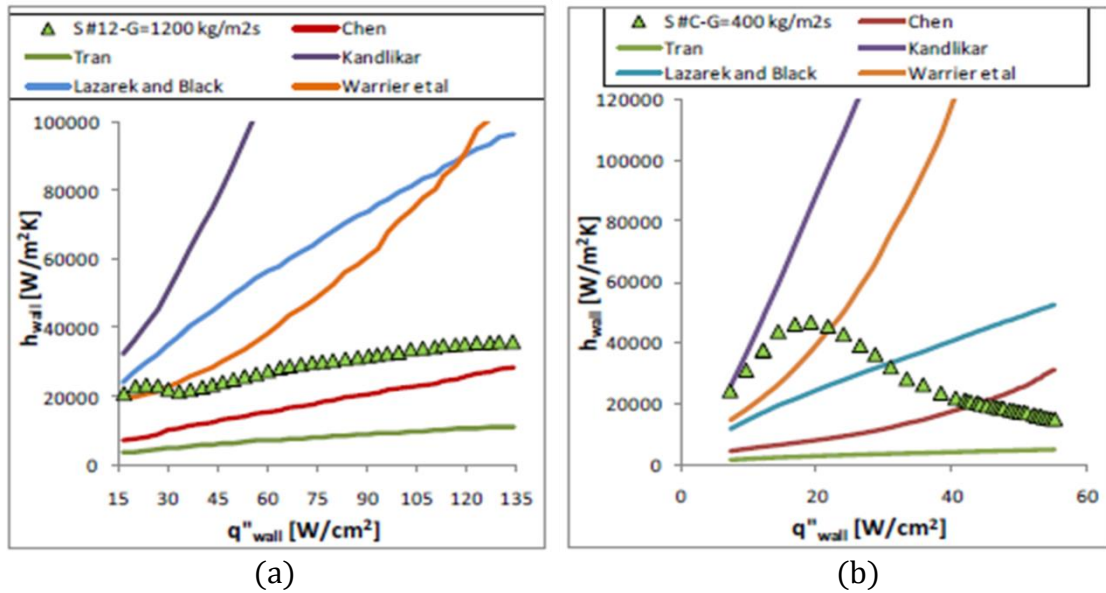


**Fig. 2.4.3: Comparison between experimental data and correlations for (a) high Reynolds numbers; and (b) low Reynolds numbers. Figures taken from [10].**

Further still, two-phase flow visualizations and data analysis [10] have indicated the presence of many complicated phenomena, including

- (1) Nucleate flow boiling

- (2) Annular film evaporation
- (3) Single-phase forced convection
- (4) Intra-microchannel flow distribution and dryout
- (5) Fin conduction and efficiency.

It should come as no surprise that standard flow boiling correlations failed to match previous experimental data, since the governing physics in FEEDS systems are not accounted for in standard correlations. Accordingly, much computational modeling work is needed to understand the complexity of FEEDS, in order to arrive at improved designs.

## ***2.5 Research Opportunities***

From Table 2.4.1, it is clear that while heat fluxes in excess of  $1 \text{ kW/cm}^2$  have been obtained using FEEDS and other methods, the corresponding vapor qualities have been far below the ICECool metric of 90%. Accordingly, much work is needed to increase vapor qualities in order to achieve the ICECool metrics. Furthermore, while previous FEEDS research has yielded impressive results, the governing physics is not yet well-understood, and much opportunity for modeling work to understand the physics of FEEDs exists. Further still, the previous FEEDS system occupies a large volume, and its heat density is far below the ICECool metric. Accordingly, work is needed to reduce the volume of the FEEDS system without sacrificing intra-microchannel flow distribution and resulting performance.

### **3 Preliminary Microchannel Modeling**

The approach towards meeting the project objectives began with creating reduced-order numerical models to probe the physics and understand how each of the five aforementioned physical phenomena affects the FEEDS system. The five physical phenomena are

- (1) Nucleate flow boiling
- (2) Annular film evaporation
- (3) Single-phase forced convection
- (4) Intra-microchannel flow distribution and dryout
- (5) Fin conduction and efficiency.

In total, five such reduced-order numerical models were created, each of which investigates one or more of the aforementioned five physical phenomena. The five models are

- (1) First-order correlation comparisons
- (2) Flow regime mapping
- (3) Annular film evaporation with physics-based void fraction model
- (4) Single-phase forced convection model
- (5) Flow tube (“streamline”) model.

#### **3.1 Preliminary Model Domains**

Since simulating the entire manifold-microchannel array is computationally expensive, all of the models simplify the domain. The symmetries inherent in a manifold-microchannel system are utilized to arrive at a “unit-cell,” which is the smallest



repeatable pattern that can be used to model a manifold-microchannel system [10, 12, 25, 42, 43]. The unit-cell of a manifold-microchannel system is shown in Fig. 3.1.1. The definitions of the geometric variables used throughout are also given in Fig. 3.1.1.

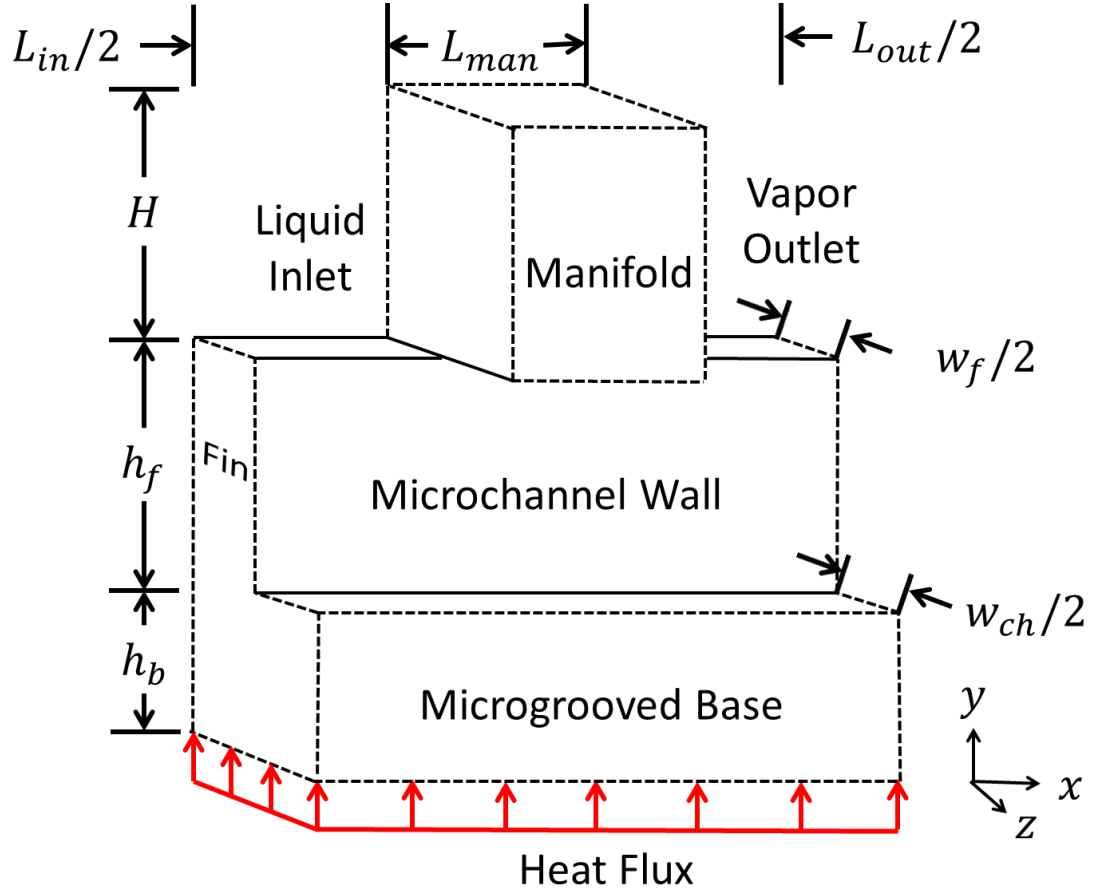


**Fig. 3.1.1: Unit cell of a manifold-microchannel system with geometric definitions.**

Due to the preliminary and first-order nature of this preliminary modeling work, the models discussed in this chapter will further simplify the domains, taking only a 1-D slice of the domain, as shown in Fig. 3.1.2.

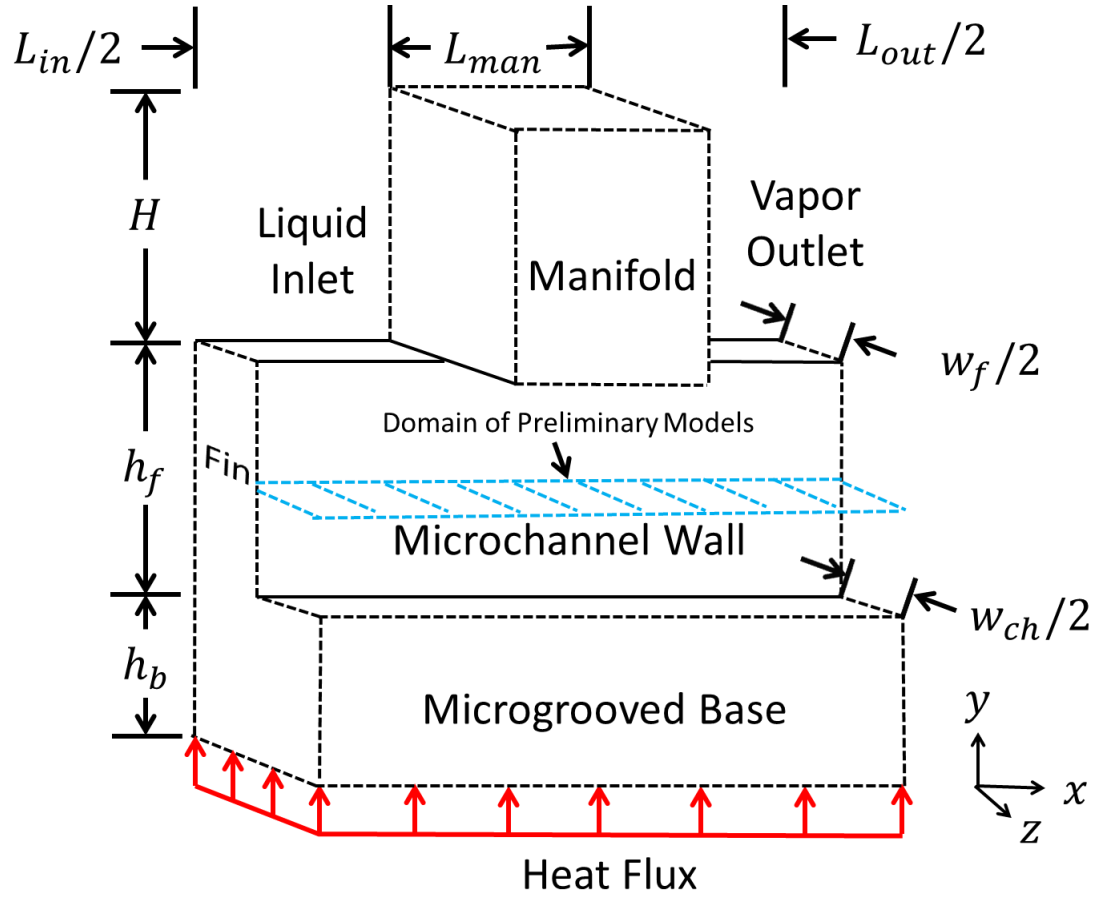


**Fig. 3.1.2: Domain of preliminary models, excluding the flow tube model.**

The basic modeling approach is now outlined. First, the effect of nucleate boiling was investigated by comparing past experimental data [10] to the available flow boiling correlations in the literature. Flow regime maps were then used to predict the expected flow regimes for the past experimental data. Next, annular film evaporation was investigated using a 1-D mixture model which computes the void fraction and subsequent liquid film thickness using the Young-Laplace equation. Third, the combined effects of single-phase fully developed and developing forced-convection on an evaporating, annular film was investigated using a 1-D model. Finally, the effects of intra-microchannel flow distribution and fin conduction were investigated using a flow-tube model, which divides the manifold-microchannel unit cell into a system of parallel, non-

interacting, evaporating streamlines and computes wall temperature using a 1-D fin equation. The preliminary modeling effort is summarized in Fig. 3.1.3.

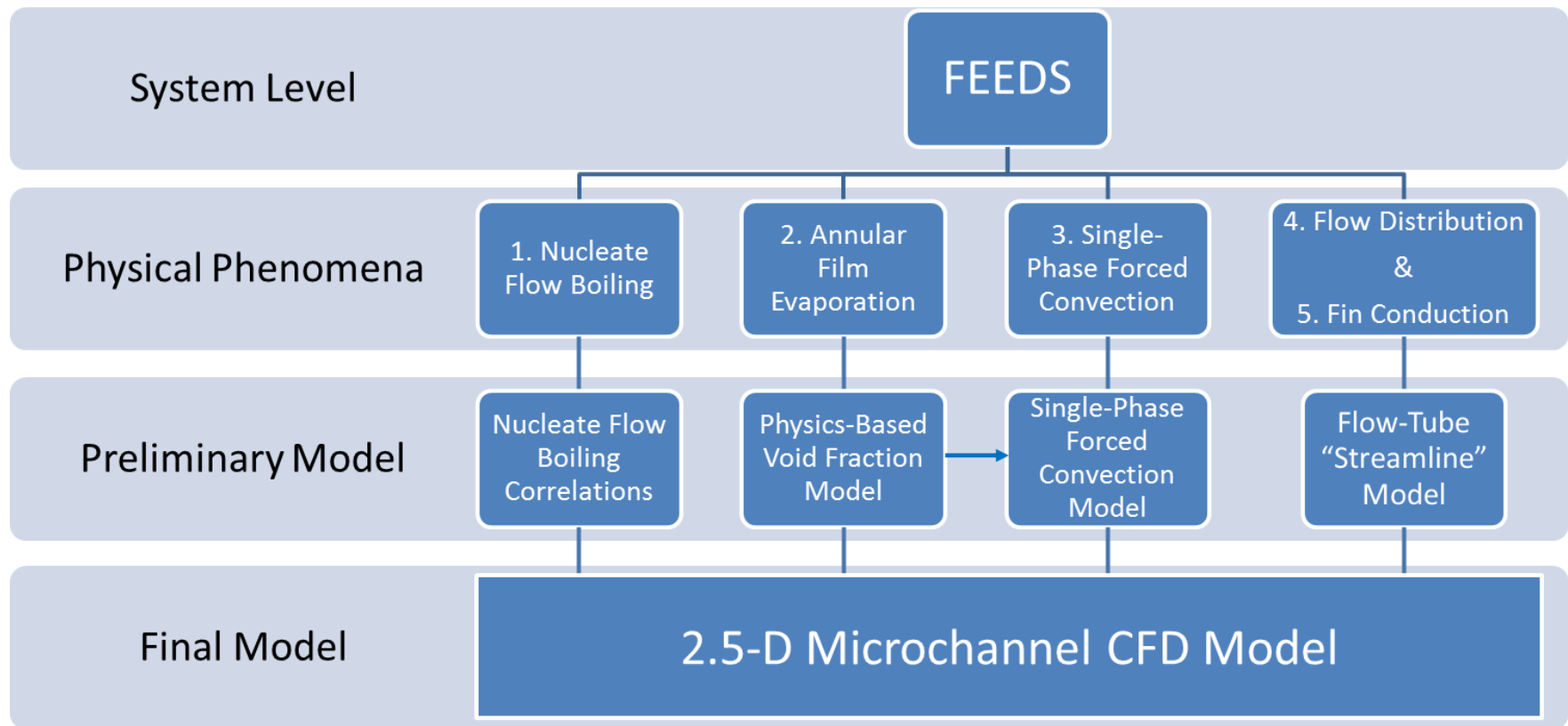


**Fig. 3.1.3: Summary of preliminary modeling effort, indicating the physical phenomena that each preliminary model attempted to probe.**

## 3.2 *Flow Boiling Correlations*

Although many flow boiling correlations exist in the literature, with more recent correlations improving on older ones, the most widely used correlations will be described here. Databases of two-phase experimental data were used to develop empirical relationships between dimensionless parameters and heat transfer rates. Two robust and widely used and cited correlations, the Chen correlation (1966) and the Kandlikar correlation (1990), will be reviewed here.

For both correlations, local heat transfer coefficient is given (either explicitly or implicitly) as a function of operational conditions and fluid properties. Since local heat transfer coefficient is given by the correlation and the average value for the heat exchanger is often desired to directly compare the performance, the correlation must be evaluated over various points in the heat exchanger and a suitable averaging scheme must be used. For the purpose of this work, an average heat flux was assumed such that the average heat transfer coefficient could be computed by averaging the local values.

### 3.2.1 **Chen Correlation**

As reviewed in Zhang et al. [44], the Chen correlation [45] assumes that the heat transfer coefficient is the sum of two components, nucleate boiling and single-phase convection:

$$h = F h_{sp} + S h_{nb} \quad (3.2.1)$$

The parameters,  $S$  and  $F$ , are defined as:

$$F = 2.35 \left( 0.213 + \frac{1}{X_{tt}} \right)^{0.736} \quad (3.2.2)$$

$$S = \frac{1}{1 + 2.53 \cdot 10^{-6} Re_l^{1.17}} \quad (3.2.3)$$

where  $X_{tt}$  is the Martinelli parameter defined as

$$X_{tt} = \left( \frac{1 - X}{X} \right)^{0.9} \left( \frac{\rho_v}{\rho_l} \right)^{0.5} \left( \frac{\mu_l}{\mu_v} \right)^{0.1} \quad (3.2.4)$$

and the Reynolds number is defined for the fluid only

$$Re_l = \frac{G(1 - X)D_h}{\mu_l} \quad (3.2.5)$$

While  $h_{sp}$  is usually taken from the Dittus-Boelter correlation for turbulent flow, since liquid flow here is laminar, a fully developed, constant Nusselt number was assumed, and  $h_{sp}$  was taken as

$$h_{sp} = 8 \frac{k_l}{D_h} \quad (3.2.6)$$

Finally,  $h_{nb}$  is taken from the Forster and Zuber correlation [46] for nucleate pool boiling:

$$h_{nb} = 0.00122 \left( \frac{k_l^{0.79} C_p^{0.45} \rho_l^{0.49}}{\sigma^{0.5} \mu_l^{0.29} h_{lv}^{0.24} \rho_v^{0.24}} \right) (\Delta T_{sat})^{0.24} (\Delta P_{sat})^{0.75} \quad (3.2.7)$$

where  $\Delta T_{sat} = T_{wall} - T_{sat}$  and  $\Delta P_{sat} = P(T_{wall}) - P(T_{sat})$ .

### 3.2.2 Kandlikar Correlation

Another widely-used correlation is that of Kandlikar et al. [47]. The Kandlikar correlation assumes that the heat transfer coefficient is the larger of two components: nucleate boiling-dominant and convective boiling-dominant.

$$h = \max(h_{nbd}, h_{cbd}) \quad (3.2.8)$$

Two correlations are given for  $h_{nbd}$  and  $h_{cbd}$ :

$$h_{nbd} = 0.6683 Co^{-0.2}(1 - X)^{0.8} h_{sp} + 1058 Bo^{0.7}(1 - X)^{0.8} F_{fl} h_{sp} \quad (3.2.9)$$

and

$$h_{cbd} = 1.136 Co^{-0.9}(1 - X)^{0.8} h_{sp} + 667.2 Bo^{0.7}(1 - X)^{0.8} F_{fl} h_{sp} \quad (3.2.10)$$

where  $Co$  and  $Bo$  are defined as

$$Co = \left( \frac{\rho_v}{\rho_l} \right)^{0.5} \left( \frac{1 - X}{X} \right)^{0.8} \quad (3.2.11)$$

and

$$Bo = q'' / (G h_{lv}) \quad (3.2.12)$$

The fluid-solid coefficient,  $F_{fl}$ , is a value usually between 0.5-3 meant to take into account fluid-solid wettability and surface tension effects. Since the authors do not provide a value for R245fa on copper, the lower limit of 0.5 was selected, which was found to match best with experimental data. Finally, the Dittus-Boelter correlation is recommended for  $h_{sp}$  for the case of turbulent flow, and since the liquid flow is laminar here, a constant Nusselt number was used, as recommended by [48]:

$$h_{sp} = 8 \frac{k_l}{D_h} \quad (3.2.13)$$

### 3.2.3 Comparison to Experiment

The Chen and Kandlikar correlations were then compared to experimental values obtained in Cetegen et al. [10]. Since local values for heat transfer coefficient are given by both the Chen and Kandlikar correlations, but average values across the heat exchanger are reported in Cetegen et al., an averaging scheme must be used when comparing correlations to experimental data. The averaging scheme in the present work assumes uniform heat flux in the manifold-microchannel unit cell. In addition, even though two-phase flow in manifold-microchannels is very complex, in the absence of a better approximation, an average or characteristic path must be assumed. In the present work, the chosen fluid path travels along the centerline of the manifold-microchannel, as shown in Fig. 3.1.2(a).

The Chen and Kandlikar correlations were then compared to experimental results obtained by Cetegen, and the results are shown in Fig. 3.2.1. Immediately, it is apparent that the Kandlikar correlation over-predicts heat transfer trends for the entire range of channel widths and mass fluxes. In addition, the Chen correlation provides increasingly accurate predictions as mass flux and channel width are increased (i.e., larger Reynolds numbers). Thus, for low Reynolds numbers, the Chen correlation might be inaccurate due to the presence of new flow regimes.



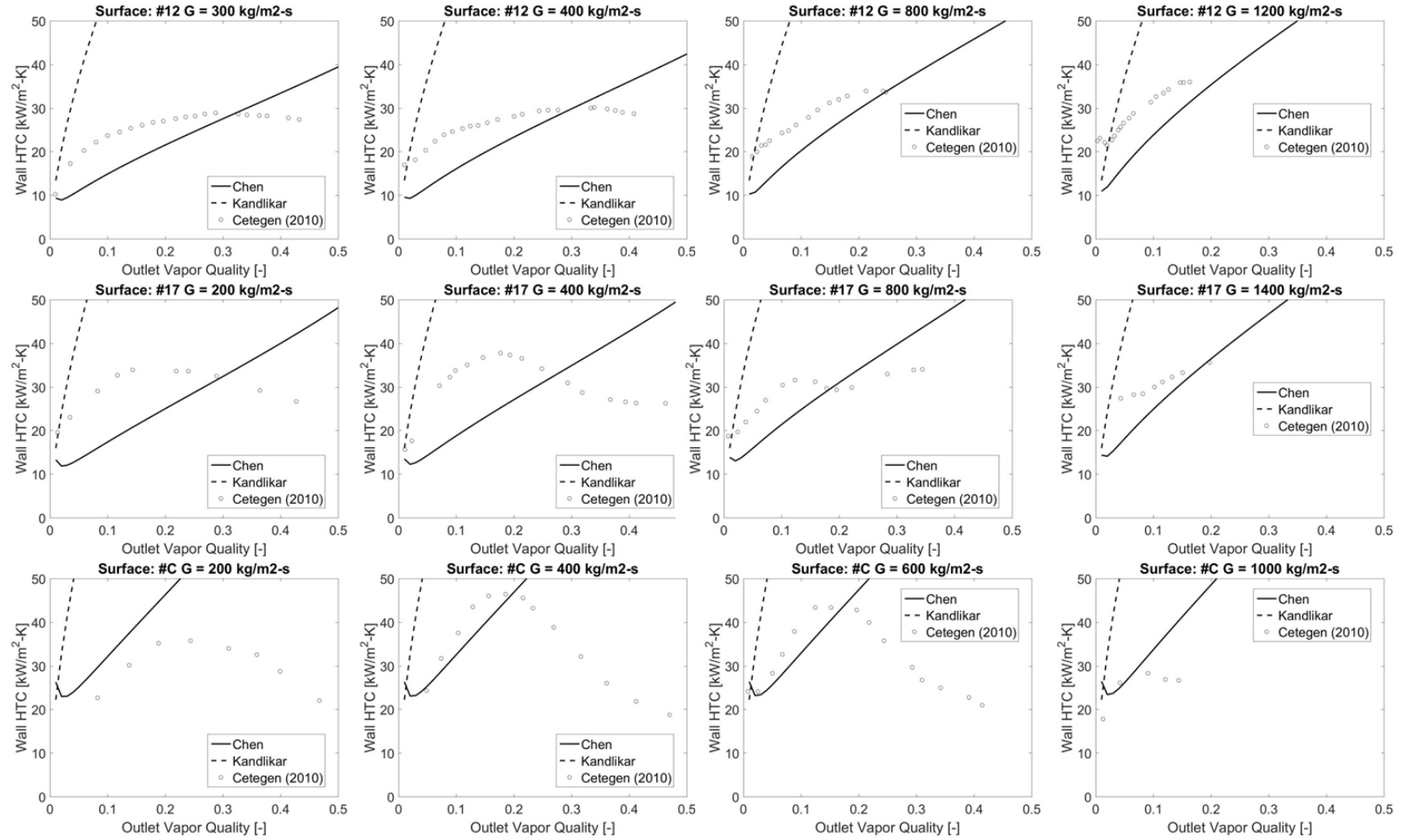


**Fig. 3.2.1: Comparison of experimental data in Cetegen et al. [10] to selected correlations.**

### **3.2.4 Summary of Flow Boiling Correlations**

Two widely-used flow boiling correlations—the Chen correlation (1966) and the Kandlikar correlation (1990)—were used to compare past experimental two-phase results. It was found that while the Kandlikar correlation significantly over-predicted the heat transfer coefficient in FEEDS channels, the Chen correlation was observed to provide sufficiently accurate results for high Reynolds numbers, potentially indicating the presence of new flow regimes or physics under these conditions.

### 3.3 Flow Regime Mapping

Before preliminary modeling can begin, it is important to know what flow regimes can be expected, since the modeling procedure and equations heavily depend on the expected flow regimes. Flow regime maps use databases of visualization experiments to establish useful maps to determine proper flow regime given the geometric and operational inputs. Many flow regime maps are available in the literature. In the present work, two select flow regime maps are investigated and used to determine the expected flow regimes of the system tested by Cetegen et al. [10]. The two flow regime maps are those developed by Taitel (1976) and Harirchian (2010).

#### 3.3.1 Taitel (1976)

Taitel [49] developed a dimensional and non-dimensional flow regime map based on force balances of the assumed transitioning mechanisms. These transitioning criteria are assumed to be universal, and to not significantly change from the macroscale to the microscale or from regular microchannels to manifold-microchannel flow configuration. The flow map defines four transition boundaries resulting in five distinct flow regimes, as shown in Fig. 3.3.1.

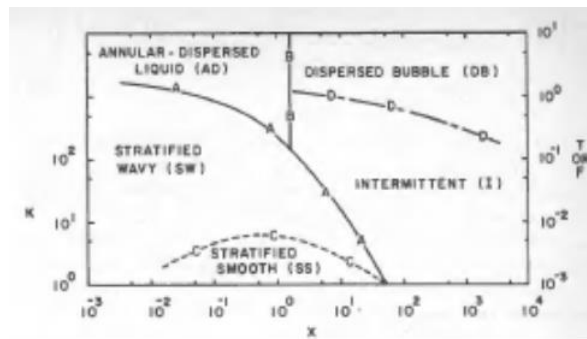


Fig. 3.3.1: Flow regime map proposed by Taitel and Duckler [49].

The five distinct flow regimes are

- (1) stratified smooth,
- (2) stratified wavy,
- (3) intermittent,
- (4) dispersed bubble,
- (5) dispersed annular.

Due to the small length scales involved in the present work, it is assumed that gravitational forces are negligible, and therefore stratified flow, which requires a body force such as gravity to exist, is not possible. Instead, it is assumed that the flow is in either annular or intermittent/dispersed bubble; accordingly, the transition between annular to dispersed bubble/intermittent flow—shown as boundary B-B in Fig. 3.3.1—is of primary concern. As detailed in Taitel and Duckler [49], the transition between annular to dispersed bubble/intermittent flow regime occurs when the liquid and vapor occupy 50% of the channel area, such that the liquid wave trough hits the bottom of the channel—thereby sustaining annular flow—before the liquid wave crest hits the top—which would otherwise cause a transition to intermittent and/or dispersed bubbly flow.

As shown in Taitel and Duckler [49], for horizontal, stratified, fully developed smooth flow, the non-dimensionalized momentum equations take on the form

$$\chi^2 \frac{\bar{S}_l/\bar{A}_l}{(\bar{u}_l \bar{D}_l)^n} \bar{u}_l^2 = \frac{\bar{S}_v/\bar{A}_g + \bar{S}_l/\bar{A}_l + \bar{S}_l/\bar{A}_v}{(\bar{u}_v \bar{D}_v)^m} \bar{u}_v^2 \quad (3.3.1)$$

where the accent  $\bar{\phantom{x}}$  indicates non-dimensionalization by  $D$  for length,  $D^2$  for area, and  $u_l^s$  and  $u_v^s$  for liquid and vapor velocities, respectively. The parameter,  $\chi$ , is the Martinelli parameter, defined as

$$\chi^2 = \frac{\frac{dP^s}{dx_l}}{\frac{dP^s}{dx_v}} = \frac{\frac{C_l}{D} \left( \frac{u_l^s D}{\nu_l} \right)^{-n} \frac{\rho_l (u_l^s)^2}{2}}{\frac{C_v}{D} \left( \frac{u_v^s D}{\nu_v} \right)^{-m} \frac{\rho_v (u_v^s)^2}{2}} \quad (3.3.2)$$

where the superscript <sup>s</sup>, refers to the superficial values, and  $C_l, C_v, n$ , and  $m$  are liquid and vapor friction factor constant and exponent, respectively. Taitel and Duckler [49] then proceeded to derive the non-dimensional geometric relations for the geometric variables using a circular channel. However, because the present work is concerned with rectangular channels, the geometric relations will have to be derived.

A smooth, stratified flow between parallel plates of width  $b$  and gap height  $h = D/2$  is shown in Fig. 3.3.2.

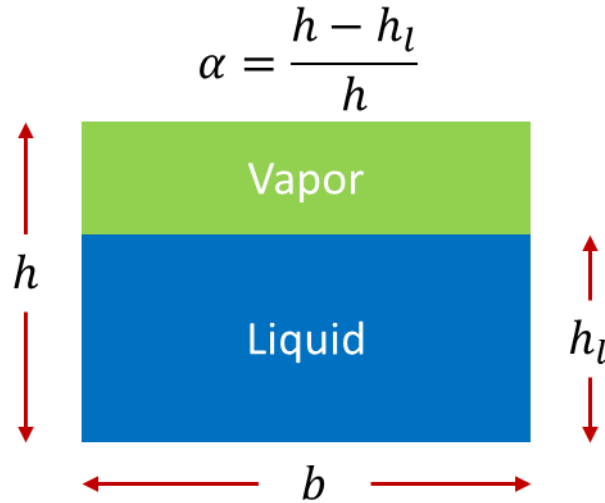


**Fig. 3.3.2: Smooth stratified flow between parallel plates.**

The non-dimensional geometric identities take on the form

$$\bar{S}_l = \frac{S_l}{D} = \frac{1}{2} \frac{b}{h} \quad (3.3.3)$$

$$\bar{S}_v = \frac{S_v + S_i}{D} = \frac{2b}{2h} = \frac{b}{h} \quad (3.3.4)$$

$$\bar{S}_l = \frac{S_l}{D} = \frac{1}{2} \frac{b}{h} \quad (3.3.5)$$

$$\bar{A}_l = \frac{A_l}{D^2} = \frac{bh_l}{(2h)^2} = \frac{bh_l}{4h^2} = \frac{1}{4} \frac{b}{h} \frac{h_l}{h} = \frac{1}{4} \frac{b}{h} (1 - \alpha) \quad (3.3.6)$$

$$\bar{A}_v = \frac{A_v}{D^2} = \frac{b(h - h_l)}{(2h)^2} = \frac{b(h - h_l)}{4h^2} = \frac{1}{4} \frac{b}{h} \frac{(h - h_l)}{h} = \frac{1}{4} \frac{b}{h} \alpha \quad (3.3.7)$$

$$\bar{A} = \frac{A}{D^2} = \frac{bh}{(2h)^2} = \frac{1}{4} \frac{b}{h} \quad (3.3.8)$$

where  $\alpha = (h - h_l)/h$  is the vapor void fraction. It is worth noting that Eqs. (3.3.3)-(3.3.8) contain  $b/h$ . Since the ratio between  $S$  and  $A$  is always taken (see Eq. (3.3.1)), the solution of Eq. (3.3.1) is not sensitive to the exact value of  $b/h$ .

The non-dimensional liquid and vapor hydraulic diameters are defined as

$$\bar{D}_l = \frac{4\bar{A}_l}{\bar{S}_l} = \frac{4 \frac{1}{4} \frac{b}{h} (1 - \alpha)}{\frac{1}{2} \frac{b}{h}} = 2(1 - \alpha) \quad (3.3.9)$$

$$\bar{D}_v = \frac{4\bar{A}_v}{\bar{S}_v} = \frac{4 \frac{1}{4} \frac{b}{h} \alpha}{\frac{b}{h}} = \alpha \quad (3.3.10)$$

It is worth noting that the term  $b/h$  cancels as well when calculating hydraulic diameter.

Similarly, the non-dimensional velocities for the liquid and vapor phases can be calculated as

$$\bar{u}_l = \frac{u_l}{u_l^s} = \frac{A}{A_l} = \frac{bh}{bh_l} = \frac{h}{h_l} = \frac{1}{1 - \alpha} \quad (3.3.11)$$

$$\bar{u}_v = \frac{u_v}{u_v^s} = \frac{A}{A_v} = \frac{bh}{b(h - h_l)} = \frac{h}{(h - h_l)} = \frac{1}{\alpha} \quad (3.3.12)$$

Recalling that the vapor void fraction is required to be 50% for the transition from dispersed bubble/intermittent to annular flow, Eqs. (3.3.3)-(3.3.12) can be directly computed using  $\alpha = 0.5$ .

For laminar liquid and vapor flow between parallel plates, the friction factor constants and exponents are given as

$$C_l = C_v = 96 \quad (3.3.13)$$

$$n = m = 1 \quad (3.3.14)$$

Thus, Eq. (3.3.1) can be solved for  $\chi$  using the definitions given in Eqs. (3.3.3)-(3.3.12) and  $n$  and  $m$  from Eq. (3.3.14). It is worth noting that the solution for  $\chi$  holds for all laminar liquid and vapor flows between horizontal parallel plates. The solution is found to be  $\chi = 2.828$ , which is larger than the  $\chi = 1.6$  reported in Taitel and Duckler for horizontal turbulent liquid and vapor flow in a circular channel.

Finally, using Eqs. (3.3.13)-(3.3.14) and the identities  $G(1 - X) = \rho_l u_l^s$  and  $GX = \rho_v u_v^s$ , Eq. (3.3.17) can be simplified to

$$\chi^2 = \left( \frac{1 - X}{X} \right) \left( \frac{\rho_v}{\rho_l} \right) \left( \frac{\mu_l}{\mu_v} \right) \quad (3.3.15)$$

where  $X$  is the thermodynamic vapor quality. Since  $\chi$  represents the value of the Martinelli parameter, whereupon bubbly-dispersed/intermittent flow transitions to annular flow, solving Eq. (3.3.15) for  $X$  yields the critical vapor quality whereupon transition occurs from bubbly-dispersed/intermittent flow to annular flow. Solving Eq. (3.3.15) yields  $X = 3.383\%$ . Accordingly, since outlet vapor qualities far exceed this threshold, annular flow is likely to be the dominant flow regime.

### 3.3.2 Harirchian (2010)

Noting that vapor confinement plays an important role in flow regimes and flow regime transitions in microchannels, Harirchian et al. [50] provide a dimensionless flow regime map specifically for microchannels, which can be used to establish the expected flow regimes for a given set of geometric and operational conditions. The authors of the work also compared their map to experimental data points, with good agreement. Their flow regime map appears in Fig. 3.3.3.

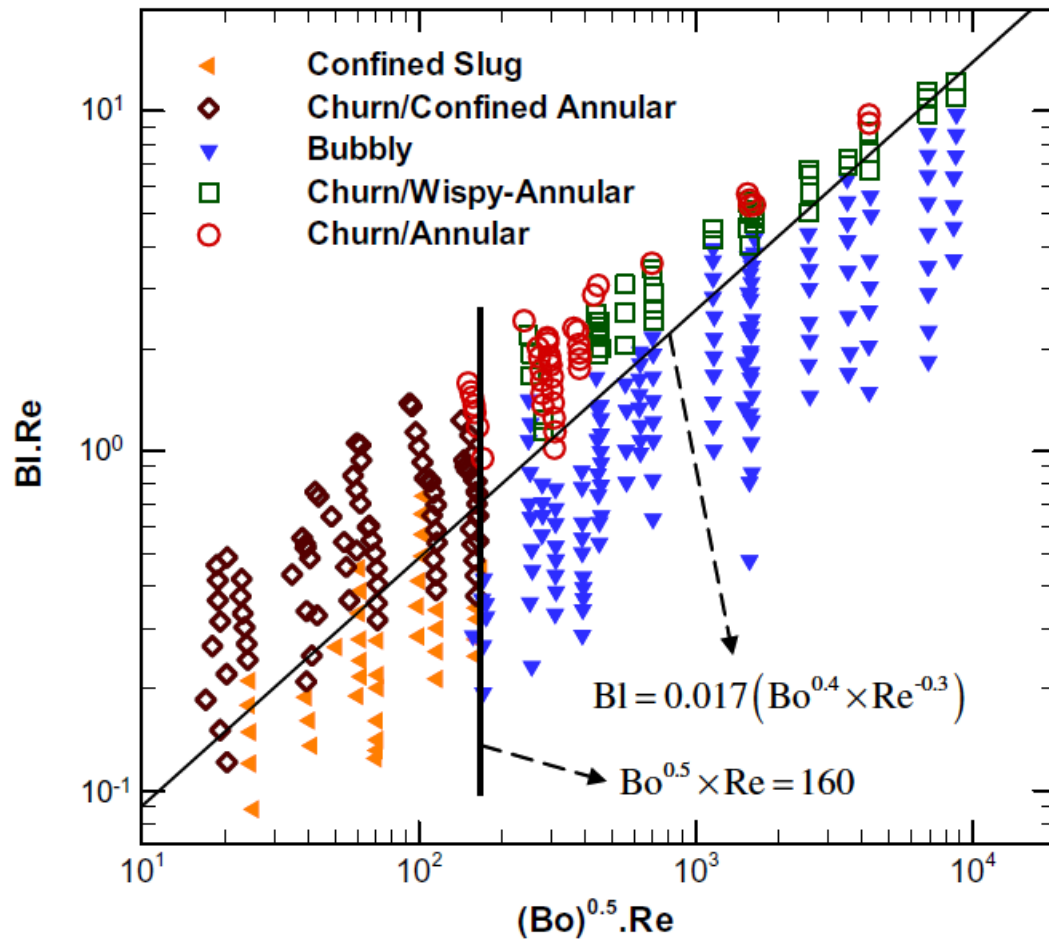


**Fig. 3.3.3: Flow regime map proposed by Harirchian et al. [50].**

Based on their experimental results, the authors noted four distinct flow regimes and two transition lines. The first transition line follows the line of



$$Bo^{0.5} Re = 160 \quad (3.3.16)$$

The second line follows

$$Bl Re = 0.017 (Bo^{0.4} Re^{0.7}) \quad (3.3.17)$$

where

$$Re = GD_h/\mu_l \quad (3.3.18)$$

$$Bo = \frac{g(\rho_l - \rho_v)D_h^2}{\sigma} \quad (3.3.19)$$

$$Bl = \frac{q''_{wall}}{G h_{lv}} \quad (3.3.20)$$

As shown in Fig. 3.3.3, there are four zones.

- (1)  $Bo^{0.5} Re > 160$  &  $Bl Re > 0.017 (Bo^{0.4} Re^{0.7}) \rightarrow$  Churn annular
- (2)  $Bo^{0.5} Re > 160$  &  $Bl Re < 0.017 (Bo^{0.4} Re^{0.7}) \rightarrow$  Bubbly
- (3)  $Bo^{0.5} Re < 160$  &  $Bl Re > 0.017 (Bo^{0.4} Re^{0.7}) \rightarrow$  Confined annular
- (4)  $Bo^{0.5} Re < 160$  &  $Bl Re < 0.017 (Bo^{0.4} Re^{0.7}) \rightarrow$  Confined slug

The flow regime map described above was then compared to the data from Cetegen [10], and the results shown in Fig. 3.3.4. The geometries tested by Cetegen are significantly out of range compared to those simulated by Haririchian, despite Haririchian specifically focusing on microchannels. Moreover, the expected range of dimensionless parameters expected to be tested in the present work is even farther away than Cetegen et al. In addition, the critical vapor quality, upon which the flow shifts from confined-slug to confined-annular is noted on the figure. The results show that flow regime becomes annular even for vapor qualities between 3-6%. Accordingly, for the present work, it appears that the annular flow regime is dominant.

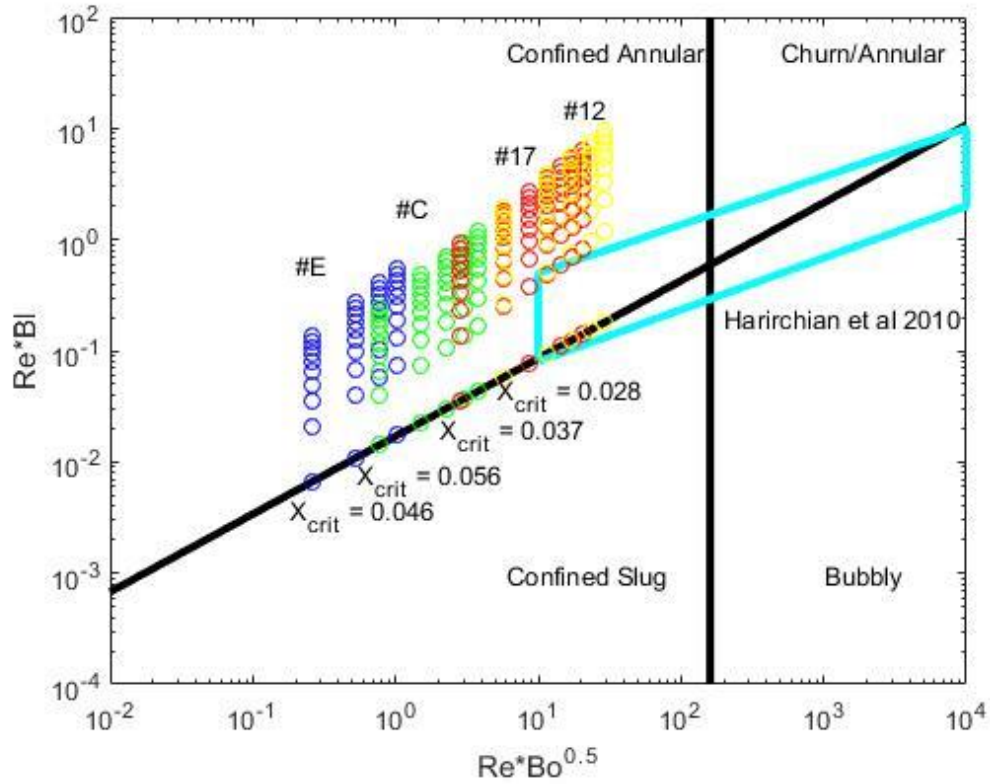


**Fig. 3.3.4: Plotting of points from Cetegen [10] on flow regime map proposed by Harirchian et al. [50]. The data points tested by Harirchian are encompassed in the cyan parallelogram. The data points tested by Cetegen are shown in green, red, and yellow. The expected range to be tested in the present work is shown in blue.**

### 3.3.3 Flow Regime Mapping Summary

Two flow regime maps—those of Taitel (1976) and Harirchian (2010)—were investigated to determine the predicted critical vapor quality under which the annular flow transition occurs. Both flow regime maps predict transition to annular flow occurs at vapor qualities between 3-6%. Since outlet vapor qualities far in excess of 6% are targeted, annular flow can be assumed to be the dominant flow regime.

### ***3.4 Annular Film Evaporation with Physics-Based Void Fraction Model***

With annular flow determined to be the dominant flow regime, understanding annular film evaporation is of prime interest. Since this film thickness is inversely proportional to the fully developed wall heat transfer coefficient, correct determination of the void fraction is crucial. Accordingly, a model was developed to simulate annular film evaporation using the Young-Laplace equation to compute the vapor void fraction directly from the physics.

#### **3.4.1 Model Domain**

Due to the preliminary nature of this model, only a 2-D slice of the 3-D manifold-microchannel unit-cell was simulated, as shown in Fig. 3.1.2.

#### **3.4.2 Model Assumptions**

The model makes the following assumptions:

- (1) 1-D steady-state, thermally fully developed, laminar, annular, diabatic two-phase flow between parallel plates;
- (2) Quadratic velocity profiles for liquid and vapor, resulting in an algebraic friction factor;
- (3) Constant wall temperature;
- (4) Constant liquid and vapor properties.

### 3.4.3 Control Volumes & Equations

In the interest of brevity, the detailed derivations of the equations provided here can be found in Appendix A, and accordingly, only the final results will be presented here. The control volumes used in the derivation are given in Fig. 3.4.1.

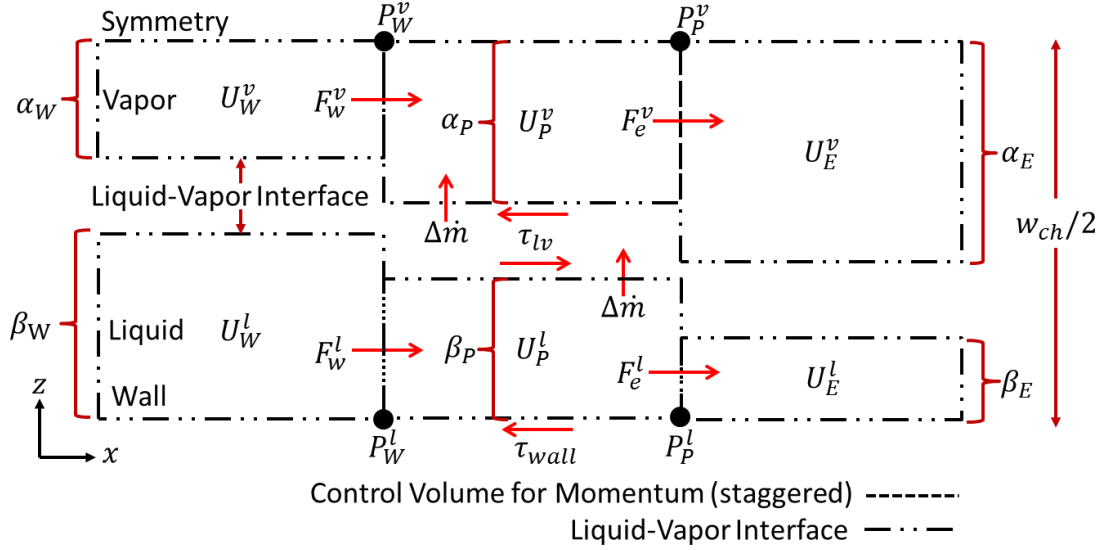


**Fig. 3.4.1: Control volumes used for discretization in the annular film evaporation with physics-based void fraction model.**

Using the control volumes found in Fig. 3.4.1, the governing momentum and continuity equations for the liquid and vapor phases can be derived. The mixture momentum equation can be derived by adding the liquid and vapor momentum equations together, and an equation for volume fraction can be derived by subtracting the liquid momentum equation from the vapor momentum equation so that the pressure drops per unit length cancel. Finally, a simple convection equation can be derived to calculate the liquid quality, which enforces conservation of species. The final forms of these equations are given below:

### Liquid Momentum

$$a_P^l U_P^l = a_W^l U_W^l + a_E^l U_E^l + b^l + A^l(P_w^l - P_e^l) \quad (3.4.1)$$

$$a_P^l = a_W^l + a_E^l + S_P^l \quad (3.4.2)$$

$$a_W^l = D_W^l + [F_W^l, 0] \quad (3.4.3)$$

$$a_E^l = D_e^l + [-F_e^l, 0] \quad (3.4.4)$$

$$b^l = S_C^l \quad (3.4.5)$$

### Vapor Momentum

$$a_P^v U_P^v = a_W^v U_W^v + a_E^v U_E^v + b^v + A^v(P_w^v - P_e^v) \quad (3.4.6)$$

$$a_P^v = a_W^v + a_E^v + S_P^v + \Delta \dot{m} \quad (3.4.7)$$

$$a_W^v = D_W^v + [F_W^v, 0] \quad (3.4.8)$$

$$a_E^v = D_e^v + [-F_e^v, 0] \quad (3.4.9)$$

$$b^v = \Delta \dot{m} U_P^l + S_C^v \quad (3.4.10)$$

### Mixture Momentum

$$a_P U_P = a_W U_W + a_E U_E + b + P_w - P_e \quad (3.4.11)$$

$$a_P = a_P^l + a_P^v \quad (3.4.12)$$

$$a_W = a_W^l + a_W^v \quad (3.4.13)$$

$$a_E = a_E^l + a_E^v \quad (3.4.14)$$

$$b = b^l + b^v + a_W^l U_W^l + a_W^v U_W^v - a_W U_W + a_E^l U_E^l + a_E^v U_E^v - a_E U_E + a_P U_P - a_P^l U_P^l - a_P^v U_P^v \quad (3.4.15)$$

### Where:

$$F_i = F_i^l + F_i^v \quad (3.4.16)$$

$$F_i^l = \rho_l \beta_i U_i^l \quad (3.4.17)$$

$$F_i^v = \rho_v \alpha_i U_i^v \quad (3.4.18)$$

$$D_i = D_i^l + D_i^v \quad (3.4.19)$$

$$D_i^l = \beta_i \mu_l / \Delta x \quad (3.4.20)$$

$$D_i^v = \alpha_i \mu_v / \Delta x \quad (3.4.21)$$

$$U_P^{lv} = \frac{6S_1 U_P^l \alpha_P + 3U_P^v \beta_P}{4S_1 \alpha_P + 3\beta_P} \quad (3.4.22)$$

$$S_C^l = \frac{24\mu_l \Delta x}{\beta_P w_{ch}^2} U_P^{lv} \quad (3.4.23)$$

$$S_P^l = \frac{48\mu_l \Delta x}{\beta_P w_{ch}^2} \quad (3.4.24)$$

$$S_C^v = \frac{12\mu_v \Delta x}{\alpha_P w_{ch}^2} U_{lv} \quad (3.4.25)$$

$$S_P^v = \frac{12\mu_v \Delta x}{\alpha_P w_{ch}^2} \quad (3.4.26)$$

$$S_1 = \frac{\mu_l}{\mu_v} \quad (3.4.27)$$

### Volume Fraction

$$A_P \beta_P = A_W \beta_W + A_E \beta_E + B \quad (3.4.28)$$

$$A_P = \left( \frac{A_P^l}{\beta_P^2} + \frac{A_P^v}{(1 - \beta_P)^2} \right) \quad (3.4.29)$$

$$A_W = \left( \frac{A_W^l}{\beta_W^2} + \frac{A_W^v}{(1 - \beta_W)^2} \right) \quad (3.4.30)$$

$$A_E = \left( \frac{A_E^l}{\beta_E^2} + \frac{A_E^v}{(1 - \beta_E)^2} \right) \quad (3.4.31)$$

$$B = 2 \left( \frac{A_P^l}{\beta_P} - \frac{A_W^l}{\beta_W} - \frac{A_E^l}{\beta_E} \right) - \left( A_P^v \frac{(1 - 2\beta_P)}{(1 - \beta_P)^2} - A_W^v \frac{(1 - 2\beta_W)}{(1 - \beta_W)^2} - A_E^v \frac{(1 - 2\beta_E)}{(1 - \beta_E)^2} \right) + \left( \frac{b^v}{A^v} - \frac{b^l}{A^l} \right) \quad (3.4.32)$$

Where:

$$A_i^l = \frac{a_i^l F_i^l}{A^l \rho_l} \quad (3.4.33)$$

$$A_i^v = \frac{a_i^v F_i^v}{A^v \rho_v} \quad (3.4.34)$$

### Liquid Quality

$$a_P^q Y_P = a_W^q Y_W + a_E^q Y_E + b^q \quad (3.4.35)$$

$$a_P^q = a_W^q + a_E^q \quad (3.4.36)$$

$$a_W^q = [F_W, 0] \quad (3.4.37)$$

$$a_E^q = [-F_E, 0] \quad (3.4.38)$$

$$b^q = -\Delta \dot{m} \quad (3.4.39)$$

Where:

$$\Delta \dot{m} = \min[\Delta \dot{m}_{potential}, \Delta \dot{m}_{max}] \quad (3.4.40)$$

$$\Delta \dot{m}_{max} = a_W^q Y_W + a_E^q Y_E \quad (3.4.41)$$

$$\Delta \dot{m}_{potential} = \frac{k_l}{\delta} \frac{2 \Delta x}{w_{ch} h_{fg}} (T_{wall} - T_{sat}) \quad (3.4.42)$$

$$\delta = \beta_P \frac{w_{ch}}{2} \quad (3.4.43)$$

And:

$$F_W^l = a_W^q Y_W + (F_W - a_W^q) Y_P \quad (3.4.44)$$

$$F_e^l = (F_e + a_E^q) Y_P - a_E^q Y_E \quad (3.4.45)$$

$$F_W^v = F_W - F_W^l \quad (3.4.46)$$

$$F_e^v = F_e - F_e^l \quad (3.4.47)$$

### 3.4.4 Model Inputs and Solution Procedure

Inputs to the model include the fluid properties, width of the channel,  $w_{ch}$ , length of the channel,  $L_{ch}$ , channel mass flux,  $G$ , and wall superheat,  $\Delta T$ . In general, the channel superheat was calibrated such that a dryout point would occur somewhere between the channel halfway point and the outlet so as to compute the full range of vapor qualities and fully utilize the mesh. It is worth noting that due to the 1-D nature of the problem, continuity can be solved sequentially and provides the velocity field. In addition, the mixture mass flow rate,  $F$ , is constant in all cells, and the momentum equations serve only to provide the pressure fields.

The solution procedure is as follows: starting with an initial guess of single-phase liquid flow, compute the liquid, vapor, and mixture pressure fields using Eqs. (3.4.1)-(3.4.15). Then, Eqs. (3.4.28)-(3.4.34) are solved and the liquid volume fraction updated. The evaporation rate can be computed using Eqs. (3.4.40)-(3.4.43), and Eqs. (3.4.35)-(3.4.39) solved for the liquid quality. The face phase fluxes can then be updated using Eqs. (3.4.44)-(3.4.47), and the momentum coefficients updated using Eqs. (3.4.16)-(3.4.27). The momentum equations can then once again be solved for the liquid, vapor, and mixture pressure field, and the process is iterated until convergence is obtained. Convergence is assessed by measuring the residual in the Young-Laplace equation based on the computed pressure drops in the liquid, vapor, and mixture. In general, a normalized tolerance of  $1e-6$  was used.

### 3.4.5 Results

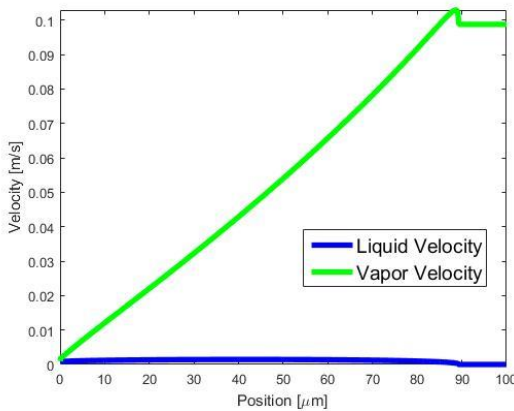
The annular film evaporation with physics-based void fraction model was then run for two limiting cases:  $G \rightarrow 0$  and  $G \rightarrow \infty$ . The results are presented in Fig. 3.4.2. The liquid and vapor average velocities are visible in Fig. 3.4.2(a)-(b). For both limiting cases, as liquid evaporates, both the liquid and vapor velocities are observed to increase. The vapor velocity increases due to evaporation, while the liquid velocity increases because the fractional reduction to liquid volume fraction is larger than the fractional liquid lost due to evaporation. For the limiting case of  $G \rightarrow 0$ , at some point along the channel, the liquid velocity peaks and begins to decrease once the evaporation rate is large enough to remove liquid faster than the liquid volume fraction is reduced. Afterwards, the liquid velocity decreases, gradually approaching zero at dryout due to viscous forces which act to dampen changes in velocity. However, for the limiting case of  $G \rightarrow \infty$ , the liquid velocity instantaneously drops to zero after it peaks, since inertial forces dominate.

Fig. 3.4.2(c)-(d) shows the liquid, vapor, and mixture pressures. However, only the vapor pressure is visible, due the liquid, vapor, and mixture pressures being equal. For the limiting case of  $G \rightarrow 0$ , the magnitude of the gradient of the pressure is observed to increase slightly along the channel. This is due to the increased friction factor at high qualities characteristic of annular, fully developed flow (this will be described in greater detail in Section 4.3.2; see Fig. 4.3.3). However, for the limiting case of  $G \rightarrow \infty$ , the slope is observed to rapidly steepen as vapor quality is increased. This is due to the acceleration of the evaporating liquid as it changes to vapor.

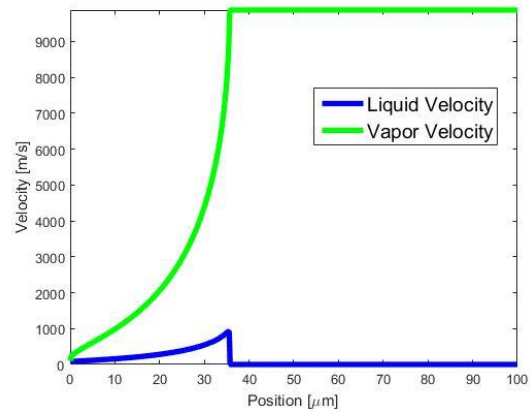


Next, the vapor quality, void fraction, and slip profiles are observed in Fig. 3.4.2(e)-(f). For both limiting cases, the slope of the vapor quality increases monotonically due to reducing film thickness and increased evaporation. The profile of the void fraction is more complicated. For both limiting cases, the slope of the void fraction at zero vapor quality is infinite, since the matching void fraction is zero, which would otherwise result in an infinite vapor velocity and an infinite pressure drop. Similarly, at large vapor qualities, the void fraction slowly approaches unity; otherwise, the liquid pressure drop would approach infinity. However, for the limiting case of  $G \rightarrow \infty$ , the observed slope is steeper due to inertia being more dominant over friction.

Finally, the void fraction vs. vapor quality relationship from this simulation can be compared to correlations available in the literature and the one derived in Appendix A. This comparison is shown in Fig. 3.4.2(g)-(h). From the figure, it is apparent that the limiting case of  $G \rightarrow 0$  matches the annular, fully developed void fraction correlation. This should come as no surprise, since frictional forces dominate, and those frictional forces were implemented in the present model. However, in the limiting case of  $G \rightarrow \infty$ , the void fraction is very close to the Zivi void fraction correlation. This is not enforced by the simulation in any trivial way, and therefore serves to validate the model.



(a)



(b)

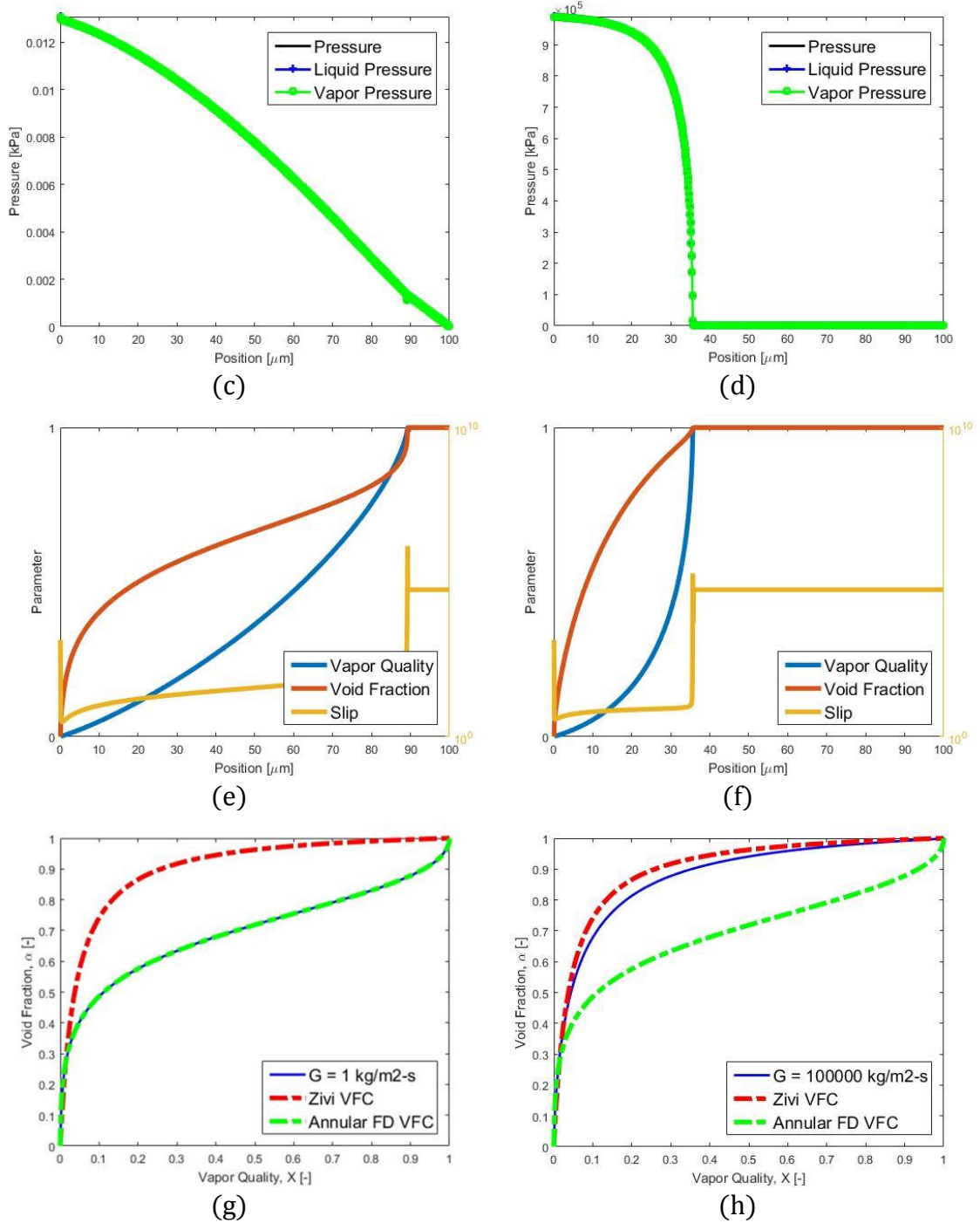
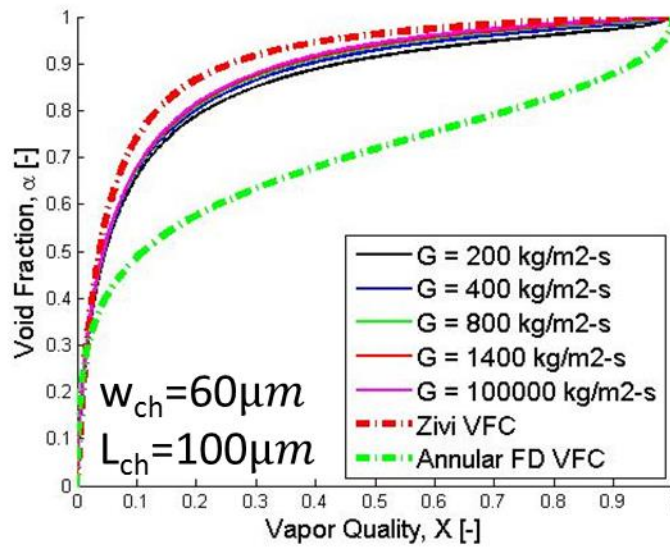


**Fig. 3.4.2: Sample results from annular film evaporation with physics-based void fraction model with R245fa at 30°C in 10 μm channel: (a) liquid and vapor mean velocities vs position; (b) liquid, vapor, and mixture pressures vs. position; (c) vapor quality, void fraction, and slip vs. position; (d) void fraction vs. vapor quality and comparison to Zivi and annular void fraction correlations.**

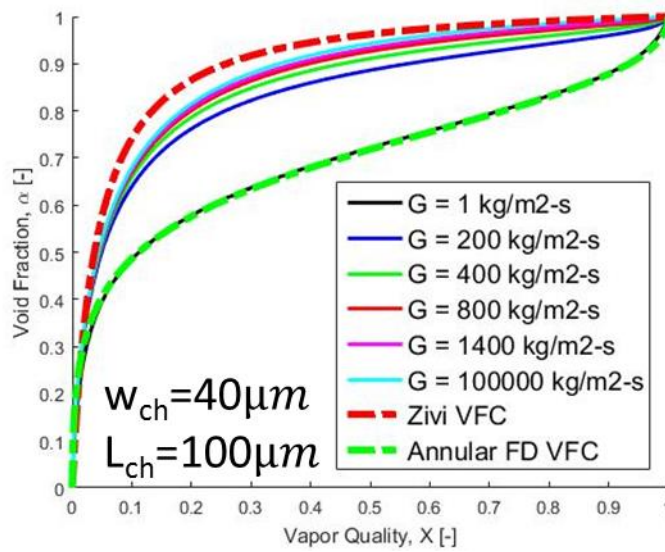
Next, the effect of mass flux on void fraction correlation was observed and is shown in Fig. 3.4.3. For large channels (see Fig. 3.4.3(a)-(b)), the effect of mass flux is small, since inertia already dominates over frictional forces, and accordingly, the void fraction is determined by balancing the accelerations of the liquid and vapor phases due to evaporation. Thus, the annular Zivi void fraction correlation is accurate for these cases regardless of mass flux, corresponding to Surface #12 (60  $\mu\text{m}$  gap) and Surface #17 (40  $\mu\text{m}$  gap), as defined by Cetegen [10].

For medium channels (see Fig. 3.4.3(c)), the effect of mass flux is more pronounced, as both frictional forces and inertia forces are important. Accordingly, an increase in mass flux shifts the void fraction from an annular, fully developed correlation to the Zivi annular void fraction correlation. However, because the curves rapidly approach and are closest to the Zivi annular void fraction correlation, this correlation will be used for Surface #C (20  $\mu\text{m}$  gap) as defined by Cetegen [10].

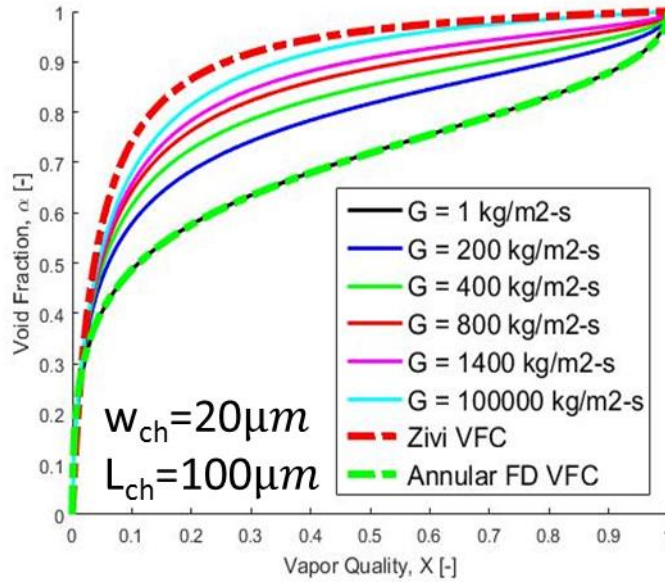
Finally, for smaller channels (see Fig. 3.4.3(d)), the effect of mass flux is very important, and frictional forces dominate until high mass fluxes are achieved. Once again, an increase in mass flux causes a shift from the annular, fully developed void fraction correlation to the Zivi annular void fraction correlation. However, for this case, for the range of mass fluxes of concern, the annular void fraction correlation provides a better estimate of the proper void fraction, and accordingly, will be used for Surface #E (10  $\mu\text{m}$  gap).



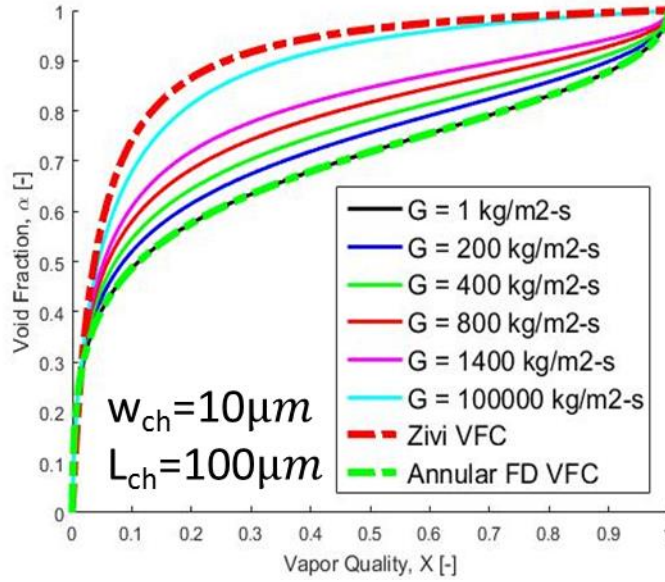
(a)



(b)



(c)



(d)

**Fig. 3.4.3: Effect of mass flux on void fraction correlation for R245fa at 30°C in channels of various widths, corresponding to those tested by Cetegen et al.: (a) 60  $\mu m$  (surface #12), (b) 40  $\mu m$  (surface #17), (c) 20  $\mu m$  (surface #C), and (d) a new surface designed in the present work (surface #E).**

### 3.4.6 Model Summary

In conclusion, the annular film-evaporation with physics-based void fraction model provided numerous insights into the physics governing FEEDS systems, including:

- (1) the void fraction correlation is always bounded between the annular, fully developed void fraction correlation (limit of  $G \rightarrow 0$ ) and the Zivi annular void fraction correlation (limit of  $G \rightarrow \infty$ );
- (2) for all other cases, the physics based model is required to predict the void fraction correlation;
- (3) for the surfaces tested by Cetegen et al., the Zivi annular void fraction correlation is an excellent approximation, while for the surfaces tested here, the annular, fully developed void fraction correlation more closely approximates the void fraction.

### ***3.5 Single-Phase Forced Convection Model***

After establishing the proper void fraction correlations to use, the role of forced-convection in annular film evaporation was investigated. A new model was created to investigate the combined effects of forced convection and evaporation for a FEEDS system tested by Cetegen et al. [10]. Like the annular film evaporation with physics-based void fraction model, this model simplifies the FEEDS setup by converting the complicated 3-D flow into a 1-D convection problem in the direction parallel to the flow and a 1-D conduction problem in the direction normal to the flow. Thus, the entire temperature distribution can be solved sequentially, by marching along the length of the microchannel solving for the 1-D temperature distribution in the direction normal to the flow.

#### **3.5.1 Modeling Domain**

As mentioned above, rather than simulate a computationally expensive and complicated flow and heat transfer problem present in a FEEDS system, the domain was simplified into a 2-D slice, consisting of just one microchannel, the length of which corresponds to half the pitch of the manifold structure, as shown in Fig. 3.1.2.

#### **3.5.2 Model Assumptions**

The following assumptions were made to simplify the model:

- (1) The velocity profile in the z-direction is uniform.

- (2) Convection effects dominate in the direction parallel to the flow (x-direction), while conduction dominates in the direction perpendicular to the flow (z-direction).
- (3) All phase change takes place on the liquid-vapor interface (no nucleate boiling).
- (4) Void fraction correlations can be used to determine the void fraction and subsequent liquid film thickness.
- (5) The liquid vapor interface temperature,  $T_i$ , is constant and equal to the saturation temperature,  $T_{sat}$  (evaporation resistance is negligible).
- (6) A uniform heat flux is applied on the wall.

### 3.5.3 Model Equations

The control volumes used in this model are shown in Fig. 3.5.1.

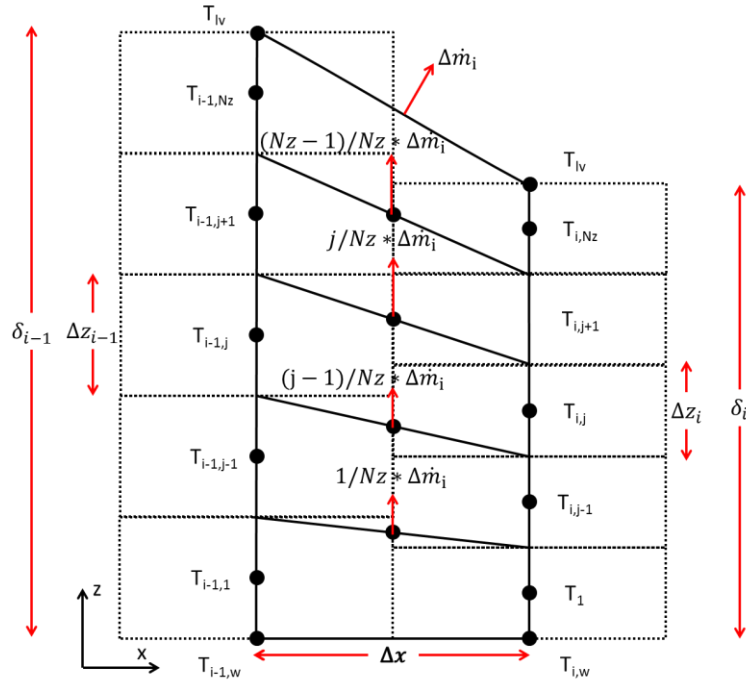


**Fig. 3.5.1: Control volumes for the forced convection model.**

To begin, the local total liquid mass flow rate must be calculated:



$$\dot{m}_i = \dot{m}_{i-1} - \Delta\dot{m}_i \quad (3.5.1)$$

The local vapor quality,  $X_i$ , can then be calculated from:

$$X_i = 1 - \frac{\dot{m}_i}{\dot{m}_0} \quad (3.5.2)$$

A void fraction correlation can then be used to relate the local vapor quality to the local void fraction,  $\alpha_i$ . Based on the result of the annular film evaporation with physics-based void fraction model, the Zivi void fraction correlation was used and is of the form:

$$\alpha_i = \frac{1}{1 + \frac{1 - X_i}{X_i} \left( \frac{\rho_v}{\rho_l} \right)^{2/3}} \quad (3.5.3)$$

The film thickness,  $\delta_i$ , is geometrically related to the channel geometry by:

$$\delta_i = \frac{(1 - \alpha_i) w_{ch}}{2} \quad (3.5.4)$$

The x-direction spacing,  $\Delta x$ , can be calculated by dividing the total length,  $L_{ch}$ , by the desired number of nodes in the x-direction,  $N_x$ :

$$\Delta x = L_{ch}/N_x \quad (3.5.5)$$

Similarly, the y-direction spacing can be calculated by dividing the film thickness,  $\delta$ , by the number of nodes in the z-direction,  $N_z$ :

$$\Delta z_i = \delta_i/N_z \quad (3.5.6)$$

It is worth noting that the while x-direction spacing is uniform and constant (and does not need to be calculated from each  $i$  coordinate), the z-direction spacing,  $\Delta z$ , varies in the x-direction, since it is dependent on the local film thickness,  $\delta$ . Accordingly, it must be calculated for each  $i$  coordinate, as indicated in Eq. (3.5.6).

Since convection is assumed to be dominant in the x-direction and conduction is assumed to be dominant in the z-direction, conservation of energy about an internal control volume,  $i,j$ , takes the form:

$$\begin{aligned}
& C_p \left( \left( \frac{\dot{m}_i}{Nz} T_{i,j} + \frac{j}{Nz} \Delta \dot{m}_i \frac{T_{i-1,j} + T_{i,j} + T_{i-1,j+1} + T_{i,j+1}}{4} \right) \right. \\
& \quad \left. - \left( \frac{\dot{m}_{i-1}}{Nz} T_{i-1,j} + \frac{j-1}{Nz} \Delta \dot{m}_i \frac{T_{i-1,j-1} + T_{i,j-1} + T_{i-1,j} + T_{i,j}}{4} \right) \right) \\
& \quad = \\
& k_l \frac{\Delta x}{2} \left( \frac{T_{i-1,j-1} - T_{i-1,j}}{\Delta z_i} + \frac{T_{i,j-1} - T_{i,j}}{\Delta z_i} - \frac{T_{i-1,j} - T_{i-1,j+1}}{\Delta z_i} - \frac{T_{i,j} - T_{i,j+1}}{\Delta z_i} \right)
\end{aligned} \tag{3.5.7}$$

The equations for the bottom and top control volumes are slightly different. For the top control volume, conservation of energy takes the form:

$$\begin{aligned}
& C_p \left( \left( \frac{\dot{m}_i}{Nz} T_{i,Nz} + \Delta \dot{m}_i \frac{T_{i-1,Nz} + T_{i,Nz} + 2T_{lv}}{4} \right) \right. \\
& \quad - \left( \frac{\dot{m}_{i-1}}{Nz} T_{i-1,Nz} \right. \\
& \quad \left. \left. + \frac{Nz-1}{Nz} \Delta \dot{m}_i \frac{T_{i-1,Nz-1} + T_{i,Nz-1} + T_{i-1,Nz} + T_{i,Nz}}{4} \right) \right) \\
& \quad = \\
& k_l \frac{\Delta x}{2} \left( \frac{T_{i-1,Nz-1} - T_{i-1,Nz}}{\Delta z_i} + \frac{T_{i,Nz-1} - T_{i,Nz}}{\Delta z_i} - \frac{T_{i-1,Nz} - T_{lv}}{\Delta z_i/2} - \frac{T_{i,Nz} - T_{lv}}{\Delta z_i/2} \right)
\end{aligned} \tag{3.5.8}$$

Similarly, for the bottom control volume, conservation of energy takes the form:

$$\begin{aligned}
& C_p \left( \left( \frac{\dot{m}_i}{Nz} T_{i,1} + \frac{1}{Nz} \Delta \dot{m}_i \frac{T_{i-1,1} + T_{i,1} + T_{i-1,2} + T_{i,2}}{4} \right) - \frac{\dot{m}_{i-1}}{Nz} T_{i-1,1} \right) \\
& \quad =
\end{aligned} \tag{3.5.9}$$

$$q''_{wall}\Delta x_i - k_l \frac{\Delta x}{2} \left( \frac{T_{i-1,1} - T_{i-1,2}}{\Delta z_i} + \frac{T_{i,1} - T_{i,2}}{\Delta z_i} \right)$$

The wall temperature can be calculated retroactively from the heat flux as

$$T_{i,w} = T_{i,1} + \frac{q''_{wall}}{k_l} \frac{\Delta z_i}{2} \quad (3.5.10)$$

Finally, the evaporation rate,  $\Delta \dot{m}_i$ , is determined by applying an energy balance at the liquid-vapor interface:

$$\Delta \dot{m}_i = \frac{k_l}{h_{fg}} \frac{\Delta x}{2} \frac{(T_{i-1,Nz} + T_{i,Nz} - 2 T_{lv})}{\Delta y_i/2} \quad (3.5.11)$$

### 3.5.4 Boundary Conditions

The desired total liquid mass flow rate,  $\dot{m}$ , initial liquid mass flow rate,  $\dot{m}_0$  and initial temperature distribution,  $T_{0,j}$  are needed.

The total liquid mass flow rate was selected to enforce the desired microchannel mass flux,

$$G = \frac{\dot{m}}{w_{ch}} \quad (3.5.12)$$

since  $\dot{m}$  is given per unit width.

For the conditions tested here,  $\dot{m}_0$  was always selected to enforce quality of zero at the inlet; that is,

$$\dot{m} = \dot{m}_0 \quad (3.5.13)$$

and  $T_{0,j}$  was selected to be uniform, and usually equal to the saturation temperature—in this case 300 K. Finally, the wall heat flux must be converted from the desired base heat flux using conservation of energy:

$$q''_{wall} = q''_{base}(w_{ch}/2 + w_f/2)/h_f \quad (3.5.14)$$

### 3.5.5 Data Analysis Equations

A few definitions are needed to conduct data analysis. First, the forced convection heat flux is defined as

$$q_{fc,i} = \frac{1}{Nz} \frac{C_p}{\Delta x} \left( \dot{m}_i \sum_{j=1}^{Nz} T_{i,j} - \dot{m}_{i-1} \sum_{j=1}^{Nz} T_{i-1,j} + \Delta \dot{m}_i (T_{lv} - T_{sat}) \right) \quad (3.5.15)$$

The evaporative heat flux is defined as

$$q_{evap,i} = \frac{\Delta \dot{m}_i h_{fg}}{\Delta x} \quad (3.5.16)$$

### 3.5.6 Mathematical Formulation and Solution Procedure

Due to the sequential nature of the solution procedure, all variables with index  $i-1$  are already known, leading to  $Nz$  unknown temperatures and one unknown evaporation rate,  $\Delta \dot{m}$ . Thus, in total,  $Nz + 1$  equations must be solved at each x-coordinate. Due to the non-linear nature of this system of equations, the equations must be linearized, put into matrix form, solved, and iterated until the residuals approach zero. A custom numerical linearizer was created to do this using finite differences; however, a commercial non-linear equation solver—such as *fsolve* in MATLAB—could have been used instead.

### 3.5.7 Results

The model was then run for various conditions from Cetegen [10]. For all cases shown, the thermodynamic outlet vapor quality (as calculated from an energy balance)

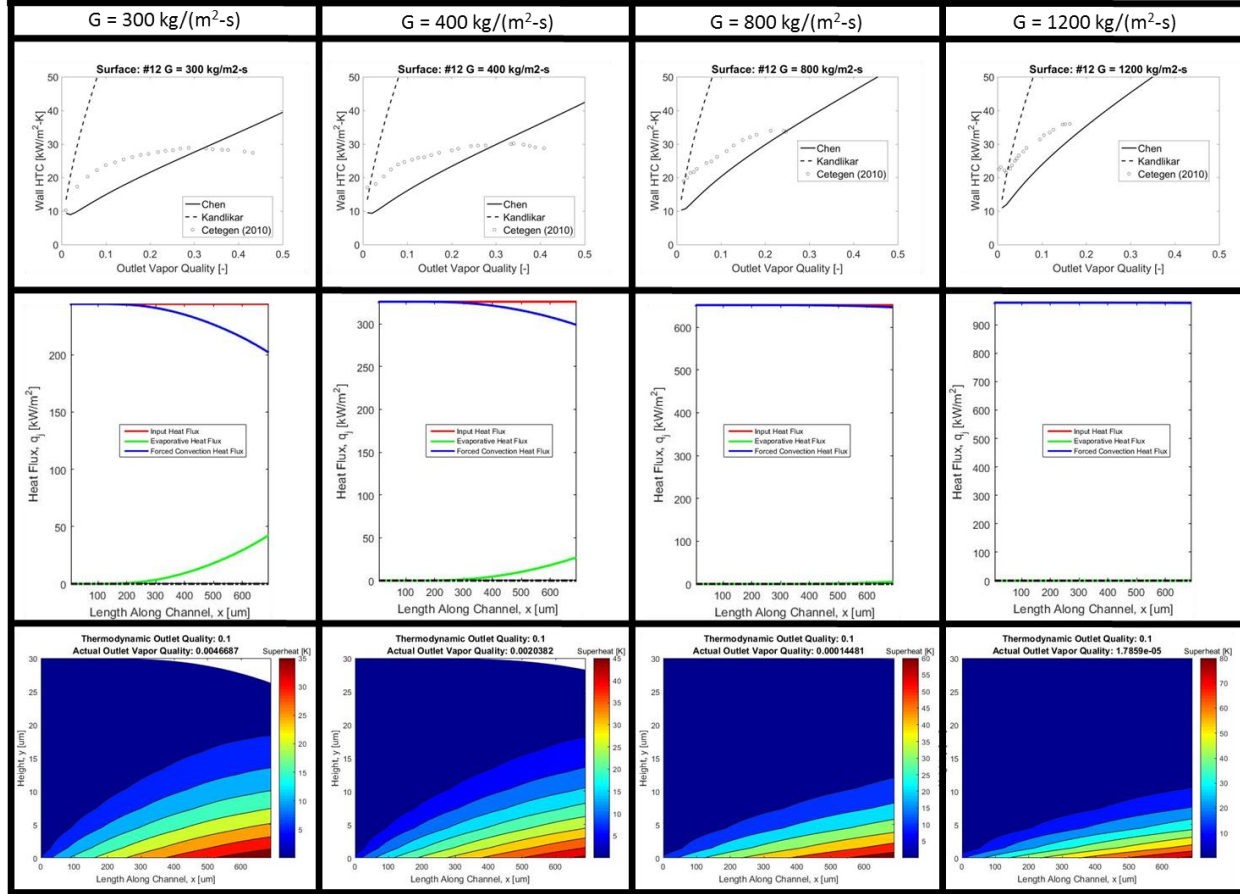
was set to be 10%, and the results are shown in Fig. 3.5.2. For convenience, the flow boiling correlations presented in Section 3.2 are presented side-by-side with the results from this simulation. Two regimes are observed, corresponding to the two cases observed by Cetegen, and shown in Fig. 2.4.3. For the widest channel (see Fig. 3.5.2(a)), it is observed that little to no evaporation occurs, except at the lowest mass fluxes. This is due to an inability of the boundary layer to reach the center of the channel where the liquid-vapor interface resides and evaporation occurs. This is a direct consequence of the fact that the flow is still thermally developing. Accordingly, single-phase forced convection is the dominant form of heat transfer, and the surface becomes significantly superheated. It is worth noting that in reality, the superheat would be lower than predicted by the model, due to the presence of nucleate boiling, which the model does not simulate. Thus, it should come as no surprise that the flow boiling correlations provide reasonable estimates of heat transfer coefficient for this surface.

However, as mass flux or channel width is reduced (see Fig. 3.5.2(b)-(c)), the boundary layer more easily reaches the channel centerline, causing evaporation on the liquid-vapor interface. Thus, significant film evaporation occurs. It is no surprise that the correlations do not provide an accurate prediction of heat transfer coefficient, and that this prediction becomes increasingly worse as mass flux or channel width is decreased.

Moreover, the model shows a delicate balance between forced convection and thin film evaporation. For the smaller channels and lower mass fluxes, a maximum wall temperature is observed in the middle of the channel (see Fig. 3.5.3(a)). This is because in the beginning of the channel, the flow is thermally developing, resulting in large heat transfer coefficients on the wall; conversely, by the end of the microchannel, high heat

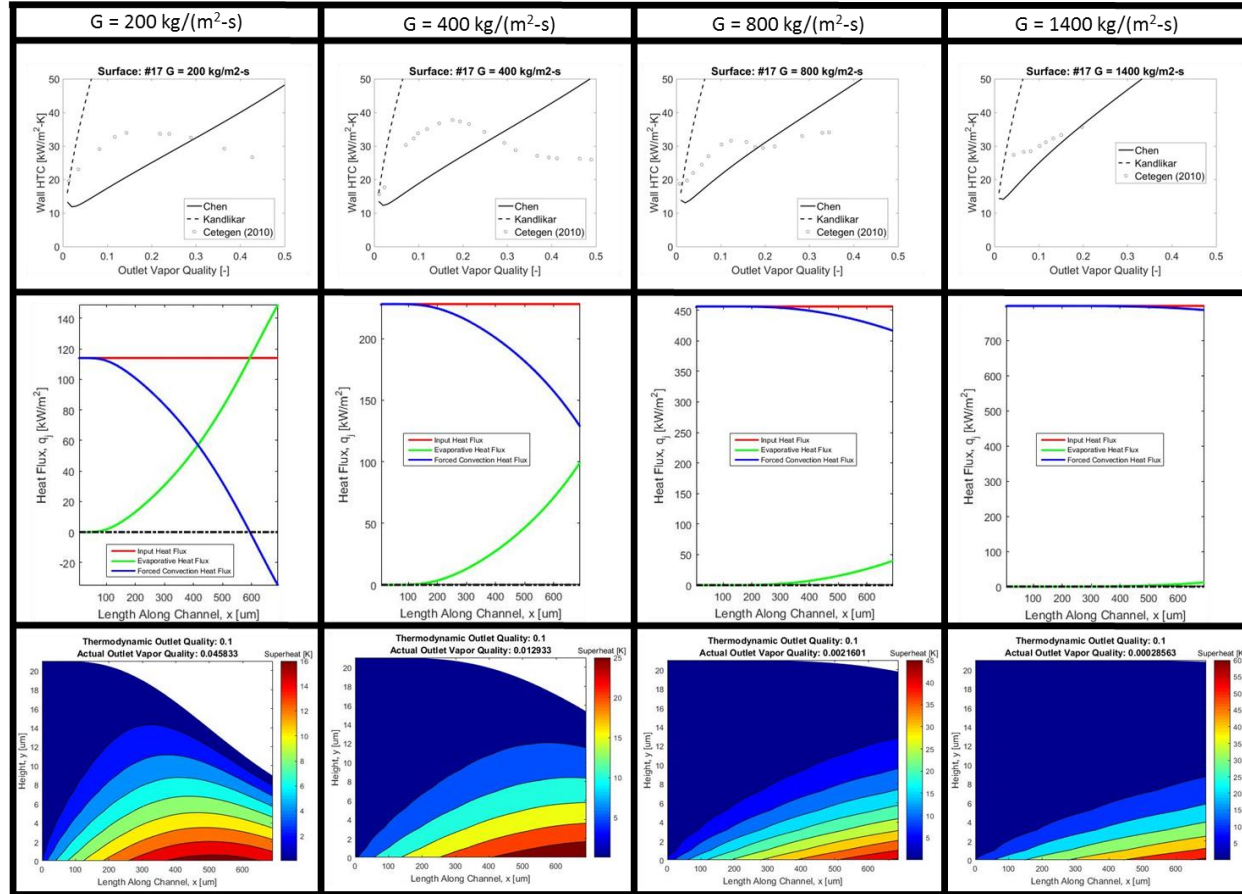
transfer coefficients are obtained not by developing flow (since the flow is already developed), but rather due to the thin film. Thus, the minimum wall heat transfer coefficient—corresponding to the highest wall temperature—is obtained in between these two regimes, where the sum of these two modes of heat transfer are minimum. This trend is noticeably absent for higher mass fluxes and wider channels, when the flow is still thermally developing and the boundary layer never reaches the channel centerline (see Fig. 3.5.3(b)).

Surface #12;  $w_{ch}=60\mu\text{m}$



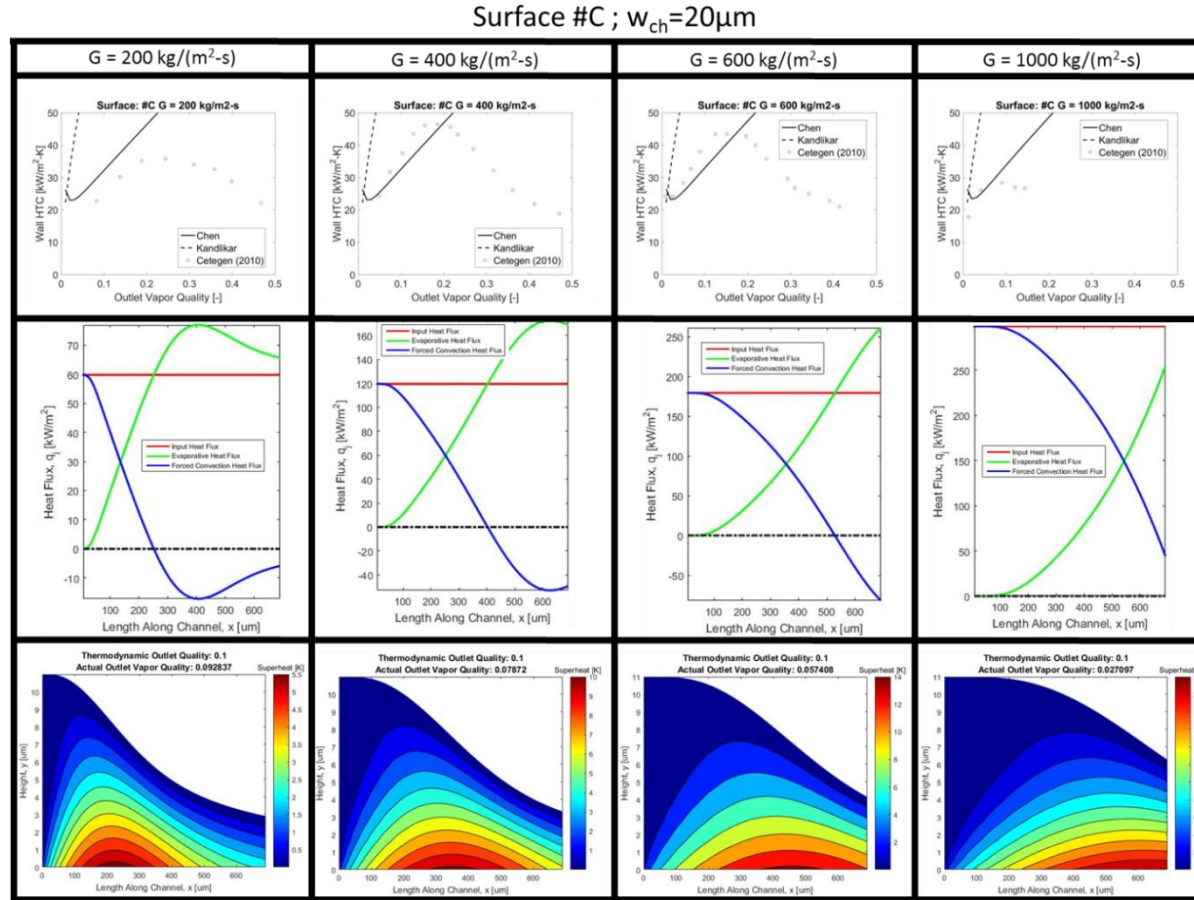
(a)

Surface #17;  $w_{ch}=40\mu\text{m}$



(b)



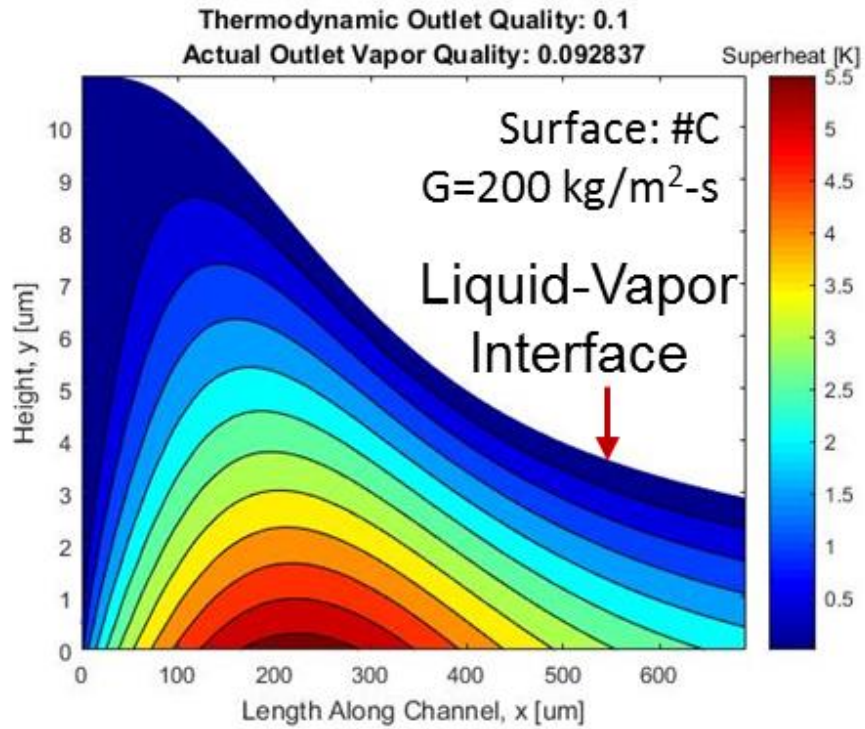


(c)

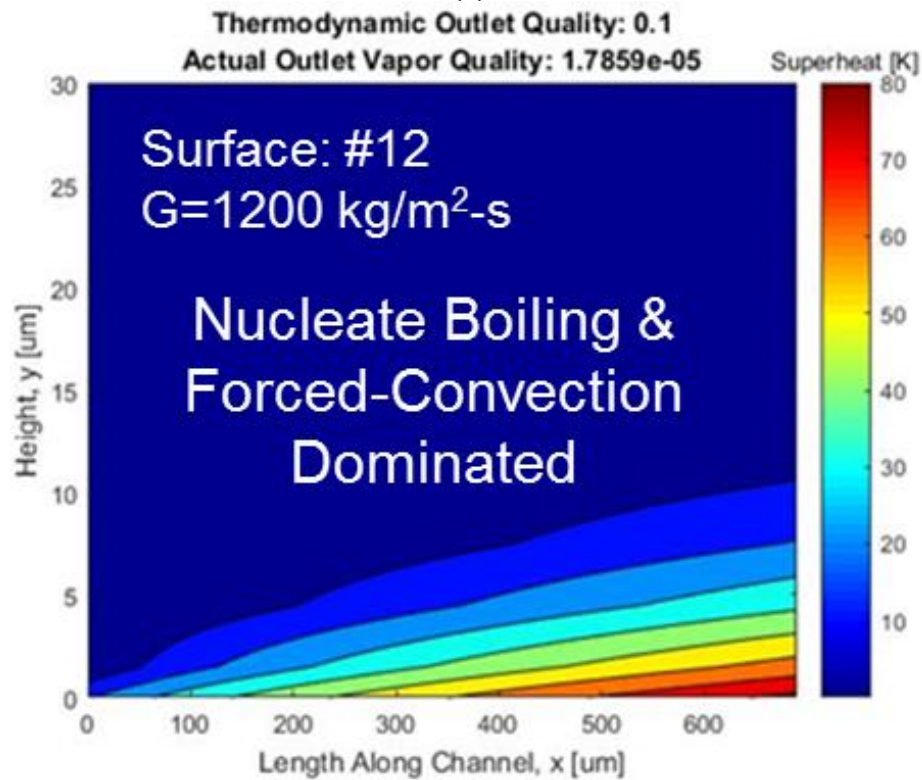
Fig. 3.5.2: Single-phase forced convection results for (a) 60  $\mu\text{m}$ , (b) 40  $\mu\text{m}$ , (c) 20  $\mu\text{m}$ -wide channel, corresponding to the geometries tested in Cetegen et al.

This idea is effectively illustrated in Fig. 3.5.3(c)-(d), where the input heat flux, evaporative heat flux, and forced convection heat flux are shown as a function of x-coordinate. From Fig. 3.5.3(c), it is apparent that forced convection dominates in the entry region of the microchannel, until the boundary layer begins to reach the liquid-vapor interface and evaporation becomes dominant. Interestingly enough, under the conditions tested here, the evaporation heat flux actually exceeds the input heat flux, and the forced convection heat flux becomes negative as the liquid releases heat and reduces in temperature. However, in Fig. 3.5.3 (d), this trend is absent. The input heat flux is only dissipated via forced convection, and evaporation barely takes place.

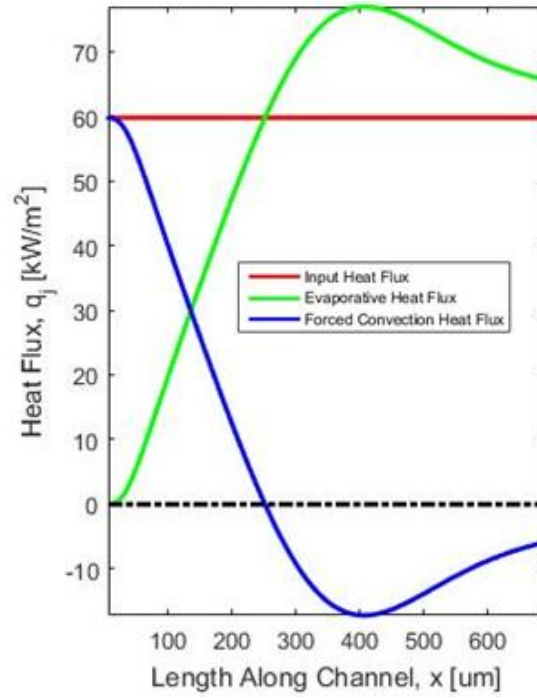
Accordingly, it should be apparent that forced convection is an important factor in determining the behavior of FEEDS systems, and could explain the sensitivity of the thermal performance of such systems to mass flow rate. Therefore, for the CFD model to be accurate, it would need to include fully developed and developing forced convection heat transfer.



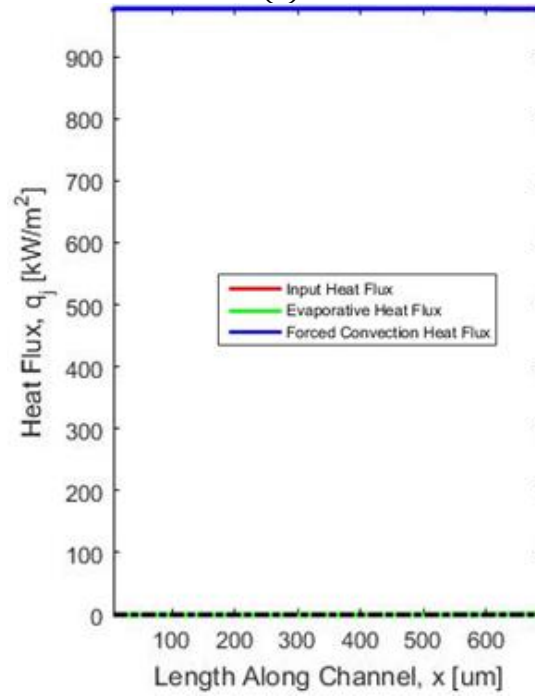
(a)



(b)



(c)



(d)

**Fig. 3.5.3: (a)-(b) Temperature contours (not to scale) for the lowest and highest Reynolds number, respectively; (c)-(d) Wall heat flux profiles, corresponding to (a)-(b).**

### **3.5.8 Model Summary**

In conclusion, the forced convection model with evaporation provided numerous insights into the physics governing FEEDS systems, including

- (1) the delicate interplay between forced convection heat transfer and thin film evaporation in FEEDS systems and the dimensionless parameters that govern this behavior;
- (2) developing flow exhibiting nucleate boiling and little thin film evaporation, due to the inability of the boundary layer (by definition) to reach the liquid-vapor interface at the center of the channel. This helps us understand the reasons for the qualitative behavior observed in previous two-phase FEEDS experiments;
- (3) the necessity to model developing forced-convection in the CFD model.

### **3.6 Flow Tube “Streamline” Model**

Utilizing the knowledge gained from the annular film evaporation with physics-based void fraction model and the forced-convection model, the role of thin film evaporation in the FEEDS system was investigated. However, rather than begin with a complicated 3-D volume of fluid (VOF), CFD-based approach, a simpler, first-order approximation was desired to see if thin film evaporation could explain the observed heat transfer coefficients. Because of this, a concession was made that the flow-tube model would be accurate only at low mass fluxes, when flow is fully developed, inertia is negligible, and film evaporation is dominant over nucleate boiling.

The heat transfer surface area was divided into parallel, non-interacting flow-tubes, and the quality, void fraction, film thickness, heat transfer coefficient, heat flux, and pressure drop were calculated sequentially along the flow-tube. The mass flow rate through each flow-tube was adjusted in order to obtain the specified pressure drop, and the value of this pressure drop was adjusted in order to obtain the desired microchannel mass flux. Finally, the average wall heat transfer coefficient was calculated, and the temperature profile in the fin was adjusted to correspond with the analytical 1-D temperature distribution of a thin fin with an average wall heat transfer coefficient and specified base superheat. The average wall heat transfer coefficients predicted by the model were then compared to the available experimental data with sufficiently good agreement with a wide variety of geometries and working fluids at low mass fluxes.

### 3.6.1 Model Domain

As with the previous models, the domain was reduced to a unit-cell of a manifold-microchannel system. However, the domain for the flow tube model is not the one shown in Fig. 3.1.2. Instead, a diagram of the unit cell appears in Fig. 3.6.1.

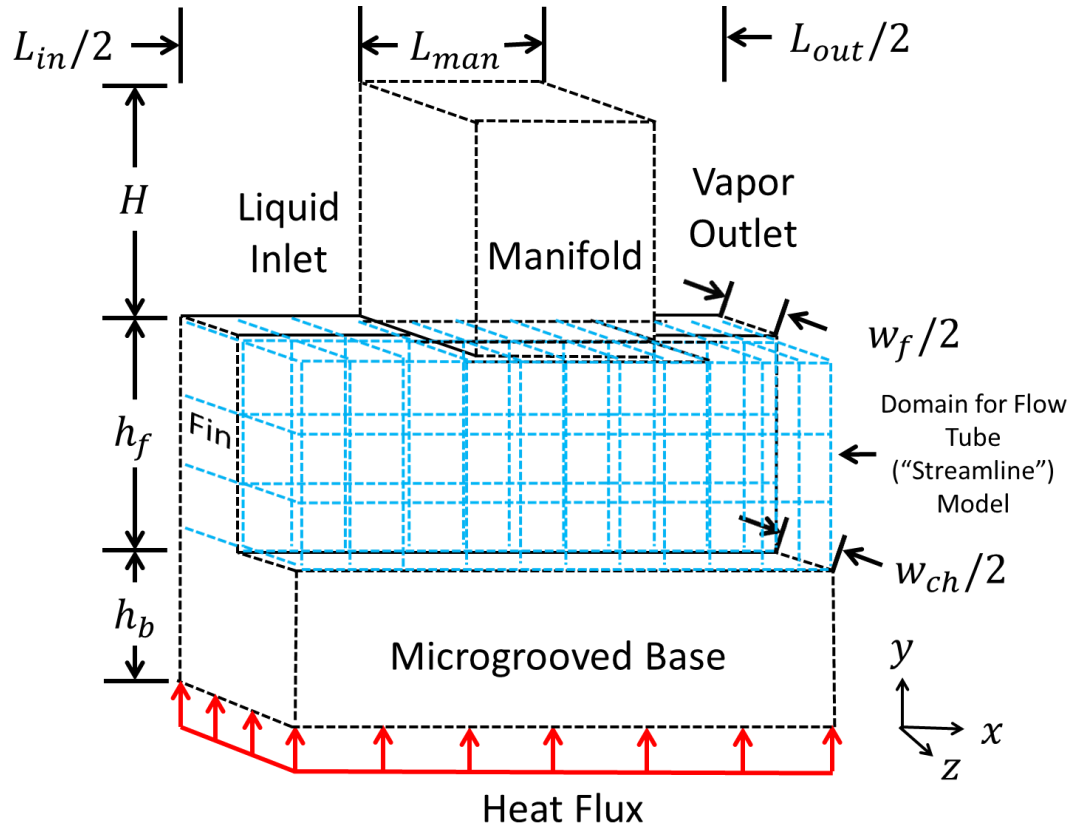


**Fig. 3.6.1: Domain for flow tube ("streamline") model.**

### 3.6.2 Model Assumptions

The following assumptions and simplifications were made in the model:

- (1) The fluid flow is steady-state, laminar, homogeneous, and hydrodynamically and thermally fully developed.
- (2) The fluid flow follows assumed flow-tubes and is one dimensional.

- (3) Flow distribution is governed by maintaining uniform pressure drop for all flow-tubes.
- (4) Pressure drop is caused by viscous stresses in the  $z$ -direction only (momentum, gravity, and shear forces between flow-tubes is neglected).
- (5) Liquid remains attached to wall and forms a thin film with vapor passing through the center of the channel (negligible liquid droplet entrainment).
- (6) All heat is transferred through 1-D conduction through the liquid film (no nucleate boiling or forced convection heat transfer).
- (7) Conduction in the fin is 1-D due to the effect of heat spreading.

The justifications for these assumptions and simplifications, as well as their implications, are detailed in the sections describing the model equations.

### 3.6.3 Meshing and Flow-Tubes

In order to impose flow-tubes, a specific mesh is needed. The meshing process begins by dividing the finned surface into three regions: the inlet, manifold, and outlet region, as shown in Fig. 3.6.2. Each domain was then meshed into a  $K \times K$  grid of cells, where  $K$  is the number of flow-tubes. Thus, the size of the mesh is  $3K \times K$ . A sample mesh is shown in Fig. 3.6.2(a). It should be noted that only three flow-tubes are shown for clarity; however, to obtain mesh independent results, approximately 25 flow-tubes were found to be needed.

Thus, the presence of flow-tubes essentially converts a 2-D flow into a series of parallel 1-D flows with known paths. The pressure drop and heat transfer characteristics for each flow-tube can be calculated independently based on the flow rate in that flow-tube.

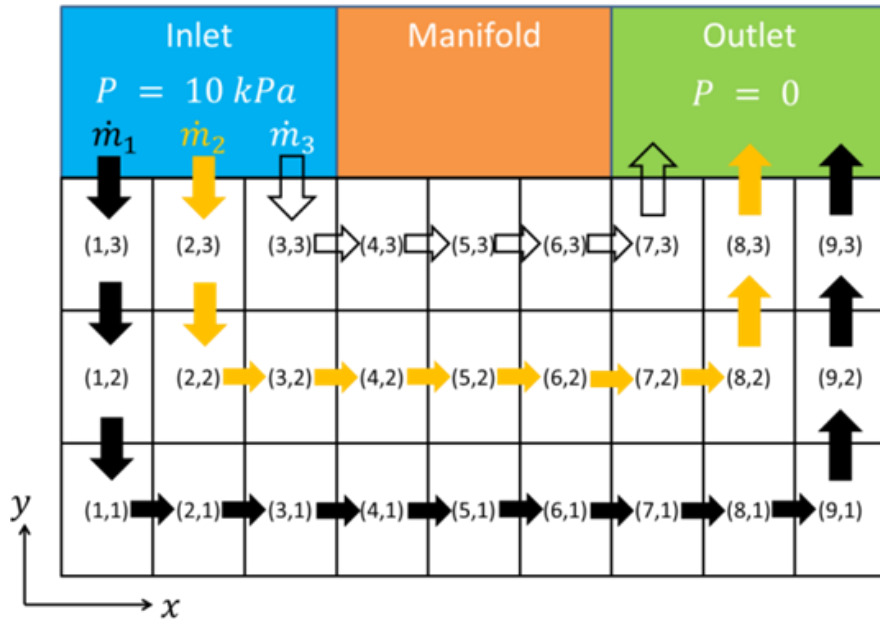


The first flow-tube for this mesh is then created by following the outer-most path; subsequent flow-tubes are then created following the next outer-most path, until all flow-tubes have been assigned. For instance, the first flow-tube consists—in  $i$  and  $j$  coordinates—of cells (1,3), (1,2), (1,1), (2,1), (3,1), (4,1), (5,1), (6,1), (7,1), (8,1), (9,1), (9,2), and (9,3), as shown Fig. 3.6.2(a).

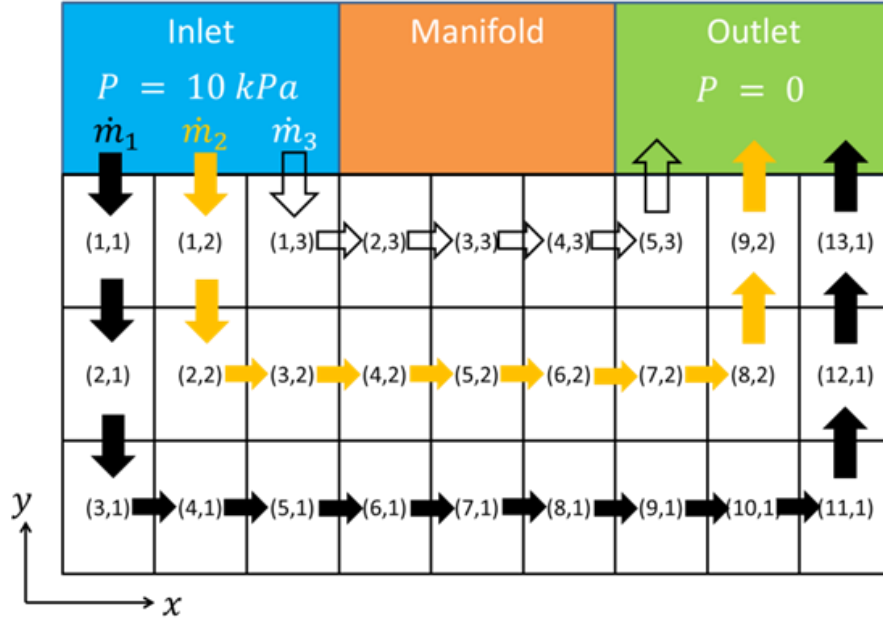
It can be shown that for the mesh described above, the number of cells,  $N_k$ , in the  $k_{th}$  flow-tube is equal to

$$N_k = 5K - 4k + 2 \quad (3.6.1)$$

Thus, after applying the flow-tubes, the  $3K \times K$  mesh in the  $i$  and  $j$  coordinates is essentially converted into a mesh in the  $n$  and  $k$  coordinates consisting of  $K$  vectors with  $N_k$  elements. A sample mesh with elements indexed in the  $n$  and  $k$  coordinates is shown in Fig. 3.6.2(b). It should be noted that the  $n$  and  $k$  coordinates are most convenient for wall heat transfer and pressure drop calculations, while the  $i$  and  $j$  coordinates are most convenient for wall temperature calculations.



(a)



(b)

**Fig. 3.6.2: Sample mesh diagram with three flow-tubes shown for clarity. To obtain mesh-independent results, approximately 25 flow-tubes were found to be needed.**

(a)  $i$  and  $j$  coordinates (b)  $n$  and  $k$  coordinates.

### 3.6.4 Wall Heat Transfer Equations

As mentioned above, the model is designed for accuracy at low mass fluxes. Based on the results from the forced-convection model, the flow is thermally fully developed, and film evaporation dominates over nucleate boiling and forced-convection. Accordingly, it will be assumed that all heat is transferred via conduction through the liquid film. Finally, since conduction through the liquid begins from the first cell attached to the inlet, the entire domain is two-phase.

To obtain the liquid film thickness, a void fraction correlation was employed. Although many void fraction correlations exist in the literature, a computationally efficient and physically realistic one is desired. In this model, the Zivi annular void fraction correlation was selected based on the result of the annular film evaporation with physics-based void fraction model. This correlation is of the form [51]:

$$\alpha_{n,k} = \frac{1}{1 + \frac{1 - X_{n,k}}{X_{n,k}} \left( \frac{\rho_v}{\rho_l} \right)^{2/3}} \quad (3.6.2)$$

This equation relates the local void fraction,  $\alpha_{n,k}$ , to the local vapor quality,  $X_{n,k}$ , and the density ratio between the vapor and liquid.

Due to the low Weber numbers, surface tension forces are assumed to dominate over inertia, preventing liquid droplet entrainment and allowing the liquid to remain attached to the wall where it can then form a thin film. Under these conditions, the local void fraction is geometrically related to the local thickness of the liquid film by

$$\delta_{n,k} = (1 - \alpha_{n,k}) w_{ch}/2 \quad (3.6.3)$$

Since the liquid film is assumed to be steady-state and thermally fully developed, and the effect of forced convection is neglected, the temperature distribution in the liquid film varies linearly from the wall temperature,  $T_{wall}$ , to the liquid-vapor interface temperature,  $T_{lv}$  [9, 52, 53]. However, except for the thinnest of films—where disjoining pressure from Van-der-Waals forces act to suppress evaporation—the liquid-vapor interface temperature,  $T_{lv}$ , is approximately equal to the saturation temperature,  $T_{sat}$  [52, 53]. Although thin films have the highest potential for heat transfer, the amount of heat is usually limited by the amount of liquid available for evaporation, as will be discussed in more detail below. Accordingly, even though accounting for the effect of disjoining pressure on evaporation suppression might act to reduce the amount of evaporated liquid for a given superheat, the amount of liquid evaporated was almost always still found to be larger than the amount of liquid available. Since a check is included to limit the evaporation rate to the available liquid, this effect can be neglected. The local mass flux

of evaporated liquid,  $(\dot{m}''_{evap})_{n,k}$ , can therefore be calculated from 1-D conduction through the liquid film:

$$(\dot{m}''_{evap})_{n,k} = \frac{\lambda_l}{\delta_{n,k}} \frac{(T_{wall})_{n,k} - T_{sat}}{h_{lv}} \quad (3.6.4)$$

The local wall heat flux,  $(q''_{wall})_{n,k}$ , and wall heat transfer coefficient,  $(h_{wall})_{n,k}$ , can be calculated from Eqs. (3.6.5) and (3.6.6), respectively:

$$(q''_{wall})_{n,k} = (\dot{m}''_{evap})_{n,k} h_{lv} \quad (3.6.5)$$

$$(h_{wall})_{n,k} = \frac{(q''_{wall})_{n,k}}{(T_{wall})_{n,k} - T_{sat}} \quad (3.6.6)$$

The resulting local quality after evaporation,  $X'_{n,k}$ , can be calculated by adding the newly-evaporated liquid flow rate,  $(\dot{m}_{evap})_{n,k}$ , into the mass flow rate of vapor entering the cell and normalizing by the total mass flow:

$$X'_{n,k} = \frac{\dot{m}_k X_{n-1,k} + (\dot{m}_{evap})_{n,k}}{\dot{m}_k} = X_{n-1,k} + \frac{(\dot{m}_{evap})_{n,k}}{\dot{m}_k} \quad (3.6.7)$$

where  $(\dot{m}_{evap})_{n,k}$  and  $(\dot{m}''_{evap})_{n,k}$  are related by the area of the control volume:

$$(\dot{m}_{evap})_{n,k} = 2 \Delta x_{n,k} \Delta y_{n,k} (\dot{m}''_{evap})_{n,k} \quad (3.6.8)$$

The resulting local quality after evaporation is substituted back into Eq. (3.6.2), and Eqs. (3.6.3)-(3.6.8) are solved sequentially until the local quality before evaporation,  $X_{n,k}$ , equals the local quality after evaporation,  $X'_{n,k}$ . This repetitive process essentially serves as an iterative method for the simultaneous solution of Eqs. (3.6.2)-(3.6.8).

It is important to ensure that the evaporation rate is limited by the liquid available to the cell in order to ensure conservation of mass and energy. For moderate to high local vapor qualities and correspondingly thin liquid films, the mass flow rate of evaporated liquid causes Eq. (3.6.7) to produce vapor qualities larger than one. When this happens, a

correction is needed: the cell is assumed to have evaporated all of the available liquid, and the mass flow rate of evaporated liquid,  $(\dot{m}_{evap})_{n,k}$ , is reset to equal the mass flow rate of liquid entering the cell,  $(\dot{m}_l)_{n,k}$ , which can be calculated from the definition:

$$(\dot{m}_{evap})_{n,k} = (\dot{m}_l)_{n,k} = (1 - X_{n-1,k}) \dot{m}_k \quad (3.6.9)$$

where  $X_{n-1,k}$  represents the quality upwind of cell  $n$  in flow-tube  $k$ .

If a correction is needed, there is no need for an iterative solution of Eqs. (3.6.2)-(3.6.8). Instead, Eqs. (3.6.5)-(3.6.6) should be recalculated with the new value of  $(\dot{m}_{evap})_{n,k}$  from Eq. (3.6.9). It is worth noting that upon local dryout, the vapor quality is constant and equal to unity; accordingly, no additional heat transfer can occur in this flow-tube, and the evaporative mass flux, heat flux, and average wall heat transfer coefficient equal zero.

### 3.6.5 Pressure Drop Equations

Even though the pressure drop through the flow-tubes is not the primary concern of this model, since it is thought to affect the two-phase heat transfer characteristics of manifold-microchannels based on the results in Cetegen [10], it is desirable to obtain a first-order approximation of pressure drop in order to assess the flow distribution through the flow-tubes. To accomplish this, the most dominant pressure drop term—the fully developed, viscous pressure drop due to shear in the  $z$ -direction—was used. Although the bending and acceleration of the flow due to evaporation contribute significantly to the pressure drop—especially at high flow rates and outlet vapor qualities—these terms were neglected because this model was designed primarily for accuracy at low mass fluxes. Likewise, the flow is also hydrodynamically fully developed due to the low mass fluxes.

Furthermore, due to the omission of the additional pressure drop components, the pressure profiles created were treated as being relative only, and not used as a physical value with which to update saturation temperature.

The pressure drop was calculated assuming laminar, homogeneous, fully developed, two-phase flow. Under these circumstances, the pressure drop can be written as

$$\Delta P_{n,k} = \frac{1}{2} \frac{f_{n,k}}{D_h} \frac{G_{n,k}^2}{\rho_{n,k}} \Delta x'_{n,k} \quad (3.6.10)$$

Due to the large aspect ratio, the hydraulic diameter can be assumed to be equivalent to the case of parallel plates. The hydraulic diameter can therefore be calculated as

$$D_h = \frac{4A_{ch}}{P_{ch}} = 2 w_{ch} \quad (3.6.11)$$

Similarly, the local friction factor,  $f_{n,k}$ , can be calculated as

$$f_{n,k} = \frac{96}{Re_{n,k}} \quad (3.6.12)$$

where the local two-phase Reynolds number,  $Re_{n,k}$ , can be calculated as

$$Re_{n,k} = \frac{G_{n,k} D_h}{\mu_{n,k}} \quad (3.6.13)$$

Substituting Eqs. (3.6.11)-(3.6.13) into Eq. (3.6.10) and simplifying yields the simpler relationship for the local pressure drop:

$$\Delta P_{n,k} = \frac{12 \mu_{n,k}}{w_{ch}^2} \frac{G_{n,k}}{\rho_{n,k}} \Delta x'_{n,k} \quad (3.6.14)$$

where the local, homogenous, two-phase density and viscosity can be calculated from [51]:

$$\rho_{n,k} = \frac{1}{\frac{1 - X_{n,k}}{\rho_l} + \frac{X_{n,k}}{\rho_v}} \quad (3.6.15)$$

$$\mu_{n,k} = \frac{1}{\frac{1 - X_{n,k}}{\mu_l} + \frac{X_{n,k}}{\mu_v}} \quad (3.6.16)$$

The local mass flux,  $G_{n,k}$ , can then be calculated based on the total mass flow rate of the flow-tube,  $\dot{m}_k$ , and the local cross sectional area of the flow,  $A_{n,k}$ :

$$G_{n,k} = \frac{\dot{m}_k}{A_{n,k}} \quad (3.6.17)$$

It is worth noting that the flow area,  $A_{n,k}$ , is the area perpendicular to the flow, the value of which changes along the flow-tube due to a change in flow direction and meshed region. The changes in flow area need to be accounted for in order to obtain the correct mass flux. In addition, it is worth noting that  $\Delta x'_{n,k}$  represents the distance in the flow direction, which changes along the flow-tube.

Finally, the total pressure drop in the  $k^{th}$  flow-tube can be calculated from a summation of the local pressure drops for all cells in the flow-tube:

$$\Delta P_k = \sum_{n=1}^N \Delta P_{n,k} \quad (3.6.18)$$

### 3.6.6 Wall Temperature Equations

Due to the small Biot numbers for the range of conditions expected of the model, conduction in the fin can be neglected in the z-direction and treated as 2-D. Furthermore, due to the presence of a thick base, which acts as a heat spreader, the fin might be more accurately modeled as having a uniform base fin temperature rather than a uniform base heat flux. Accordingly, conduction in the fin can be approximated as 1-D in the y-

direction. For a 1-D rectangular fin with a known base superheat,  $\Delta T_{base}$ , and average base heat flux,  $\bar{q}''_{base}$  (defined in Eq. (3.6.24)), the average wall heat transfer coefficient,  $\bar{h}_{wall}$ , fin efficiency,  $\eta$ , and parameter,  $m$ , can be calculated implicitly from Eqs. (3.6.19)-(3.6.21) [3]:

$$\bar{h}_{wall} = \frac{\bar{q}''_{base}}{\Delta T_{base}} \left( \frac{w_{ch} + w_f}{2 \eta h_f + w_{ch}} \right) \quad (3.6.19)$$

$$\eta = \frac{\tanh(m h_f)}{m h_f} \quad (3.6.20)$$

$$m = \sqrt{\frac{2 \bar{h}_{wall}}{w_f \lambda_s}} \quad (3.6.21)$$

Upon the solution of Eqs. (3.6.19)-(3.6.21) for  $\bar{h}_{wall}$ ,  $\eta$ , and  $m$ , the temperature distribution in the wall as a function of  $y$  can then be calculated from

$$T_{i,j} = T_{sat} + \Delta T_{base} \frac{\cosh(m(h_f - y_{i,j}))}{m h_f} \quad (3.6.22)$$

The temperature distribution in the fin can therefore be calculated for the 2-D mesh by substituting the  $y$ -value of the cell centroids into Eq. (3.6.22).

Furthermore, for a known wall heat flux profile,  $(q''_{wall})_{i,j}$ , the total heat,  $Q_{ch}$ , and the average base heat flux,  $\bar{q}''_{base}$ , can be calculated from Eqs. (3.6.23) and (3.6.24), respectively:

$$Q_{ch} = \sum_{j=1}^K \sum_{i=1}^{3K} 2 q''_{wall,i,j} \Delta x_{i,j} \Delta y_{i,j} \quad (3.6.23)$$

$$\bar{q}''_{base} = \frac{Q_{ch}}{(w_{ch} + w_f) L_{ch}} \quad (3.6.24)$$



### 3.6.7 Data Analysis Equations

Some additional definitions are needed. If all the flow rates,  $\dot{m}_k$ , through the flow-tubes,  $K$ , are known, the average mass flux through the microchannel area can be calculated by summing the flow rates through each flow-tube and dividing by the microchannel area:

$$\bar{G}_{ch} = \frac{1}{w_{ch} h_f} \sum_{k=1}^K \dot{m}_k \quad (3.6.25)$$

In addition, the average outlet vapor quality can be calculated from the definition,

$$\bar{X}_{out} = \frac{Q_{ch}}{\bar{G}_{ch} w_{ch} h_f h_{lv}} \quad (3.6.26)$$

### 3.6.8 Solution Algorithm

A process flow diagram of the solution algorithm appears in Fig. 3.6.3. To begin, two operational conditions are needed: the desired base superheat,  $\Delta T_{base}$ , and microchannel mass flux,  $G_{ch}$ . Then, a number of initial guess values are needed: the mass flow rates through each flow-tube,  $\dot{m}_k$ , the pressure drop,  $\Delta P_{ch}$ , needed to create the desired microchannel mass flux,  $G_{ch}$ , and the average wall heat transfer coefficient,  $\bar{h}_{wall}$ .

The algorithm then proceeds as follows:

- (1) Using Eqs. (3.6.21)-(3.6.22), compute the temperature distribution from the base superheat,  $\Delta T_{base}$ , and average wall heat transfer coefficient,  $\bar{h}_{wall}$ .
- (2) Starting with the first cell in the flow-tube, solve Eqs. (3.6.2)-(3.6.8) simultaneously to obtain the local vapor quality, film thickness, evaporative mass

flux, wall heat flux, and wall heat transfer coefficient using the upwind value of quality,  $X_{n-1,k}$ , as an initial guess of vapor quality.

- (3) Repeat step (2) for all  $N_k$  cells in a flow-tube. The local pressure drops,  $\Delta P_{n,k}$ , are then calculated from Eqs. (3.6.11)-(3.6.10), and the total pressure drop through the flow-tube,  $\Delta P_k$ , is calculated from Eq. (3.6.18).
- (4) Adjust the mass flow rate through the flow-tube,  $\dot{m}_k$ , in order to achieve the desired pressure drop,  $\Delta P_{ch}$ , and return to step (2).
- (5) Repeat steps (2)-(4) for all flow-tubes,  $K$ , and calculate the average microchannel mass flux,  $\bar{G}_{ch}$ , from Eq. (3.6.25).
- (6) Adjust the pressure drop,  $\Delta P_{ch}$ , in order to achieve the desired microchannel mass flux,  $G_{ch}$ , and return to step (2).
- (7) Calculate the average base heat flux,  $\bar{q}_{base}''$ , from Eqs. (3.6.23)-(3.6.24), and the average wall heat transfer coefficient,  $\bar{h}_{wall}$ , from Eqs. (3.6.19)-(3.6.21). Return to step (1) until the value of the average wall heat transfer coefficient converges.

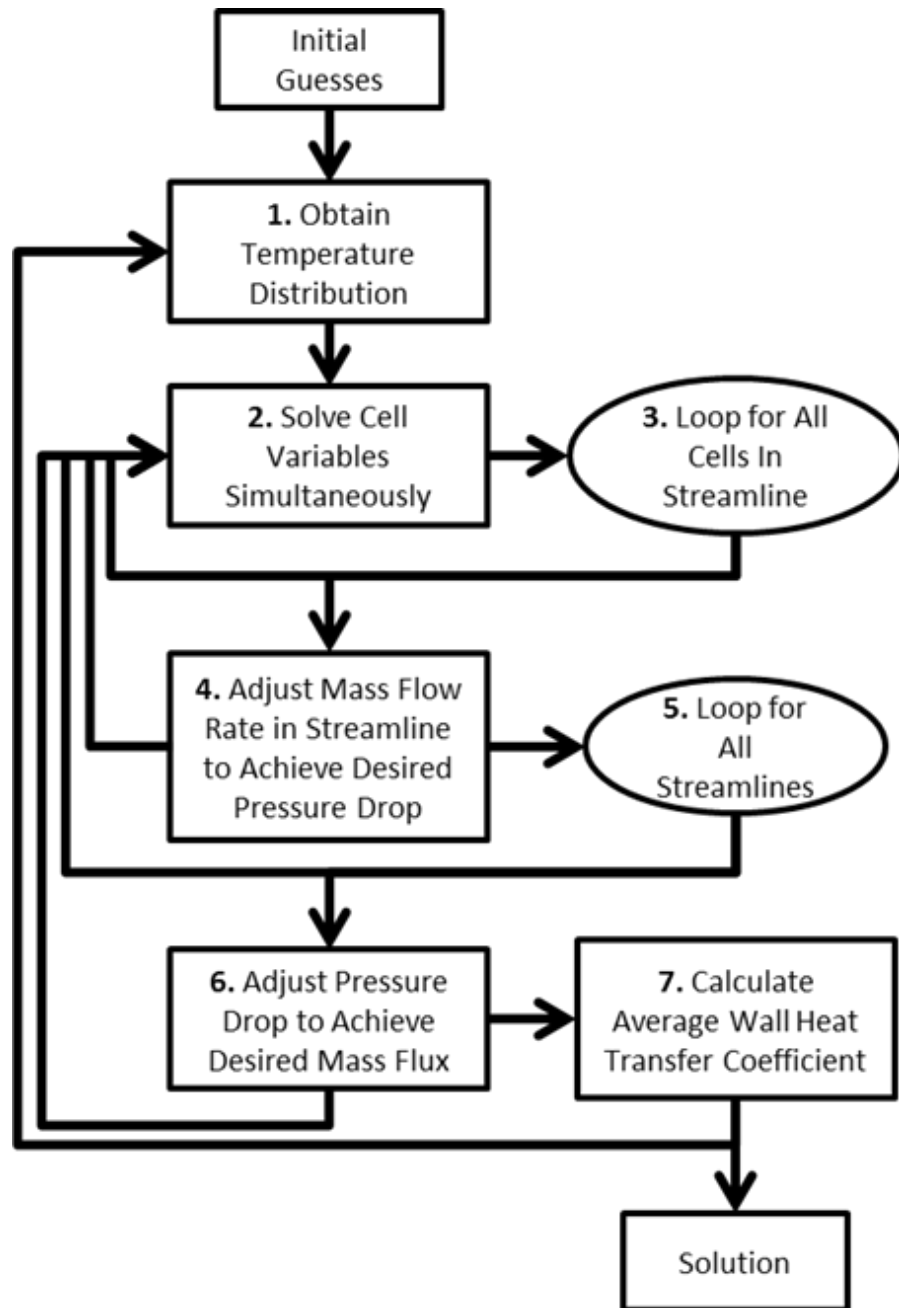
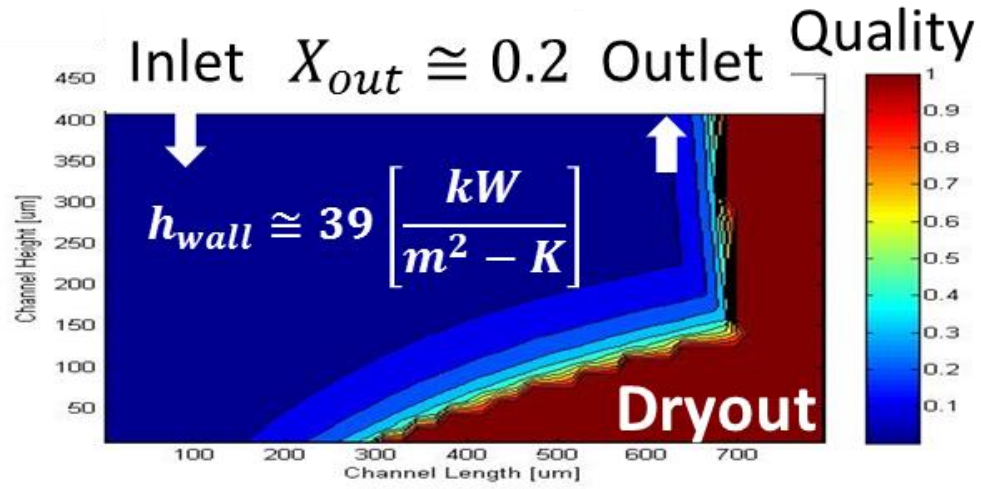


**Fig. 3.6.3: Process flow diagram of the flow-tube model algorithm.**

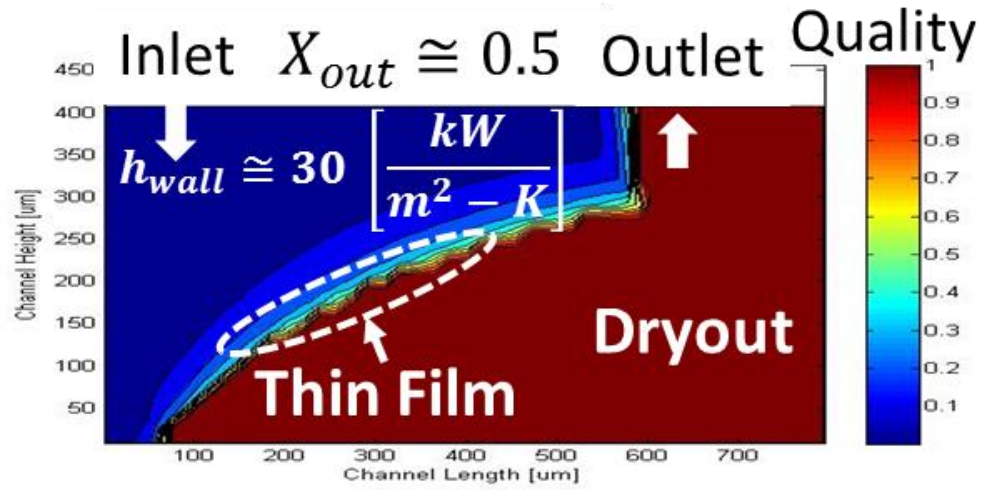
### 3.6.9 Results

The manifold-microchannel apparatus described in Cetegen [10] was used to run experiments in order to compare them to the model. The surface and manifold geometric specifications appear in Cetegen [10]. Various surface designs and working fluids were tested with the same manifold design. A comparison between the average wall heat transfer coefficient predicted by the model and that obtained experimentally appears in Fig. 3.6.6. It is clear that the model presented here matches well with experimental results—both qualitatively and quantitatively—especially when considering the lack of agreement between experimental results and conventional two-phase heat transfer correlations, shown in Fig. 2.4.3. Accordingly, the model does a more accurate job at representing the essential physics than the available correlations.

Furthermore, the model implies that film evaporation alone is capable of achieving the high heat transfer coefficients observed in Cetegen and provides some insight into experimental trends. First, it is worth noting that most surface/working fluid combinations produced a trend of increasing average wall heat transfer coefficient for low average outlet vapor qualities, and a decreasing average wall heat transfer coefficient for average outlet vapor qualities larger than some optimum value. The trend of increasing average wall heat transfer coefficient was found to be due to an increased area of a thin liquid film. However, once the average outlet vapor quality became too large, large regions of dryout were found to develop directly underneath the outlet on the bottom of the microchannel due to the asymmetric liquid feeding and heating, as shown in Fig. 3.6.4. These large regions of dryout acted to dilute the effect of the thin film and ultimately caused the average wall heat transfer coefficient to decrease.



(a)



(b)

**Fig. 3.6.4: Contours of vapor quality at various outlet vapor qualities: (a) 20% and (b) 50%.**

In addition, the model also predicts the effect of varying the liquid-vapor density ratio. Due to the appearance of this ratio in the void fraction correlation (see Eq. (3.6.2)), the void fraction is dependent on liquid-vapor density ratio. The Zivi annular void fraction correlation is plotted in Fig. 3.6.5 for the two working fluids tested here, R245fa and R134a. The results show that for the same vapor quality, R245fa produces a higher void fraction, and subsequently, a thinner film. Accordingly, heat transfer coefficients with R245fa were expected to be higher, and this expectation was met, as shown in Fig.

3.6.6. This is in stark contrast to the effect of liquid-vapor density ratio on nucleate boiling, where lower density ratios involve higher system pressures, which, from Forster and Zuber's correlation [46], will result in an increased heat transfer coefficient (see Eq. (3.2.7)).

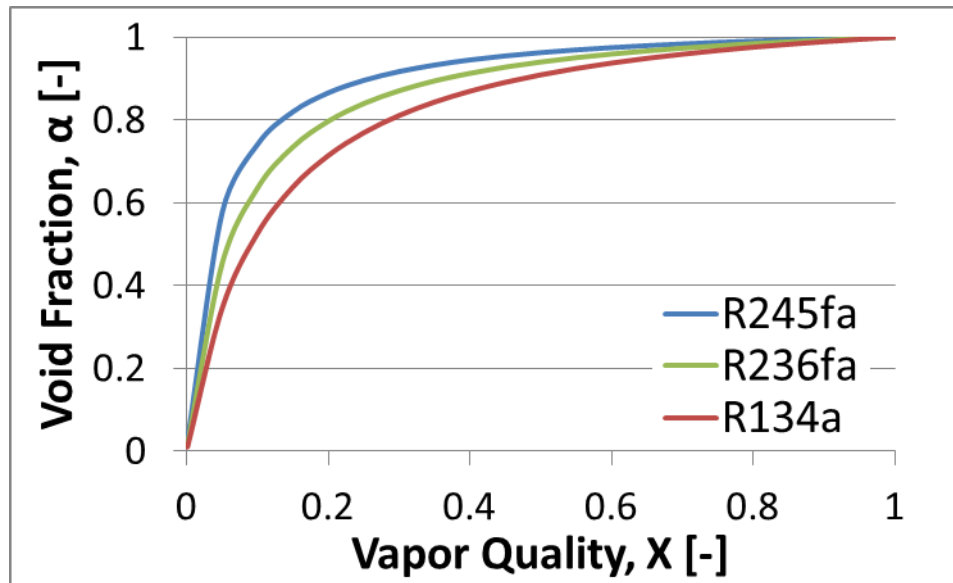
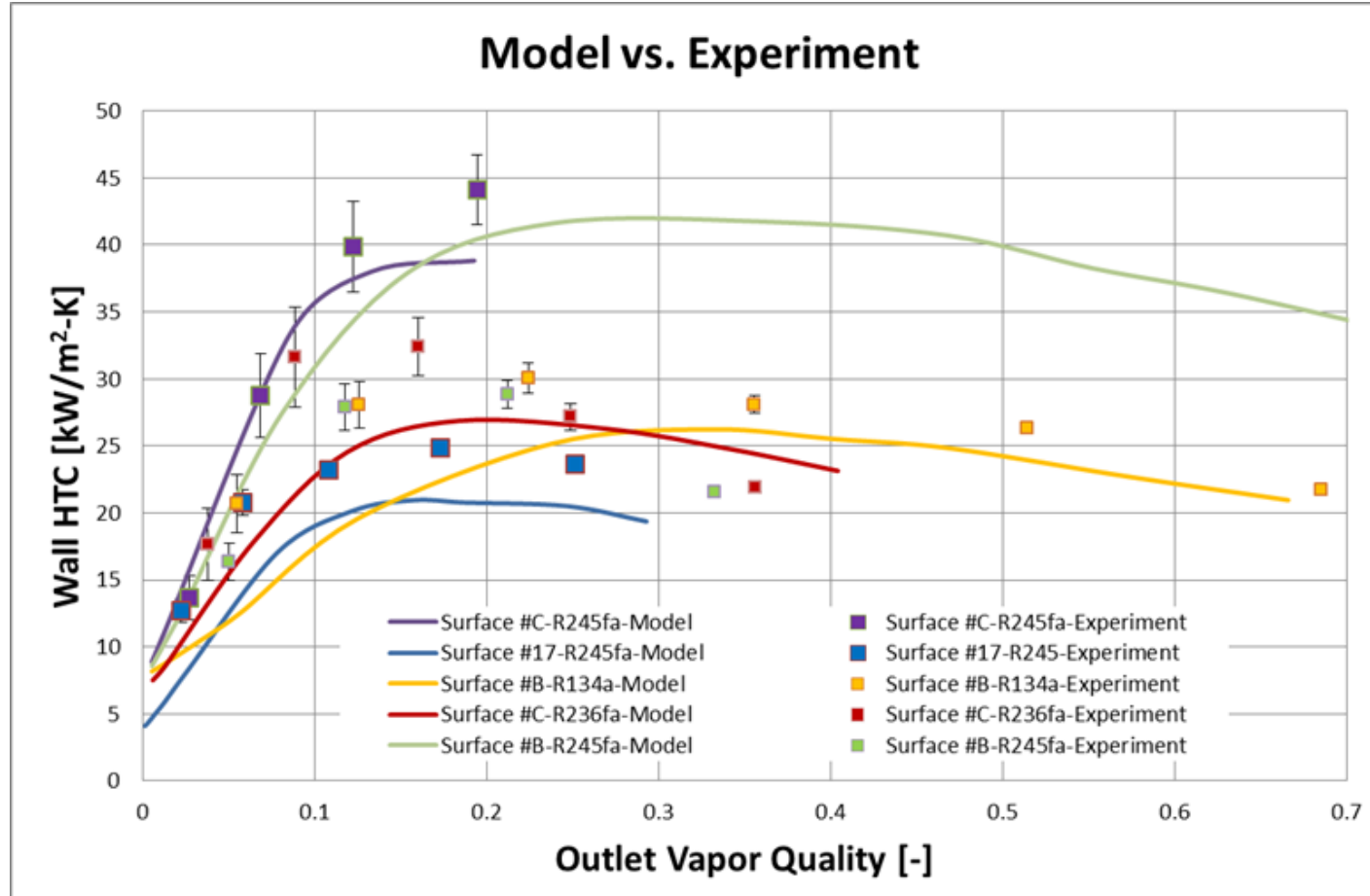


Fig. 3.6.5: Void fraction vs. vapor quality from the Zivi void fraction correlation.



**Fig. 3.6.6: Comparison of experimental results with those predicted by the model for various surfaces and working fluid combinations. Experiment design and surface design details are given in Cetegen [10].**

### **3.6.10 Model Summary**

A simplified flow-tube model was developed to predict the two-phase thermal performance of manifold-microchannels. It was found that the model

- (1) shows significantly improved accuracy when compared to the available correlations in the literature;
- (2) suggests that two-phase heat transfer on the walls of thin-gapped microchannels is governed by conduction through the thin liquid film;
- (3) indicates that partial dryout on the walls of the microchannels is responsible for the experimentally-found optimum outlet vapor quality;
- (4) predicts that higher density ratio fluids will produce higher heat transfer coefficients in film evaporation, in contrast to the effect of increased density ratio on nucleate boiling, where decreased density ratio (increased system pressure) results in increased nucleate boiling heat transfer coefficient.



### ***3.7 Preliminary Modeling Summary***

First, the available flow boiling correlations in the literature were surveyed and compared to past experimental data. It was found that while the Kandlikar correlation over-predicted heat transfer coefficient, the Chen correlation provided increasingly accurate predictions for high Reynolds numbers. In addition, flow regime maps were reviewed and used to predict flow regime transitions. These maps revealed that the transition to annular flow occurs at very low vapor qualities ( $\leq 6\%$ ), thereby highlighting the need to focus on annular flow modeling.

Next, annular film evaporation was investigated using a 1-D mixture model that computes the void fraction and subsequent liquid film thickness using the Young-Laplace equation. In the end, a significant effect of mass flux was found: for low mass fluxes, the volume fraction matches that predicted by the analytical solution for laminar, annular, two-phase flow between parallel plates; for high mass fluxes, the liquid volume fraction approaches the solution from the Zivi annular void fraction correlation. Since liquid volume fraction is directly related to film thickness, knowledge of the correct liquid volume fraction is critical for determining the correct heat transfer coefficient.

Third, the combined effect of single-phase, fully developed and developing forced convection on an evaporating film was investigated. For low mass fluxes (i.e. thermally fully developed flow), the thermal boundary layer quickly reaches the liquid-vapor interface, resulting in significant evaporation and little forced convection; however, for larger mass fluxes (i.e. thermally developing flow), the thermal boundary layer never reaches the liquid-vapor interface, resulting in little evaporation, and consequently the heat transfer is dominated by forced convection and nucleate boiling. Accordingly, the

balance between single-phase forced-convection and annular film evaporation is critical, and should be modeled.

Finally, the effects of intra-microchannel flow distribution and fin conduction were investigated using a flow-tube model, which divides the manifold-microchannel unit cell into a system of parallel, non-interacting evaporating streamlines, and computes wall temperature using a 1-D fin equation. In the end, it was established that due to the asymmetric liquid feeding and heating, dryout occurred on the wall of the microchannel at vapor qualities below 10%, resulting in extremely thin film and a heat transfer coefficient that increases with increasing outlet vapor quality. However, as outlet vapor quality is increased, a significant area of the microchannel wall becomes dry, resulting in a decreasing wall heat transfer coefficient and an optimum vapor quality significantly lower than that of straight microchannels.

The preliminary modeling effort highlighted the roles of nucleate boiling, single-phase, fully developed and developing forced-convection heat transfer, liquid and vapor volume fraction, intra-microchannel flow distribution, and fin conduction in accurately predicting heat transfer coefficients in FEEDS systems. Accordingly, the final model, presented in Chapter 4, will include all of these effects.

## 4 2.5-D Microchannel Model

Computational fluid dynamics is a powerful tool for simulating thermal and hydrodynamic performance of complex heat exchangers. For single-phase laminar flow of a Newtonian fluid, few assumptions and simplifications need to be made, and the Navier-Stokes equations can be solved using a finite-volume or finite-element method. For two-phase flows, the interface between the separate phases must be tracked, often requiring very fine meshes to obtain mesh-independent results. In addition, the need to track the interface of the phases puts a limit on the time step for numerical stability [54-56]. This limit is called the Courant number, and is defined as:

$$C = u \frac{\Delta t}{\Delta x} \leq C_{max} \quad (3.7.1)$$

For explicit numerical schemes,  $C_{max} = 1$ . Since the Courant number is inversely proportional to mesh spacing,  $\Delta x$ , for smaller geometries, the time step must be reduced. In addition, because fine meshes are often required to obtain mesh-independent results, the Courant number constraint would require smaller time steps, which would then require more time steps for the same simulation time. Accordingly, two-phase simulations run with the volume of fluid (VOF) method often require fine meshes and small time steps—with Courant numbers as low as 0.05 [55] and time steps as low as  $10^{-8}$  s [56]—and it can take weeks to perform enough iterations to arrive at a solution. Therefore, other approaches, if they can be found to provide sufficiently accurate predictions, are highly desirable.

Accordingly, an alternate approach was taken here. The preliminary models presented in the previous chapter provided the foundation for a master model, capable of

taking into account the physics simulated in each of the preliminary models. However, in the interest of understanding the effects of the physical phenomena as well as troubleshooting the model, the model was formulated so as to keep the various physical assumptions independent. In addition, due to the non-standard assumptions and model couplings, a custom numerical code was developed in-house. The governing 2-D Navier Stokes equations were discretized using the first-order upwind scheme and solved using the SIMPLE algorithm. These equations were coupled to the VOF via the fluid mixture density, and the VOF equation was coupled to the liquid and wall temperature via two-phase heat and mass transfer.

The custom code was first validated by comparing single-phase thermal and hydrodynamic predictions in fully developed and developing flow to those obtained using 3-D ANSYS Fluent. Then, the effect of the various two-phase physics options was investigated, and past two-phase experimental results [10] were compared to the model. Finally, a parametric study was performed on the effect of various geometry variables, and a baseline design was obtained to meet the ICECool metrics.

## 4.1 *Model Domain*

Like previous models, the symmetries inherent to a manifold-microchannel system were utilized to simplify the domain down to a unit cell. This simplification relies on the assumption of an even inter-microchannel flow distribution. This assumption is valid if the manifold is designed properly, such that an even inter-microchannel flow distribution is obtained. Since a manifold model (described in the next chapter) will be used to properly design the manifold, this assumption was considered to be valid.

However, unlike previous preliminary models, this model is not intended to merely to probe the physics, to be accurate only at low mass fluxes, or to predict only heat transfer coefficient. Rather, it is intended to provide an as accurate-as-possible prediction of heat transfer and pressure drop. Accordingly, the domain was simulated in two dimensions: two parallel, aligned 2-D meshes were used—one to simulate the fluid and to simulate the solid. The domain and sample mesh are shown in Fig. 4.3.7.

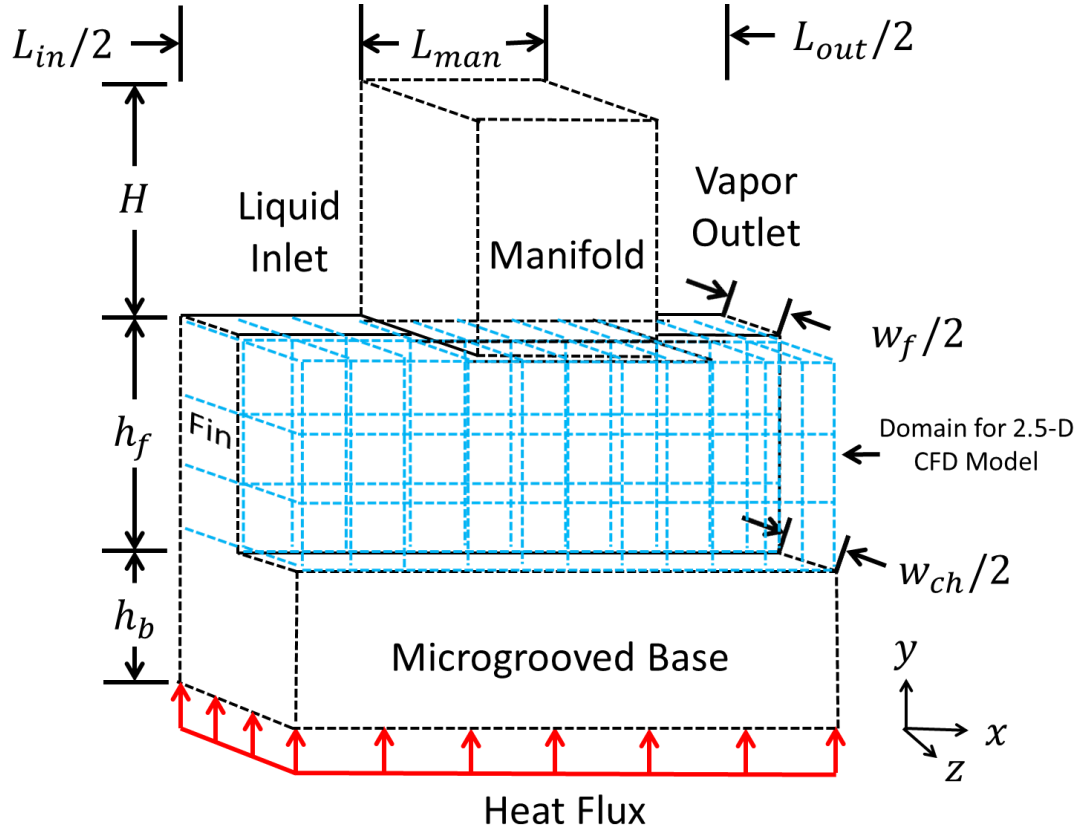


**Fig. 4.1.1: Model domain and sample mesh for the 2.5-D microchannel model**

## 4.2 Model Assumptions

The following assumptions and simplifications were made in the model:

- (1) The fluid flow is 2-D, steady-state, laminar and can be modeled as a mixture.
- (2) A friction factor and Nusselt number can be used to simulate the effect of the third dimension (z-coordinate), which is not simulated.
- (3) Liquid remains attached to the wall and forms a thin film with vapor passing through the center of the channel (no liquid droplet entrainment).
- (4) Wall temperature distribution is 2-D in the x- and y-coordinates (Biot number  $\ll 1$ ).

- (5) The effect of base spreading on the temperature distribution at the base of the fin is ignored.

### 4.3 *Model Equations*

The equations used in the 2.5-D microchannel model will be presented in this subsection. The term “2.5-D” is used here to highlight the assumptions and simplifications made to the model, which allow the 3-D domain to be simulated by a 2-D mesh. Two adjacent 2-D meshes—one for the fluid domain and one for the solid domain—were used to simulate fluid flow and conjugate conduction, respectively. Boundary layer assumptions in the third dimension provided realistic flow resistances and heat transfer coefficients, and void fraction correlations provided an estimate of liquid film thickness and volume fraction in two-phase mode. Due to the unique physics and model couplings, commercially available codes were not used. Instead, a 2-D CFD code was developed in Matlab.

#### 4.3.1 Continuity Equations

The steady-state continuity equation for the mixture is given in [54] as

$$\nabla \cdot (\rho_m \vec{v}_m) = 0 \quad (4.3.1)$$

where

$$\vec{v}_m = \frac{\sum_{k=1}^n \alpha_k \rho_k \vec{v}_k}{\rho_m} \quad (4.3.2)$$

$$\rho_m = \sum_{k=1}^n \alpha_k \rho_k \quad (4.3.3)$$

This partial differential equation can be converted into an algebraic equation using the control volumes shown in Fig. 4.3.1.

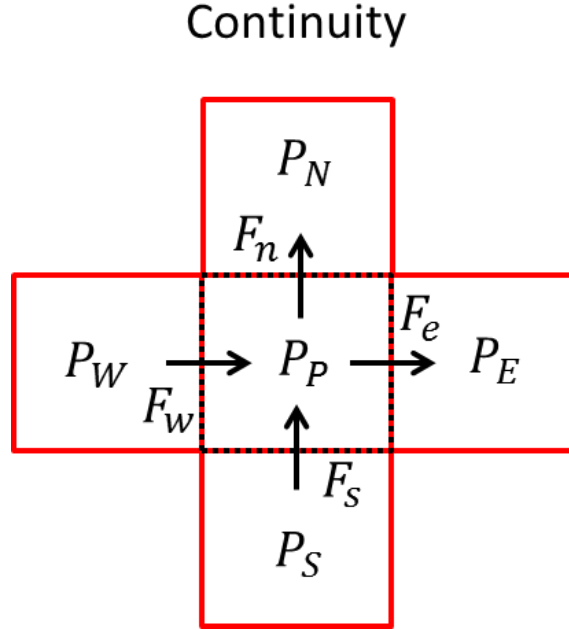


**Fig. 4.3.1: Control volumes for the continuity equation (pressure).**

The continuity equation can therefore be written as

$$F_w + F_s - F_e - F_n = 0 \quad (4.3.4)$$

It is worth noting that the continuity equation for the mixture does not depend on the phase change rate, since, an equal mass of liquid becomes vapor. Therefore, the phase change rate does not appear in the continuity equation for the mixture. In addition, following the SIMPLE algorithm for pressure-velocity coupling, these control volumes can be used to derive an equation for pressure, as detailed in Patankar [57]. Accordingly, those equations will not be given here.

### 4.3.2 Momentum Equations

The steady-state momentum equation for the mixture is given in [54] as



$$\begin{aligned} \nabla \cdot (\rho_m \vec{v}_m \vec{v}_m) = & -\nabla p + \nabla \cdot (\mu_m (\nabla \vec{v}_m + \nabla \vec{v}_m^T)) + \vec{F}_{vol} + \\ & \nabla \cdot \left( \sum_{k=1}^n \alpha_k \rho_k \vec{v}_{p,m} \vec{v}_{p,m} \right) \end{aligned} \quad (4.3.5)$$

where

$$\vec{v}_{p,m} = \vec{v}_p - \vec{v}_m \quad (4.3.6)$$

$$\vec{v}_m = \frac{\sum_{k=1}^n \alpha_k \rho_k \vec{v}_k}{\rho_m} \quad (4.3.7)$$

$$\rho_m = \sum_{k=1}^n \alpha_k \rho_k \quad (4.3.8)$$

$$\mu_m = \sum_{k=1}^n \alpha_k \mu_k \quad (4.3.9)$$

and  $F_{vol}$  is the volumetric force representing the shear stress force on the fluid due to the microchannel wall.

This partial differential equation can be converted into an algebraic equation using the control volumes shown for x- and y-momentum equations in Fig. 4.3.2(a) and (b), respectively

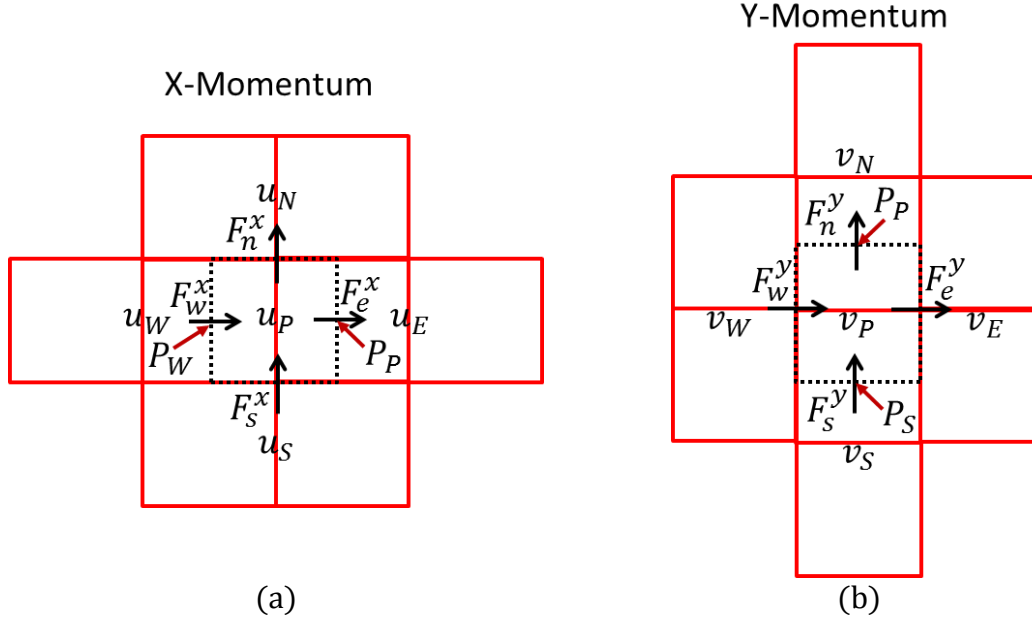


**Fig. 4.3.2: Control volumes for (a) x- and (b) y-momentum equations.**

where a staggered grid was used in accordance with the SIMPLE algorithm. The upwind discretization scheme found in Patankar [57] can therefore be used to obtain coefficients to form an algebraic system of equations. However, due to the use of the mixture model, an additional source term is required, which is similar in form to that found in the annular film evaporation with physics based void fraction model (see Eq. (3.4.15)). Moreover, the momentum coefficients themselves are, in fact, the summation of the liquid and vapor momentum coefficients, as in the annular film evaporation with physics-based void fraction model. Accordingly, after expanding the annular film evaporation with physics-based momentum equations to two-dimensions, the momentum equations take the following form:

#### X-Liquid Momentum

$$a_{PX}^l U_P^l = a_{WX}^l U_W^l + a_{EX}^l U_E^l + a_{SX}^l U_S^l + a_{NX}^l U_N^l + b_X^l + A_X^l (P_w^l - P_e^l) \Delta y \quad (4.3.10)$$

$$a_{PX}^l = a_{WX}^l + a_{EX}^l + a_{SX}^l + a_{NX}^l + S_{PX}^l \quad (4.3.11)$$

$$a_{WX}^l = \beta_w \mu_l \frac{\Delta y}{\Delta x} + [F_w^l, 0] \quad (4.3.12)$$

$$a_{EX}^l = \beta_e \mu_l \frac{\Delta y}{\Delta x} + [-F_e^l, 0] \quad (4.3.13)$$

$$a_{SX}^l = \beta_s \mu_l \frac{\Delta x}{\Delta y} + [F_s^l, 0] \quad (4.3.14)$$

$$a_{NX}^l = \beta_n \mu_l \frac{\Delta x}{\Delta y} + [-F_n^l, 0] \quad (4.3.15)$$

$$b^l = 0 \quad (4.3.16)$$

### X-Vapor Momentum

$$a_{PX}^v U_P^v = a_{WX}^v U_W^v + a_{EX}^v U_E^v + a_{SX}^v U_S^v + a_{NX}^v U_N^v + b_X^v + A_X^v (P_w^v - P_e^v) \Delta y \quad (4.3.17)$$

$$a_{PX}^v = a_{WX}^v + a_{EX}^v + a_{SX}^v + a_{NX}^v + S_{PX}^v + \Delta \dot{m}_X \quad (4.3.18)$$

$$a_{WX}^v = \alpha_w \mu_v \frac{\Delta y}{\Delta x} + [F_w^v, 0] \quad (4.3.19)$$

$$a_{EX}^v = \alpha_e \mu_v \frac{\Delta y}{\Delta x} + [-F_e^v, 0] \quad (4.3.20)$$

$$a_{SX}^v = \alpha_s \mu_v \frac{\Delta x}{\Delta y} + [F_s^v, 0] \quad (4.3.21)$$

$$a_{NX}^v = \alpha_n \mu_v \frac{\Delta x}{\Delta y} + [-F_n^v, 0] \quad (4.3.22)$$

$$b_X^v = \Delta \dot{m}_X U_P^l \quad (4.3.23)$$

### X-Mixture Momentum

$$a_{PX} U_P = a_{WX} U_W + a_{EX} U_E + a_{SX} U_S + a_{NX} U_N + b_X + (P_w - P_e) \Delta y \quad (4.3.24)$$

$$a_{PX} = a_{PX}^l + a_{PX}^v \quad (4.3.25)$$

$$a_{WX} = a_{WX}^l + a_{WX}^v \quad (4.3.26)$$

$$a_{EX} = a_{EX}^l + a_{EX}^v \quad (4.3.27)$$

$$a_{SX} = a_{SX}^l + a_{SX}^v \quad (4.3.28)$$

$$a_{NX} = a_{NX}^l + a_{NX}^v \quad (4.3.29)$$

$$\begin{aligned} b_X = & b_X^l + b_X^v + a_{WX}^l U_W^l + a_{WX}^v U_W^v - a_{WX} U_W + a_{EX}^l U_E^l + a_{EX}^v U_E^v - a_{EX} U_E \\ & + a_{SX}^l U_S^l + a_{SX}^v U_S^v - a_{SX} U_S + a_{NX}^l U_N^l + a_{NX}^v U_N^v - a_{NX} U_N \\ & + a_{PX} U_P - a_{PX}^l U_P^l - a_{PX}^v U_P^v \end{aligned} \quad (4.3.30)$$

### Y-Liquid Momentum

$$a_{PY}^l V_P^l = a_{WY}^l V_W^l + a_{EY}^l V_E^l + a_{SY}^l V_S^l + a_{NY}^l V_N^l + b_Y^l + A_Y^l (P_s^l - P_n^l) \Delta x \quad (4.3.31)$$

$$a_{PY}^l = a_{WY}^l + a_{EY}^l + a_{SY}^l + a_{NY}^l + S_{PY}^l \quad (4.3.32)$$

$$a_{WY}^l = \beta_w \mu_l \frac{\Delta y}{\Delta x} + [F_w^l, 0] \quad (4.3.33)$$

$$a_{EY}^l = \beta_e \mu_l \frac{\Delta y}{\Delta x} + [-F_e^l, 0] \quad (4.3.34)$$

$$a_{SY}^l = \beta_s \mu_l \frac{\Delta x}{\Delta y} + [F_s^l, 0] \quad (4.3.35)$$

$$a_{NY}^l = \beta_n \mu_l \frac{\Delta x}{\Delta y} + [-F_n^l, 0] \quad (4.3.36)$$

$$b^l = 0 \quad (4.3.37)$$

### Y-Vapor Momentum

$$a_{PY}^v V_P^v = a_{WY}^v V_W^v + a_{EY}^v V_E^v + a_{SY}^v V_S^v + a_{NY}^v V_N^v + b_Y^v + A_Y^v (P_s^v - P_n^v) \Delta x \quad (4.3.38)$$

$$a_{PY}^v = a_{WY}^v + a_{EY}^v + a_{SY}^v + a_{NY}^v + S_{PY}^v + \Delta \dot{m}_Y \quad (4.3.39)$$

$$a_{WY}^v = \alpha_w \mu_v \frac{\Delta y}{\Delta x} + [F_w^v, 0] \quad (4.3.40)$$

$$a_{EY}^v = \alpha_e \mu_v \frac{\Delta y}{\Delta x} + [-F_e^v, 0] \quad (4.3.41)$$

$$a_{SY}^v = \alpha_s \mu_v \frac{\Delta x}{\Delta y} + [F_s^v, 0] \quad (4.3.42)$$

$$a_{NY}^v = \alpha_n \mu_v \frac{\Delta x}{\Delta y} + [-F_n^v, 0] \quad (4.3.43)$$

$$b_Y^v = \Delta \dot{m}_Y V_P^l \quad (4.3.44)$$

### Y-Mixture Momentum

$$a_{PY} V_P = a_{WY} V_W + a_{EY} V_E + a_{SY} V_S + a_{NY} U_N + b_Y + (P_s - P_n) \Delta x \quad (4.3.45)$$

$$a_{PY} = a_{PY}^l + a_{PY}^v \quad (4.3.46)$$

$$a_{WY} = a_{WY}^l + a_{WY}^v \quad (4.3.47)$$

$$a_{EY} = a_{EY}^l + a_{EY}^v \quad (4.3.48)$$

$$a_{SY} = a_{SY}^l + a_{SY}^v \quad (4.3.49)$$

$$a_{NY} = a_{NY}^l + a_{NY}^v \quad (4.3.50)$$

$$\begin{aligned} b_Y = & b_Y^l + b_Y^v + a_{WY}^l V_W^l + a_{WY}^v V_W^v - a_{WY} V_W + a_{EY}^l V_E^l + a_{EY}^v V_E^v - a_{EY} V_E \\ & + a_{SY}^l V_S^l + a_{SY}^v V_S^v - a_{SY} V_S + a_{NY}^l V_N^l + a_{NY}^v V_N^v - a_{NY} V_N \\ & + a_{PY} V_P - a_{PY}^l V_P^l - a_{PY}^v V_P^v \end{aligned} \quad (4.3.51)$$

Three friction factors are available to simulate the effect of finite thickness in the z-dimension: homogenous friction factor, annular fully developed friction factor, and

developing flow friction factor. Homogenous friction factor is similar to that found in the flow-tube (“streamline”) model presented in Section 3.6, and assumes laminar, homogenous fully developed flow. The annular friction factor is derived in Appendix A, and assumes laminar, annular, fully developed flow. Finally, the developing friction factor is derived in Section 4.3.6 and assumes laminar, annular, developing flow. The friction factors can be expressed as:

$$S_P^l = \begin{cases} \frac{12\mu_l\beta_P\Delta x\Delta y}{w_{ch}^2} & \text{Homogenous Friction} & (4.3.52a) \\ \frac{24\mu_l}{w_{ch}^2} \frac{\beta_P^2\Delta x\Delta y}{(\beta_P^*)^2(3-\beta_P^*)} & \text{Annular Friction} & (4.3.52b) \\ \frac{24\mu_l}{w_{ch}^2} \frac{\beta_P^2\Delta x\Delta y C_{(fRe)fd}}{(\beta_P^*)^2(3-\beta_P^*)} & \text{Developing Friction} & (4.3.52c) \end{cases}$$

$$S_P^v = \begin{cases} \frac{12\mu_v\alpha_P\Delta x\Delta y}{w_{ch}^2} & \text{Homogenous Friction} & (4.3.53a) \\ \frac{24S_1\mu_v}{w_{ch}^2} \frac{\alpha_P^2\Delta x\Delta y}{3\alpha_P^* + (2S_1 - 3)(\alpha_P^*)^3} & \text{Annular Friction} & (4.3.53b) \\ \frac{24S_1\mu_v}{w_{ch}^2} \frac{\alpha_P^2\Delta x\Delta y C_{(fRe)fd}}{3\alpha_P^* + (2S_1 - 3)(\alpha_P^*)^3} & \text{Developing Friction} & (4.3.53c) \end{cases}$$

It is worth noting that the accent \* in this section is used to indicate fully developed value: that is, the solution of Eqs. (4.3.112) and (4.3.113c), as described in Appendix A.

A comparison between the pressure drops obtained using the homogenous friction factor and the annular friction factor for a given total (liquid and vapor) mass flow rate as a function of vapor quality is given in Fig. 4.3.3.

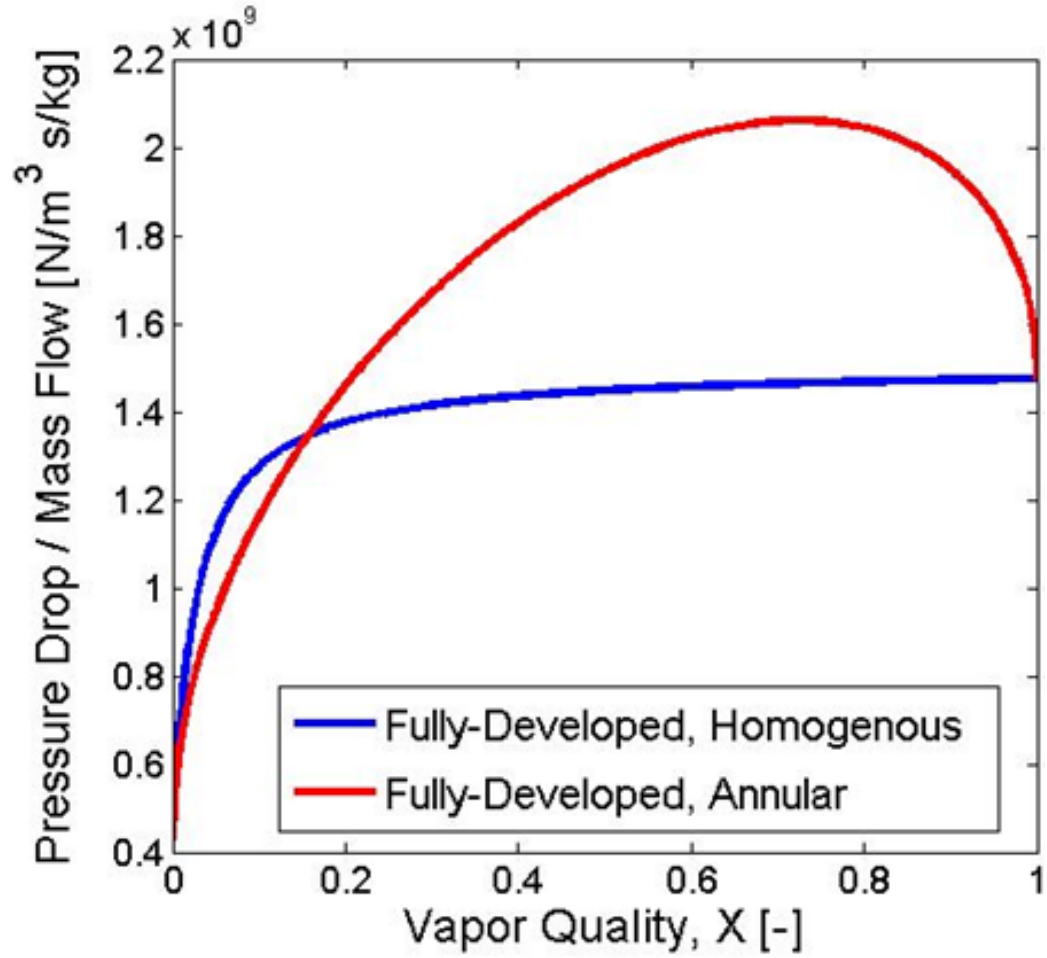


**Fig. 4.3.3: Comparison between pressure drop assuming homogenous and annular friction factor.**

At low vapor qualities, annular friction factor is observed to give a lower pressure drop than homogenous friction factor; however, at high vapor qualities, annular friction factor predicts a higher pressure drop than homogenous.

### 4.3.3 Conservation of Liquid Species

The steady-state conservation of species equation for the mixture is given in [54] as

$$\nabla \cdot (\alpha_p \rho_p \vec{v}_m) = -\nabla \cdot (\alpha_p \rho_p \vec{v}_{p,m}) + S \quad (4.3.54)$$

It is shown in Appendix B that Eq. (4.3.54) is equivalent to

$$\nabla \cdot (Y_p \rho_m \vec{v}_m) = S \quad (4.3.55)$$

This partial differential equation can be converted into an algebraic equation using the control volumes shown in Fig. 4.3.4.

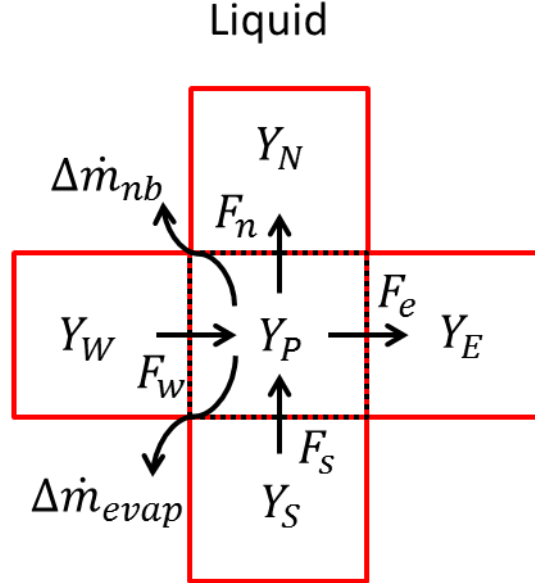


**Fig. 4.3.4: Control volumes used to derive conservation equations for liquid species.**

The upwind discretization scheme found in Patankar [57] can be used to derive the algebraic system of equations. However, it is worth noting that based on the results of the preliminary modeling, two phase-change mechanisms are present: nucleate boiling and film evaporation. Two phase change source terms— $\Delta\dot{m}_{nb}$  and  $\Delta\dot{m}_{evap}$ —are therefore included to represent the phase change rates due to nucleate boiling and evaporation, respectively. Since phase change is from the liquid phase to the vapor phase, these source terms are negative. In addition, since the control volumes are assumed to be of unit width, the source terms must be divided by the microchannel width. The conservation of species equation therefore takes the form:

$$a_P^q Y_P = a_W^q Y_W + a_E^q Y_E + a_S^q Y_S + a_N^q Y_N + b^q \quad (4.3.56)$$

$$a_P^q = a_W^q + a_E^q + a_S^q + a_N^q \quad (4.3.57)$$

$$a_W^q = [F_w, 0] \quad (4.3.58)$$

$$a_E^q = [-F_e, 0] \quad (4.3.59)$$

$$a_S^q = [F_S, 0] \quad (4.3.60)$$

$$a_N^q = [-F_N, 0] \quad (4.3.61)$$

$$b^q = -(\Delta\dot{m}_{nb} + \Delta\dot{m}_{evap}) = -\Delta\dot{m} \quad (4.3.62)$$

Nucleate boiling is assumed to act directly on the wall, carrying away heat via phase change, and thereby couples the wall temperature to the saturation temperature. The nucleate boiling phase-change rate is modeled using the relationship recommended by Forster and Zuber [46]:

$$\Delta\dot{m}_{nb}^0 = 0.00122 \frac{2 \Delta x \Delta y}{w_{ch}} \left( \frac{k_l^{0.79} C_p^{0.45} \rho_l^{0.49}}{\sigma^{0.5} \mu_l^{0.29} h_{lv}^{1.24} \rho_v^{0.24}} \right) (T_P^w - T_P^{sat})^{1.24} (\Delta P_{sat})^{0.75} \quad (4.3.63)$$

where  $\Delta P_{sat} = P_{sat}(T_P^w) - P_{sat}(T^{sat})$ .

Film evaporation takes two forms, depending on the selected physics options. If the flow is considered to be thermally fully developed, then the evaporation rate is assumed to be the result of direct conduction from the wall through the liquid film to the liquid-vapor interface; in this case, film evaporation is similar to nucleate boiling in that it acts directly on the wall and couples the wall temperature to the saturation temperature. If the flow is thermally developing, then the evaporation rate is the result of direct conduction from the liquid bulk to the liquid-vapor interface; in this case, film evaporation acts on the liquid, cooling the liquid to saturation temperature. Both of these cases can be modeled as:



$$\Delta\dot{m}_{evap}^0 = \begin{cases} \frac{k_l}{\delta} \frac{2 \Delta x \Delta y}{w_{ch} h_{fg}} (T_P^w - T_P^{sat}) & \text{Thermally, Fully Developed} \quad (4.3.64a) \\ \frac{k_l}{\delta/2} \frac{2 \Delta x \Delta y}{w_{ch} h_{fg}} (T_P^l - T_P^{sat}) & \text{Therm. Dev. or Dev. Nu} \quad (4.3.64b) \end{cases}$$

The total potential evaporation is therefore the sum of the two components:

$$\Delta\dot{m}^0 = \Delta\dot{m}_{evap}^0 + \Delta\dot{m}_{nb}^0 \quad (4.3.65)$$

Similar to the annular film evaporation with physics-based volume fraction model, the phase change rate needs to be limited to the amount of liquid entering the cell.

The total liquid entering a cell is given, conveniently, by:

$$\Delta\dot{m}_{max} = a_w^q Y_w + a_e^q Y_e + a_S^q Y_S + a_N^q Y_N \quad (4.3.66)$$

Defining the wetted-fraction,  $\lambda$ , as

$$0 \leq \lambda = \min \left[ \frac{\Delta\dot{m}_{max}}{\Delta\dot{m}^0}, 1 \right] \leq 1 \quad (4.3.67)$$

The phase change rates can then be corrected

$$\Delta\dot{m}_{evap} = \lambda \Delta\dot{m}_{evap}^0 \quad (4.3.68)$$

$$\Delta\dot{m}_{nb} = \lambda \Delta\dot{m}_{nb}^0 \quad (4.3.69)$$

$$\Delta\dot{m} = \lambda \Delta\dot{m}^0 \quad (4.3.70)$$

Finally, the effective nucleate boiling heat transfer coefficient can be computed by scaling the corrected phase-change rate. However, the selected value depends on the selected physics options. If the flow is assumed to be thermally fully developed, then, as mentioned above, the film evaporation and nucleate boiling components both act directly on the wall; accordingly, the proper phase-change rate is the total rate (nucleate boiling and film evaporation). For thermally developing flow, only the nucleate boiling acts

directly on the wall, and therefore, only the nucleate boiling phase-change component is considered when computing this term. Mathematically, this can be written as:

$$h_{nb} = \begin{cases} \frac{w_{ch}}{2\Delta x \Delta y} \frac{h_{lv}}{T^w - T^{sat}} \Delta \dot{m} & \text{Thermally, Fully Developed} \quad (4.3.71a) \\ \frac{w_{ch}}{2\Delta x \Delta y} \frac{h_{lv}}{T^w - T^{sat}} \Delta \dot{m}_{nb} & \text{Thermally Dev. or Developing Nu} \quad (4.3.71b) \end{cases}$$

#### 4.3.4 Conservation of Energy in the Liquid Domain

The steady-state conservation of energy equation for the mixture is given in [54] as

$$\nabla \cdot \sum_{k=1}^n \alpha_k \rho_k \vec{v}_k C_k T_k = \nabla \cdot (k_{eff} \nabla T_l) + S \quad (4.3.72)$$

where  $S$  is a volumetric heat source term, and

$$k_{eff} = \sum_{k=1}^n \alpha_k k_k \quad (4.3.73)$$

It is shown in Appendix B that after neglecting the heat capacity of and heat transfer in the vapor phase, Eq. (4.3.72) can be simplified to

$$\nabla \cdot (\rho_m \vec{v}_m Y_p C_{p,l} T_l) = \nabla \cdot (\alpha_l k_l \nabla T_l) + S \quad (4.3.74)$$

This partial differential equation can be converted into an algebraic equation using the control volumes given in Fig. 4.3.5.

## Liquid Energy

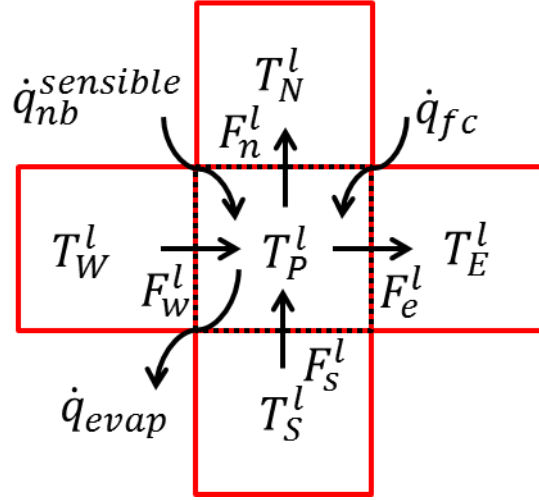


**Fig. 4.3.5: Control volumes used to derive conservation of energy in the liquid domain.**

where the volumetric source term,  $S$ , is made up three components— $\dot{q}_{nb}^{sensible}$ ,  $\dot{q}_{evap}$ , and  $\dot{q}_{fc}$ —as described in more detail below.

Upwind discretization can be used to derive the algebraic system of equations, as described in Patankar [57]. However, it is worth noting three source terms— $\dot{q}_{nb}^{sensible}$ ,  $\dot{q}_{evap}$ , and  $\dot{q}_{fc}$ —which correspond to the sensible heat load due to nucleate boiling (heat is added to the liquid phase, since the liquid is assumed to cool to saturation before vaporizing), the total (sensible and latent) heat loss due to evaporation, and the heat load due to forced convection on the wall. The heat load due to forced convection on the wall is linearized using a forced convection heat transfer coefficient, and an implicit and an explicit source term are added to the algebraic system of equations. The heat load and heat loss due to nucleate boiling and evaporation, on the other hand, are treated as explicit source terms, and two explicit source terms are added to the algebraic system of equations. This is because the liquid evaporation rate is often limited by the wetted fraction (see Eq. (4.3.67)). Accordingly, under this condition, the evaporation rate is no

longer linearly proportional to liquid temperature, but rather held constant. Accordingly, an explicit source term was always used.

In addition, it is worth noting that diffusion is also present due to the thermal conductivity of the liquid. Patankar [57] provides simple formulas for diffusion. However, due to the presence of a two-phase mixture, those formulas must be scaled by the liquid volume fraction (liquid level height), since no diffusion occurs when no liquid is present.

Thus, the liquid temperature equation takes the following form:

$$a_P^l T_P^l = a_W^l T_W^l + a_E^l T_E^l + a_S^l T_S^l + a_N^l T_N^l + b^l \quad (4.3.75)$$

$$a_P^l = a_W^l + a_E^l + a_S^l + a_N^l + a_P^{l0} \quad (4.3.76)$$

$$a_W^l = k^l \frac{\Delta y}{\Delta x} \tilde{\beta}_w + C_p Y_W [F_w, 0] \quad (4.3.77)$$

$$a_E^l = k^l \frac{\Delta y}{\Delta x} \tilde{\beta}_e - C_p Y_E [F_e, 0] \quad (4.3.78)$$

$$a_S^l = k^l \frac{\Delta y}{\Delta x} \tilde{\beta}_s + C_p Y_S [F_s, 0] \quad (4.3.79)$$

$$a_N^l = k^l \frac{\Delta y}{\Delta x} \tilde{\beta}_n - C_p Y_N [F_n, 0] \quad (4.3.80)$$

$$b^l = a_P^{l0} T_P^w + \Delta \dot{m}_{evap} (C_p (T_P^l - T^{sat}) - h_{lv}) + \Delta \dot{m}_{nb} (C_p (T_P^l - T^{sat})) \quad (4.3.81)$$

$$a_P^{l0} = \frac{2\Delta x \Delta y}{w_{ch}} h_{fc} \quad (4.3.82)$$

The forced-convection heat transfer coefficient couples the wall temperature to the liquid temperature and depends on the selected physics options. For the case of thermally fully developed flow, forced-convection is neglected; for the case of thermally developing flow, forced convection heat transfer coefficient is computed using the fully developed Nusselt number,  $Nu = 7.54$ ; for the case when Nusselt number is assumed to be developing, the local value of the Nusselt number is used (see Section 4.3.6 for a

discussion on how the local Nusselt number is computed). It is worth noting that for consistency, the forced convection heat transfer coefficient is scaled by the liquid wetted fraction,  $\lambda$ . Mathematically, the relationship can be written as:

$$h_{fc} = \begin{cases} 0 & \text{Thermally, Fully Developed} & (4.3.83a) \\ \lambda \frac{k_l}{4\delta} 7.54 & \text{Thermally Developing} & (4.3.83b) \\ \lambda \frac{k_l}{4\delta} Nu & \text{Developing } Nu & (4.3.83c) \end{cases}$$

Finally, it is worth noting that both the nucleate boiling and film evaporation phase-change rates appear in the source term for the liquid (see Eq. (4.3.81)). However, whereas the film evaporation rate provides a sensible and latent term, the nucleate boiling phase change rate provides only a sensible term. This is due to the fact that for nucleate boiling, the latent heat is assumed to be provided by the wall, whereas the sensible term is assumed to be provided by the liquid, in order to maintain an overall energy balance in the liquid.

#### 4.3.5 Conservation of Energy in the Solid Domain

The governing equation for conservation of energy in a solid is given by

$$\nabla \cdot (k \nabla T_w) + S = 0 \quad (4.3.84)$$

This partial differential equation can be converted into an algebraic equation using the control volumes shown in Fig. 4.3.6.

## Solid Energy

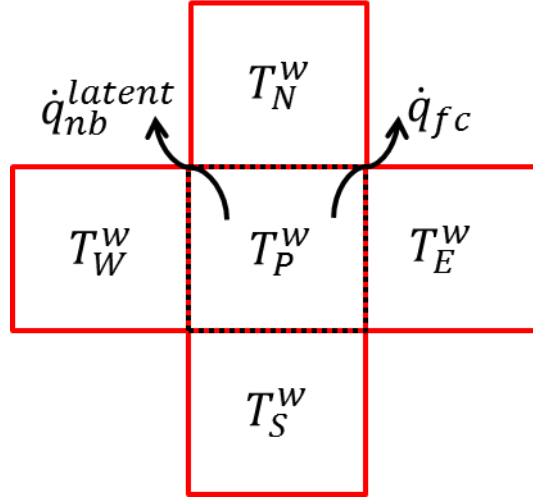


**Fig. 4.3.6: Control volumes used to derive conservation of energy in the solid domain.**

Since no convection is present, only the diffusion formulas found in Patankar [57] were used to discretize the solid domain. In addition, two source terms are present— $\dot{q}_{nb}^{latent}$  and  $\dot{q}_{fc}$ —the heat loss due to latent heat from nucleate boiling, and the heat loss due to forced convection on the wall, respectively. Both of these terms are linearized using a heat transfer coefficient (see Eq. (4.3.71) and (4.3.83)), and an implicit and an explicit source term are added to the algebraic system of equations.

The wall temperature equation therefore takes the form:

$$a_p^w T_P^w = a_W^w T_W^w + a_E^w T_E^w + a_S^w T_S^w + a_N^w T_N^w + b^w \quad (4.3.85)$$

$$a_p^w = a_W^w + a_E^w + a_S^w + a_N^w + a_p^{w0} + a_p^{w1} \quad (4.3.86)$$

$$a_W^w = k^w \frac{\Delta y}{\Delta x} \quad (4.3.87)$$

$$a_E^w = k^w \frac{\Delta y}{\Delta x} \quad (4.3.88)$$

$$a_S^w = k^w \frac{\Delta y}{\Delta x} \quad (4.3.89)$$

$$a_N^w = k^w \frac{\Delta y}{\Delta x} \quad (4.3.90)$$

$$b^w = a_p^{w0} T_p^{sat} + a_p^{w1} T_p^l \quad (4.3.91)$$

$$a_p^{w0} = \frac{2\Delta x \Delta y}{w_f} h_{fc} \quad (4.3.92)$$

$$a_p^{w1} = \frac{2\Delta x \Delta y}{w_f} h_{nb} \quad (4.3.93)$$

It is worth noting that the forced-convection heat transfer coefficient acts to couple the wall temperature to the liquid temperature, whereas the nucleate boiling heat transfer coefficient acts to couple the wall temperature directly to the saturation temperature. Moreover, as with all the previous equations, since the mesh is assumed to be of unit width, the source terms that act upon the frontal area must be normalized by the width of the fin, as shown in Eq. (4.3.92)-(4.3.93).

#### 4.3.6 Streamline Equation

One of the major findings of the force convection model is the important contribution of thermally developing flow to the forced convection heat transfer. While correlations exist which relate the average (apparent) friction factor or Nusselt number as a function of microchannel length, obtaining local values is often more difficult. However, the local value can be computed with knowledge of the average value using the definition of an average value. For instance, the average friction factor [58] and Nusselt number [3] for developing flow between parallel plates are commonly correlated as:

$$\overline{fRe} = \sqrt{\left(\frac{3.44}{\sqrt{x^+}}\right)^2 + (fRe)_{fd}^2} \quad (4.3.94)$$

$$\overline{Nu} = 7.54 + \frac{0.03/x^*}{1 + 0.016/(x^*)^{2/3}} \quad (4.3.95)$$

where:

$$x^+ = \frac{S}{Re_{D_h} D_h} \quad (4.3.96)$$

$$x^* = \frac{S}{Re_{D_h} D_h Pr} \quad (4.3.97)$$

where  $S$  is the distance down the streamline.

Using the definition of average,  $\bar{f}(x) = \frac{1}{x} \int_0^x f(x) dx$ , the local value can be computed from:

$$f(x) = \frac{d}{dx} (x \bar{f}(x)) = \bar{f}(x) + x \bar{f}'(x) \quad (4.3.98)$$

Therefore, the local friction factor and Nusselt number can be computed as:

$$fRe = \frac{1}{2} \frac{3.44^2 + 2 * (fRe)_{fd}^2 x^+}{\sqrt{3.44^2 x^+ + ((fRe)_{fd} x^+)^2}} \quad (4.3.99)$$

$$Nu = 7.54 + \frac{0.02 * 0.016 / (x^*)^{5/3}}{(1 + 0.016 / (x^*)^{2/3})^2} \quad (4.3.100)$$

Since two different correlations will be used to compute friction factor, it is useful to normalize the developing friction factor by its fully developed value so that any correlation can be used. Noting that for parallel plates, fully developed friction factor can be computed as  $(fRe)_{fd} = 24$ , we can define a developing flow friction multiplier as

$$C_{(fRe)_{fd}} = \frac{fRe}{(fRe)_{fd}} = \frac{1}{48} \frac{3.44^2 + 2 * 24^2 x^+}{\sqrt{3.44^2 x^+ + (24^2 x^+)^2}} \quad (4.3.101)$$

However, as of now, it is still unclear how to compute  $x^+$  and  $x^*$  since they depend on the distance the fluid has traveled along the streamline,  $S$ . For a 2-D flow, it is not immediately obvious how to calculate the length along the streamline.



With only a few lines, an equation for the length along the streamline can be derived as a partial differential equation. By definition, any field function,  $S$ , must satisfy the identity,

$$dS = \frac{\partial S}{\partial x} dx + \frac{\partial S}{\partial y} dy \quad (4.3.102)$$

In addition, the formula for the length of a curve is

$$dS = |v| dt = \frac{|v|}{u} dx = \frac{|v|}{v} dy \quad (4.3.103)$$

Substituting these two equations into each other, one arrives at the following partial differential equation:

$$u \frac{\partial S}{\partial x} + v \frac{\partial S}{\partial y} = |v| \quad (4.3.104)$$

The form of this partial differential equation is a convection equation with a source term equal to the velocity magnitude. Following Patankar [57], Eq. (4.3.104) can be discretized using the upwind scheme as:

$$a_P^s S_P = a_W^s S_W + a_E^s S_E + a_S^s S_S + a_N^s S_N + b^s \quad (4.3.105)$$

$$a_P^s = a_W^s + a_E^s + a_S^s + a_N^s \quad (4.3.106)$$

$$a_W^s = [F_w, 0] \quad (4.3.107)$$

$$a_E^s = [-F_e, 0] \quad (4.3.108)$$

$$a_S^s = [F_s, 0] \quad (4.3.109)$$

$$a_N^s = [-F_n, 0] \quad (4.3.110)$$

$$b^s = \sqrt{(a_W^s \Delta x)^2 + (a_E^s \Delta x)^2 + (a_S^s \Delta y)^2 + (a_N^s \Delta y)^2} \quad (4.3.111)$$

### 4.3.7 Void Fraction Correlation

From the annular film evaporation with physics-based void fraction model, it is known that the void fraction is always bounded between the fully developed annular void fraction correlation and the Zivi annular void fraction correlation.

The generic formula for void fraction is given by [51]:

$$\alpha = \frac{1}{1 + \frac{1-X}{X} \frac{S}{S_0}} \quad (4.3.112)$$

where  $X$  is the vapor quality,  $S_0 = \rho_l/\rho_v$  is the density ratio of the liquid and vapor, and the slip,  $S = U_v/U_l$  is given by [51]:

$$S = \begin{cases} 1 & \text{Homogenous VFC} & (4.3.113a) \\ S_0^{1/3} & \text{Zivi Annular VFC} & (4.3.113b) \\ \frac{(3 - 2S_1)(\alpha)^2 - 3}{\beta(3 - \beta)} & \text{Fully - Developed Annular VFC} & (4.3.113c) \end{cases}$$

where  $S_1 = \mu_l/\mu_v$  is the viscosity ratio of the liquid and vapor. It is worth noting that the equation for slip for fully developed annular void fraction correlation is itself a function of the void fraction. Accordingly, iteration is required to solve for the void fraction.

### 4.3.8 Face Densities, Fluxes, and Velocities

The face density is given as the area-weighted average of the liquid and vapor densities on the face [54]:

$$\rho_X = \beta_X \rho_l + \alpha_X \rho_v \quad (4.3.114)$$

$$\rho_Y = \beta_Y \rho_l + \alpha_Y \rho_v \quad (4.3.115)$$

where the liquid and vapor volume fractions,  $\beta$ , and  $\alpha$ , are computed from Eq. (4.3.112) and the desired equation for slip from Eq. (4.3.113). In addition, it is worth noting that

the liquid and vapor volume fractions must be computed on the appropriate faces using a suitable averaging technique; accordingly, the value in the x- and y-directions are different.

The face liquid-phase fluxes can be computed in a similar manner to the way they are calculated in the annular film evaporation with physics-based void fraction model:

$$F_w^l = a_w^q Y_w + (F_w - a_w^q) Y_P \quad (4.3.116)$$

$$F_e^l = (F_e + a_e^q) Y_P - a_e^q Y_E \quad (4.3.117)$$

$$F_s^l = a_s^q Y_s + (F_s - a_s^q) Y_P \quad (4.3.118)$$

$$F_n^l = (F_n + a_n^q) Y_P - a_n^q Y_N \quad (4.3.119)$$

The face vapor-phase fluxes are the difference between the total face flux and the liquid-phase face flux:

$$F_w^v = F_w - F_w^l \quad (4.3.120)$$

$$F_e^v = F_e - F_e^l \quad (4.3.121)$$

$$F_s^v = F_s - F_s^l \quad (4.3.122)$$

$$F_n^v = F_n - F_n^l \quad (4.3.123)$$

Finally, the face phase velocities can be computed as follows:

$$U = \frac{F_X}{\rho \Delta y} \quad (4.3.124)$$

$$U^l = \frac{F_X^l}{\rho_l \beta_X \Delta y} \quad (4.3.125)$$

$$U^v = \frac{F_X^v}{\rho_v \beta_X \Delta y} \quad (4.3.126)$$

$$V = \frac{F_Y}{\rho \Delta x} \quad (4.3.127)$$

$$V^l = \frac{F_Y^l}{\rho_l \beta_Y \Delta x} \quad (4.3.128)$$

$$V^v = \frac{F_Y^v}{\rho_v \beta_Y \Delta x} \quad (4.3.129)$$

#### 4.3.9 Liquid Film Thickness

Finally, the liquid film thickness can be computed from the geometry as

$$\delta = (1 - \tilde{\alpha}) w_{ch} / 2 = \tilde{\beta} w_{ch} / 2 \quad (4.3.130)$$

It is important to note that the liquid and vapor volume fractions,  $\tilde{\beta}$  and  $\tilde{\alpha}$ , respectively, are accented with a  $\sim$  to indicate that the volume fractions computed in this section for the purpose of calculating the film thickness are separate from the void fractions computed in the above equations for the purpose of computing momentum and mixture density. While these void fractions ideally should be identical, in practice, it might be desirable to decouple the problem in order to troubleshoot, understand the role of physics, or to increase numerical stability.

#### 4.3.10 Boundary Conditions and Meshing

The boundary conditions are shown in Fig. 4.3.7.

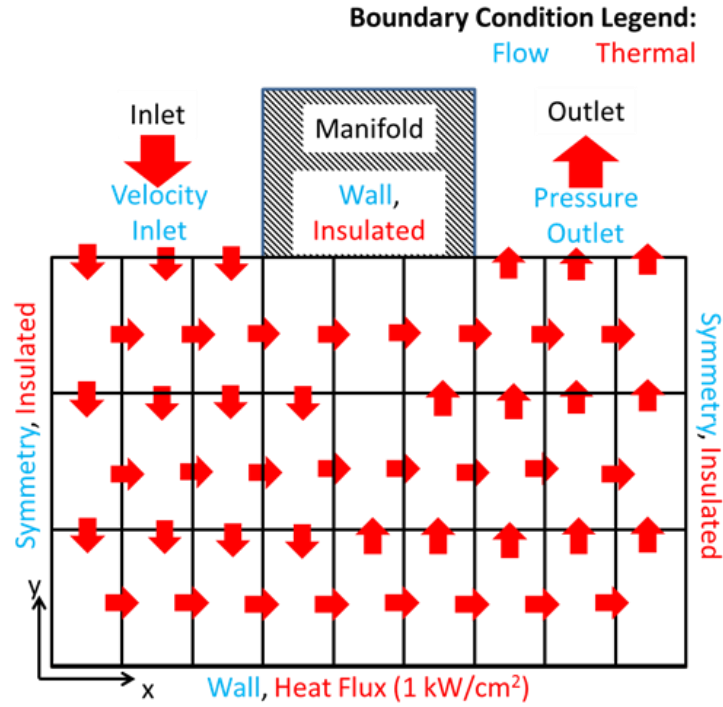


**Fig. 4.3.7: Boundary conditions for 2.5-D microchannel model.**

However, rather than adjust the equations themselves for cells on the boundaries, fictitious cells were used to impose the boundary conditions, as shown in Fig. 4.3.8.

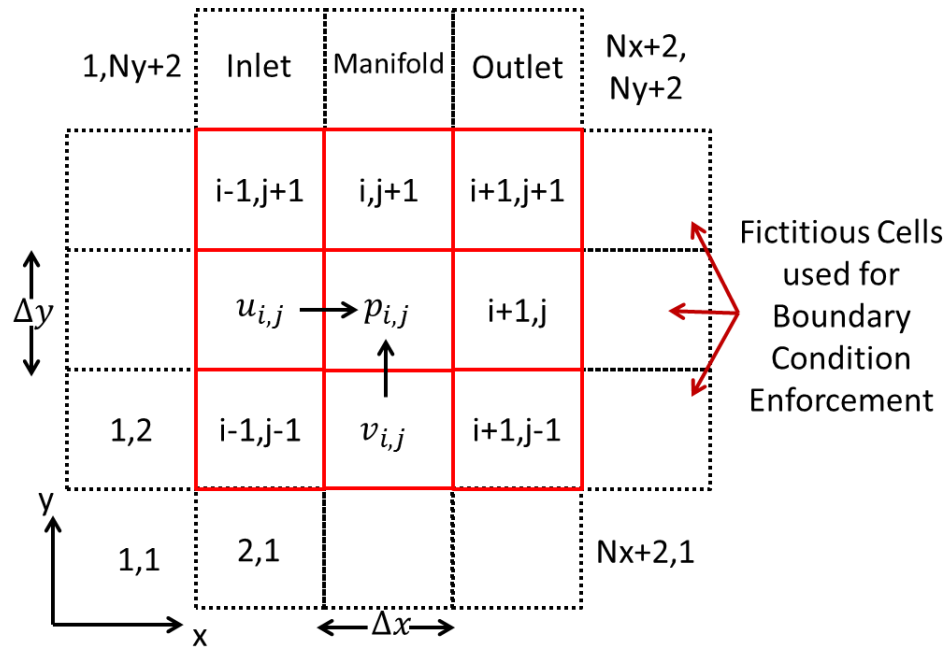


**Fig. 4.3.8: Boundary condition enforcement using fictitious cells.**

For instance, to impose a general boundary value,  $X_b$ , on the interface between cells  $a$  and  $c$ , one requires that, for a uniform mesh,

$$X_b = \frac{X_a + X_c}{2} \quad (4.3.131)$$

Solving for the value of  $X_a$ —the fictitious cell—results in:

$$X_a = 2X_b - X_c \quad (4.3.132)$$

Thus, Eq. (4.3.132) can be used in general to impose a certain boundary value.

Similarly, to impose a flux,  $F_b$ , between cells  $a$  and  $c$ , one requires that

$$F_b = -c_1 \frac{\partial X}{\partial x} \cong -c_1 \frac{X_c - X_a}{\Delta x} \quad (4.3.133)$$

where  $c_1$  is the diffusion coefficient, and  $\Delta x$  is the grid spacing.

Rearranging and solving for  $X_a$  yields

$$X_a = X_c + \frac{F_b \Delta x}{c_1} \quad (4.3.134)$$

At the velocity inlet, a normal velocity, quality, liquid temperature, and density were specified as well as zero shear stress for the normal velocity component. At the outlet, pressure was set equal to zero as well as zero shear stress for the velocity component normal to the outlet. On the manifold section, a wall boundary condition was applied. On the side walls, a symmetry boundary condition was applied. At the base, a wall was applied for flow, and a heat flux was applied for energy. All remaining boundaries were considered thermally insulated.

The mesh is both Cartesian and uniform in each direction. The grid spacing  $\Delta x$  and  $\Delta y$  were selected to be as square as possible, for a given geometry and mesh size. To obtain interfacial values, linear interpolation was used, as described in Patankar [57].

#### 4.3.11 Solution Algorithm

The SIMPLE algorithm was used to solve the coupled pressure, velocity, and other conservative equations. Details of this algorithm are given in Patankar [57], and are not duplicated here. However, a figure summarizing the SIMPLE algorithm is given in Fig. 4.3.9, below, and the procedure will be briefly described.

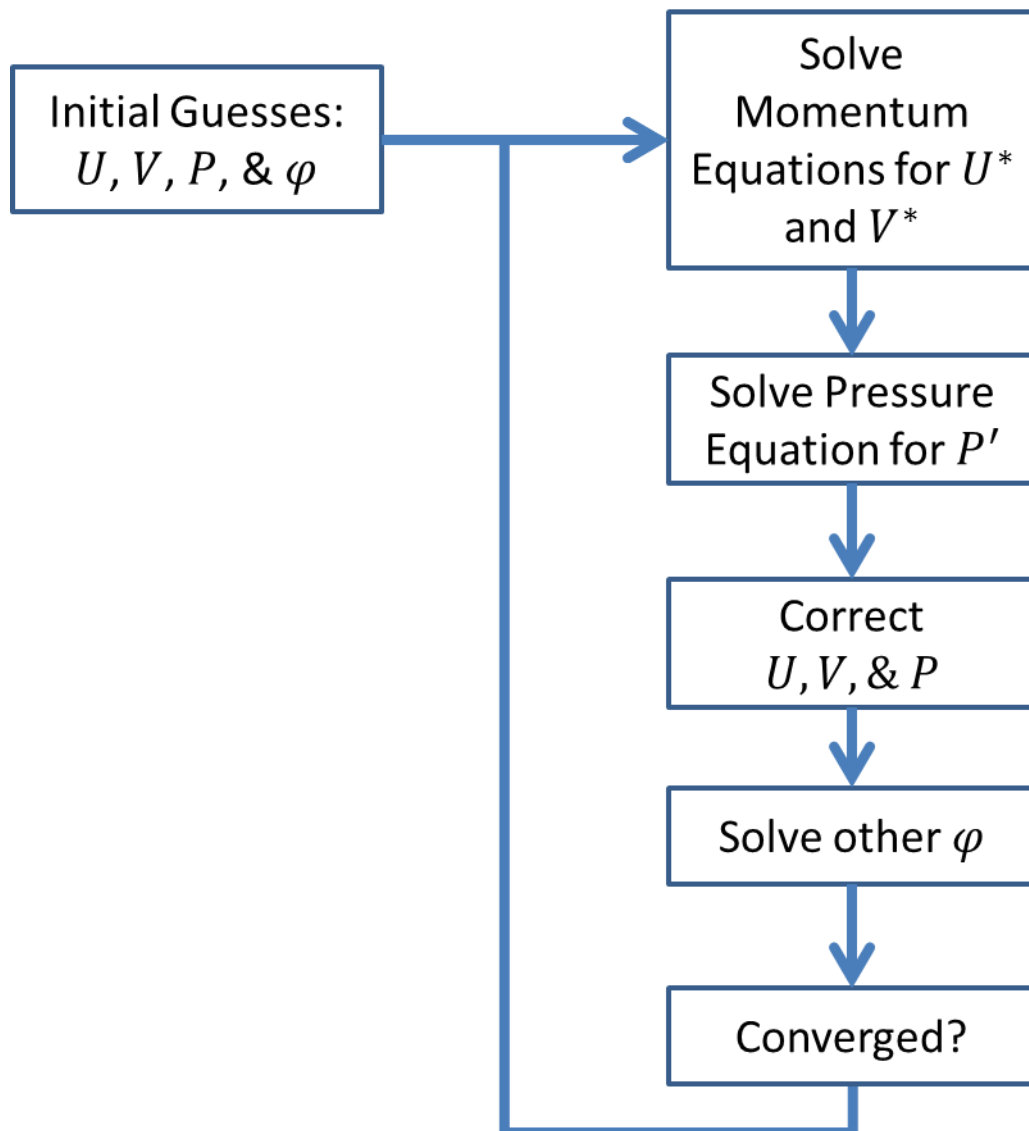


**Fig. 4.3.9: The SIMPLE Algorithm.**

Thus, the model consists of seven sets of independent variables:  $U, V, P, Y, T_l, T_w$  and  $S$ , with the  $\varphi$  being  $Y, T_l, T_w$  and  $S$ . Starting with initial

guesses for all variables, the momentum coefficients can be calculated from Eqs. (4.3.10)-(4.3.53), and the momentum equations solved. Then, the pressure coefficients are calculated using the procedure described by Patankar [57] and the pressure correction equation solved. The velocities and pressures are then corrected using the formulas in Patankar, and a mass conserving velocity field is obtained. The procedure continues by computing the liquid quality coefficients from Eqs. (4.3.56)-(4.3.70), and the liquid quality equation solved. The nucleate boiling heat transfer coefficient defined by Eq. (4.3.71) can then be updated using the appropriate physics options. The liquid temperature coefficients are then calculated from Eqs. (4.3.75)-(4.3.83), and the liquid temperature equation solved. Similarly, the wall temperature coefficients are computed from Eqs. (4.3.85)-(4.3.93), and the wall temperature solved. Finally, the streamline coefficients can be computed from Eqs. (4.3.105)-(4.3.111), and the streamline equation solved. The Nusselt number can then be updated from Eq. (4.3.100), and the friction factor multiplier can then be updated from Eq. (4.3.101). Finally, the void fraction, face densities, fluxes, velocities, and film thicknesses are updated using Eqs. (4.3.112)-(4.3.130), and the momentum coefficients can be calculated again using Eqs. (4.3.10)-(4.3.53).

The iterative procedure then repeats itself until convergence. A reduction of the normalized residuals by a factor of  $1e-4$  was typically used for convergence. Implicit damping was used for the momentum equations, while explicit damping was used for the remaining equations. Damping coefficients of 0.7 for velocity, 0.5 for quality, and 0.7 for liquid temperature were found to be sufficient. No damping was found to be necessary



for conservation of wall energy and pressure correction. All equations were solved using sparse linear solvers in Matlab.

#### 4.3.12 Data Analysis Equations

To obtain the pressure drop,  $\Delta P$ , and outlet temperature,  $T_{out}^l$ , mass flow rate weighted averaging was used. To obtain fin base superheat,  $\Delta T_{fin}$ , area-weighted averaging on the fin base was used. The total mass flow rate can be calculated as

$$\dot{m} = \rho_{in} V_{in} w_{ch} L_{in} / 2 \quad (4.3.135)$$

To obtain the mass flux,  $G$ , the total mass flow rate is divided by the area:

$$G = \frac{\dot{m}}{w_{ch} h_f} \quad (4.3.136)$$

The total heat can be calculated as

$$Q = q''_{base} (w_{ch} + w_f) L_{ch} = q''_{fin} w_f L_{ch} \quad (4.3.137)$$

where  $q''_{base}$  is the heat flux with respect to the total base area and  $q''_{fin}$  is the heat flux with respect to the fin area. It is worth noting that  $q''_{fin}$  is used to impose the heat flux boundary condition when solving conservation of energy, since the conservation of energy equations are essentially divided by  $w_f$ .

The outlet vapor quality can be calculated as

$$\bar{X}_{out} = \frac{Q}{\dot{m} (h_{lv} - C_p (T_{out}^l - T_{in}^l))} \quad (4.3.138)$$

To obtain the fin heat transfer coefficient, the base heat flux,  $q''_{base}$  is divided by the fin base superheat,  $\Delta T_{fin}$ :

$$h_{fin} = \frac{q''_{base}}{\Delta T_{fin}} \quad (4.3.139)$$

Finally, the average wall heat transfer coefficient,  $\bar{h}_{wall}$ , can then be calculated from

$$\bar{h}_{wall} = h_{fin} \left( \frac{w_{ch} + w_f}{2 \, \eta \, h_f + w_{ch}} \right) \quad (4.3.140)$$

where

$$\eta = \frac{\tanh(m \, h_f)}{m \, h_f} \quad (4.3.141)$$

$$m = \sqrt{\frac{2 \, \bar{h}_{wall}}{w_f \, k_s}} \quad (4.3.142)$$

Thus, since  $\bar{h}_{wall}$  depends on  $\eta$ , which itself depends on  $\bar{h}_{wall}$ , Eqs. (4.3.140)-(4.3.142) must be solved simultaneously.

Finally, the effective heat transfer coefficient on the base,  $h_{base}$ , can be computed by adding in the thermal resistance of the substrate base:

$$h_{base} = \left( \frac{1}{h_{fin}} + \frac{h_b}{k^s} \right)^{-1} \quad (4.3.143)$$

## **4.4 Model Validation**

The 2.5-D microchannel model was then validated through a series of tests. First, fully developed and developing single-phase tests were conducted wherein the 2.5-D model was compared to a full 3-D CFD simulation, comparing hydrodynamic and thermal performance. Then, the effects of two-phase physics options were investigated, and the model was compared to two-phase experimental data.

### **4.4.1 Single-Phase Validation**

To validate the model, the model was first run in single-phase mode for a wide range of flow rates, manifolds, and surface geometries and fluids relating to those encountered during the course of the experiments performed in the present study and the geometries tested by Cetegen [10]. The pressure drop and overall heat transfer coefficient was then compared to that obtained from a commercial 3-D CFD software.

The test cases can be divided into two categories: fully developed and developing. The flow rates, manifolds, surfaces and fluids encountered in the present work tend to be fully developed, while those from Cetegen tend to be developing. The geometries of the test cases are given in Table 4.4.1. The fully developed comparison is given in Fig. 4.4.1, while the developing flow comparison is given in Fig. 4.4.2.

For fully developed flow, the 2.5-D model is exceedingly accurate, as the solid lines (2.5-D CFD) almost always intersect the data points (3-D CFD), as shown in Fig. 4.4.1. In fact, when 2.5-D CFD prediction is plotted against the 3-D prediction, most of the data points fall within 5% of the 2.5-D CFD prediction, as shown in Fig. 4.4.4(a).

**Table 4.4.1: Summary of manifold and microchannel geometries**

<b>Manifolds</b>				
<b>Name</b>	<b><math>L_{in}</math> [<math>\mu\text{m}</math>]</b>	<b><math>L_{man}</math> [<math>\mu\text{m}</math>]</b>	<b><math>L_{out}</math> [<math>\mu\text{m}</math>]</b>	<b><math>L_{ch} = L_{in}/2 + L_{man} + L_{out}/2</math> [<math>\mu\text{m}</math>]</b>
Ti64SS	100	400	100	500
Ti64S	150	350	150	500
Ti64	200	300	200	500
Half	250	250	250	500
Quarter	100	100	200	250
Cetegen	200	450	500	800
<b>Surfaces</b>				
<b>Name</b>	<b><math>w_{ch}</math> [<math>\mu\text{m}</math>]</b>	<b><math>w_f</math> [<math>\mu\text{m}</math>]</b>	<b><math>h_f</math> [<math>\mu\text{m}</math>]</b>	<b><math>h_b</math> [<math>\mu\text{m}</math>]</b>
#E	10	10	100	400
#Eb	10	5	100	400
#C	22	40	415	200
#17	42	85	483	200
#12	60	118	406	200

The surfaces tested by Cetegen reveal a more complicated trend, as shown in Fig.

4.4.2. For these surfaces, at low flow rates (e.g. surface #17;  $G=200 \text{ kg/m}^2\text{-s}$ ), the flow is fully developed, and the fully developed models for friction and Nusselt number (solid lines) are accurate. However, as mass flux is increased (e.g. surface #17;  $G=400\text{-}600 \text{ kg/m}^2\text{-s}$ ), the flow transitions from fully developed to developing, and the developing correlations for friction and Nusselt (dashed lines) are needed to match 3-D CFD predictions. As the mass flux is increased even higher (e.g. surface #17;  $G>600 \text{ kg/m}^2\text{-s}$ ), inertia acts to cause secondary flows to develop underneath the inlet and below the outlet, as shown in Fig. 4.4.3, resulting in non-negligible z-velocity component: i.e., a 3-D flow. The pressure drop and heat transfer coefficient are therefore observed to increase, and the 2.5-D model with developing flow (dashed lines) no longer provides accurate predictions since this simplified model does not simulate 3-D flow. The accuracy of the developing flow cases is shown in Fig. 4.4.4(b). For cases where the flow remains 2-D, the 2.5-D

model with developing flow correlations provides accurate predictions to within 5%. However, as expected, when the flow is 3-D, the accuracy of the 2.5-D model is reduced to 20%. Further work is required to characterize under what conditions the flow can be assumed to remain 2-D, such that the 2.5-D model can accurately predict thermal and hydrodynamic performance without the need to double-check with 3-D CFD.

Nevertheless, it is worth noting that the error associated with this simplified model is largely one directional: for both heat transfer coefficient and pressure drop, this model will tend to under-predict. Thus, this model, in its present form, can still be used to provide conservative estimates of heat transfer coefficient, and reasonable estimates of pressure drop, with the understanding that both pressure drops and heat transfer coefficients might be higher than predicted. Moreover, the model can also be used as a computationally inexpensive means of obtaining a starting point for optimization using a full 3-D CFD model.

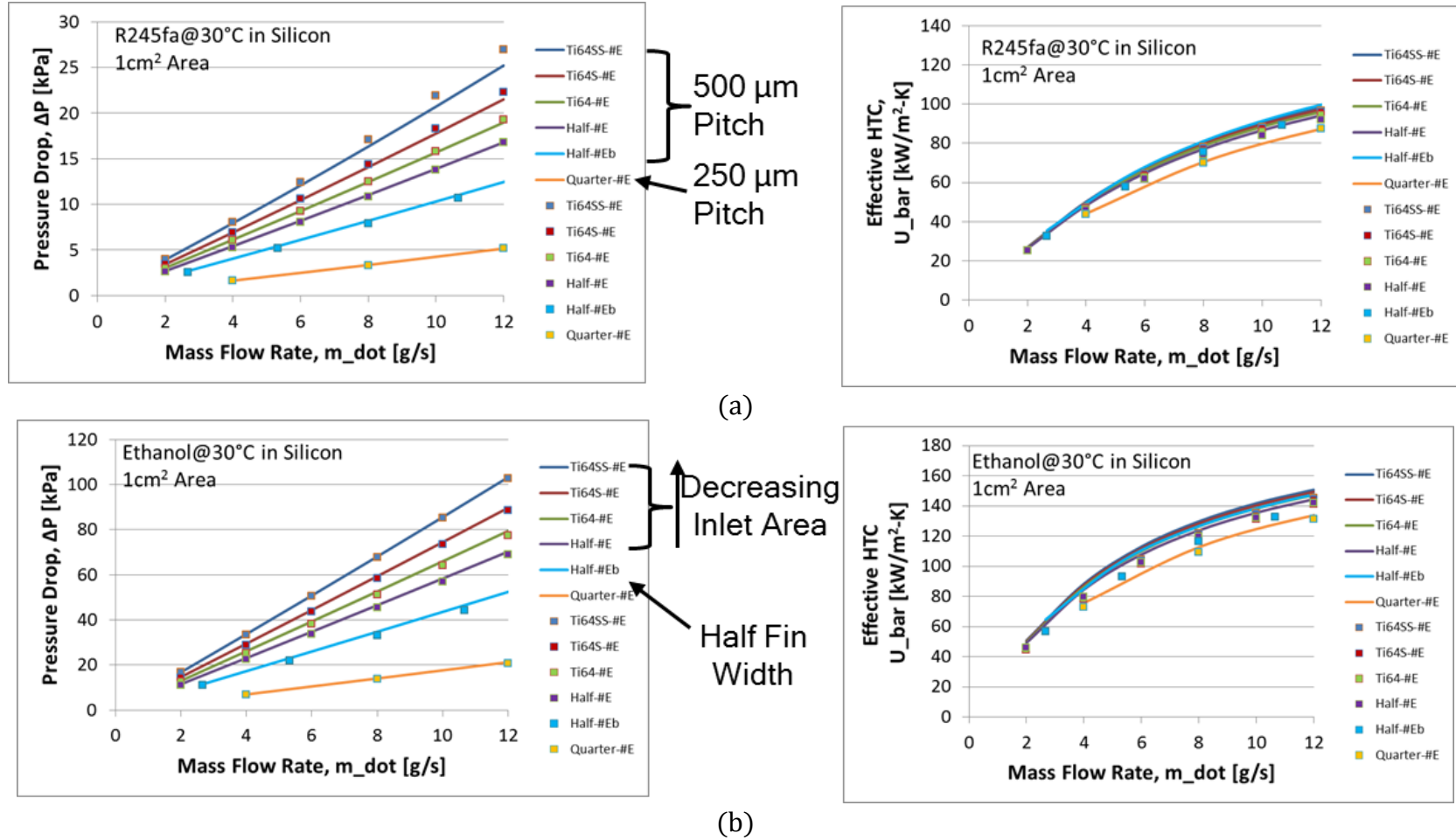
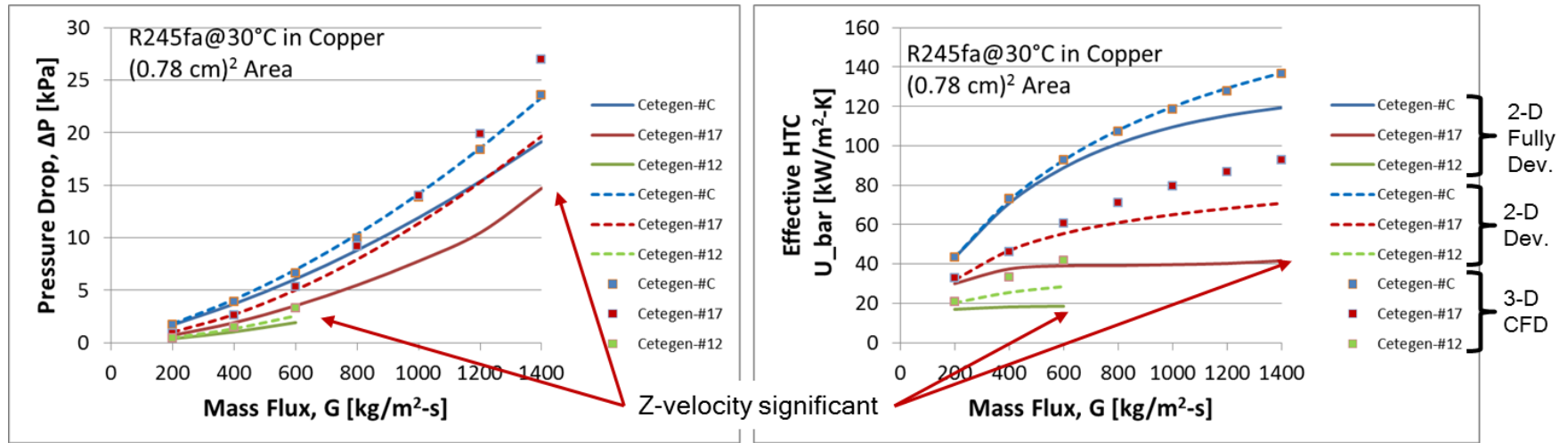
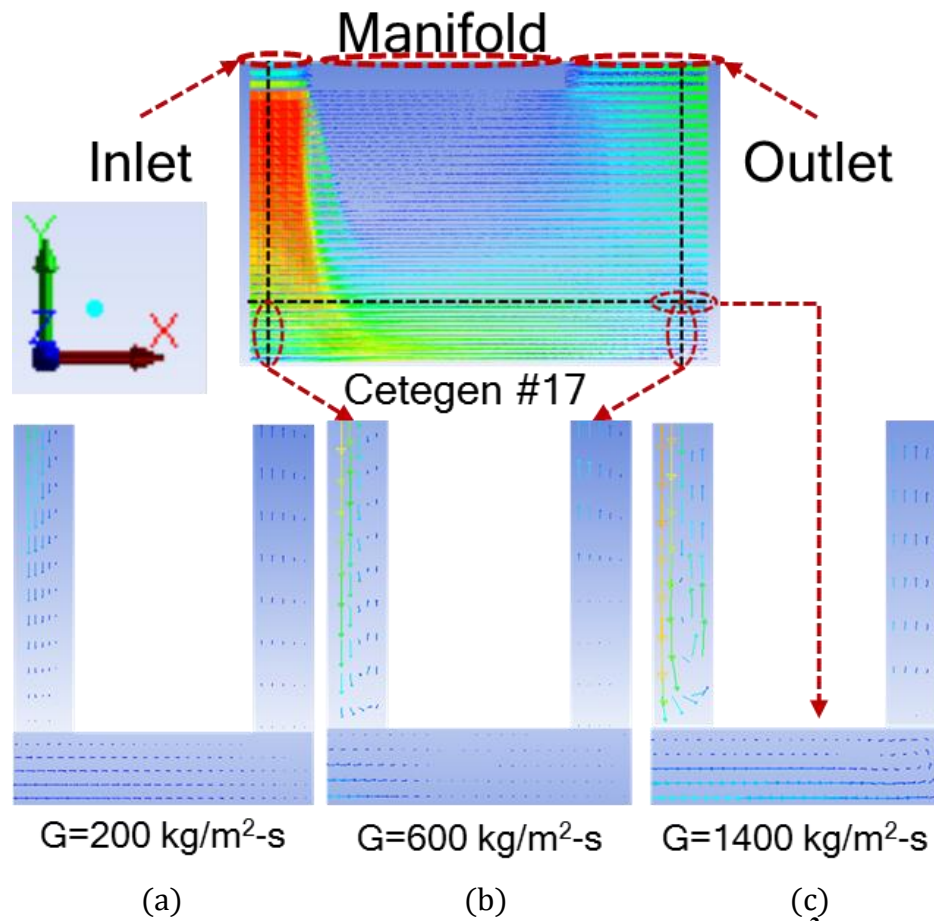


Fig. 4.4.1: Single phase fully developed comparison between 2.5-D to 3-D Model with (a) R245fa and (b) ethanol. Data points represent the 3-D CFD while lines represent the 2.5-D model.

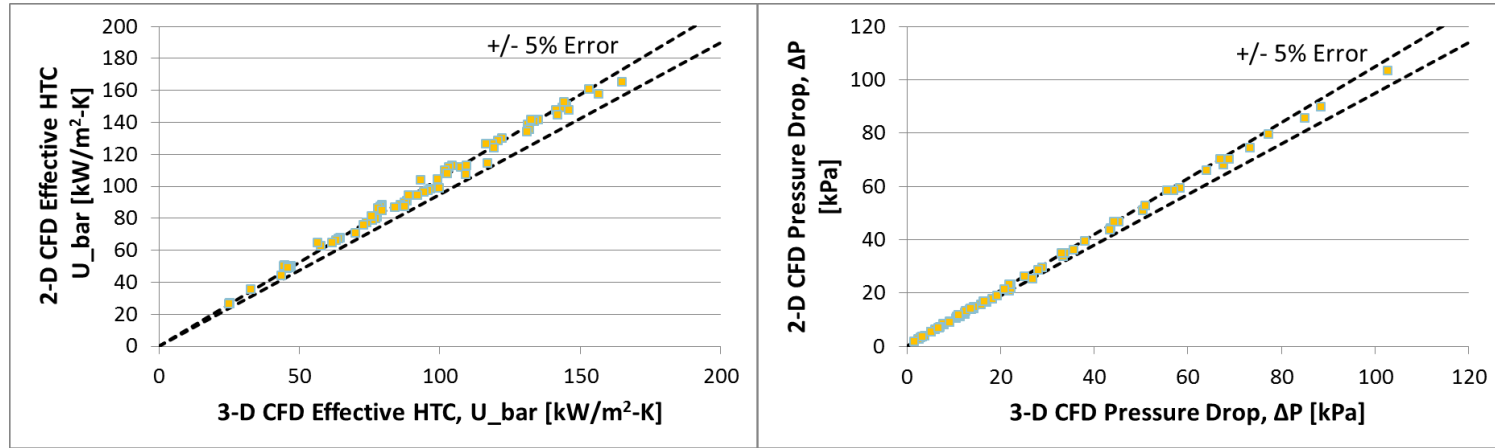


**Fig. 4.4.2: Single-phase developing flow comparison between 2.5-D to 3-D models with R245fa. Data points represent 3-D CFD, solid lines represent fully developed assumption using 2.5-D CFD, and dashed-lines represent developing flow assumption in the 2.5-D CFD model.**

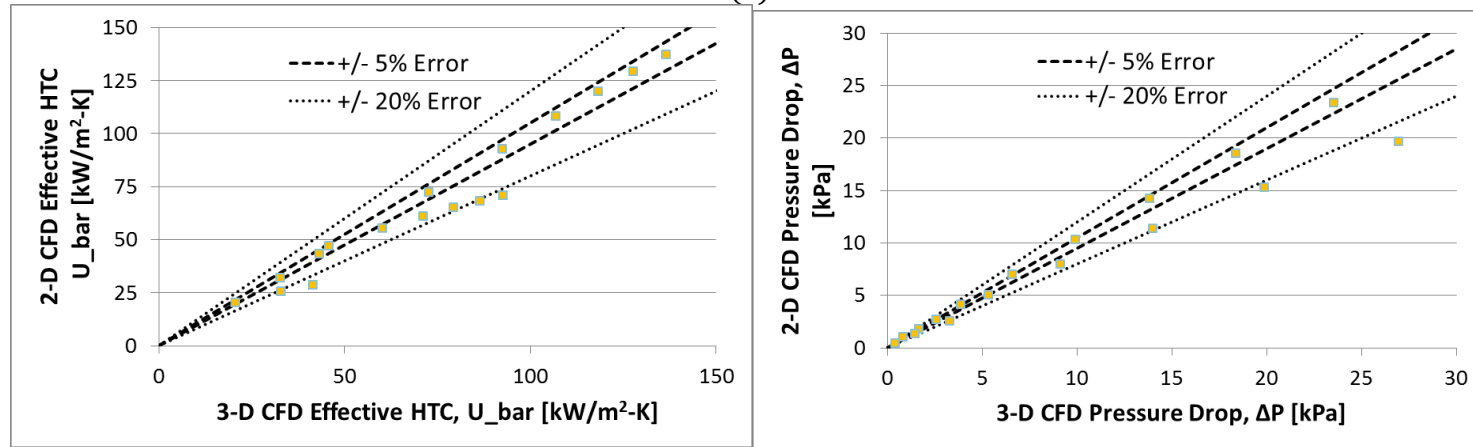


**Fig. 4.4.3: Cross sectional cuts of velocity vectors for Surface #17: (a)  $G=200 \text{ kg/m}^2\text{-s}$ , (b)  $G=600 \text{ kg/m}^2\text{-s}$ , (c)  $G=1400 \text{ kg/m}^2\text{-s}$ . As mass flux is increased, flow becomes increasingly three-dimensional.**





(a)



(b)

**Fig. 4.4.4: Accuracy of 2.5-D model in single-phase mode: (a) fully developed, and (b) developing.**

#### 4.4.2 Effect of Physics

Next, the effect of varying the physical models used to predict two-phase flow was assessed. Surface #17 was selected as a candidate for varying the physics since both trends were observed in the experimental data from Cetegen [10]. The dimensions of surface #17 are given in Table 4.4.1. The physical models were changed sequentially, and all changes were cumulative. The results are shown in Fig. 4.4.6. A summary of the physics options is given in Table 4.4.2.

Initially, the momentum and friction is set to homogenous, and the void fraction set to Zivi. Homogenous void fraction was not used since the flow is expected to be annular, and the homogenous void fraction would predict extremely thin film thicknesses, which would predict order-of-magnitude larger heat transfer coefficients. The liquid was also assumed to be thermally fully developed. A plot of the wall heat transfer coefficient vs. outlet vapor quality is given in Fig. 4.4.5(e). The plot shows that even as the mass flux is increased from  $200 \text{ kg/m}^2\text{-s}$  to  $1400 \text{ kg/m}^2\text{-s}$ , the heat transfer coefficient is largely unaffected. In stark contrast, the location of the thin film is observed to change significantly with mass flux: as mass flux increases, inertia carries the flow toward the bottom of the channel, as shown in Fig. 4.4.5(a)-(d). However, heat transfer coefficient remains unaffected since the conductance of the copper fin is much larger than the wall heat transfer coefficient. Accordingly, the exact location of the thin film is relatively unimportant, compared to the thickness of the film.

First, physics options which affect the wall heat transfer coefficient were changed one-by-one. The model was then run with forced-convection turned on, and the wall heat transfer coefficients were observed to decrease, for the two mass fluxes given in Fig.

4.4.6. The addition of forced-convection heat transfer acts to superheat the liquid before evaporating it. This, in turn, results in lower local vapor qualities and subsequently thicker films, reducing wall heat transfer coefficient. Nucleate boiling was then turned on, and the heat transfer coefficient was observed to increase significantly. For surface #17, heat transfer coefficient from nucleate boiling tends to be larger than the heat transfer coefficient from film evaporation, due to the relatively wide channels of surface #17. Lastly, developing Nusselt was turned on, and the wall heat transfer coefficient was observed to increase further. However, the relative increase was larger for the larger mass flux of  $800 \text{ kg/m}^2\text{-s}$  than for the lower mass flux of  $200 \text{ kg/m}^2\text{-s}$ , since the lower flow rate was nearly fully developed.

Next, the physics options which affect pressure drop were changed. The friction factor was changed from homogenous to annular, and the pressure drop for both mass fluxes was observed to increase. However, the increase was not nearly as large as one would expect from the pressure drop vs. quality plot shown in Fig. 4.3.3. This is because only a small area of the channel was operating at high vapor qualities below 100%, where annular pressure drop is larger than homogenous (see Fig. 4.3.3). As shown in Fig. 4.4.5(a)-(d), a large area of the channel was actually dry, despite the outlet vapor quality being only 10%. Accordingly, only a small portion of the total pressure drop is generated by flow in the moderate quality range, and accordingly, the pressure drop does not increase as drastically as one might expect. Finally, the friction factor was changed to developing, and the pressure drop was observed to increase. However, the increase was significantly larger for the higher mass flux case ( $G=800 \text{ kg/m}^2\text{-s}$ ) since the higher mass flux was more in the developing regime.

Accordingly, the most accurate physics options are assumed to be homogenous momentum, developing friction, Zivi void fraction correlation, and developing Nusselt number.

**Table 4.4.2 Summary of various independent and mutually exclusive physics options, as well as corresponding equations**

<b>Momentum</b>	<b>Friction</b>	<b>Void Fraction/Slip</b>	<b>Liquid Temperature</b>
Homogenous void fraction correlation Eq. (4.3.113a)	Homogenous, fully developed Eqs. (4.3.52a) & (4.3.53a)	Homogenous void fraction correlation Eq. (4.3.113a)	Thermally fully developed: Eqs. (4.3.64a) & (4.3.71a) & (4.3.83a)
Zivi void fraction correlation Eq. (4.3.113b)	Annular, fully developed Eqs. (4.3.52b) & (4.3.53b)	Zivi void fraction correlation Eq. (4.3.113b)	Thermally developing: Eqs. (4.3.64b) & (4.3.71b) & (4.3.83b)
Fully developed annular Eq. (4.3.113c)	Developing Eqs. (4.3.52c) & (4.3.53c)	Fully developed annular Eq. (4.3.113c)	Developing Nu Eqs. (4.3.64b) & (4.3.71b) & (4.3.83c)

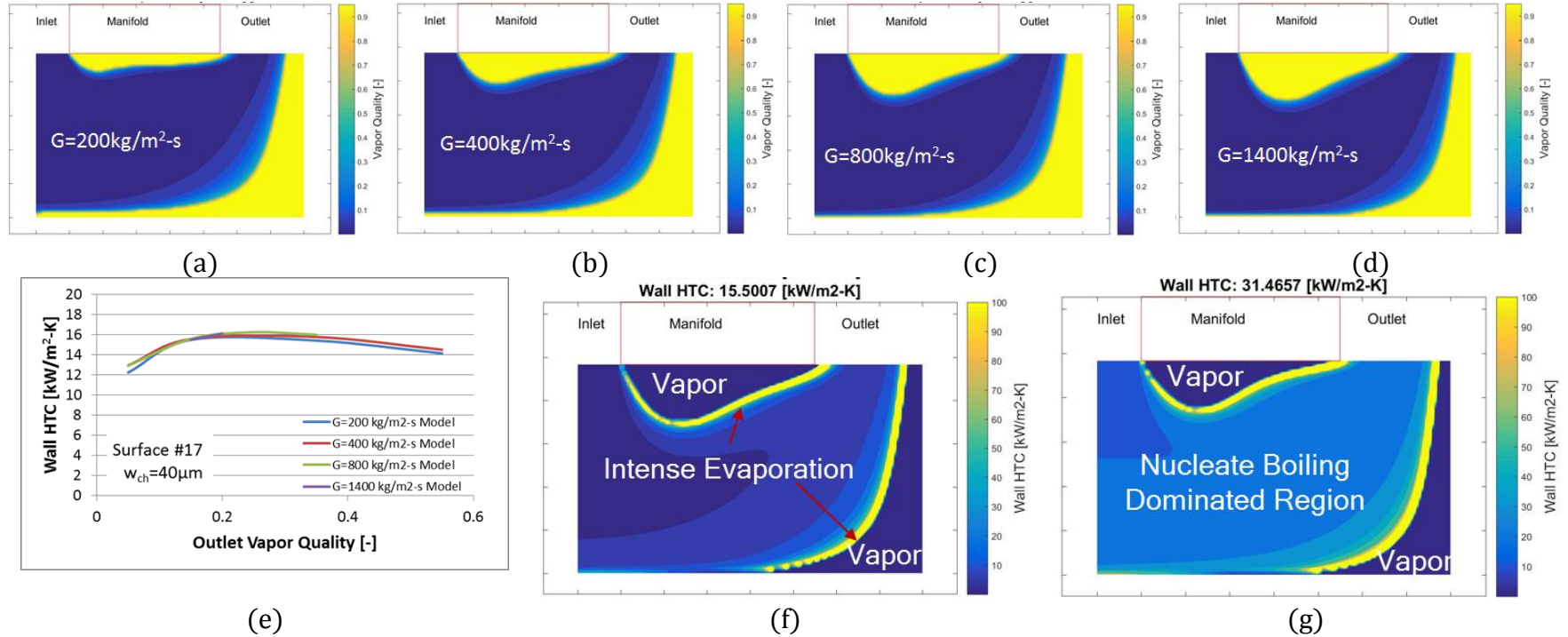


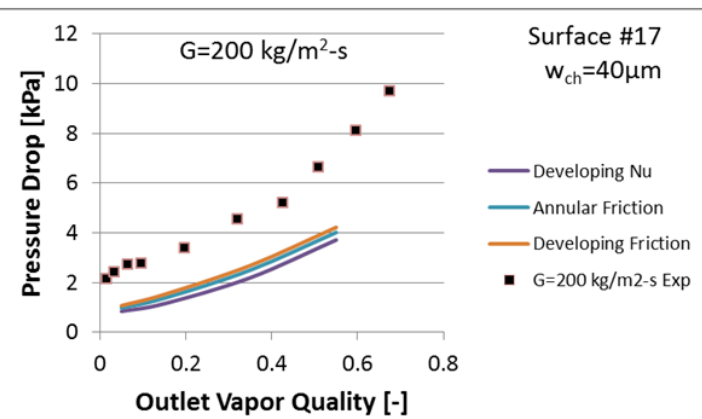
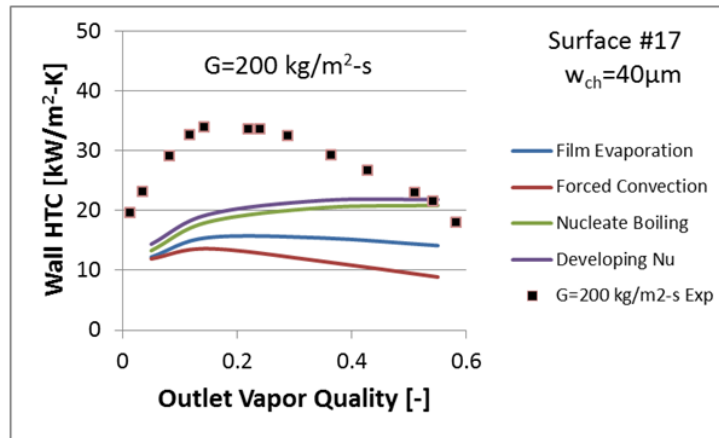
**Fig. 4.4.5: Effects of physics: (a)-(d) Liquid quality contours for various mass fluxes in surface #17 at 10% thermodynamic outlet vapor quality; (e) corresponding wall HTC vs. vapor quality graph; (f) wall HTC contours for thermally fully developed film evaporation with nucleate boiling turned off; (g) wall HTC contours for thermally fully developed film evaporation with nucleate boiling turned on.**

G

## Wall HTC vs. Quality

## Pressure Drop vs. Quality

200  
kg/m<sup>2</sup>-s



800  
kg/m<sup>2</sup>-s

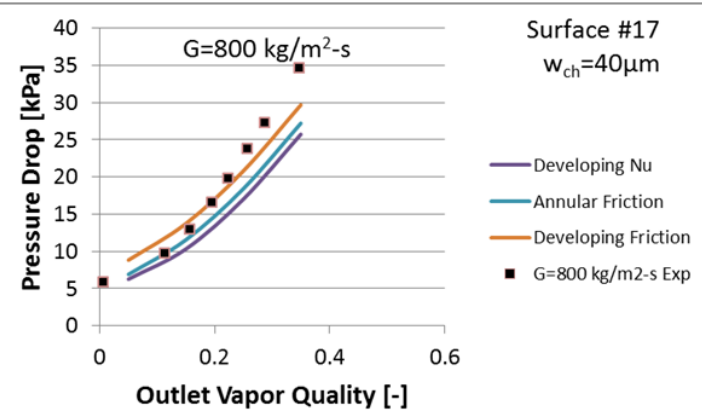
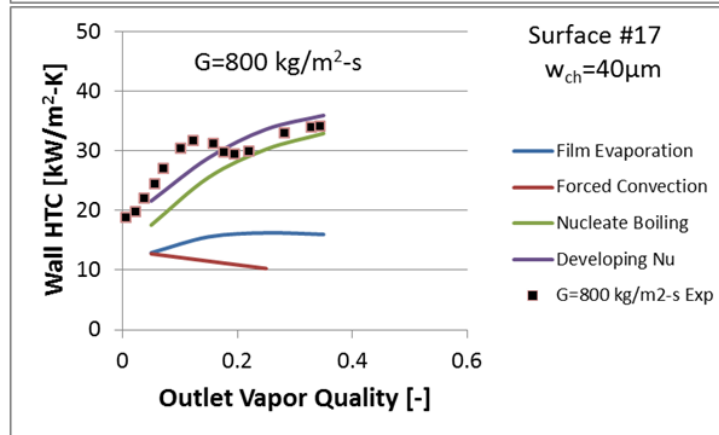


Fig. 4.4.6: Effects of physics.

### 4.4.3 Two-Phase Model Validation

The simulation results with the most accurate physics options were then compared to the two-phase results obtained by Cetegen [10], and the results shown in Fig. 4.4.7. Unlike the results of Cetegen, the trends predicted by the model are more organized. For all cases, at the same vapor quality, an increase in the mass flux will increase the wall heat transfer coefficient. In addition, for cases when the flow is observed to be thermally developing (surface #17 & #12:  $G > 800 \text{ kg/m}^2\text{-s}$ ) the heat transfer coefficient closely matches the experiment. This result is in agreement with the result of the preliminary forced-convection model, which showed that for these conditions, wall heat transfer was nucleate boiling dominant, and when heat transfer coefficient was nucleate boiling dominant, nucleate boiling correlations provided reasonable estimates of heat transfer. However, when flow is film-evaporation dominant, predictive accuracy decreases.

Pressure drop predictions for surface #C and surface #17 are very accurate at low vapor qualities. However, accuracy decreases as vapor quality increases. This could be due to a shift from laminar to turbulent flow, which was not modeled. The fact that the divergence occurs at lower vapor qualities as mass flux is increased seems to indicate that transition from laminar to turbulent flow is responsible for the lack of agreement. Finally, it is worth noting that some cases (surface #C,  $G = 1000 \text{ kg/m}^2\text{-s}$ ; surface #12  $G = 800$  &  $1200 \text{ kg/m}^2\text{-s}$ ) do not match well with the model. However, for these cases, the pressure drop at low vapor qualities exceeds the value predicted by single-phase 3-D CFD. Accordingly, the accuracy of those data sets is questionable, and those data sets were removed when assessing accuracy of the model. With these data points removed, the predicted values matched experiment to within 30% (see Fig. 4.4.8).



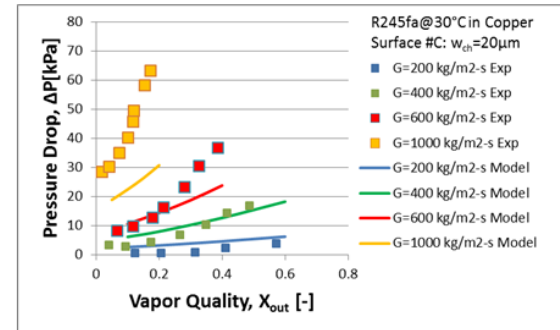
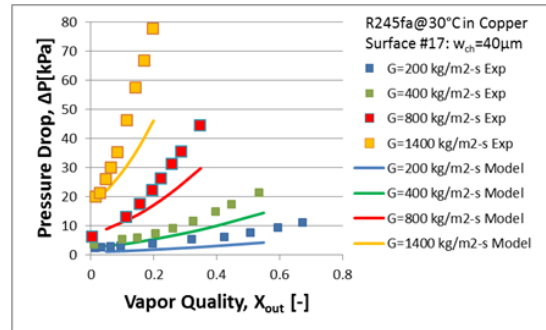
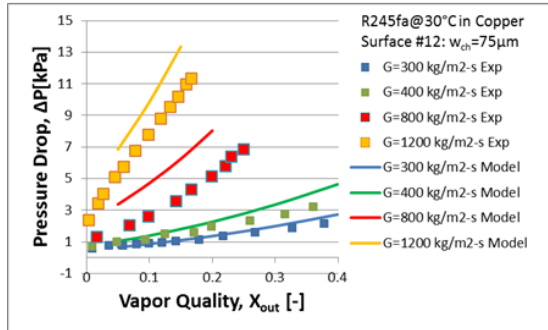
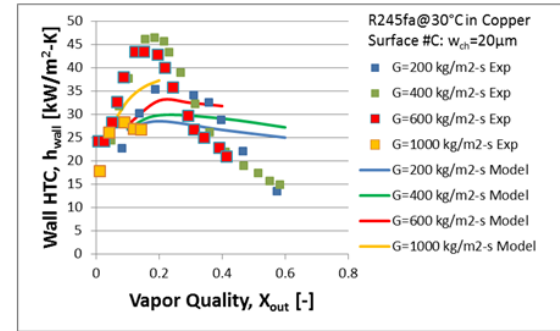
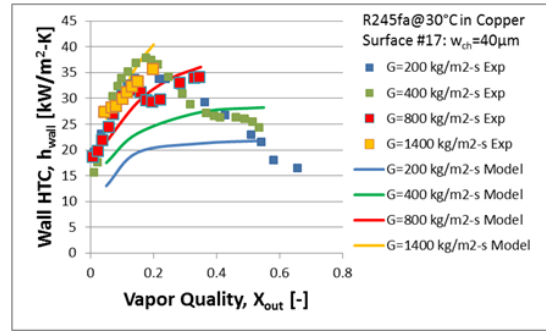
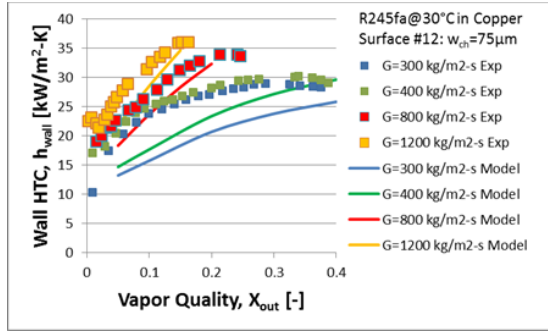


Fig. 4.4.7: Two-phase model validation; comparison to experimental results from Cetegen [10].

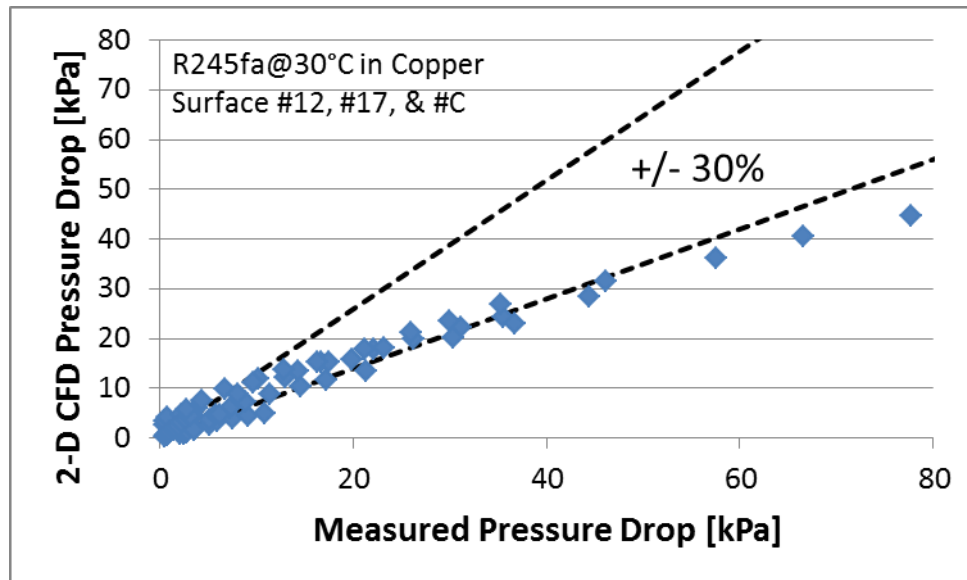


Fig. 4.4.8: Comparison between predicted and measured pressure drop for surfaces #12, #17, and #C.

## 4.5 *Discovery of Baseline Geometry & Parametric Study*

The CFD model was then used to simulate various surface and manifold geometries until one was found that could deliver the goals of the project. This geometry then became the baseline geometry for experimental design. It is worth noting that since the preliminary annular film evaporation with physics-based void fraction model predicted that the annular void fraction correlation is more accurate for the channel widths tested here, the annular void fraction correlation was used instead of the Zivi annular void fraction correlation. The geometries tested to arrive at the baseline design are given in Table 4.5.1, and serve as a parametric study on the effects of varying geometric parameters.

The contours of vapor quality, pressure drop and wall superheat are given in Fig. 4.5.1. For the initial guess, it is observed that a large area of the fin is dry; this, in turn, causes a large imbalance in the fin temperature, forcing it to spread from the dry side to where the surface is wetted. In addition, while the pressure drop is below the threshold for ICECool ( $10\% P_{sat} \cong 18 \text{ kPa}$ ), the base superheat is above it ( $30\text{K}$ ). Accordingly, the inlet and outlet widths were reduced. Reducing the inlet and outlet width increases pressure drop by forcing the fluid through a narrower gap and by requiring the flow to travel a longer distance through the microchannel. The increased distance between the inlet and outlet also acts to force the liquid to spread out inside the microchannel, as the microchannel approaches a straight microchannel, rather than the U-shape of a manifold-microchannel. This, in turn, increases heat transfer coefficient by causing more of the microchannel area to be wetted with liquid. These predictions are in line with observed trends, as shown in Fig. 4.5.1(b).

Next, since the liquid was observed not to reach the bottom of the channel, it was thought that the dry region on the bottom of the channel was wasted, and heat transfer could be improved by reducing the fin height by the length of the dry region: i.e., ~20  $\mu\text{m}$ . However, when this was done, the liquid was still observed to not reach the bottom of the channel (see Fig. 4.5.1(c)). As the liquid approaches the bottom of the channel from the inlet side, pressure builds up due to stagnation, causing the liquid to slow down and turn. Because of the low velocities in this region, the liquid can easily heat up and evaporate. The rapidly expanding vapor then acts to push the liquid in the opposite direction. Therefore, decreasing the height of the fin does not improve the wetting at the bottom of the channel. Instead, decreasing the height of the channel increases base temperature because of the reduced surface area and increases pressure drop because of the reduced flow area. Accordingly, decreasing the fin height is not desirable and this change was not carried to the next trial. Thus, the initial height was restored.

Finally, the fin width was reduced. The base temperature was observed to decrease slightly, and pressure drop was observed to decrease to below the threshold value. The base temperature decreases because reducing the fin thickness increases surface area enhancement faster than it decreases fin efficiency. In addition, pressure drop is reduced because more flow area is added, thereby reducing velocities. Accordingly, because the pressure drop is within the specifications and base temperature is close, this design was selected as the baseline design.

**Table 4.5.1: Geometries tested to arrive at baseline manifold and microchannel geometry**

Name	Manifolds						
	$w_{ch}$ [ $\mu\text{m}$ ]	$w_f$ [ $\mu\text{m}$ ]	$h_f$ [ $\mu\text{m}$ ]	$L_{in}$ [ $\mu\text{m}$ ]	$L_{man}$ [ $\mu\text{m}$ ]	$L_{out}$ [ $\mu\text{m}$ ]	$L_{ch} = L_{in}/2 + L_{man} + L_{out}/2$ [ $\mu\text{m}$ ]
0. Initial Guess	10	10	100	100	100	200	250
1. Squeeze Inlet & Outlet	10	10	100	50	175	100	250
2. Reduce Fin Height	10	10	80	50	175	100	250
3. Reduce Fin Thickness: Baseline	10	5	100	50	175	100	250

- Starting Point:
- ❑ 10  $\mu\text{m}$  fin & channel
- ❑ 0.25 mm pitch

### 1. Squeeze inlet & outlet

- ❑ Liquid forced to spread
- ❑ Reduced base temperature
- ❑ Increased pressure drop

### 2. Reduce fin height

- ❑ Allow liquid to impinge bottom?
- ❑ Expanding vapor prevents this...

### 3. Reduce fin width (5 $\mu\text{m}$ )

- ❑ Increase flow area & surface area enhancement
- ❑ Reduces pressure drop & temperature

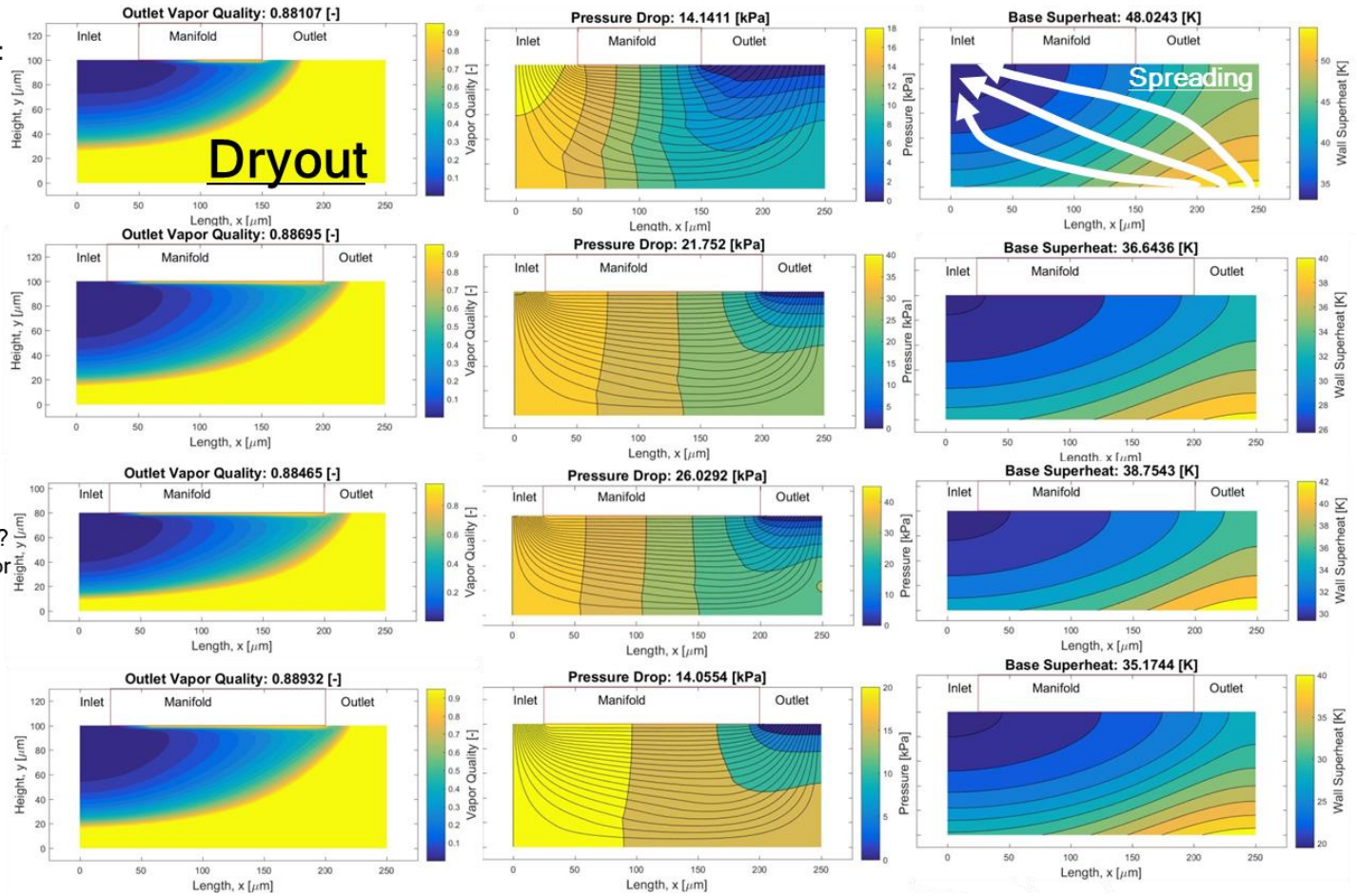


Fig. 4.5.1: Arriving at a baseline geometry & parametric study.

#### **4.6 2.5-D Microchannel Model Summary**

A 2.5-D microchannel model was created by combining the physics simulated in each of the preliminary models. The 2.5-D is designed to provide reasonable predictions of heat transfer coefficient and pressure drop for all channel widths and mass fluxes. The 2.5-D model was first validated by comparing its fully developed and developing single-phase thermal and hydrodynamic predictions to those obtained by a commercially available 3-D CFD program. For fully developed and developing flow where the flow remains 2-D, predictions within 5% were obtained. However, as inertia increased, the flow was shown to become 3-D, and the accuracy of the 2.5-D model could no longer be guaranteed. Further work is needed to determine under what conditions the flow can be considered to remain 2-D so that the model can be used without needing to validate the results with 3-D simulations.

The model was then compared to two-phase experimental results obtained by Cetegen [10], and was shown to predict the correct order of magnitude and trends for heat transfer coefficient. In addition, accuracy was observed to increase when nucleate boiling was the dominant two-phase heat transfer mechanism. Pressure drop predictions overall were observed to be accurate to within 30% for the whole range of mass fluxes, vapor qualities, and surface geometries, and accuracy could be improved at higher flowrates and vapor qualities by incorporating a turbulent friction factor.

Finally, a parametric study on the effects of various geometric parameters was performed, and used to arrive at a baseline geometry capable of achieving the ICECool metrics.

## 5 Experimental Design

With a baseline design defined, the next step was an experiment to validate the model and demonstrate the potential of an embedded, two-phase FEEDS system. Thus, this chapter will discuss the design of the FEEDS experiment. First, an analysis of working fluids will be conducted, specifically as it relates to meeting the objectives of the ICECool program. Second, a manifold model will be presented, allowing for the evaluation of different manifold configurations, and design of a manifold to provide an even flow distribution.

### 5.1 *Working Fluid Selection*

One of the first decisions when attempting to design an experiment to meet the ICECool requirements is working fluid selection. Often, designers are confronted with two working fluids, each with different favorable properties. To select the best working fluid, a designer must know how all the working fluid properties, together, will affect system performance. Accordingly, a system-level model was created, based on the ICECool operating conditions and requirements, to determine optimal working fluid selection. Working fluid selection was conducted at room temperature (30°C) for Si test chips.

#### 5.1.1 System Level Model

A system-level model was created based on the ICECool nominal operational conditions and requirements. The baseline design presented in Table 4.5.1 was used to



calculate velocities, flow rates, pressure drops, and fluxes. The definitions of the referenced geometric variables are given in Fig. 3.1.1.

The fluid properties for various fluids were then obtained from the built-in database in EES software [59]. Density,  $\rho$ , and viscosity,  $\mu$ , were called assuming saturated conditions at the chosen temperature. Latent heat,  $h_{lv}$ , was calculated manually by computing the difference in enthalpy between saturated vapor and saturated liquid at the specified operational temperature. The outlet vapor quality,  $X_{out}$ , was assumed to be 90%, and the system power,  $P_{sys}$ , was assumed to be 1 kW. The total system mass flow rate,  $\dot{m}_{sys}$ , was then calculated from energy balance:

$$P_{sys} = \dot{m}_{sys} X_{out} h_{lv} \quad (5.1.1)$$

Similarly, the power per channel,  $P_{ch}$ , and mass flow rate per channel,  $\dot{m}_{ch}$ , can be computed from the geometry,

$$P_{ch} = \dot{m}_{ch} X_{out} h_{lv} = L_{ch} (w_{ch} + w_f) q'' \quad (5.1.2)$$

where  $P_{sys}$  is related to  $q''$  via the footprint area,  $A$ , which is always equal to  $1 \text{ cm}^2$ :

$$P_{sys} = q'' A \quad (5.1.3)$$

Superficial velocities for the liquid and vapor phases,  $U_l$  and  $U_v$ , respectively, can be computed via the total mass flow rate, cross sectional area, and densities of the liquid and vapor phases:

$$\dot{m}_{ch}^l = \dot{m}_{ch} (1 - X_{out}) = \rho_l w_{ch} h_f U_l \quad (5.1.4)$$

$$\dot{m}_{ch}^v = \dot{m}_{ch} X_{out} = \rho_v w_{ch} h_f U_v \quad (5.1.5)$$

The liquid and vapor Reynolds numbers can then be computed from their definitions:

$$Re_l = \frac{\rho_l U_l D_h}{\mu_l} \quad (5.1.6)$$

$$Re_v = \frac{\rho_v U_v D_h}{\mu_v} \quad (5.1.7)$$

where hydraulic diameter,  $D_h$ , is computed from:

$$D_h = \frac{4A_c}{P} = \frac{2w_{ch}h_f}{w_{ch} + h_f} \cong 2 w_{ch} \quad (5.1.8)$$

The liquid and vapor friction factors,  $f_l$  and  $f_v$ , can then be computed for laminar flow:

$$f_l = 96/Re_l \quad (5.1.9)$$

$$f_v = 96/Re_v \quad (5.1.10)$$

The characteristic pressure per unit length for the liquid and vapor phases,  $dP_l/dx$  and  $dP_v/dx$ , can be computed from:

$$\frac{dP_l}{dx} = \frac{1}{2} \frac{f_l}{D_h} \rho_l U_l^2 \quad (5.1.11)$$

$$\frac{dP_v}{dx} = \frac{1}{2} \frac{f_v}{D_h} \rho_v U_v^2 \quad (5.1.12)$$

While these characteristic pressure drops per unit length might not be physically accurate for the system, they are very useful when comparing working fluids to each other to give an idea of the relative performance.

The vapor void fraction,  $\alpha$ , can be computed using the Zivi void fraction correlation:

$$\alpha = \frac{1}{1 + \frac{1 - X_{out}}{X_{out}} \left( \frac{\rho_v}{\rho_l} \right)^{\frac{2}{3}}} \quad (5.1.13)$$

The film thickness,  $\delta$ , can then be computed geometrically:

$$\delta = (1 - \alpha)w_{ch}/2 \quad (5.1.14)$$

and the expected wall heat transfer coefficient from thin film evaporation,  $h_{tfe}$ , can be computed assuming thermally developed conditions using the liquid thermal conductivity,  $k$ :

$$h_{tfe} \cong k/\delta \quad (5.1.15)$$

Similarly, the wall heat transfer coefficient from nucleate boiling,  $h_{nb}$ , can be computed using the correlation by Forster and Zuber [46]:

$$h_{nb} = c_1 \left( \frac{k^{0.79} C_p^{0.45} \rho_l^{0.49}}{\sigma^{0.5} \mu_l^{0.29} h_{lv}^{0.24} \rho_v^{0.24}} \right) \Delta T_{sat}^{0.24} \Delta P_{sat}^{0.75} \quad (5.1.16)$$

Finally, the expected change in saturation temperature for a 20 kPa pressure drop,  $\Delta T_{sat,20kPa}$ , can be computed directly from fluid property tables. A 20 kPa pressure drop was chosen because it is a reasonable pressure drop and roughly corresponds to the DARPA metric requiring a less than 10% absolute pressure drop across the microchannel when R245fa is used as a working fluid.

## 5.1.2 System Level Results & Working Fluid Selection

The results for various working fluids in order of increasing saturation pressure are given in Fig. 5.1.1. The table is color coded, with green indicating (relatively) superior performance and red indicating (relatively) inferior performance. Low-pressure refrigerants, such as water and acetone, are not preferable despite their favorable thermal properties, due to the low vapor volume and resulting large vapor velocities. This holds true despite the significantly larger latent heats that these fluids possess, compared to refrigerants, which would otherwise reduce the volumetric flow rate needed to dissipate a given heat load. In addition, high pressure refrigerants are less desirable due to

hermeticity requirements and increased structural support needed. In the end, the working fluid R245fa was selected for room temperature experiments due to its low pressure and high vapor density. In addition, the authors of this work also had past experience working with this fluid, and were therefore able to compare system performances.

Refrigerant	P	k	h <sub>wall_nb</sub>	h <sub>wall_tfe</sub>	h <sub>lv_bar</sub>	V <sub>in</sub>	V <sub>out</sub>	dp <sub>idx</sub>	dp <sub>vdv</sub>	dT <sub>sat_20kPa</sub>	
	[Pa]	[W/m-K]	[W/m <sup>2</sup> -K]	[W/m <sup>2</sup> -K]	[J/m <sup>3</sup> ]	[m/s]	[m/s]	[N/m <sup>3</sup> ]	[N/m <sup>3</sup> ]	[C]	
Water	4246	0.6029	6554	1.11E+09	2.42E+09	0.004593	677	586269	2.17E+09	34.3	Pressure Too Low
Acetone	38057	0.16	7572	2.62E+07	4.12E+08	0.02695	105	1.27E+06	2.57E+08	10.7	
n-Pentane	82618	0.1154	9847	8.27E+06	2.23E+08	0.04978	56.1	1.45E+06	1.23E+08	6.249	
Isopentane	109030	0.1122	9569	6.60E+06	2.08E+08	0.05349	44.75	1.75E+06	1.06E+08	5.049	
R245fa	177175	0.07966	10508	3.71E+06	2.48E+08	0.04476	26.34	2.72E+06	8.73E+07	3.041	Pressure Too High
n-butane	283934	0.1025	17384	3.42E+06	2.02E+08	0.05514	19.63	1.34E+06	4.88E+07	2.289	
R142b	390851	0.08906	15785	2.56E+06	2.18E+08	0.0509	14.48	2.66E+06	5.48E+07	1.681	
Isobutane	404456	0.08739	19309	2.20E+06	1.76E+08	0.0631	14.69	1.44E+06	3.72E+07	1.724	
SulfurDioxide	461976	0.1926	29935	7.82E+06	4.74E+08	0.02342	11.2	900726	4.75E+07	1.325	
Dimethylether	684343	0.1422	37349	3.30E+06	2.57E+08	0.04327	8.905	996401	2.72E+07	1.039	
R152a	690683	0.09841	31111	2.14E+06	2.41E+08	0.04604	8.562	1.14E+06	2.93E+07	1.002	
R134a	770642	0.0808	30928	1.47E+06	2.06E+08	0.05404	7.696	1.58E+06	3.00E+07	0.8946	
Ammonia	1.17E+06	0.4714	135949	1.39E+07	6.81E+08	0.01631	4.821	327622	1.54E+07	0.5729	

**Fig. 5.1.1: Working fluid selection. Fluids presented in order of increasing vapor pressure. Metrics are color coded with red signifying relatively inferior performance and green signifying relatively superior performance.**

### 5.1.3 Working Fluid Selection Summary

A system-level working fluid model was created in EES based off the ICECool metrics. Various working fluids were evaluated. Low pressure fluids—such as water and acetone—are not favorable, due to the miniscule densities of their saturated vapor phase, which would result in excessive velocities. Similarly, refrigerants with high saturation pressures require robust structure to prevent system rupture, and are not desirable. Accordingly, R245fa was selected as a working fluid, due to its moderate pressure and acceptable vapor density.

## ***5.2 Manifold Model & Configuration Selection***

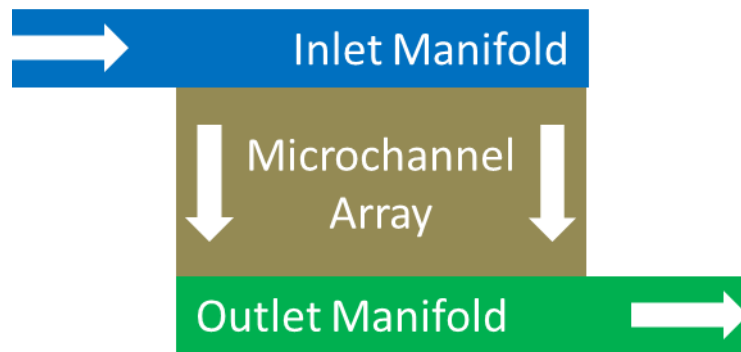
One of the main challenges of this project was to scale down the manifold, to allow for a more compact form factor to enable use of manifold-microchannel technology in real-world embedded heat sinks. Reducing the form factor of the footprint presents challenges, since this size reduction cannot come at the cost of flow distribution. This challenge is especially difficult in high heat flux, high vapor quality two-phase systems, where unevenness in flow distribution becomes exacerbated by rapidly boiling fluid, and could result in permanent system damage if large regions of dryout are present. Accordingly, manifold design is a top priority, and modeling is a crucial tool in ensuring the manifold provides an even inter-microchannel flow distribution.

Similarly, when modeling an embedded two-phase FEEDS system, it is also desirable to assume an even inter-microchannel flow distribution in order to shrink the domain down to a unit cell, or else the entire array of microchannels would have to be simulated simultaneously, resulting in drastically increased computational cost. Thus, the aforementioned microchannel models will only match experimental data if an even flow distribution is obtained. To ensure this was the case, a manifold model was created to predict the pressure distribution in the inlet and outlet manifolds and resulting microchannel flow distribution for a given geometry and manifold configuration.

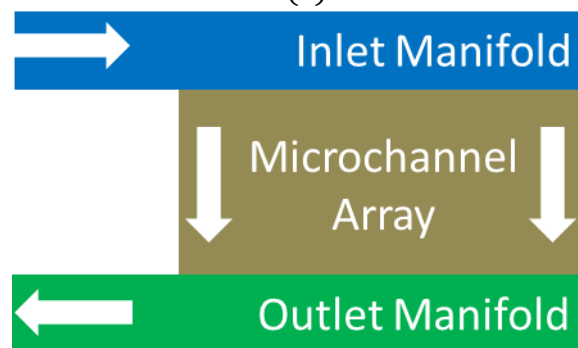
Thus, our approach was to first model the various manifold configurations found in the literature, and select one that was compatible with the high heat flux, two-phase characteristics of ICECool. Second, a manifold was designed for the baseline geometry given in Table 4.5.1.

### 5.2.1 Z-Type and C-Type Manifold Configurations

One of the first decisions in manifold design is the manifold configuration. There are two common types of manifolds found in the literature: Z-type & C-type, each named for the shape the flow creates as it passes from the inlet, through the microchannel array, and to the outlet. In Z-type manifolds, flow enters the inlet manifold from one side (left), where it then turns (downward) into the microchannels, and is subsequently vented in the outlet manifold in the **opposite** direction that it originally entered (right), as shown in Fig. 5.2.1(a). In C-type manifolds, flow enters the inlet manifold from one side (left), where it then turns (downward) into the microchannels, and is subsequently vented in the outlet manifold in the **same** direction that it originally entered (left), as shown in Fig. 5.2.1(b).



(a)



(b)

**Fig. 5.2.1: Manifold flow configurations (a) Z-type and (b) C-type.**

For single-phase flows with identical inlet and outlet geometry, it is reasonable to assume that Z-type manifolds would provide a more even flow distribution than C-type, since regardless of the path the fluid takes, the total flow length is the same for Z-type. In addition, since pressure drop in the manifold is proportional to velocity, if an even flow distribution is obtained, the pressure gradient will be steepest near the entrances of the inlet and outlet and flattest near the ends of the inlet and outlets. For the Z-type channel, the gradients will be going in the same direction (see Fig. 5.2.2(a)), whereas for the C-type, the gradients will be going in opposite directions (see Fig. 5.2.2(b)). Accordingly, the pressure profiles might look something like what is shown in Fig. 5.2.2. Therefore, from this simple analysis, the Z-type manifold is more likely to provide a more even flow distribution. However, it is worth noting that the flow distribution in both configurations is likely to be excellent if the pressure drops in the inlet and outlet manifold are both negligible compared to the pressure drop in the microchannel array. Thus, a more even flow distribution can be obtained simply by increasing the pressure drop in the microchannels. Accordingly, a model is needed to predict the inlet and outlet manifold pressure drops so that an appropriate design and configuration can be selected.

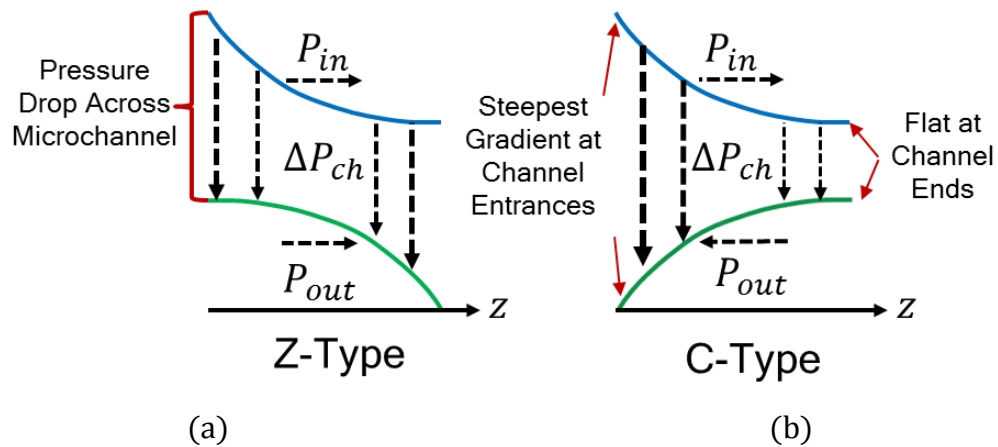


**Fig. 5.2.2: Expected pressure drop distribution in inlet and outlet manifolds for (a) Z-type (b) C-type.**

### 5.2.2 Model Assumptions and Simplifications

The following assumptions were made in this model:

- (1) Steady-state, fully developed 1-D flow;
- (2) The flow distribution to each manifold inlet is equal;
- (3) Viscous effects can be simulated using a laminar or turbulent fully developed friction factor;
- (4) The inlet is saturated liquid, and the outlet is saturated vapor, regardless of flow distribution;
- (5) The momentum and continuity equations can be treated as continuous, despite the presence of discrete fins and microchannels;
- (6) The pressure drop in the microchannel is assumed to scale linearly with velocity;
- (7) The operational conditions match those specified by the ICECool metrics:
  - a. The flow rate is selected to obtain 100% outlet vapor quality at  $1 \text{ kW/cm}^2$
  - b. The average pressure drop across the microchannels is assumed to be maximum value allowed: 10% of  $P_{sat}$ .

It is worth noting that even though the ICECool requirements specify only 90% vapor quality, 100% vapor quality was used to model the manifold configuration, since only a rough comparison between manifold configurations is needed to select a manifold configuration. In addition, using 100% vapor quality simplifies the outlet manifold calculations, since single-phase vapor flow is more straightforward to model than a two-phase mixture.



In addition, since the microchannel flow rate and outlet vapor quality are decoupled, the accuracy of the model declines when the flow distribution is poor. In fact, when the model predicts a poor flow distribution, the actual flow distribution is likely to be even worse. However, when the model predicts a uniform flow distribution, the outlet vapor quality, if it were coupled to microchannel flow rate, would be uniform as well. Thus, since we are interested only in geometries and configurations which provide a uniform flow distribution, this simplified assumption is worth avoiding the added complexity of coupling the microchannel flow rate with vapor quality.

### **5.2.3 Model Domain and Variables**

The model domain is shown in Fig. 5.2.3. Regardless of configuration, the manifold length is assumed to be the entire length of the chip, 1 cm. Since an even flow distribution between manifold inlets is assumed, only one inlet and outlet pair needs to be simulated, as shown in Fig. 5.2.3.

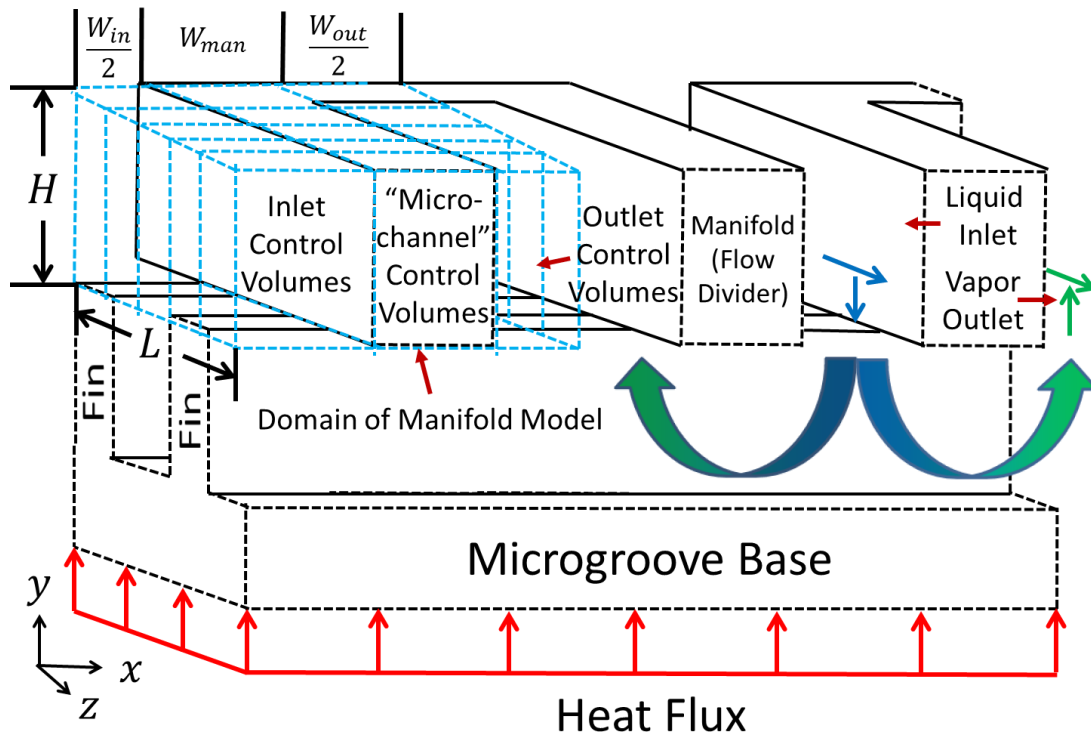
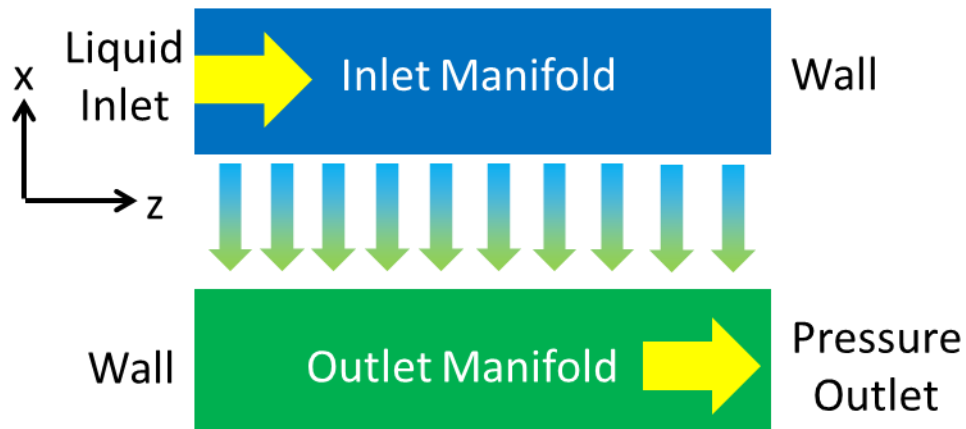


**Fig. 5.2.3: Manifold model domain.**

## 5.2.4 Model Boundary Conditions

The boundary conditions for the two manifold flow configurations are shown in Fig. 5.2.4. Although the two different manifold configurations require different couplings and boundary conditions, the governing physics are the same.



(a)

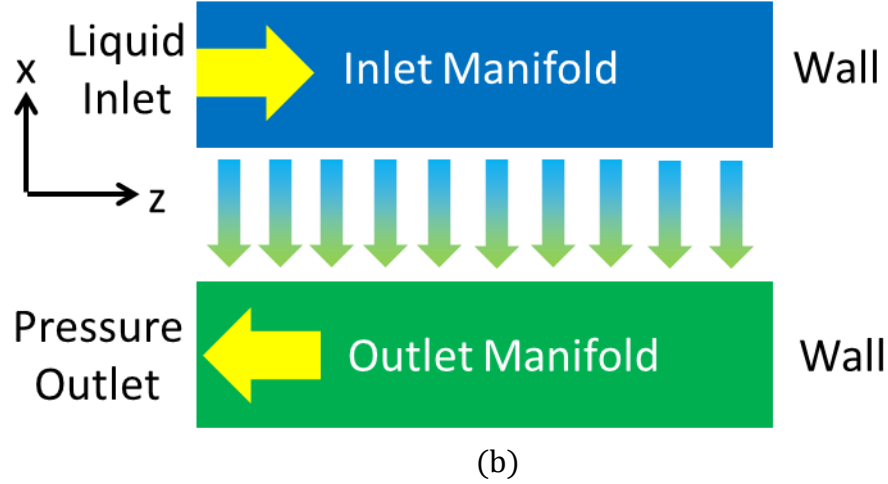


**Fig. 5.2.4: Manifold model boundary conditions: (a) Z-type and (b) C-type.**

### 5.2.5 Model Equations

The governing continuity and Navier-Stokes equations were discretized in 1-D using first-order upwind discretization, similar to that presented in the 2.5-D microchannel model.

#### 5.2.5.1 Conservation of Mass

The control volumes for conservation of mass are shown in Fig. 5.2.5.

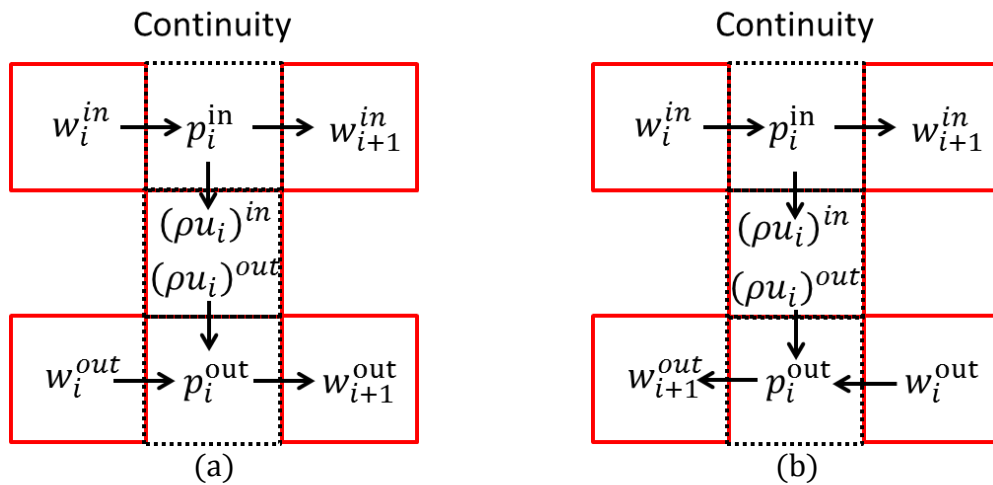


**Fig. 5.2.5: Control volumes used for conservation of mass for each manifold configuration: (a) Z-type and (b) C-type.**

From Fig. 5.2.5, conservation of mass takes the form,

$$\rho_{in}(w_i^{in} - w_{i+1}^{in}) = \rho_{in}u_i^{in} \Delta z/H \quad (5.2.1)$$

for the inlet manifold, and

$$\rho_{out}(w_i^{out} - w_{i+1}^{out}) = \rho_{out}u_i^{out} \Delta z/H \quad (5.2.2)$$

for the outlet manifold. It is worth mentioning that for the configurations considered here,

$\rho_{in}$  is the saturated liquid density— $\rho_l$ —and  $\rho_{out}$  is the saturated vapor density— $\rho_v$ .

In addition, conservation of mass in the microchannel takes the form,

$$\rho_{in}u_i^{in}W_{in} = \rho_{out}u_i^{out}W_{out} \quad (5.2.3)$$

### 5.2.5.2 Conservation of Z-Momentum

The control volumes for conservation of Z-momentum are given in Fig. 5.2.6.

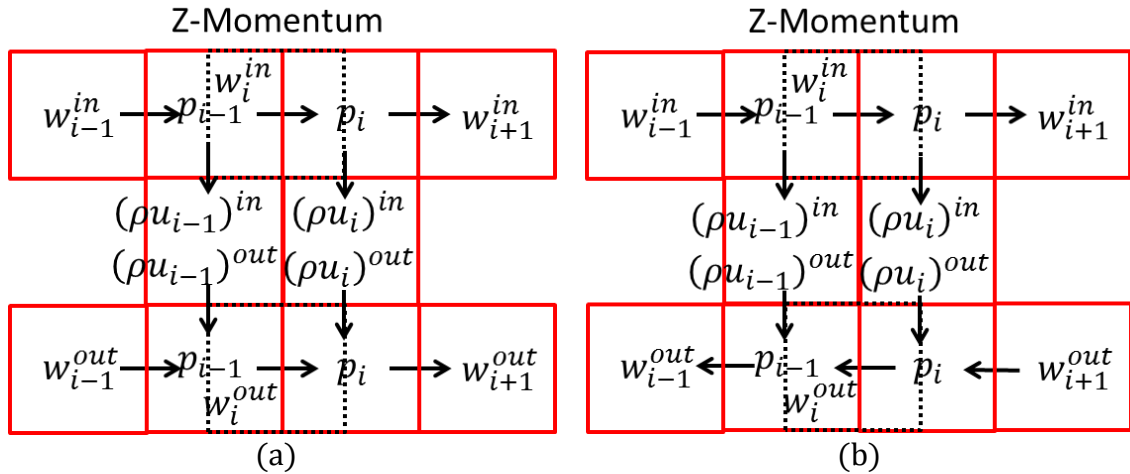


**Fig. 5.2.6: Control volumes used for conservation of momentum for each manifold configuration: (a) Z-type and (b) C-type.**

The governing equation for conservation of z-momentum in the inlet is of the form,

$$\begin{aligned}
& \rho_{in} \frac{w_{i-1}^{in} + w_i^{in}}{2} w_{i-1}^{in} + p_{i-1}^{in} \\
& = \rho_{in} \frac{w_{i+1}^{in} + w_i^{in}}{2} w_i^{in} + \rho_{in} \frac{u_{i-1}^{in} + u_i^{in}}{2} \frac{\Delta z}{H} w_i^{in} + p_i^{in} \quad (5.2.4) \\
& + \Delta z \frac{\partial p^{in}}{\partial z}
\end{aligned}$$

for the inlet, where a momentum source term,  $\partial p / \partial z$ , has been added to simulate the friction associated with the 3-D flow:

$$\frac{\partial p}{\partial z} = \frac{1}{2} \frac{f}{D_h} \rho w_i^2 \quad (5.2.5)$$

The friction factor,  $f$ , is taken for laminar or turbulent flow:

$$f = \begin{cases} 96/Re & Re < 2300 \\ (0.79 \ln(Re) - 1.64)^{-2} & Re > 2300 \end{cases} \quad (5.2.6)$$

and the hydraulic diameter,  $D_h$ , is calculated based on the manifold inlet geometry:

$$D_h = \frac{4A_c}{P} = \frac{2WH}{W+H} \quad (5.2.7)$$

It is worth noting that this source term can be computed for both the inlet and outlet manifolds by using the appropriate geometry ( $W_{in}$  or  $W_{out}$ ), fluid properties ( $\rho_{in}$  or  $\rho_{out}$ ), and velocities ( $w_i^{in}$  or  $w_i^{out}$ ).

The governing equation for conservation of momentum in the outlet manifold takes on two forms, depending on manifold configuration. For the Z-type manifold configuration, conservation of Z-momentum takes the form,

$$\begin{aligned}
& \rho_{out} \frac{w_{i-1}^{out} + w_i^{out}}{2} w_{i-1}^{out} + p_{i-1}^{out} \\
& = \rho_{out} \frac{w_{i+1}^{out} + w_i^{out}}{2} w_i^{out} \\
& + \rho_{out} \frac{w_{i-1}^{out} + w_i^{out}}{2} \frac{\Delta z}{H} w_i^{out} + p_i^{out} + \Delta z \frac{\partial p^{out}}{\partial z}
\end{aligned} \tag{5.2.8}$$

For the C-type manifold, the flow direction is assumed to be reversed, and so the upwind scheme requires a slightly different form:

$$\begin{aligned}
& \rho_{out} \frac{w_{i-1}^{out} + w_i^{out}}{2} w_i^{out} + p_{i-1}^{out} \\
& = \rho_{out} \frac{w_{i+1}^{out} + w_i^{out}}{2} w_{i+1}^{out} \\
& + \rho_{out} \frac{w_{i-1}^{out} + w_i^{out}}{2} \frac{\Delta z}{H} w_i^{out} + p_i^{out} + \Delta z \frac{\partial p^{out}}{\partial z}
\end{aligned} \tag{5.2.9}$$

where  $\partial p / \partial z^{out}$  can be computed from Eqs. (5.2.5)-(5.2.7) using the outlet manifold geometry.

### 5.2.5.3 Conservation of X-Momentum (Equation for Inlet-Outlet Pressure Difference)

Since velocity components perpendicular to the flow direction are present (despite the 1-D nature of this model), an additional set of equations is needed to relate the difference in pressure between the inlet and outlet in order to fully define the system. As stated above, the pressure drop in the microchannel was modeled as scaling linearly with velocity. Therefore, the following equation can be used to relate the difference in inlet and outlet pressure to the velocity entering the microchannels:

$$P_i^{in} - P_i^{out} = c_0 u_i^{in} \tag{5.2.10}$$

where  $c_0$  is a constant, the value of which is assumed to be set such that the average pressure drop between the inlet and outlet manifolds is equal to the metric defined by the ICECool program. Thus, the model assumes that the microchannel is designed such that it meets the ICECool metrics for pressure drop under the design conditions.

#### 5.2.5.4 Applying Boundary Conditions

Only four boundary conditions are needed. Two of these boundary conditions are in the inlet manifold: the initial inlet velocity,  $w_1^{in} = V_{in}$ , and the velocity at the end of the manifold,  $w_{N+1}^{in} = 0$ . The other two boundary conditions—the pressure and velocity at the entrance and end of the outlet manifold, respectively—depend on the manifold configuration. For Z-type manifolds, the boundary conditions are  $w_1^{out} = 0$  and  $p_N^{out} = P_{sat}$ , while for C-type manifolds the boundary conditions are  $p_1^{out} = p_{sat}$  and  $w_{N+1}^{out} = 0$ .

The inlet velocity,  $V_{in}$ , can be computed using the geometry and ICECool requirements. In particular,  $V_{in}$  may be computed by assuming that all of the flow entering the inlet manifold is completely evaporated and that the average heat flux over the domain of the model is  $1 \text{ kW/cm}^2$ :

$$2(W_{in}/2 + W_{man} + W_{out}/2)Lq'' = \dot{m}h_{lv} = \rho_{in}W_{in}H V_{in} h_{lv} \quad (5.2.11)$$

where  $h_{lv}$  is the enthalpy of evaporation, and  $L, W_{in}, W_{man}, W_{out}$ , and  $H$  are defined in Fig. 5.2.3.

#### 5.2.5.5 Mathematical Formulation and Solution

Thus, three sets of variables— $w, u$ , and  $p$ —must be solved. The discretized equations were formulated and solved using EES, a commercial software package

capable of solving systems of nonlinear equations. EES is also particularly well suited for this application, since it has a built-in database of fluid properties, and can be used to implicitly find the value of  $c_0$  needed to make the average pressure drop between the liquid and vapor 10% of  $P_{sat}$ , as per the ICECool requirement.

#### 5.2.5.6 Mesh Independence and Verification

Approximately 250 cells were found to be required to obtain mesh-independent results. The model was verified by comparing it to analytical solutions and verifying conserved quantities.

#### 5.2.5.7 Data Analysis Equations

In order to gauge the inter-microchannel flow maldistribution, a parameter,  $\beta$ , was defined as

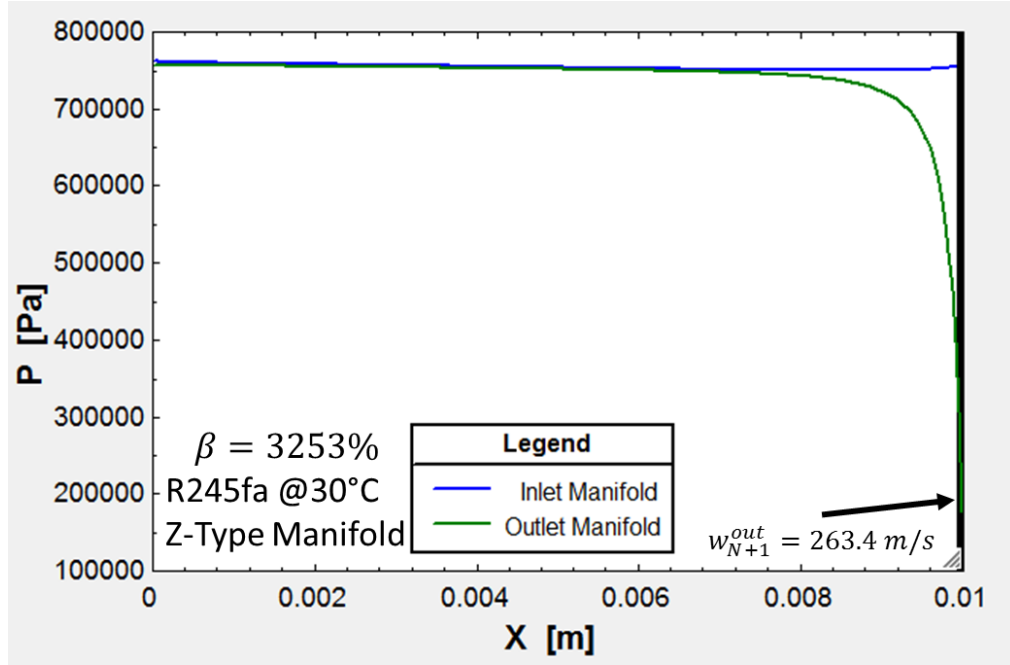
$$\beta = \frac{u_{max}^{in} - u_{min}^{in}}{u_{mean}^{in}} \quad (5.2.12)$$

which is the difference in maximum and minimum microchannel inlet velocity divided by the mean. Large values of  $\beta$  indicate large flow maldistribution, and should be avoided.

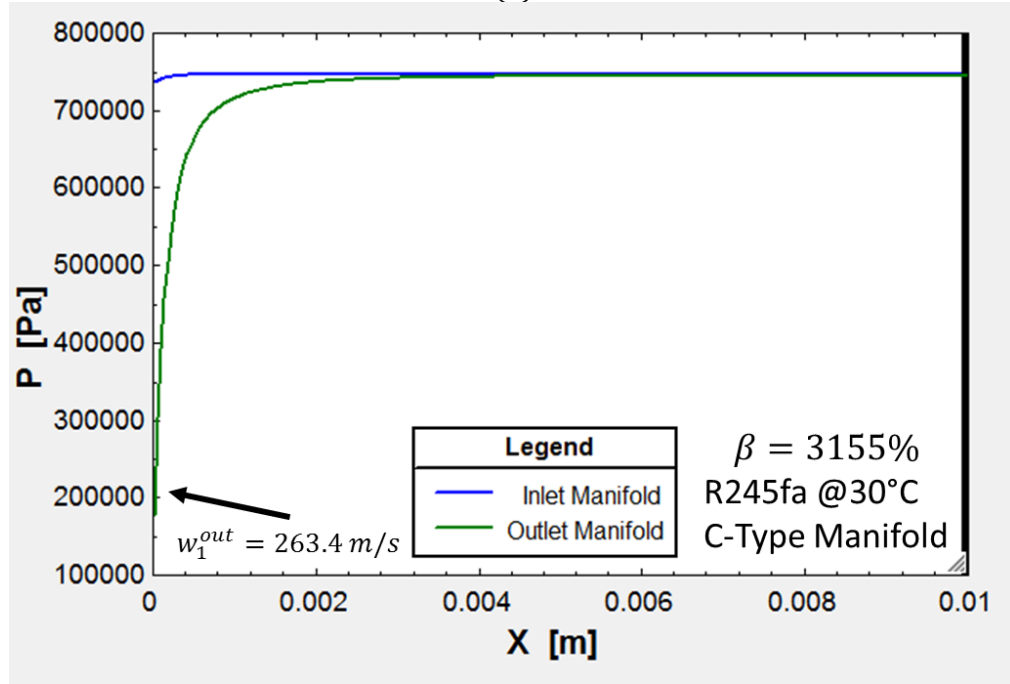
#### 5.2.6 Manifold Configuration Results

The model was then run for the geometry shown in Fig. 5.2.3 for both manifold configurations. The resulting inlet and outlet pressure profiles are shown in Fig. 5.2.7, below, along with their accompanying flow maldistribution parameter,  $\beta$ :





(a)



(b)

**Fig. 5.2.7: Inlet and outlet pressure profiles for all three manifold configurations: (a) Z-type and (b) C-type. Both configurations have enormous pressure drops on the outlet due to the confined vapor and consequent large velocities, resulting in terrible flow distribution.**

From Fig. 5.2.7, it is clear that Z-type and C-type manifold configurations are unacceptable. As expected, the large volumetric flow rates associated with single-phase

vapor flow causes a large pressure drop in the manifold outlet, while the pressure drop in the liquid phase is almost invisible by comparison. Thus, the pressure difference between the inlet and outlet manifolds varies wildly, resulting in excess of 3000% flow maldistribution for the C-type and Z-type manifolds. This shouldn't be surprising, given that vapor velocity peaks at 264.3 m/s at the entrance of the outlet for both Z-type and C-type manifolds.

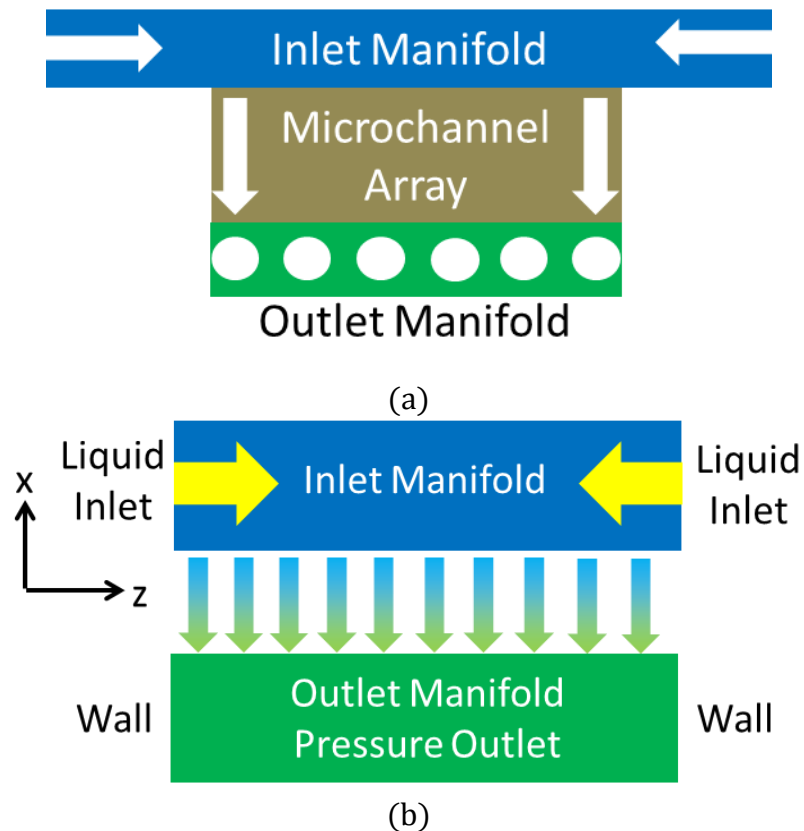
Thus, while Z-type and C-type manifolds work well for single-phase flow, since flow length might be even or pressure gradients might be balanced, these advantages do not translate to two-phase systems, in which the symmetry between the inlet and outlet is not present due to changing fluid properties (and in fact, this can be true of single-phase flow as well if a large enough temperature change occurs between the inlet and outlet manifolds). Accordingly, a new manifold flow configuration is needed.

### **5.2.7 L-Type Manifold Configuration and Results**

Due to the enormous flow maldistribution from Z-type and C-type manifolds, a new manifold configuration was proposed and modeled. The so-called L-type manifold configuration is shown in Fig. 5.2.8(a). Fluid enters the inlet manifold from the left and right sides, where it then flows through the microchannel array, and vents vertically, perpendicular to the other two flow directions.

At first glance, L-type manifolds might seem drastically inferior, since they neither guarantee an equal flow length for all fluid paths nor possess matched pressure gradients in the inlet and outlet manifolds, since the flow in the outlet manifold is perpendicular to the flow in the inlet. However, there are a few key advantages that make L-type manifolds desirable for this application. First, the flow is simpler, since the outlet

manifold is not coupled to the inlet via microchannel pressure drop; in fact, the pressure in the outlet manifold is uniform in the z-direction, and the pressure drop through the outlet manifold acts as an additional pressure drop to the microchannel array, thereby only serving to improve flow distribution. Accordingly, to obtain an even flow distribution with an L-type manifold, the pressure drop in **only** the inlet manifold must be much less than the pressure drop in the microchannel array and outlet manifold combined. This is especially important for two-phase systems when the outlet contains vapor, since orders-of-magnitude higher velocities and volumetric flow rates are likely to occur, resulting in larger pressure gradients than on the inlet side. Therefore, L-type manifolds have the added advantage that if the manifold provides an even distribution in single-phase, it will work for two-phase as well. This is not the case for Z-type and C-type manifolds, and drastically simplifies design.



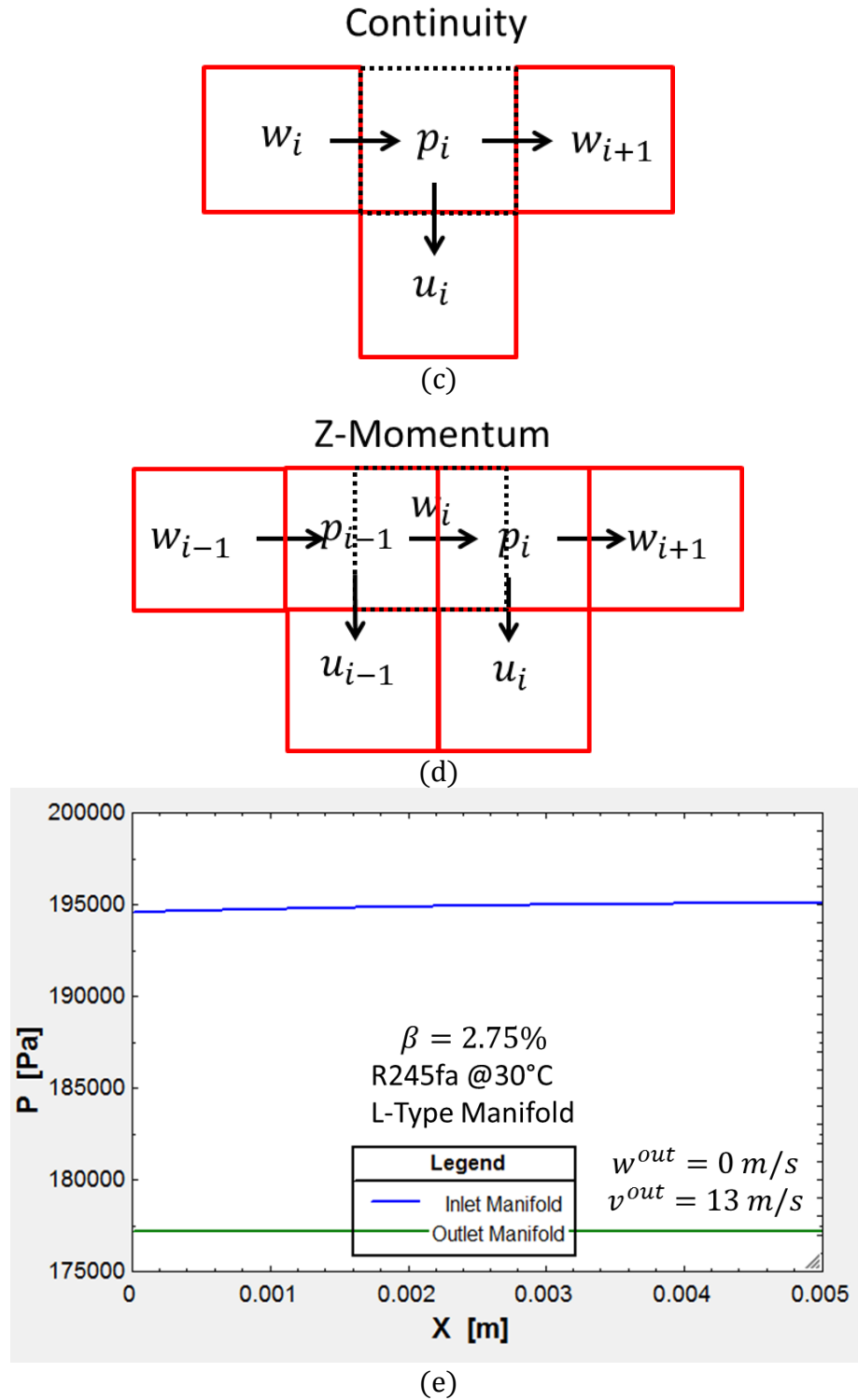


**Fig. 5.2.8: L-type: (a) flow diagram, (b) boundary conditions, (c) control volume for continuity, (d) control volume for momentum, (e) inlet and outlet pressure profiles. L-type manifold maintains reasonable vapor-side velocities, and therefore achieves orders-of-magnitude better flow distribution than Z- and C-type manifolds.**

The boundary condition for the L-type manifold is given in Fig. 5.2.8(b). The control volumes for continuity and conservation of momentum in the inlet manifold are given in Fig. 5.2.8(c) and Fig. 5.2.8(d), respectively. Continuity and conservation of momentum in the outlet manifold are not needed, since the outlet manifold is not part of the domain. Instead, the outlet manifold is assumed to be at a uniform pressure equal to the saturation pressure; thus, the pressure drop through the outlet manifold, which could only result in improved flow distribution for the reasons given above, was not modeled. The boundary conditions for the inlet are unchanged from the previous formulation, except that the inlet velocity is half the value given by Eq. (5.2.11) since there are two inlets (see Fig. 5.2.8(a)-(b)).

The pressure distribution is shown in Fig. 5.2.8(e). The flow maldistribution parameter for the L-type manifold is shown to be approximately 3%, indicating that this is the preferred manifold configuration. This should come as no surprise, due to the simpler flow configuration as well as the reduced vapor velocity in the outlet (see Fig. 5.2.8(e)). Accordingly, all future work will be conducted with L-type manifolds only.

### **5.2.8 Design of Manifold**

Once a manifold configuration was selected, improvements to the model could be made so that a working manifold could be designed. Since the L-type manifold was selected, the outlet manifold could be excluded from the computational domain. The performance, therefore, should not fundamentally change between single-phase and two-phase operation, and the manifold could be designed for single-phase operation. Indeed, a manifold which can perform well in single-phase and over a wide range of flow rates is desirable, since it enables testing the of the system in single phase mode—for which

conventional CFD software can be used to assess system performance by comparing system pressure drop and thermal performance to the values predicted by the CFD simulations.

In order to accurately predict manifold performance at various flow rates, the response of the microchannels to various flow rates must be known and accurately modeled. In addition, the assumption that the average pressure drop will always meet the ICECool metrics was abandoned since we desired to test our system in single-phase mode and at flow rates not related to ICECool. To obtain a more accurate representation of the relationship between pressure drop and microchannel inlet velocity, the CFD model was run for the geometries of interest. It is worth noting that the CFD model is very accurate for these conditions, since the flow is fully developed, single-phase and adiabatic (see Fig. 4.4.1). In the end, a quadratic correlation of the form,

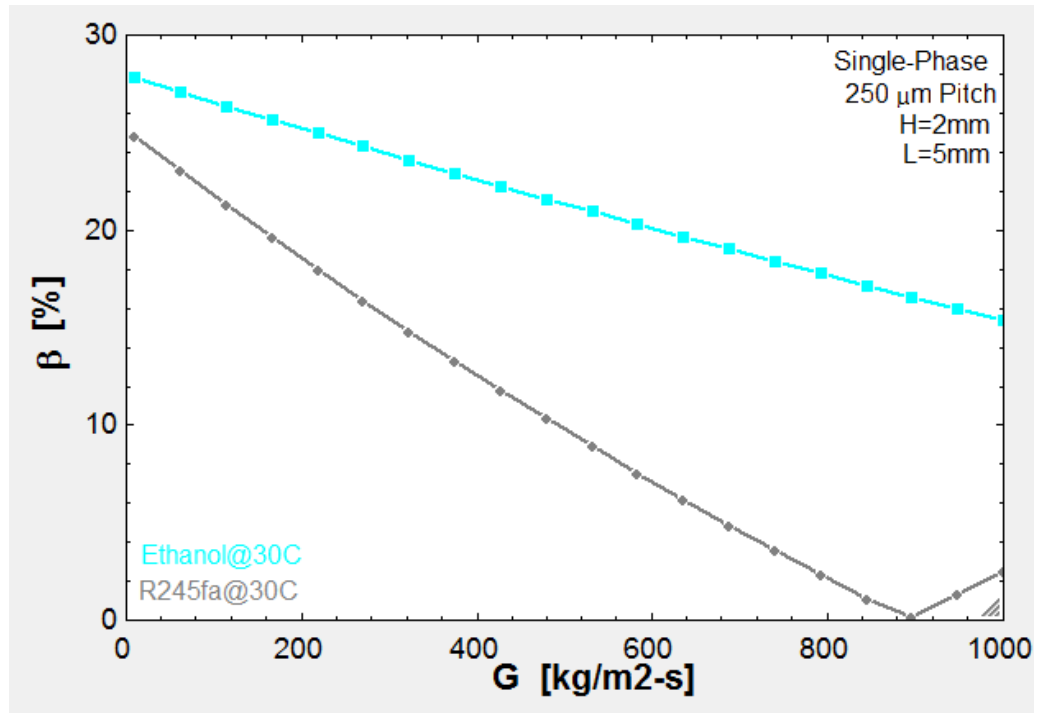
$$dP = (c_0|u_i| + c_1)u_i \quad (5.2.13)$$

where  $c_0$  and  $c_1$  are fitting constants, was found to fit the CFD data. This method is equivalent to the method used by other researchers, such as Arie et al. [19]. Thus, in the improved model, Eq. (5.2.13) replaces Eq. (5.2.10). In addition, since the L-type manifold has been selected, Eqs. (5.2.2), (5.2.8) and (5.2.9) are not needed, since they refer to the outlet manifold, which is no longer in the domain.

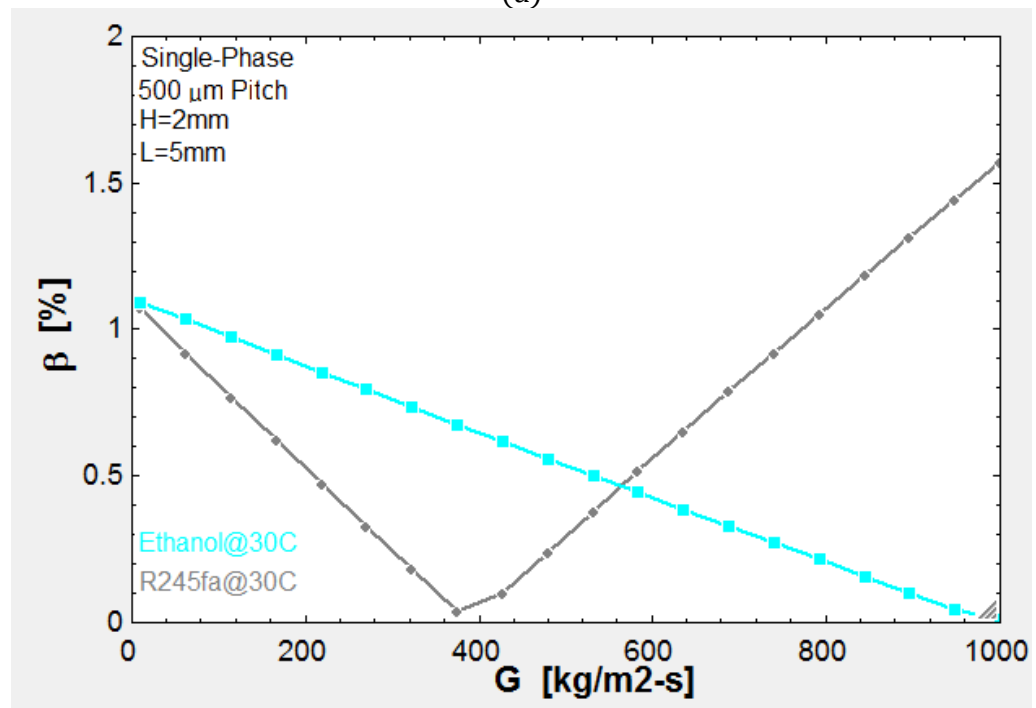
Since R245fa was selected as the refrigerant in the previous section, the pressure drop-velocity relationship for the microchannels was determined with these fluids. In addition, since ethanol was desired to be used as a single-phase validation fluid, simulations were also run with ethanol to ensure a good flow distribution would be obtained even during single-phase tests. The results are presented in Fig. 5.2.9.

From the figure, it is clear that the flow maldistribution initially decreases with increasing mass flux until flow maldistribution hits 0%, where it then begins to increase with increasing mass flux. The reason for this is the balance of viscous and inertia forces. For low mass fluxes, friction is dominant over inertia. Accordingly, the pressure in the inlet manifold decreases in the z-direction. However, for very high mass fluxes, inertia is dominant over friction. Accordingly, the pressure increases in the z-direction due to stagnation of the flow. Therefore, there exists a critical, moderate mass flux at which the pressure drop due to viscous forces and the pressure increase due to stagnation perfectly cancel, resulting in a very uniform flow distribution.

In addition, it is clear that even with a 2 mm-tall inlet channel—a much taller channel than could be manufactured with a single Si wafer in a MEMS processes—the 250  $\mu\text{m}$  pitch will not allow for a uniform flow distribution for the whole range of mass fluxes and fluids desired. Accordingly, the pitch was doubled to 500  $\mu\text{m}$ , where a uniform flow ( $\beta \leq 2\%$ ) would be obtained for the whole range of mass fluxes and fluids desired. However, as mentioned above, this geometry could no longer be fabricated with Si using standard MEMS processes. Accordingly, 3-D printing was selected as the fabrication method.



(a)



(b)

**Fig. 5.2.9: Flow maldistribution vs microchannel mass flux for R245fa and ethanol:  
(a) 250  $\mu\text{m}$  pitch and (b) 500  $\mu\text{m}$  pitch.**



### **5.2.9 Manifold Model Summary**

In conclusion, a 1-D manifold model was developed in support of the CFD model in order to predict the inter-microchannel flow distribution through the manifold system. The 1-D manifold model also allowed for the evaluation of two standard single-phase manifold configurations. In the end, the model showed that for high heat flux two-phase flow, these two manifold configurations would not provide an even flow distribution. Therefore, a third manifold configuration—the L-type configuration—was proposed here, achieving sufficiently low flow maldistribution.

In addition, the model was able to predict the resulting inter-microchannel flow distribution for the baseline geometry discovered with the 2.5-D microchannel model. Unfortunately, no reasonable manifold geometry could be found for that pitch which could provide a uniform flow for a wide range of flow rates and working fluids. Accordingly, the pitch was doubled, and a manifold which provided uniform flow for a wide range flow rates and for two fluids was obtained.

### ***5.3 Experimental Design Summary***

A system-level model based on the ICECool requirements was created and used to select a working fluid for room temperature experiments in Si. Next, a manifold model was created to assess the applicability of conventional single-phase manifold flow configurations for a two-phase flow system. In the end, it was shown that the novel manifold configuration designed in the present work is necessary for proper functioning of large area ( $1 \text{ cm}^2$ ) two-phase high heat flux manifold-microchannel systems. A manifold was then designed with this model to provide an even flow distribution over a wide range of fluids, mass fluxes, and vapor qualities.

## 6 Press-Fit FEEDS Experiment

After modeling the manifold and arriving at a configuration and design that provides an even flow distribution for single-phase and two-phase flow for a few different working fluids, the next step was to design and fabricate the remaining components. To begin, a modular “press-fit” design, in which the test section components could be disassembled, cleaned, and mixed-and-matched, was selected. Before the final test section design was obtained, numerous test section design iterations were tried. In the interest of simplicity, only the final design is shown here (see Fig. 6.2.1), but previous versions will be briefly discussed.

### 6.1 *Failed Experimental Designs*

First, the header and lid were 3-D printed in Ultem plastic, leading to erosion of the header and clogging of the microchannels at high liquid flow rates. This part was subsequently fabricated from stainless steel to avoid erosion and allow for operation at higher temperatures. The lid was also switched from plastic to aluminum to enable high-temperature operation ( $\sim 200^{\circ}\text{C}$ ).

Second, initially, the RTD-heater was wired via press fitting the electrical connections together. Upon experimental testing, excessive temperatures were observed to cause plastic parts to melt, due to the high current and large contact resistance between wires. Accordingly, all current-carrying electrical connections were soldered together, including the chip to the circuit board, and the circuit board to the external power source. This change necessitated further revisions to other components, in order to allow for test section to be assembled.

In addition, numerous versions of the manifold were produced in order to arrive at a design without broken, wavy, and non-parallel grooves. As mentioned in Section 5.2.8, 3-D printing was selected as the manufacturing method. The selected material was alumina due to the increased accuracy of the 3-D printing, as well as its ability to be polished and lapped. The first generation of manifolds arrived mostly in-tact, the channels were smooth, but the grooves were not straight and parallel to each other (see Fig. 6.1.1(a)).

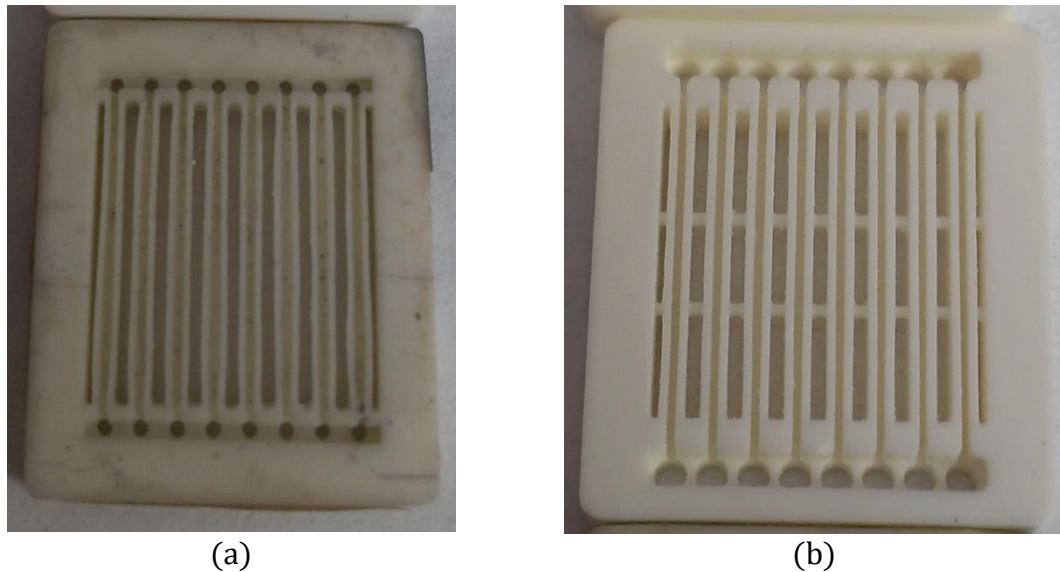
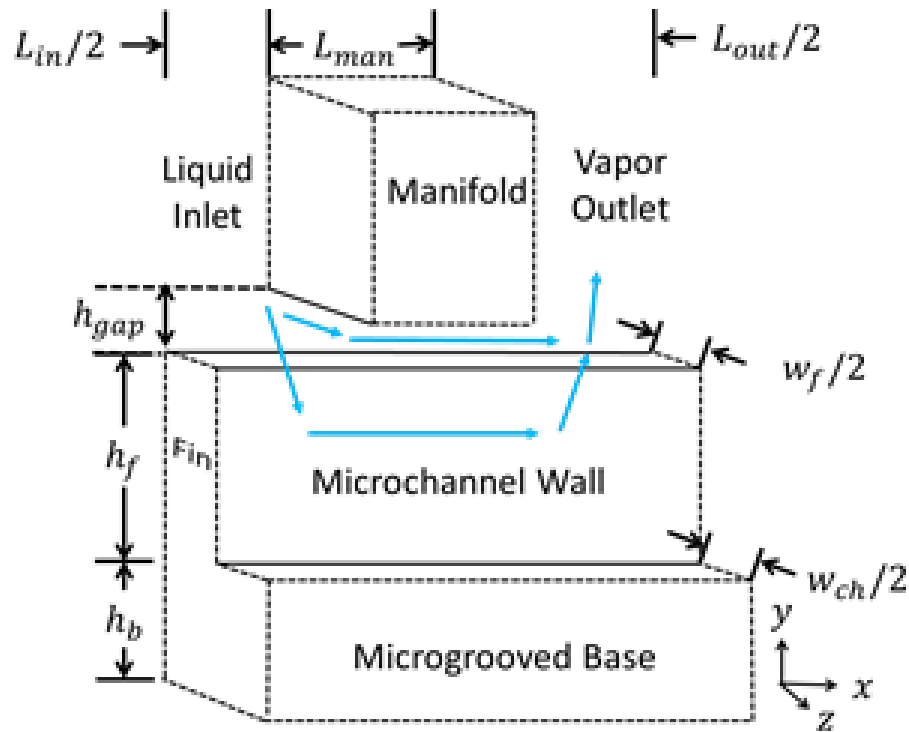


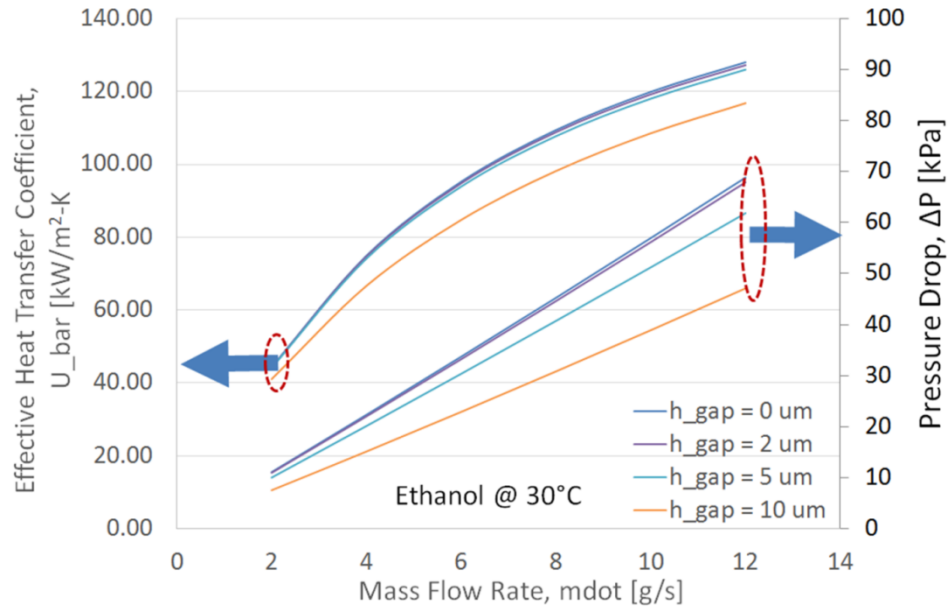
**Fig. 6.1.1: 3-D printed alumina manifold design revisions: (a) first generation with wavy, non-parallel fins and (b) final generation with braces to prevent warping.**

It is thought that thermal expansion during the firing step of the 3-D printing process caused the channels to warp. Accordingly, the second generation of manifolds was fitted with “braces” to hold the liquid and vapor channels parallel. However, upon firing, some grooves fractured due to stress concentrations. Accordingly, in a final iteration, braces were rounded as much as possible to reduce stress concentrations. These manifolds arrived intact, without broken grooves, and with parallel and smooth channels (see Fig. 6.1.1(b)). In addition, the effect of a gap between the manifold and

microchannel fin tips was investigated with a 3-D single-phase CFD simulation (see Fig. 6.1.2(a)). The results show that sub-micron roughness and flatness is required in order to prevent any significant flow leakage, which could potentially result in reduced heat transfer coefficient and pressure drop (see Fig. 6.1.2(b)). Flow leakage would be especially detrimental to a high heat flux, two-phase system (not shown in Fig. 6.1.2(b)), where, if the microchannels dried out due to bypassed flow, the surface temperatures would increase rapidly, potentially damaging the system.



(a)



(b)

**Fig. 6.1.2: Single-phase 3-D CFD simulation to determine the effect of a gap between the manifold and chip on heat transfer coefficient and pressure drop: (a) model geometry and (b) heat transfer coefficient (left) & pressure drop (right) vs. mass flow rate.**

Finally, numerous generations of test chips were fabricated. The first generation of test chips lacked a thick enough oxide layer to prevent dielectric breakdown due to the high voltages applied. The next generation possessed a sputtered oxide layer, which did not sufficiently seal the heater from the Si, resulting in oxide layer breakdown at small voltages. Subsequent generations of chips possessed either a thermal oxide or a thermal oxide-nitride-oxide stack. These generations provided sufficient dielectric strength to prevent oxide layer breakdown, but caused reversible resistance drops upon exceeding approximately 100 V. To investigate this problem, the extra voltage taps to enable each branch of the serpentine heater to be used as an independent RTD were removed, and the heater was placed 0.5 mm from the edge of the chip, but to no avail. In the end, it was concluded that electrical arcing was occurring from the circuit board to the Si chip through the refrigerant vapor gap. To prevent this, high-temperature Kapton tape was

placed over the entire heater, with only small holes cut out for soldering, thereby blocking the suspected arcing paths (see Fig. 6.1.3).

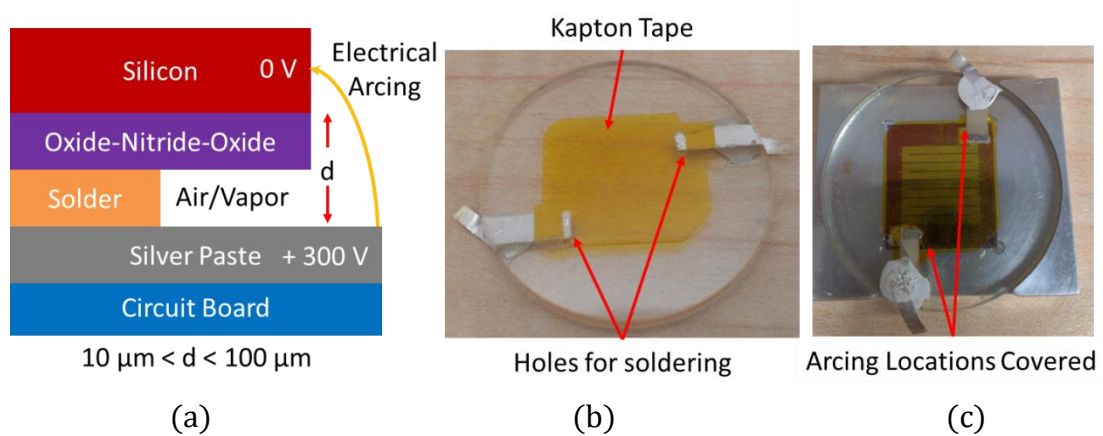


**Fig. 6.1.3: Kapton tape to prevent electrical arcing: (a) suspected arcing location, (b) Kapton tape placement to prevent arcing locations, (c) soldered chip with Kapton tape in soldering alignment tool.**

## 6.2 Experimental Design

The final press-fit experimental design was achieved through numerous iterations of most of the test section parts. The final test section design is shown in Fig. 6.2.1. The test section consists of six basic components:

- (1) the header, which directs the separate liquid and vapor flows,
- (2) the shim, which aligns and houses the manifolds and test chips,
- (3) the manifold, which directs the liquid and vapor flow into the microchannels,
- (4) the test chip with embedded heat sink and thin film platinum RTD-heater, which is the main focus of this work,
- (5) the circuit board, which provides electrical connections to the test chip,
- (6) the lid, which houses the circuit board and provides screw-holes for clamping of assembly.

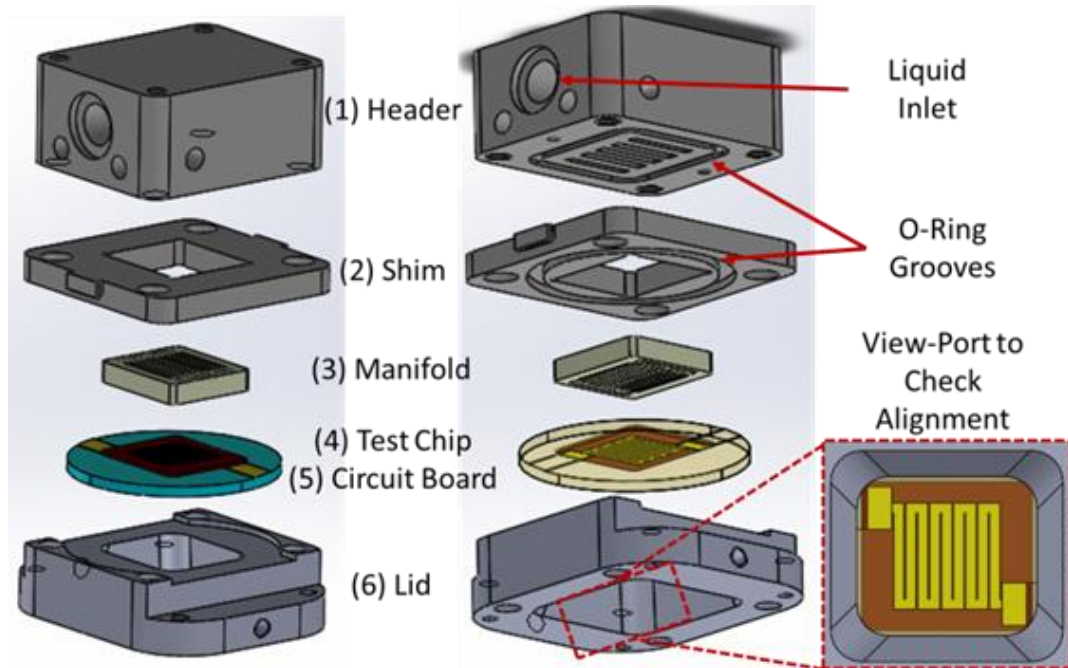


**Fig. 6.2.1: Final test section design for press fit test section.**

The internal flow path through the header and manifold is shown in Fig. 6.2.2. The flow enters the header through 1/4" tubing. It then is routed over to the sides of the manifold (see Fig. 6.2.2(a)), where it enters through small holes on the inlet side of the manifold. The flow then enters the inlet manifold channels and it is fed into the microgrooves, where it evaporates, taking heat with it, and vents vertically to the vapor outlet (see Fig. 6.2.2(b)). This vertical ventilation configuration is a major feature of this manifold and enables large area ( $1 \text{ cm}^2$ ) manifold-microchannels to operate in two-phase flow, as mentioned in the previous chapter.



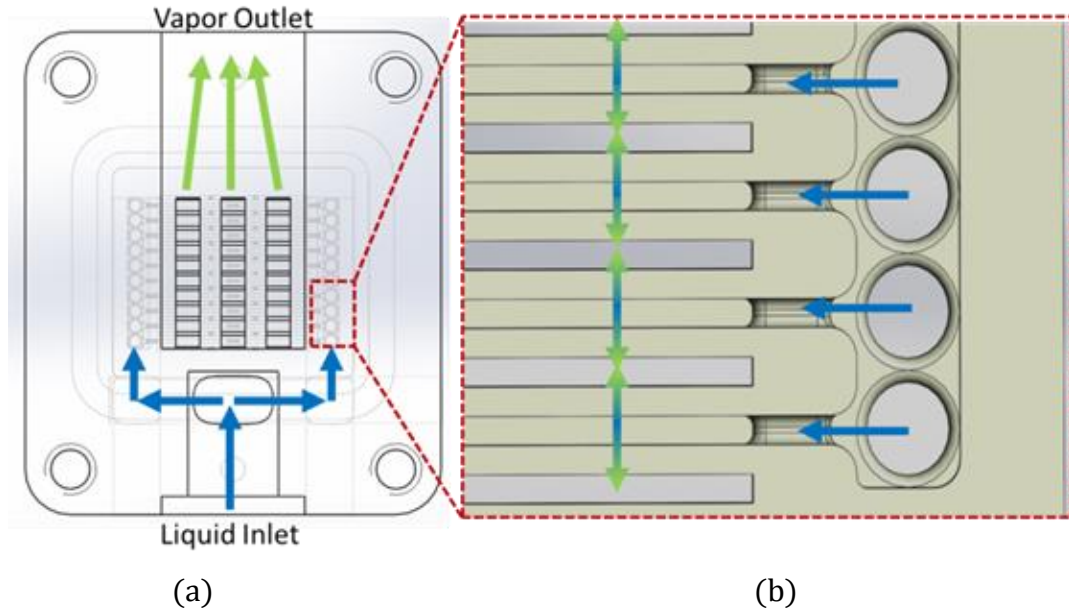


**Fig. 6.2.2: Internal flow path through the (a) header and (b) manifold.**

The header was machined from stainless steel. Internal plumbing was made with drill holes, which were later welded closed (see Fig. 6.2.1). The shim was machined in high-temperature Teflon. The manifold was 3-D printed in alumina. Liquid- and vapor-side braces were needed for additional structural integrity in order to maintain parallel inlet and outlet channels after firing, as shown in Fig. 6.1.1(b). Braces were elongated in the direction of flow (which is different for liquid and vapor side channels) for minimum impact on the flow. As mentioned above, the alumina manifolds were also sent out to a third party for lapping and polishing to achieve 1-micron parallelism and 100-nm surface roughness in order to avoid microscopic gaps between the manifold and heat sink, which could potentially adversely impact system performance. The circuit boards were made in both glass and sapphire, and the metal pattern screen-printed in the laboratory. The lid was machined from aluminum. A gasket was cut from Teflon and placed between the manifold and header to seal the liquid and vapor sides, and to absorb and spread screw-tightening force to prevent the chip, manifold, or circuit board from cracking during

assembly. Viton O-rings were used for sealing and placed in the O-ring grooves (see Fig. 6.2.1).

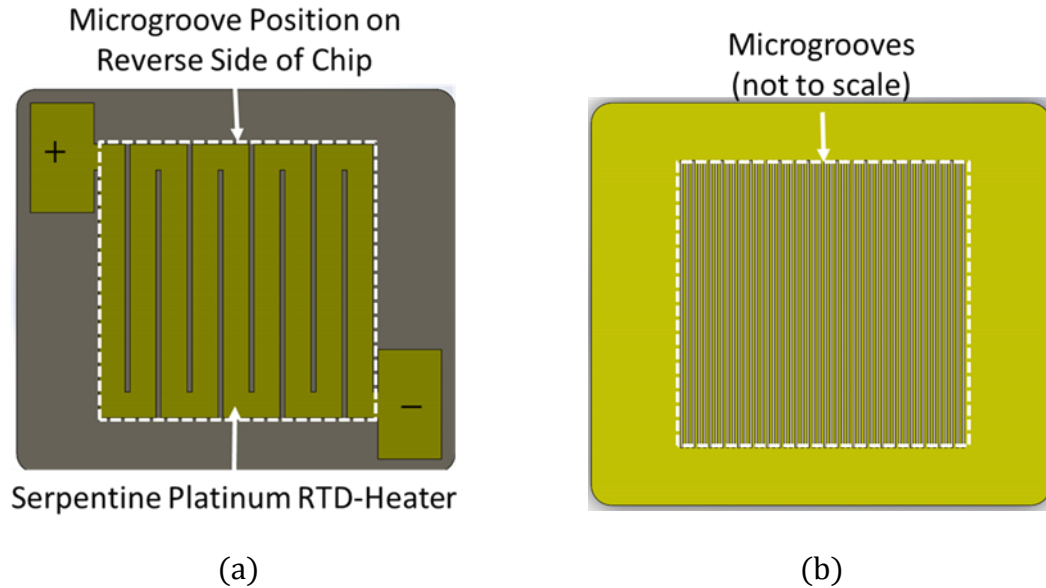


**Fig. 6.2.3: (a) Thin-film platinum RTD-heater and (b) DRIE embedded heat sink.**

The test chips were microfabricated from 0.5 mm-thick silicon wafers. A thin oxide-nitride-oxide stack was deposited on one side of the wafer for enhanced electrical insulation at high temperatures, and consisted of approximately 80% oxide and 20% nitride by volume. A thin-film platinum heater-RTD approximately 400 nm-thick was then deposited onto the oxide, targeting  $50\ \Omega$  at room temperature. A nitride overglass layer approximately 50 nm-thick was deposited over the heater to protect them from the elements and prevent melted solder from wicking onto the heater during soldering. The thin overglass layer covering the contact pads was then removed with a precisely-timed etch. However, it is worth noting that even if a little platinum is removed during the etch step, the presence of a significantly thicker layer of solder—approximately 10-20  $\mu\text{m}$ —will reduce electrical resistance in this area to negligible levels. Finally, microchannels approximately  $10\ \mu\text{m} \times 100\ \mu\text{m}$  in cross section were etched into the other side of the

The diagram illustrates a closed-loop experimental facility. The flow starts at the bottom, passing through a Pump, a Filter, and a Preheater. It then enters a Condenser, where temperature  $T$  is measured at two points. The flow continues to a Test Section, which is connected to a Chiller. A differential pressure sensor ( $\Delta P$ ) is located between the Test Section and the Chiller. The flow returns to the Condenser through a Filter and a Preheater. Various other sensors are indicated: temperature  $T$  at multiple points, pressure  $P$ , and a green arrow indicating a specific flow path.

A diagram of the test loop appears in Fig. 6.2.4. The test loop consists of a pump, a preheater, test section, test section isolation valves, condenser, and particulate filters. Instrumentation includes refrigerant and water-side mass flow rate measurements, absolute and differential pressure measurement on the test section, refrigerant inlet and outlet temperature measurements on the test section, water-side inlet and outlet temperature measurements on the condenser, and voltage drop and current measurements for the RTD temperature measurements. Table 6.2.1 summarizes the instrumentation, as well as the corresponding uncertainties, where applicable.

**Table 6.2.1 Summary of equipment specifications and uncertainties**

<b>Equipment</b>	<b>Specifications</b>	<b>Uncertainty</b>
Refrigerant Coriolis mass flow meter	0-28 g/s	$\pm 0.25$ % FS
Waterside Coriolis mass flow meter	0-555 g/s	$\pm 0.5$ % FS
Absolute pressure transducer	0-100 psia	$\pm 0.25$ % FS
Differential pressure transducer	0-15 psig	$\pm 0.25$ % FS
Pump	0-1760 mL/min, 0-5 V control	n/a
Chiller	2.41 kW	n/a
Power supply	1.2 kW @ 300 V & 4A, 0-5 V control	n/a
Data acquisition system	8 Slot USB Chassis	n/a
Voltage cDAQ card	16ch, $\pm 10$ V, 100 kS/s	$\pm 0.01$ %
Thermocouple cDAQ card	16ch w/ built-in cold junction compensation	$\pm 0.8^{\circ}\text{C}$
Voltage divider resistors	1 & 30 M $\Omega$ , 0.5 W	$\pm 1$ %, 200 ppm/ $^{\circ}\text{C}$
Platinum thin-film RTD Heater	$\sim 62.5$ $\Omega$ , 1 kW @ 4 A	$\pm 1^{\circ}\text{C}$
Current-sense voltage transducer	$\sim 2$ $\Omega$ , 32 W @ 4 A	$\pm 0.01$ % FS

Since the platinum RTD also functions as a heater, the voltages were too large to read directly by the data acquisition (DAQ) card. Accordingly, a voltage divider circuit was used to reduce the voltage from 300 V down to less than 10 V, which could be directly read by the card. The voltage divider circuit is shown in Fig. 6.2.5. To ensure resistive heating and current losses in the voltage divider would be reduced to negligible levels, resistors between 1-30 M $\Omega$  were selected. The voltage divider was calibrated manually by applying a known voltage as an input and measuring the output voltage, in order to eliminate the effects of uncertainty in manufacturer-specified nominal resistance values. Because of the high output impedance of this signal, a simultaneously sampling voltage card was required to prevent signal ghosting. Three 3  $\Omega$ , 120 W resistors were

wired in parallel and served as a  $1\ \Omega$  current-sensing voltage transducer with negligible self-heating effects, as shown in Fig. 6.2.5. Four wire measurements were used for both RTD voltage drop and RTD current-sense measurements to ensure accurate results.

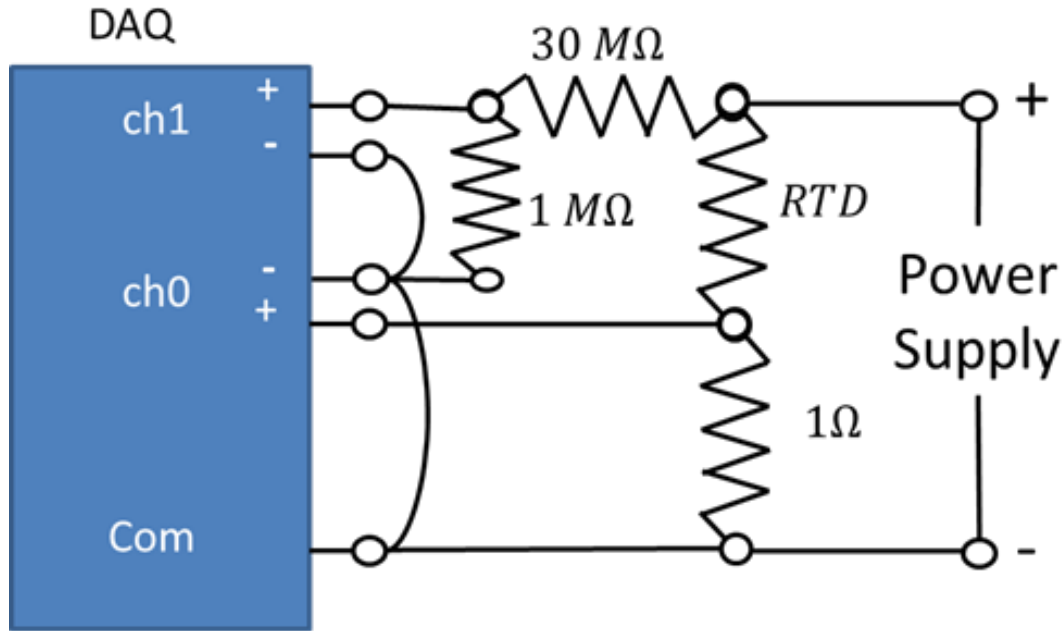


**Fig. 6.2.5: Voltage divider circuit for RTD measurement with DAQ.**

A PID-controlled pump was used to supply the desired flow rates, ranging from 2-12 g/s corresponding to microchannel mass fluxes of 200-1200  $\text{kg/m}^2\text{-s}$ . Chiller temperature was always set to  $30^\circ\text{C}$  as a reference for fluid properties for comparisons to CFD simulations, and to ensure that the condenser was always above room temperature for the two-phase tests. A  $10\ \Omega$  coiled nichrome resistance-heater wire embedded into a Teflon tube served as a preheater. LABVIEW was used for all experimental monitoring, control, and data acquisition.

The RTD-heater power supply was controlled in LABVIEW to ensure the fastest possible reaction time upon reaching critical heat flux. The RTD-heater was controlled in two ways: (1) manually, by adjusting voltage and current limits inputted into the power supply, and (2) PID to maintain the desired set point temperature. Regardless of the

control mode used, RTD temperature was sampled at 100 Hz to determine whether it exceeded the preset temperature limit. Upon exceeding this limit, the power supply voltage and current control signals would be reduced to zero to prevent overheating and damage from critical heat flux. The power supply would then remain off until a reset button was engaged, in order to prevent the control system from automatically reengaging the power upon RTD temperature dropping below the limit.

### **6.3 *Test Chip Soldering and Alignment***

A solder alignment tool was machined out of aluminum to hold and align the chip and circuit board (see Fig. 6.1.3(c)). The test chip is placed in the recess in the center of the tool, and then the circular circuit board is placed into the groove on top of the chip. An Sn3.5Ag eutectic solder (liquidous point of 221°C) paste syringe was used to deposit a controllable and minute amount of solder onto the chip leads. After solder was deposited and a satisfactory alignment was achieved, the solder alignment tool was placed onto a preheated hotplate set to 300°C. Metal tongues were used to apply force to the circuit board to enhance thermal contact and ensure complete solder coverage on the pads. Pressure was applied until there was visual confirmation that the solder had melted, after which the alignment tool was removed from the hot plate and placed on a cold aluminum brick. Pressure was applied to minimize the gap between chip and board. After the solder had frozen, the circuit board was hastily removed from the alignment tool to prevent potential damage to the chip resulting from the board becoming stuck in the tool due to the larger thermal contraction of the aluminum tool compared to the glass circuit board.

## 6.4 *RTD Calibration*

The RTD was calibrated using the same equipment and DAQ system configuration used during testing. The assembled test section was placed on a temperature-controlled hotplate and covered on all sides with high-temperature insulation. The RTD resistance was then calibrated using thermocouples embedded into the test section. A battery was used to apply a 10 mA test current to measure resistance, producing less than 5 mW of power dissipation and resulting in less than 0.1°C of RTD self-heating. All resistance measurements were performed upon RTD resistance and thermocouple temperature reaching steady-state, which was found to take in excess of one hour per sampling point. Three sampling points were taken to assess linearity. The obtained calibration curve is given in Fig. 6.4.1, and was observed to be linear. Uncertainties in RTD temperature from resistance and thermocouple temperature measurement errors total to a maximum of  $\pm 1^\circ\text{C}$ .

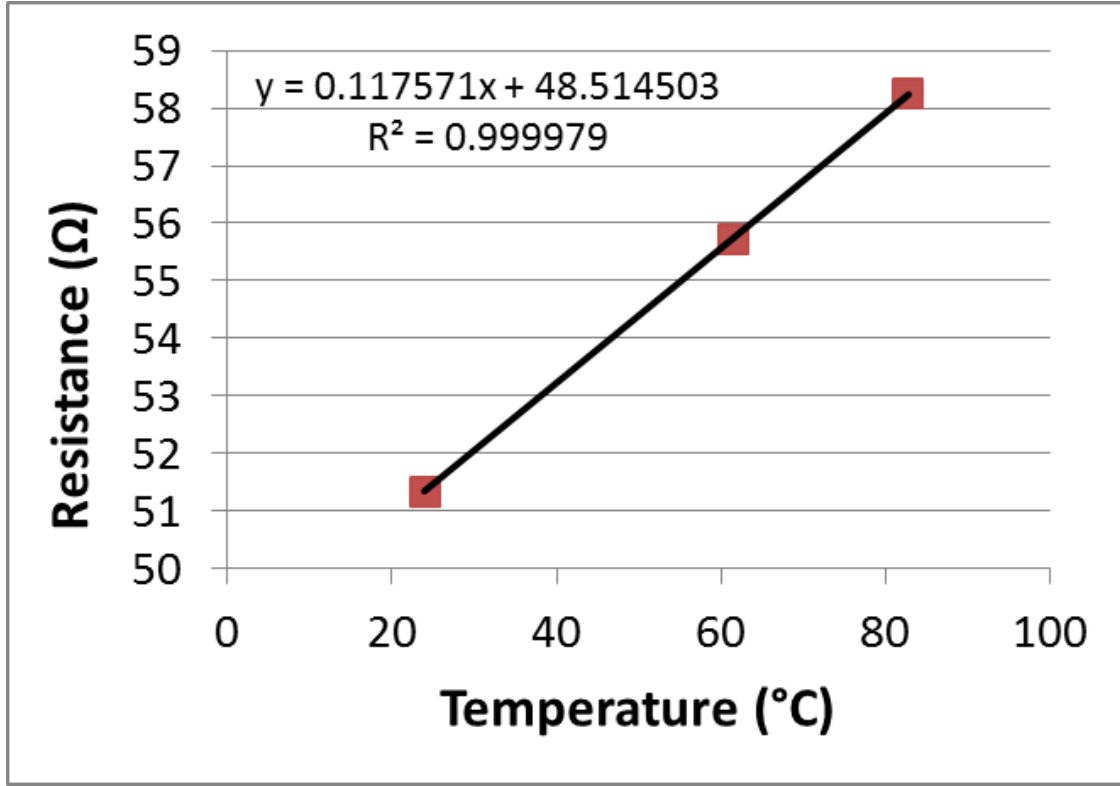


Fig. 6.4.1: RTD calibration curve.

## 6.5 Data Analysis Equations

The heat load is calculated from Ohm's law:

$$q'' = I^2 R_{RTD} / A \quad (6.5.1)$$

where  $A$  is the base area of  $1 \text{ cm}^2$ .

The base superheat is defined as temperature rise above refrigerant saturation temperature:

$$\Delta T_{base} = T_{base} - T_{ref} \quad (6.5.2)$$

where  $T_{base}$  is the RTD temperature and  $T_{ref}$  is a reference temperature. For single-phase tests,  $T_{ref}$  is the fluid inlet temperature; for two-phase tests,  $T_{ref}$  is the saturation temperature and is determined by computing the static pressure of the inlet and outlet of the microchannel and averaging the corresponding saturation temperatures,



$$T_{sat} = \frac{T_{sat}(P_{ch,in}) + T_{sat}(P_{ch,out})}{2} \quad (6.5.3)$$

The static pressure in the inlet of the microchannel is computed using the Bernoulli equation, accounting for the change in area and the pressure loss due to contraction

$$P_{ch,in} = P_1 + \frac{1}{2}\rho_l v_1^2 - \frac{1}{2}\rho_l v_{in}^2(1 + K_c) \quad (6.5.4)$$

where  $P_1$  is the measured static pressure at the inlet of the test section.

The contraction coefficient,  $K_c$ , can be determined from [58]

$$K_c = 0.42(1 - \sigma^2) \quad (6.5.5)$$

$$\sigma = \frac{w_{ch}}{w_{ch} + w_f} \quad (6.5.6)$$

and the velocities,  $v_1$  and  $v_{in}$ , can be determined from mass balance and the appropriate areas

$$v_1 = \frac{\dot{m}_{ref}}{\rho_l A_1} \quad (6.5.7)$$

$$v_{in} = \frac{\dot{m}_{ref}}{\rho_l A_{in}} \quad (6.5.8)$$

$$A_1 = \frac{\pi D_1^2}{4} \quad (6.5.9)$$

$$A_{in} = N_{ch} w_{ch} L_{in} / 2 \quad (6.5.10)$$

$$N_{ch} = \frac{A_{chip}}{(w_{ch} + w_f) L_{ch}} = 10,000 \quad (6.5.11)$$

Similarly, the static pressure in the outlet of the microchannel can be computed as

$$P_{ch,out} = P_2 + \frac{1}{2}\rho_2 v_2^2 + \frac{1}{2}\rho_{out} v_{out}^2 (K_e - 1) \quad (6.5.12)$$

where  $P_2$  is the measured static pressure at the test section outlet,  $\rho_2$  is the density of the two-phase mixture at the outlet of the test section,  $\rho_{out}$  is the two-phase mixture density at the outlet of the microchannel,  $v_2$  and  $v_{out}$  are the appropriate velocities at the outlet of the test section and outlet of the microchannel, respectively, and  $K_e$  is the expansion loss coefficient.

The density of the two-phase mixture at the outlet of the test section,  $\rho_2$ , can be assumed to be homogenous, due to the presence of entrained liquid droplets in the flow:

$$\rho_2 = (1 - \alpha_H)\rho_l + \alpha_H\rho_v = \frac{1}{\frac{1 - X_{out}}{\rho_v} + \frac{X_{out}}{\rho_v}} \quad (6.5.13)$$

where  $\alpha_H$  is the homogenous vapor void fraction given by

$$\alpha_H = \frac{1}{1 + \frac{1 - X_{out}}{X_{out}} \frac{\rho_v}{\rho_l}} \quad (6.5.14)$$

The density of the two-phase mixture at the outlet of the microchannel,  $\rho_{out}$ , can be assumed to be computed from the area-weighted average of the liquid and vapor densities assuming annular flow. For annular flow, the Zivi annular void fraction correlation can be used, and is of the form

$$\alpha_Z = \frac{1}{1 + \frac{1 - X_{out}}{X_{out}} \left(\frac{\rho_v}{\rho_l}\right)^{2/3}} \quad (6.5.15)$$

Accordingly, the two-phase mixture density of the outlet of the microchannel can be computed as

$$\rho_{out} = (1 - \alpha_Z)\rho_l + \alpha_Z\rho_v \quad (6.5.16)$$

The expansion loss coefficient,  $K_e$ , can be computed as [58, 60]

$$K_e = (1 - \sigma)^2 \quad (6.5.17)$$

Finally, the velocities,  $v_2$  and  $v_{out}$ , can be computed using the appropriate areas and densities

$$v_2 = \frac{\dot{m}_{ref}}{\rho_2 A_2} \quad (6.5.18)$$

$$v_{out} = \frac{\dot{m}_{ref}}{\rho_{out} A_{out}} \quad (6.5.19)$$

$$A_2 = \frac{\pi D_2^2}{4} \quad (6.5.20)$$

$$A_{out} = N_{ch} w_{ch} L_{out} / 2 \quad (6.5.21)$$

The base heat transfer coefficient (HTC) is defined as

$$h_{base} = q'' / \Delta T_{base} \quad (6.5.22)$$

The fin heat transfer coefficient (HTC) is defined by removing the thermal conductances of the oxide-nitride-oxide layer thickness,  $t_{SiO_2}$ , and silicon substrate height,  $h_b$ , as

$$h_{fin} = \left( \frac{1}{h_{base}} - \frac{t_{SiO_2}}{k_{SiO_2}} - \frac{h_b}{k_{Si}} \right)^{-1} \quad (6.5.23)$$

The wall heat transfer coefficient can be computed from the fin heat transfer coefficient using the fin efficiency equations:

$$h_{wall} = h_{fin} \frac{w_{ch} + w_f}{2 \zeta h_f} \quad (6.5.24)$$

$$\zeta = \frac{\tanh(m h_f)}{m h_f} \quad (6.5.25)$$

$$m = \sqrt{\frac{2 h_{wall}}{k_{Si} w_f}} \quad (6.5.26)$$

The temperature dependence of thermal conductivity of silicon was accounted for by assuming the following relationship [61]:

$$k_{Si} = a_0 \left( \frac{a_1}{273.15 + T} \right)^n \quad (6.5.27)$$

where  $a_0 = 152$  [W/m-K],  $a_1 = 298$ , and  $n = 1.334$ , and  $T$  is in °C. The values for the constants  $a_0$ ,  $a_1$ , and  $n$  were taken from [61] and validated using the EES material property database [59] to within less than 1%. The thermal resistance of the nitride layer was neglected, due to its relatively thinner length and significantly higher thermal conductivity.

Finally, thermodynamic outlet vapor quality is calculated from

$$X_{out} = \frac{q'' - \dot{m}_{ref} C_{p,l} \Delta T_{sub}}{\dot{m}_{ref} h_{lv}} \quad (6.5.28)$$

where the sub-cooling,  $\Delta T_{sub}$ , is defined as temperature difference between saturation and inlet

$$\Delta T_{sub} = T_{sat} - T_{in} \quad (6.5.29)$$

## 6.6 Uncertainty Propagation

All data analysis was conducted in Matlab, using a custom script to load each test data file, temporally average the values in the data file, propagate errors using finite differences, and conveniently plot the results. Uncertainty was propagated using the standard formula for 95% confidence

$$\begin{aligned}
\Delta U_1 &= \sqrt{\left(\frac{\partial U_1}{\partial x_1} \Delta x_1\right)^2 + \left(\frac{\partial U_1}{\partial x_2} \Delta x_2\right)^2 + \cdots + \left(\frac{\partial U_1}{\partial x_n} \Delta x_i\right)^2} \\
\Delta U_2 &= \sqrt{\left(\frac{\partial U_2}{\partial x_1} \Delta x_1\right)^2 + \left(\frac{\partial U_2}{\partial x_2} \Delta x_2\right)^2 + \cdots + \left(\frac{\partial U_2}{\partial x_n} \Delta x_i\right)^2} \\
&\quad \dots \\
\Delta U_j &= \sqrt{\left(\frac{\partial U_j}{\partial x_1} \Delta x_1\right)^2 + \left(\frac{\partial U_j}{\partial x_2} \Delta x_2\right)^2 + \cdots + \left(\frac{\partial U_j}{\partial x_n} \Delta x_i\right)^2}
\end{aligned} \tag{6.6.1}$$

where  $U_j$  is a value calculated from one of the above equations for which uncertainty propagation is desired—for example, Eqs. (6.5.1)-(6.5.29)—and  $x_i$  is a measured variable with a given uncertainty—for example,  $R_{RTD}$ ,  $I$ ,  $T_{RTD}$ ,  $T_{in}$ ,  $P_1$ ,  $P_2$ , and  $\dot{m}_{ref}$ .

To obtain the partial derivatives, finite differences were used. For instance, to obtain the uncertainty in  $q''$ , Eq. (6.5.1) was evaluated using the nominal values of  $R_{RTD}$  and  $I$ . Then, the uncertainty in  $R_{RTD}$  was added to the nominal value, and Eq. (6.5.1) was evaluated again. The partial derivative was then evaluated as

$$\frac{\partial q''}{\partial R_{RTD}} = \frac{q''(R_{RTD} + \Delta R_{RTD}) - q''(R_{RTD})}{\Delta R_{RTD}} \tag{6.6.2}$$

This process was then repeated for every measured variable with uncertainty—even those not appearing in Eq. (6.5.1)—in order to make the uncertainty propagating program robust and easily upgradable, so that it requires no explicit knowledge of how a formula is computed in order to propagate errors on it. It is worth noting that if a measured variable does not appear in the formula, the difference in the value of the formula will be zero, yielding a partial derivative of zero as well, as expected. The total uncertainty in  $q''$

was then evaluated using Eq. (6.6.1). This process was then repeated for each formula for which propagation of errors is desired—for example, Eqs. (6.5.2)-(6.5.29).

In general, the finite difference takes the form,

$$\frac{\partial U_j}{\partial x_i} = \frac{U_j(x_i + \Delta x_i) - U_j(x_i)}{\Delta x_i} \quad (6.6.3)$$

where  $i$  is an index that cycles between measured variables with uncertainty, and  $j$  is an index that cycles between calculated parameters for which uncertainty must be propagated. Thus,  $\frac{\partial U_j}{\partial x_i}$  is a 2-D matrix and  $\Delta U_j$  is a 1-D vector. The uncertainty in  $U_j$  can be written compactly using index notation as

$$\Delta U_j = \sqrt{\left(\frac{\partial U_j}{\partial x_i} \Delta x_i\right)^2} \quad (6.6.4)$$

where  $x_i x_i$  implies  $\sum_i x_i x_i$ .

## 6.7 SEM Images of the Microchannels and Manifold

In order to have an accurate geometry to compare to CFD, SEM images and measurements of the chip and manifold dimensions were taken. The SEM images are shown in Fig. 6.7.1, and Table 6.7.1 compares the nominal, measured, and simulated values for the microchannel and manifold dimensions.

When viewed in cross-section (see Fig. 6.7.1(b)), the microchannels were observed to be wider towards the top ( $\sim 12 \mu\text{m}$ ), and narrower at the bottom ( $\sim 6 \mu\text{m}$ ). Due to the cubic dependence of pressure drop on channel width for a given mass flow rate, most of the flow will remain in the wider portion of the channel. Thus, the effective hydrodynamic and thermal channel width will be larger than that computed using the

arithmetic average. Nevertheless, the arithmetic average value of 9  $\mu\text{m}$  was used for simulation purposes, keeping in mind that the effective channel width—and therefore measured pressure drop—should be lower than predicted with this channel width. However, it is worth noting that a diluted effect on heat transfer coefficient is expected, due to the presence of additional thermal resistances between the heat source and heat sink, and the effective heat transfer coefficient is expected to reduce less-than-linearly.

**Table 6.7.1 Comparison between nominal and actual values for microchannel and manifold dimensions of the press-fit test section**

Dimension [Variable]	Nominal [ $\mu\text{m}$ ]	Measured [ $\mu\text{m}$ ]	Simulated [ $\mu\text{m}$ ]
Microchannel width [ $w_{\text{ch}}$ ]	10	9	9
Microchannel fin width [ $w_{\text{f}}$ ]	10	11	11
Microchannel fin height [ $h_{\text{f}}$ ]	100	105	105
Substrate base thickness [ $h_{\text{b}}$ ]	400	405	405
Manifold Inlet [ $L_{\text{in}}$ ]	250	284	300
Manifold Wall [ $L_{\text{man}}$ ]	250	234	225
Manifold Outlet [ $L_{\text{out}}$ ]	250	296	300
Manifold Length [ $L_{\text{ch}}$ ]	500	524	525

Similarly, the arithmetic average value of 11  $\mu\text{m}$  for fin thickness was also used.

As shown in Fig. 6.7.1(b)-(c), the measured fin height was 105  $\mu\text{m}$ , which is close to the 100  $\mu\text{m}$  nominal value. Finally, the substrate thickness was measured to be 405  $\mu\text{m}$ , which is also exceedingly close to the nominal value of 400  $\mu\text{m}$ , as shown in Fig. 6.7.1(c).

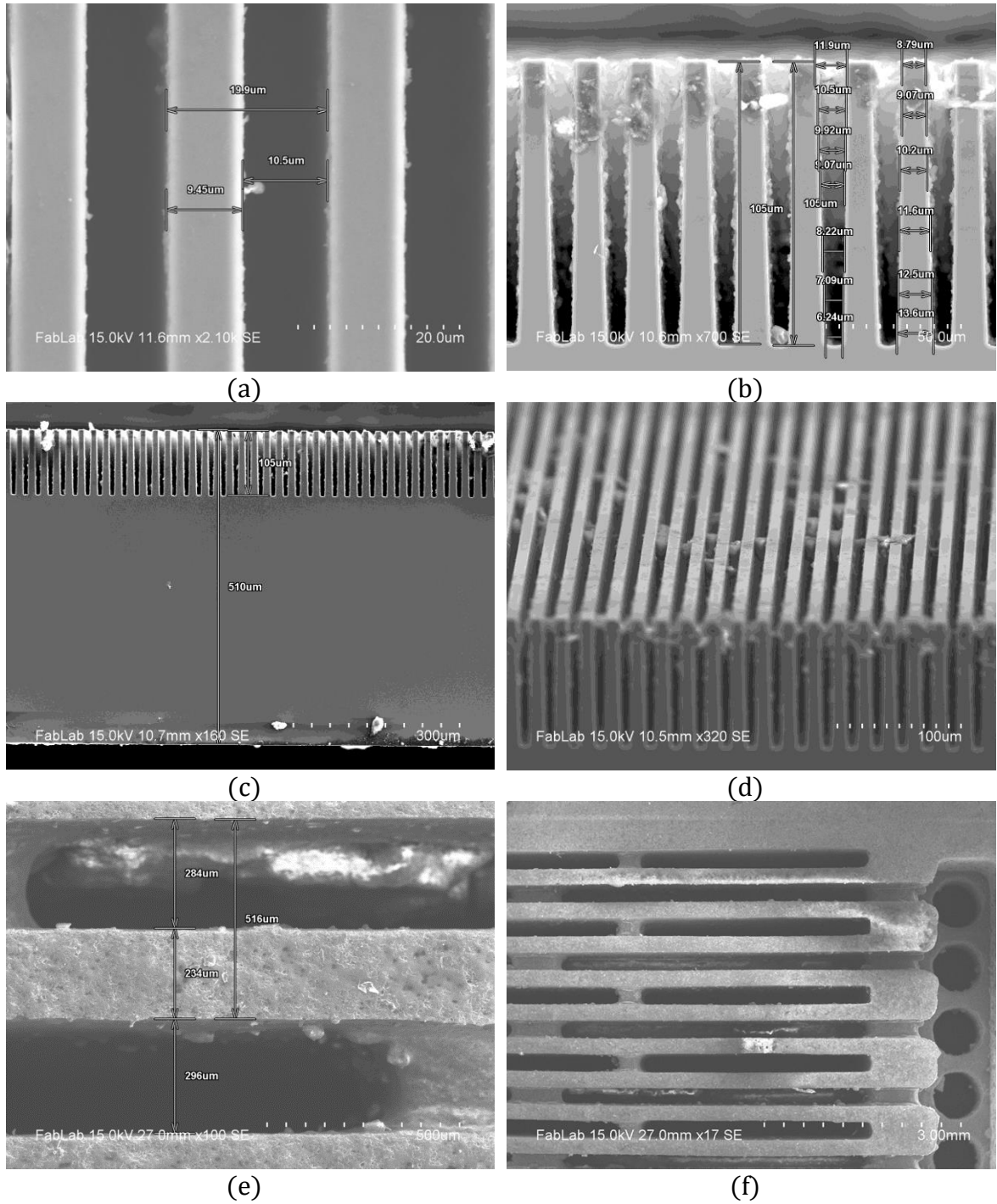


**Fig. 6.7.1: SEM images of (a) microchannels, (b) cross-section of microchannels, (c) cross-section view of substrate, (d) angled view of microchannels with particulate clogging (e) manifold, and (f) manifold far view.**

The manifold dimensions were also measured, and are shown in Fig. 6.7.1(e)-(f).

While the channels are observed to be relative smooth, straight and parallel, some



deviations from nominal dimensions were observed. Both the inlets and outlets were observed to be wider than nominal by 14-18%, while the manifold wall was observed to be approximately 6% shorter. Thus, the pitch of the manifold was observed to be larger than the nominal value by only 3-5%. The manifold dimensions used for simulation are given in Table 6.7.1.

## **6.8 *Single-Phase Test Results***

After the RTD was calibrated and the manifold and microchannel surface was characterized with SEM, the assembled test section was placed into the loop, evacuated of air, and charged with R245fa. Due to the use of a custom-made RTD as a heater and the use of a voltage divider circuit to scale the RTD voltage down to a value readable to the card, it was desirable to validate system performance by comparing it to some known metric. Since single-phase CFD is much simpler and more accurate to perform using commercial software, single-phase tests were conducted before two-phase tests in order to compare pressure drop and heat transfer coefficient to CFD to validate system performance.

Single-phase operation was achieved by constricting the valve on the outlet-side of the test section, thereby increasing the pressure in the test section (see Fig. 6.2.4). The valve was constricted until the pressure in the test section was high enough such that the saturation temperature was higher than the RTD. Doing so ensures no phase-change occurs, and the flow remains single-phase. Since the pressure drop and RTD temperature depends on the refrigerant flow rate, the constriction of the valve was adjusted manually for each flow rate.

First, pressure drop measurements were taken without any heat flux for refrigerant flow rates ranging from 2-12 g/s. These pressure drop measurements are directly comparable to the CFD simulations performed. Then, a heat flux of  $50 \text{ W/cm}^2$  was applied to the RTD-heater, and the refrigerant flow rate was varied from 4-12 g/s. Due to an inability to maintain single-phase operation, 2 g/s could not be tested under  $50 \text{ W/cm}^2$  heat flux. Although pressure drop measurements were also recorded for this case, due to the effect of changing fluid properties with temperature, the pressure drop measurements were lower than the adiabatic value, and are not directly comparable to CFD, which assumes constant fluid properties.

The single-phase results are given in Fig. 6.8.1. The pressure drop measurements are observed to be approximately 75% higher than CFD predicts, while the heat transfer coefficient were approximately 33% lower. This is qualitatively consistent with particulate clogging. Particulate clogging is a possibility, as a second filter immediately before the test section was not installed in the loop (see Fig. 6.2.4). Accordingly, after two-phase tests were conducted and repeated, heat transfer and pressure drop measurements were observed to change.

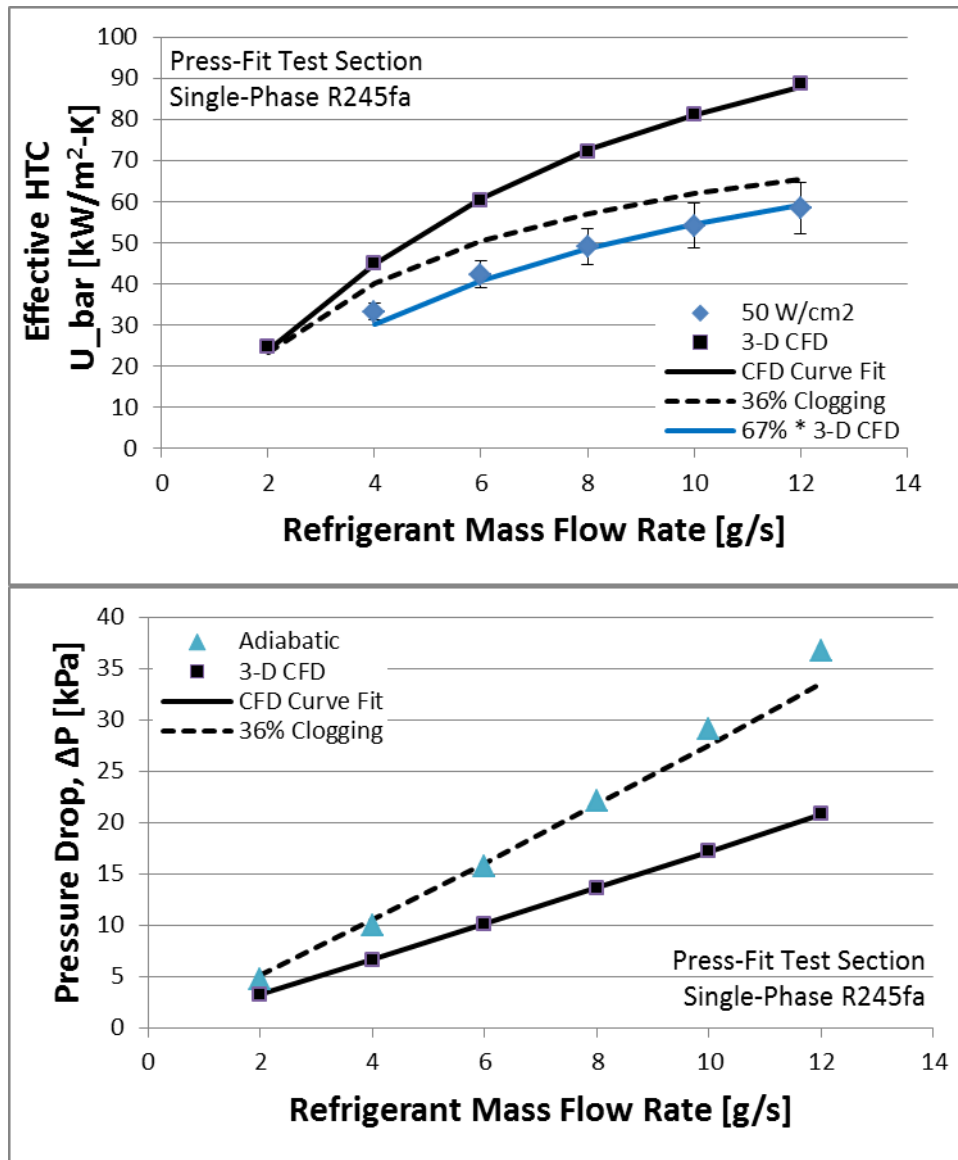


**Fig. 6.8.1: Single-phase test results for press-fit test section before cleaning.**

Therefore, a one-micron particulate filter was installed immediately before the test section, and the test section was opened, cleaned from particulates, and re-installed. Pressure drop and heat transfer coefficient measurements were taken again and are shown in Fig. 6.8.2.

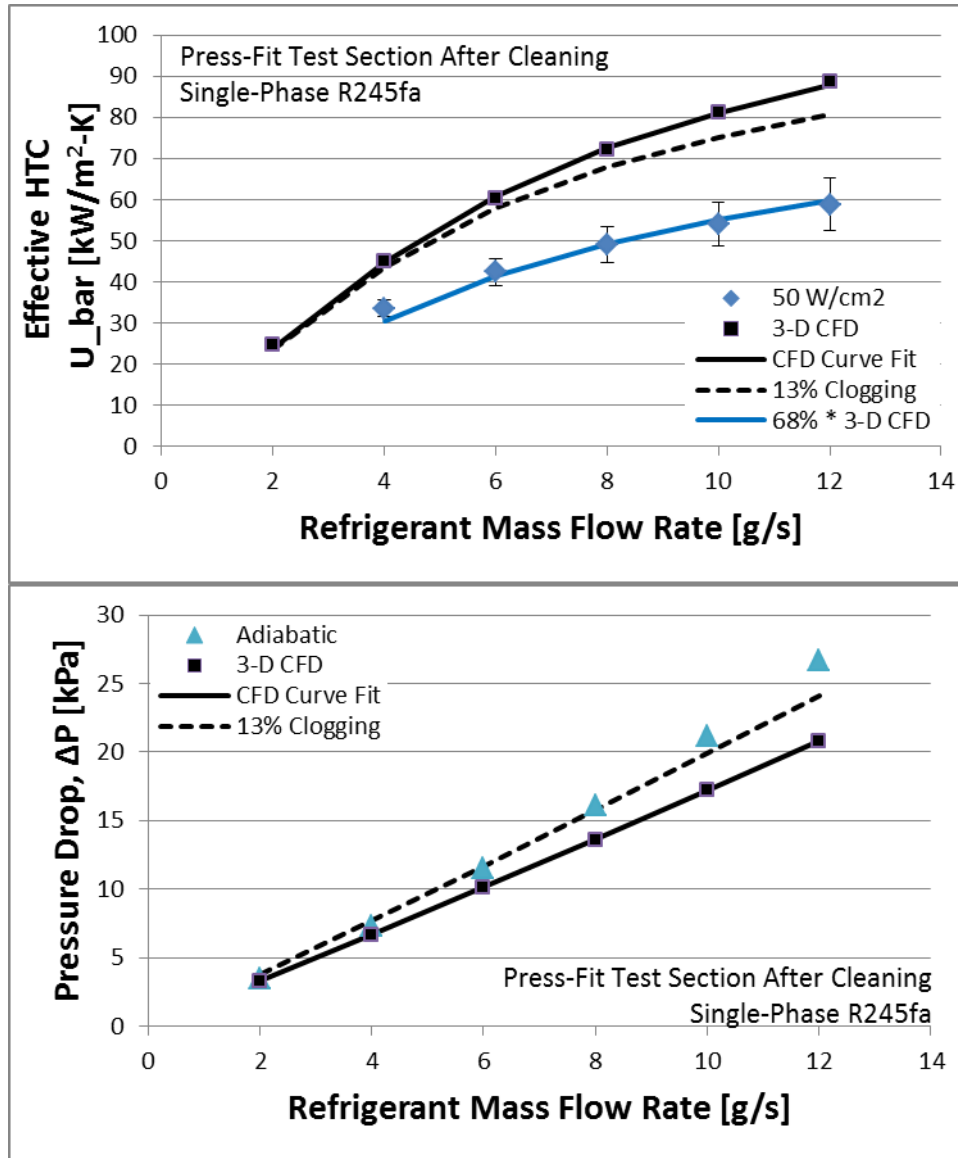


**Fig. 6.8.2: Single-phase test results for press-fit test section after cleaning.**

It is observed that while pressure drop measurements decreased from 75% to 33% higher than CFD, heat transfer coefficient remained relatively constant. Thus, while particulate clogging might explain the increased pressure drop, the removed particles did not significantly affect heat transfer. This is possible if the clogging is uniform and located on the tips of the microchannels in the inlet manifold. Under these circumstances, as long as the channel entrances are not completely blocked, the clogging acts only to increase pressure drop with only a small effect on heat transfer. In fact, upon opening the

test section, particles were observed to collect on the tips of the fins on the inlet-side of the manifold, as shown in Fig. 6.8.3(a)-(b). These are the particles that were removed upon cleaning. However, upon examination with a microscope, particles were still observed to be embedded inside the microchannels, and could not be removed, as shown in Fig. 6.8.3(c)-(d).

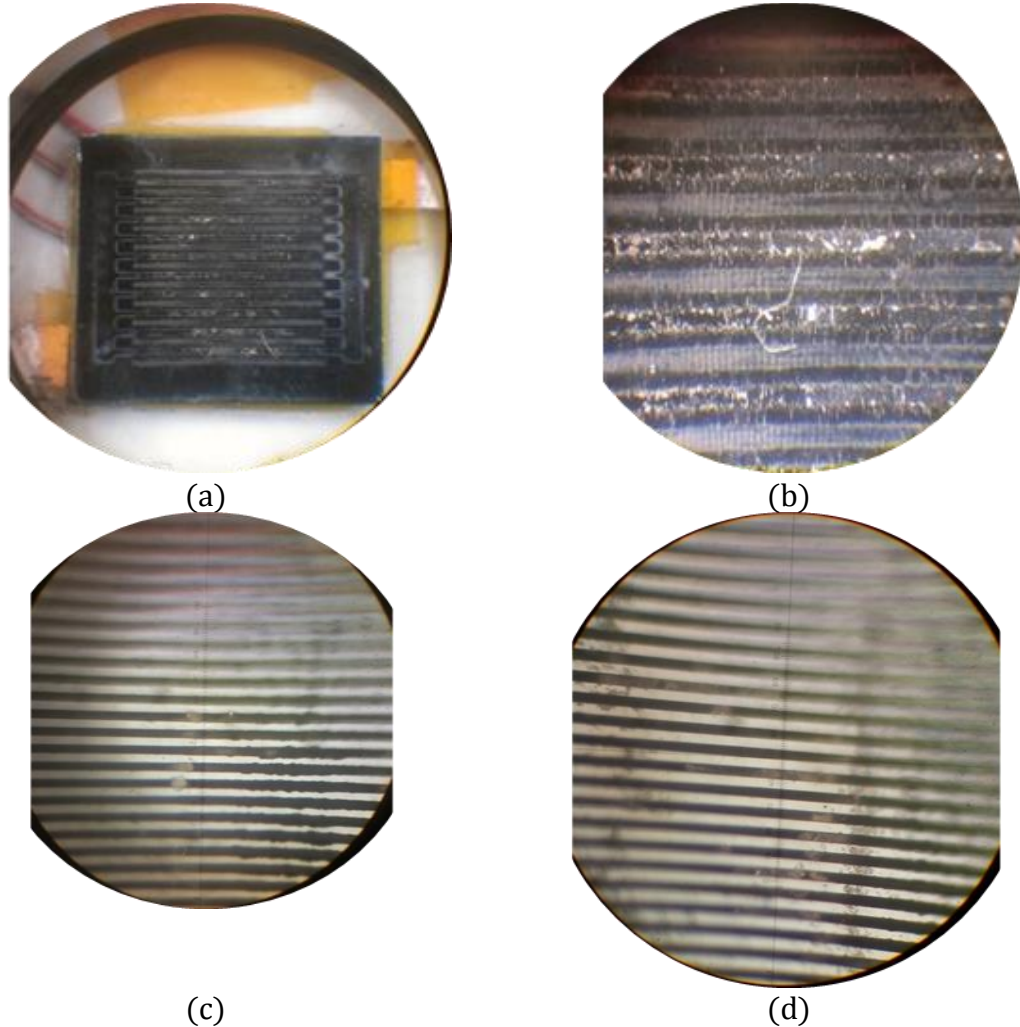


**Fig. 6.8.3: Particle accumulation after opening up press-fit test section: (a)-(b) on tips of channels in manifold inlet region and (c)-(d) embedded into microchannels.**

Thus, the remaining 42% pressure drop increase and heat transfer reduction could be due to these embedded particles. It is worth noting that due to the tapered nature of the microchannels, the pressure drop was expected to be below the CFD prediction, as

described in Section 6.7; however, from the fact that pressure drop was still observed to be larger than the CFD prediction, it is possible that the amount of clogging is underestimated.

In order to quantitatively estimate the effect of particulate clogging, a simple analysis was conducted. If the percentage of clogged channels,  $\omega$ , is known, the effective increase in mass flow rate (per area) can be calculated from:

$$\dot{m}'_{ref} = \frac{\dot{m}_{ref}}{1 - \omega} \quad (6.8.1)$$

The new expected pressure drop for the chip at this new mass flow rate can then be computed using a quadratic curve fitted to the CFD predictions; that is,

$$\Delta P' = a_0 \dot{m}'_{ref} + a_1 \dot{m}'_{ref}^2 \quad (6.8.2)$$

where  $a_0$  and  $a_1$  are parameters obtained from the curve fit.

Similarly, the thermal performance for clogged channels can be estimated using the effective mass flow rate and the known relationship between mass flow rate and heat transfer coefficient from 3-D CFD. The form of this curve-fit is derived from the analytical solution from the  $\varepsilon - NTU$  method for flow over an isothermal surface. The curve-fit is of the form,

$$h_{base} = a_2 \dot{m}'_{ref} \left( 1 - \exp \left( - \frac{a_3}{\dot{m}'_{ref}} \right) \right) \quad (6.8.3)$$

However, because only a fraction of the area is actively engaged in heat transfer, the effective base heat transfer coefficient must be reduced by this fraction:

$$h'_{base} = (1 - \omega) h_{base} \quad (6.8.4)$$

Using Eqs. (6.8.1)-(6.8.2) to match the experimental pressure drop measurements, the clogging fraction was estimated to be 36% before cleaning and 13% after cleaning, as

shown in Fig. 6.8.1 and Fig. 6.8.2, respectively. Clogging fraction was estimated by minimizing the sum of the percent errors between the experimental pressure drop measurements and the predictions. Then, Eqs. (6.8.3)-(6.8.4) can be used to predict the resulting heat transfer coefficient. As shown in Fig. 6.8.1, before cleaning, clogging is capable of explaining a majority of the reduced heat transfer coefficient. However, after cleaning, this analysis suggests that clogging cannot reduce heat transfer coefficient down to the values obtained experimentally, as shown in Fig. 6.8.2. Accordingly, clogging alone cannot explain the reduced performance.

Therefore, it was assumed that other effect(s) was/were at least partially responsible for the reduced heat transfer coefficient. One possible explanation is that the tapered microchannels encourage more flow to pass through the regions of the microchannel with wider cross-section. This, in turn, reduces the effective area involved in heat transfer, and, due to the increased width, increases the thermal resistance between the wall and fluid. Given that the channel width reduces by a factor of two from the tip of the microchannel to the bottom, the flow rate may differ by a factor of eight, resulting in reduced performance.

## 6.9 Two-Phase Test Results

After single-phase testing, two-phase testing commenced. Pressure drop and base temperature measurements were performed at four different mass flow rates—3, 6, 9, and 12 g/s—and heat flux increased until surface temperature approached 100°C. For all tests, chiller temperature was held close to 30°C, and an inlet sub-cooling of less than 5°C was maintained for consistency. All tests were conducted twice to assess repeatability.

Stable operation at heat fluxes in excess of 1 kW/cm<sup>2</sup> was obtained at outlet qualities near 45% and pressure drops below 90 kPa, as shown in Fig. 6.9.1. For all tested mass fluxes, heat flux and pressure drop measurements appear repeatable between sets to within the experimental uncertainty for the vast majority of data points. However, it is worth noting that temperature and heat transfer coefficient data for the highest mass flow rate of set 1 are missing, due to electrical problems, which caused an error in the RTD reading. Accordingly, for the highest mass flow rate (12 kg/s), only set 2 data are shown.

Referring to Fig. 6.9.1(a), it is observed that for low heat fluxes, a higher mass flow rate will require a higher superheat for the same heat flux. This is intuitive, since a higher mass flow rate will be operating at a lower outlet vapor quality for the same heat flux, and therefore, heat transfer coefficient will be lower. As heat flux increases, vapor quality increases, and heat transfer coefficient increases as a result, as shown in Fig. 6.9.1(b)-(d). However, similar to Cetegen [10] and others [41], an optimal vapor quality was found, at which increases to vapor quality resulted in reduced heat transfer coefficient. Thus, each heat flux will have an optimal flow rate that would produce a maximum heat transfer coefficient. However, because optimal vapor quality varies with heat transfer coefficient, the optimal mass flow rate cannot easily be predicted.



Nevertheless, because the optimal vapor quality is observed to decrease with increasing mass flow rate, linear interpolation or extrapolation can be used to obtain the optimal flow rate.

Furthermore, unlike previous experimental two-phase results where optimal vapor qualities were between 10-20% [10] or 2.5-12.5% [41], in the present work, optimal vapor qualities were found to be between 30-50%. This is due to the increased ratio of microchannel flow length relative to the height of the fin: when the microchannel flow length is significantly larger than the height of the fin—in the present work the ratio is 5—the manifold-microchannel system becomes closer to a straight microchannel, which tends to have optimal vapor qualities in excess of 75% [3].

In addition, comparing Fig. 6.9.1(c) and (d), it is apparent that the Si substrate conductance and the oxide-nitride-oxide dielectric barrier present a significant barrier to heat transfer, and base heat transfer coefficient is significantly limited by substrate conduction and oxide layer thickness. Nevertheless, fin heat transfer coefficients in excess of  $300 \text{ kW/m}^2\text{-K}$  are possible at heat fluxes exceeding  $850 \text{ W/cm}^2$ . In addition, at a heat flux of  $1 \text{ kW/cm}^2$ , a fin heat transfer coefficient in excess of  $260 \text{ kW/m}^2\text{-K}$  was obtained at 40% outlet vapor quality, highlighting the potential of FEEDS. In contrast, at  $1 \text{ kW/cm}^2$  heat flux, Cetegen et al. [10] obtained heat transfer coefficients on the order of  $190 \text{ kW/m}^2\text{-K}$  and vapor qualities below 20%.

Referring to Fig. 6.9.1(c)-(d), it is apparent that an increase in mass flow rate results in an increase in heat transfer coefficient at the same vapor quality. This is partially due to an increase in superheat, which leads to an increase in nucleate boiling heat transfer coefficient (see Eq. (3.2.7)) [46]. However, from the annular film

evaporation with physics-based void fraction model, an increase in mass flow rate results in a shift from the annular, fully developed void fraction correlation—which predicts a thicker film—to the Zivi annular void fraction correlation—which predicts a thinner film. Accordingly, an increase in mass flow rate could be reducing average film thickness and thereby, increase heat transfer coefficient.

Finally, referring to Fig. 6.9.1(e), it is clear that at the same vapor quality, a higher mass flow rate will have a higher pressure drop. This is intuitive, since pressure drop is proportional to velocity. However, referring to Fig. 6.9.1(f), it is observed that under certain circumstances, at the same heat flux, a lower flow rate has a higher pressure drop. The explanation is that for the same heat flux, a lower flow rate will be operating at a higher quality. As vapor quality increases, the fraction of the channel that is wetted decreases, and the wall may be periodically wetted and dried out. A steep change in slope is observed for these cases. It is thought that the steep change in slope is due to some of the channels entering unstable regions where the channel wets and dries out, increasing average pressure drop. Accordingly, when this occurs, it is possible that a lower flow rate will produce a higher pressure drop at the same heat flux.

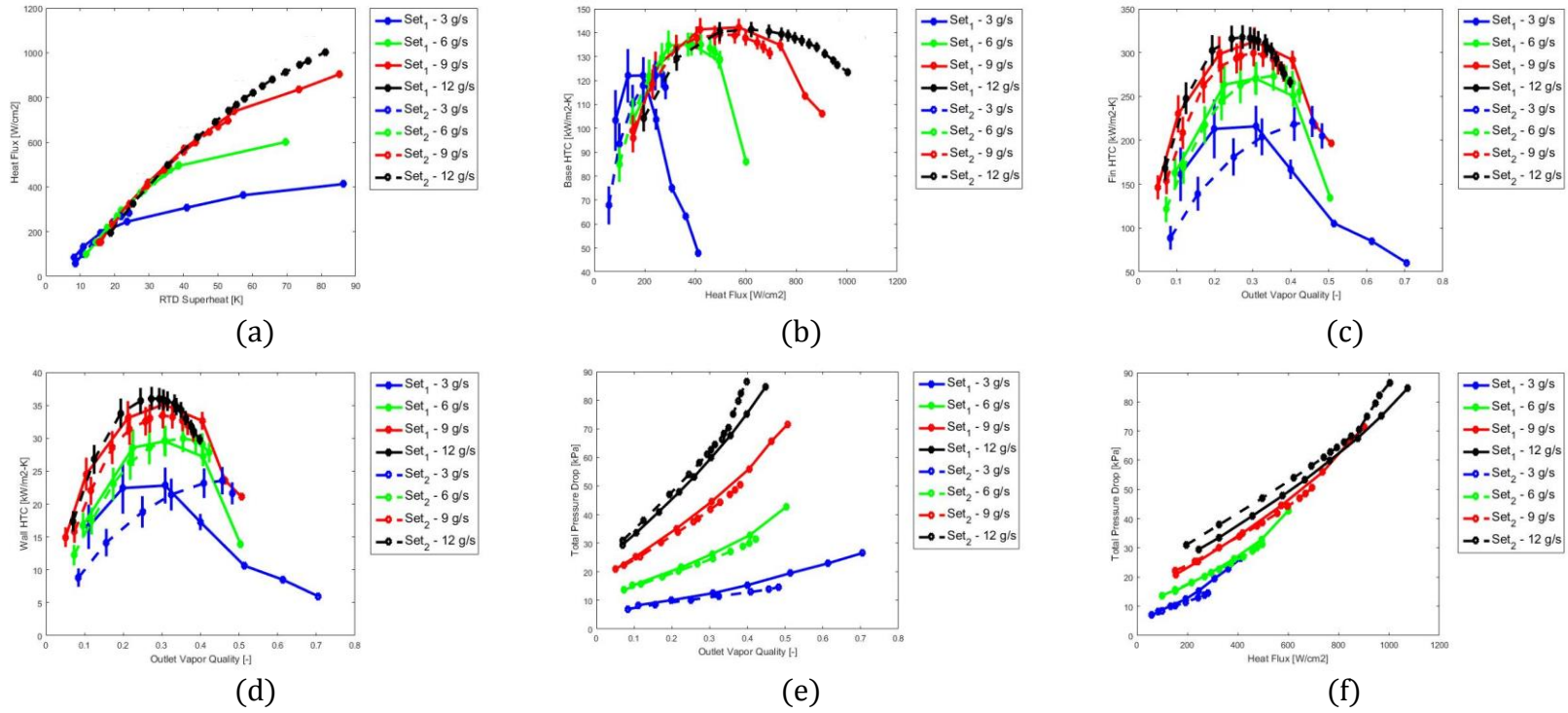
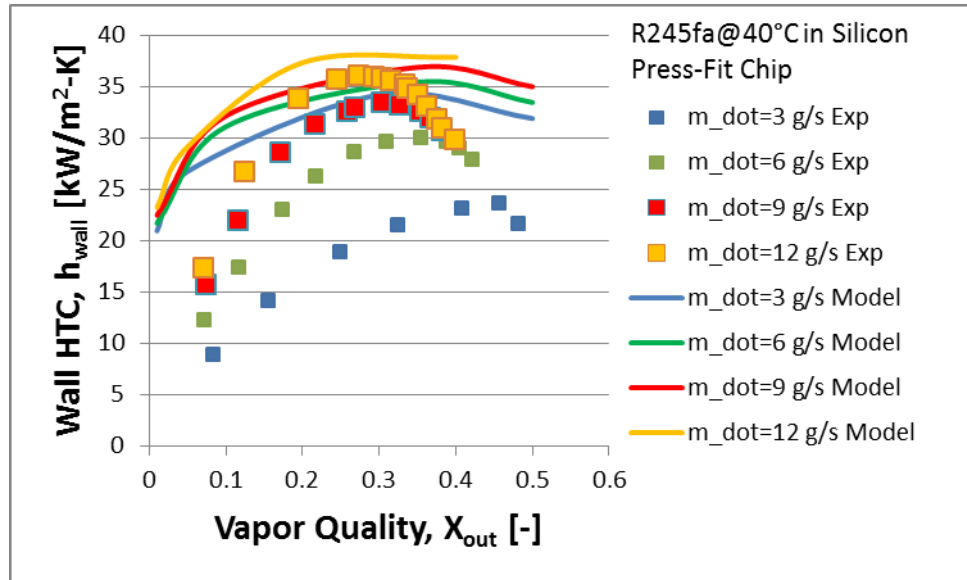


**Fig. 6.9.1: Two-phase test results: (a) heat flux vs. RTD superheat; (b) base heat transfer coefficient vs. heat flux; (c) fin heat transfer coefficient vs. outlet vapor quality; (d) wall heat transfer coefficient vs. outlet vapor quality; (e) total pressure drop vs. outlet vapor quality; (f) total pressure drop vs. heat flux.**

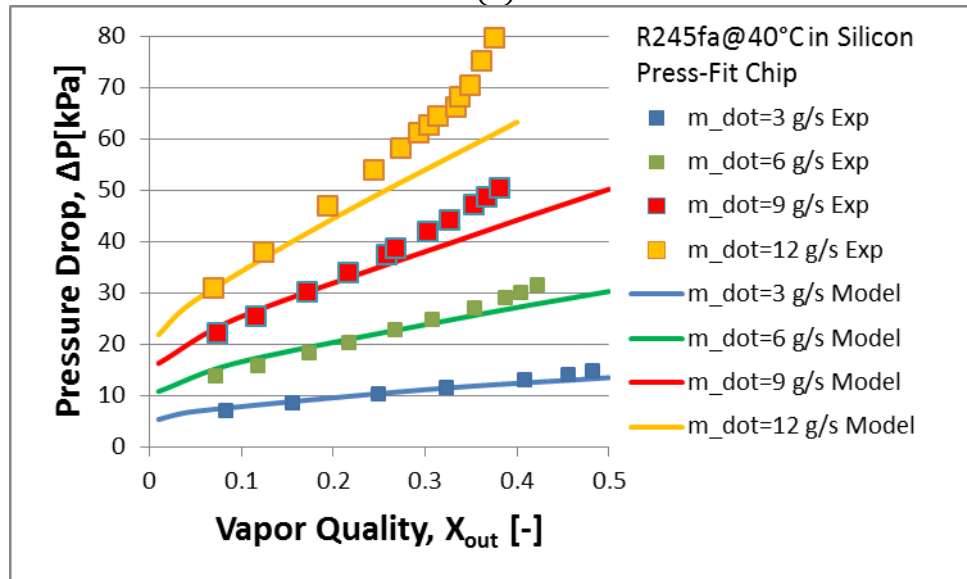
## **6.10 Comparison to Model**

The 2.5-D microchannel model was then compared to the experimental data obtained here. The physics options used are similar to those used to compare to the data in Cetegen et al. [10], except that, based on the result of the annular film evaporation with physics-based void fraction model, the fully developed annular void fraction correlation was used to calculate film thickness instead of the Zivi annular void fraction correlation. The comparison is presented in Fig. 6.10.1.

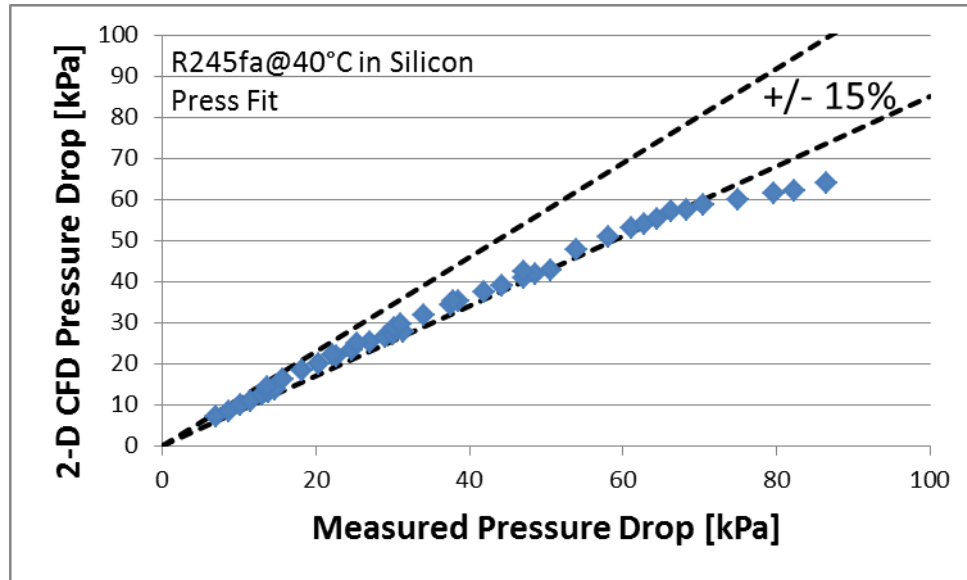
As before, the wall heat transfer predictions are the correct order of magnitude, and unlike correlations in the literature, follow the correct trends, predicting an optimum vapor quality to maximize wall heat transfer coefficient. However, the predictions are less sensitive to mass flow rate than experiments suggest, and overestimate heat transfer coefficients. However, this is somewhat expected, due to the tapered cross-section, which encourages more flow where the microchannel is wider, thereby, yielding reduced heat transfer coefficients. Pressure drop measurements, on the other hand, are more accurate, with most of the data points falling within 15% of the values predicted by the model (see Fig. 6.10.1(c)). However, while the tapered cross-section of the microchannels should lead to reduced pressure drop, the presence of 13% clogging in single-phase mode acts to increase pressure drop, which could at least partially cancel out this effect. Thus, good agreement between model and experiment is obtained.



(a)



(b)



(c)

**Fig. 6.10.1:** Comparison between model and experimental results obtained here: (a) wall heat transfer coefficient vs. vapor quality, (b) pressure drop vs. vapor quality, and (c) comparison between predicted and measured pressure drop.

### **6.11 *Press-Fit FEEDS Summary***

In summary, a press-fit FEEDS, embedded two-phase cooled experiment was designed, fabricated, and tested. Numerous experimental challenges were resolved, and a working chip capable of achieving in excess of  $1 \text{ kW/cm}^2$  was obtained at 45% vapor quality despite the presence of clogging in some of the microchannels. In addition, experiment was compared to model, with qualitative and quantitative agreement for heat transfer coefficient, and excellent agreement for pressure drop to within 15%.

## 7 Bonded FEEDS Experiments

Despite the success of the modular test section at achieving heat fluxes in excess of  $1\text{kW}/\text{cm}^2$ , a few concerns remained. First, the thermal performance was sensitive to alignment and possible movement of the manifold with respect to the chip, and the press-fit apparatus is not a suitable design for a real-world application as a final thermal demonstration vehicle (TDV). Second, gaskets must be used to seal the inlet and outlet of the manifold and the manifold to the test section header; if this is done improperly during test-section assembly, flow leakage or flow blockage will occur, possibly creating flow bypass zones or flow distribution problems, reducing flow to the microchannels. Finally, despite the chip and manifold both being flat to a tolerance of less than a micron, after soldering the chip to the circuit board, up to a six-micron bow deflecting away from the manifold (towards the circuit board) was measured on some chips using the P-1 Long Scan Profilometer. This bow creates a gap between the Si chip and manifold, which is on the same order as the size of the microchannels; accordingly, a significant amount of flow might be diverted over the channels, rather than through them, and could contribute to reduced thermal performance (see Fig. 6.1.2(b)). To resolve this issue, intimate contact between the manifold and chip must be ensured. One such way to guarantee intimate contact is by bonding the chip directly to the manifold, and a new test section was designed for direct bonding to the chip.

### 7.1 *Header-Manifold*

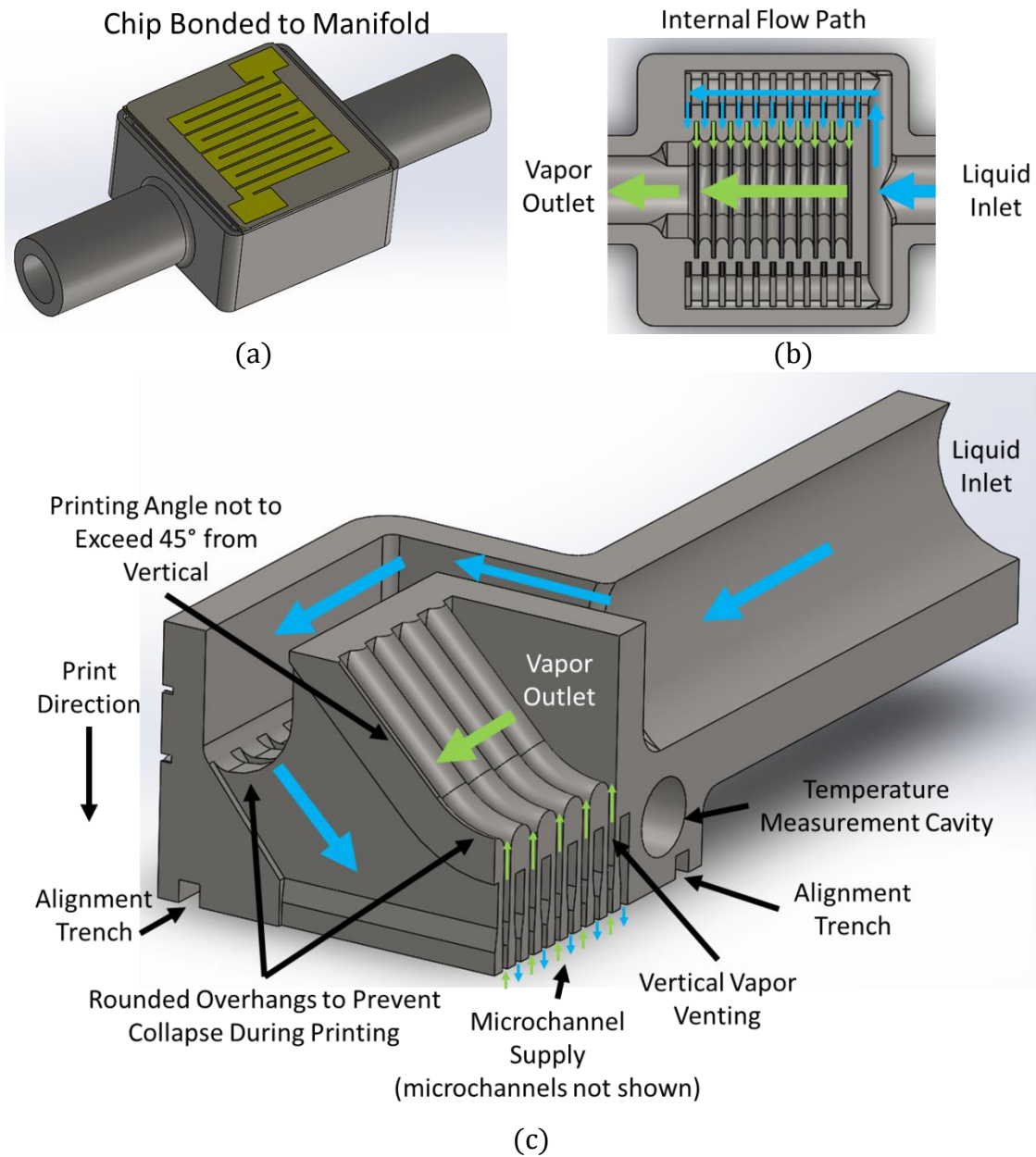
A new test section was designed to alleviate these problems by bonding a monolithic header-manifold (see Fig. 7.1.1(a)) directly to the chip. The liquid flow



entered from one side (right), where it was diverted around the perimeter to the liquid inlet channels (see Fig. 7.1.1(b)). The flow then passed through the microchannels (not shown) and was collected by the vapor outlet channels. Finally, the vapor outlet channels were collected into one main channel that vents the vapor flow from the other side (left). To ensure that an even flow distribution was maintained, the same manifold dimensions from the press-fit test section were used. However, due to the increased flow area (see Fig. 7.1.1(c)), the flow distribution should only be improved in the press-fit design. Nevertheless, flow distribution was simulated separately in the inlet and outlet regions using laminar single-phase liquid and vapor flow, respectively, for the highest expected mass flow. Since pressure drops in the inlet and outlet regions were found to be orders of magnitude lower than the pressure drop in the microchannels, it was safe to assume an even flow distribution would be obtained.

The header-manifold was 3-D printed as one monolithic structure to eliminate the potential for flow leakage points between manifold and header. Careful attention was paid to print orientation and design—ensuring rounded overhangs and slopes not exceeding  $45^\circ$  from the vertical—to prevent horizontal overhangs which would collapse (see Fig. 7.1.1(d)). The print material was selected to be Ti64 alloy for two main reasons: it has low thermal conductivity and its coefficient of thermal expansion (CTE) is the closest possible match to Si. The bonding of the header-manifold directly to the chip significantly improves the thermal contact, and drastically increases the potential for boiling to occur in the manifold, which could wreak havoc on flow distribution. Therefore, a low thermal conductivity material was desirable to prevent and/or limit the amount of boiling that can occur. In addition, close CTE was desirable to minimize

residual stresses on the chip after bonding to the header-manifold. The design also takes advantage of 3-D printing technology to increase the internal flow area for the liquid inlets to further improve flow distribution and range of possible flow rates. Finally, the design reduces the size and footprint of the test section down to the same size as the chip itself, thereby enabling use of such a device in real-world applications.



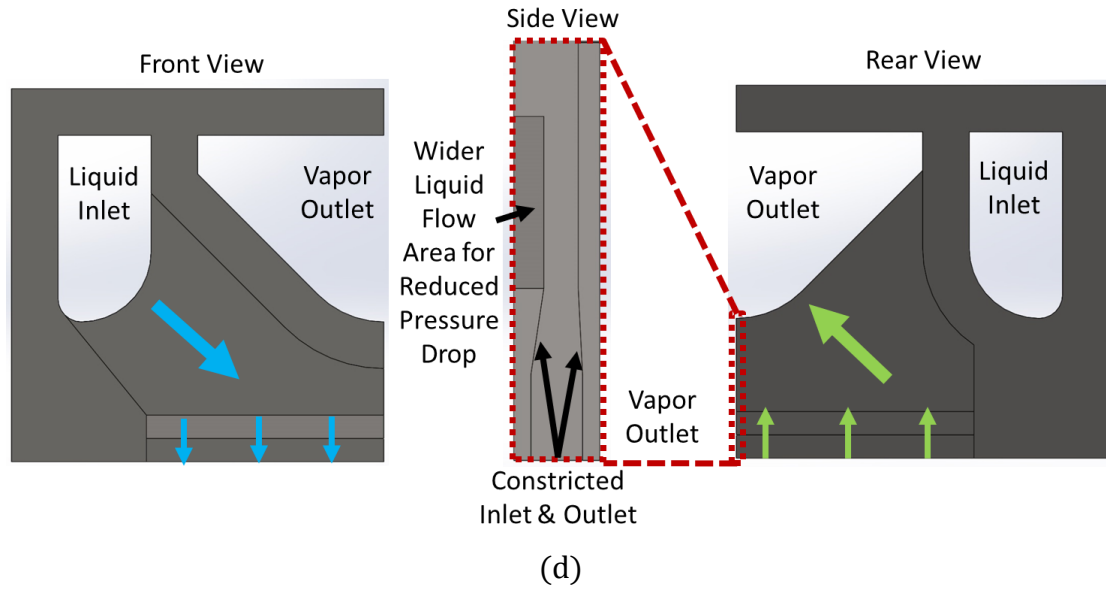


**Fig. 7.1.1: CAD drawing of header-manifold test section: (a) chip bonded to header-manifold, (b) internal flow cavities and path, (c) sectioned isometric view, and (d) manifold unit-cell pattern.**

Despite the advantages of the new header-manifold, some challenges remained. First, titanium is a difficult material to metallize and solder to, due to its rapidly forming native oxide layer when exposed to air at room temperature. Second, due to the presence of small microchannels, the layer thickness and total volume of the solders must be reduced as much as possible, to avoid the potential for clogging the microchannels upon solder melting. Third, because of the reduced solder constraint, the flatness of the manifold must be on par with that of the Si/SiC chip and significantly less than the expected solder thickness, in order to achieve a uniform bond and hermetic seal.

## **7.2 Solder Selection & Metalization**

First, the solder composition had to be selected. Three solder formulations are common in the literature for die bonding—Au-In [62, 63], Au-Sn [27] and Ag-Sn [25, 64]. Ag-Sn solder was selected primarily due to the reduced cost: eutectic Au-Sn solder

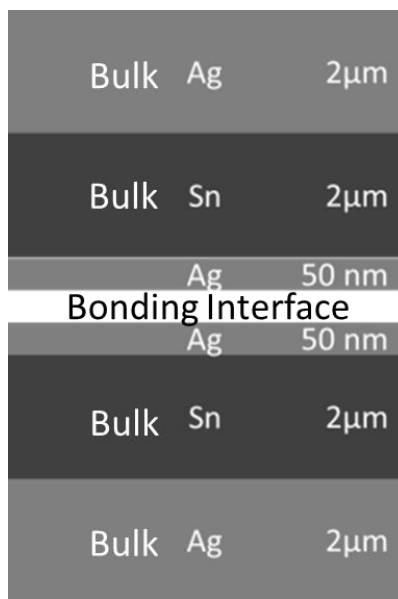
(80%Au20%Sn) would be too expensive to sputter using the available equipment, due to the inherent bow of the 3-D printed manifolds (2-4  $\mu\text{m}$ ) and subsequent thickness of solder required to obtain a hermetic bond. An Ag-Sn solder composition similar to that used by Kermani et al. [25] was used instead.

The solder deposition (metalization) process began by loading the desired components—Si chips, Si wafers, or manifolds—into the AJA sputtering machine. Then, a 10-minute reverse sputter was performed to remove the native oxide layer from the Ti manifolds, ensuring proper wetting onto the metal. A thin, 20 nm-thick Ti adhesion layer was then sputtered to allow adhesion of solders onto the Si surface, followed by a 100 nm-thick Ni layer to serve as a diffusion barrier and a 2  $\mu\text{m}$  bulk layer of Ag to serve as solder. The wafers were then removed from the sputtering machine, as the Ag layer would protect the Ti from oxidation. The chips, wafers and/or manifolds were then loaded into the Angstrom evaporator, where a 2  $\mu\text{m}$ -thick layer of Sn was applied, followed by a 50 nm-thick passivation layer of Ag. The passivation layer served to protect the Sn from oxidation upon exposure to air. The Angstrom evaporator was used to evaporate Sn due to the slow sputtering rates of Sn. For all cases, solder was applied to both the chip and the manifold.

While Sn melts at 232°C, bonding at this temperature is not possible since the interface will remain solid due to the presence of the 50 nm-thick silver passivation layer (see Fig. 7.2.1(a)). To successfully bond, the liquidous point of the interface must be reached. The liquidous point of the interface can be estimated by assuming that upon reaching the melting point of Sn, Ag begins dissolving into the Sn bulk at equal rates from the passivation layer and from the Ag bulk. The computed atomic fraction is 93%

Sn, 7% Ag (see Fig. 7.2.1(b)), corresponding to a liquidous point of 280°C (see Fig. 7.2.1(c)). Accordingly, for this solder composition, 280°C is the minimum possible bonding temperature.

It is worth noting that the liquidous point for the entire mixture is significantly higher. Computing the atomic mass fraction results in a mixture of 40% Sn, resulting in a mixture liquidous point of approximately 550°C (see Fig. 7.2.1(c)). Thus, to fully melt and alloy the sputtered metals, a temperature in excess of 550°C must be reached. Temperatures lower than this limit will result in a liquid layer of Sn-Ag near the interface, and an un-melted, un-mixed silver layer.



(a)

- Bonding Interface must be liquid for bond to form
- Assume dissolution rate equal in both directions
- Need to reach liquidous point of interface (280°C) for bond to form
- Liquidous point of mixture is significantly higher (550°C)



(b)

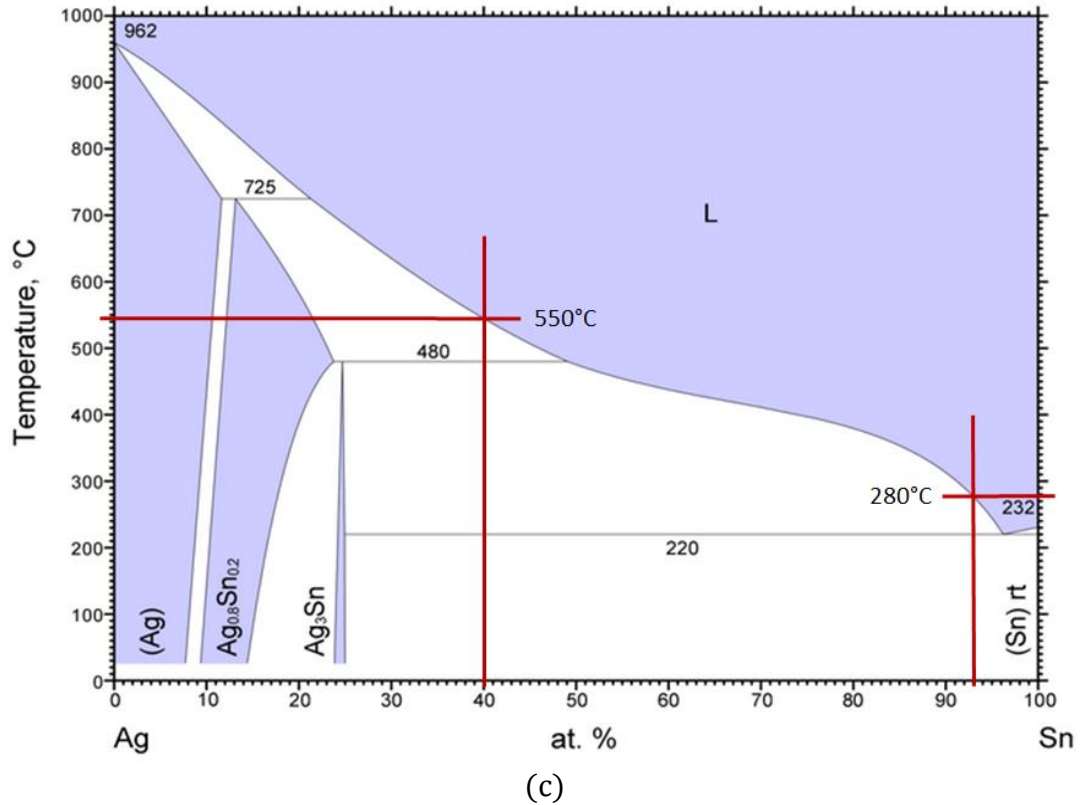


**Fig. 7.2.1: (a) Solder layer thicknesses, (b) solder atomic composition, and (c) Ag-Sn phase diagram [65].**

SEM images of a sample chip after solder was deposited in this way are given in Fig. 7.2.2. The solder before bonding is given in Fig. 7.2.2(a), while the solder after being heated to 600°C in a controlled environment is given in Fig. 7.2.2(b). The surface after solder deposition was observed to be very rough, and could require higher-than-ideal bonding temperatures in order to melt a smooth layer and achieve a hermetic seal. Upon reaching the liquidous point, the solder was observed to coalesce via surface tension forces to minimize surface area. Solder also coalesced on the sidewalls of the channels, indicating some solder was deposited on the side walls, which could constrict flow and increase pressure drop.

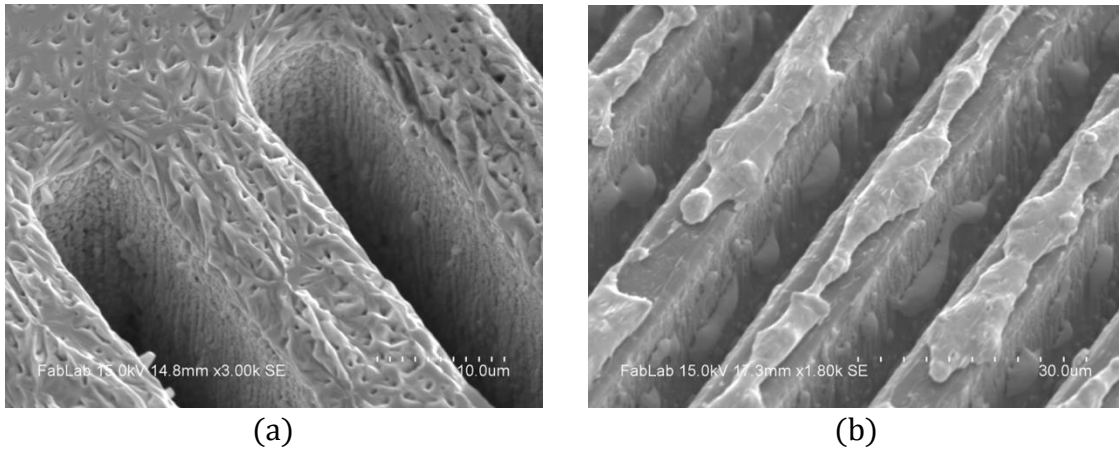


**Fig. 7.2.2: SEM images of a working chip with solder on it: (a) before bonding and (b) after heating to 600°C in controlled environment.**

### ***7.3 Preliminary Si-Si Bonding Work***

With the solder selected, the next step was to establish a bonding mechanism and recipe. However, rather than immediately begin by bonding header-manifolds to working chips, silicon blank pieces were first bonded to each other to establish a working bonding technique. Once a bonding technique was established and repeated, silicon blanks were then bonded to working manifolds, and only once those bonds were satisfactory were working silicon chips bonded to manifolds.

To find the proper technique with the selected solder, numerous heating methods, clamping mechanisms, and bond testing apparatuses were tested and evaluated, but these will not be detailed here. Table 7.3.1 provides a summary of the bonding methods that were evaluated. In the end, a hotplate in open atmosphere with manual clamping force and a razor wedge to test bond strength and uniformity were found to be sufficient.

**Table 7.3.1: Summary of tested heating methods, clamping mechanisms, and bond-testing apparatuses and methods**

Heating Method	Clamping Mechanism	Bond Testing Apparatus
Air furnace	Differential CTE clamp	Light-weight shear tester
Vacuum furnace	Spring clamp	Heavy-duty shear tester
Reducing-gas furnace	Weights	Razor wedge
Hotplate	Manual force	Microscope

With the bonding, clamping, and testing methods determined, the next step was to determine the range of bonding parameters—such as ramp rate, peak temperature, and clamping pressure—needed to obtain a uniform and strong bond. It is worth noting that minimum ramp rate, peak temperature and clamping pressures were desirable to reduce thermal stresses, cooldown stresses, and potential for solder clogging the channels, respectively.

While the minimum bonding temperature was computed to be 280°C, testing with silicon blanks indicated that a temperature of 400°C was required to obtain a strong and uniform bond. This is likely due to an inability to apply uniform clamping pressure and the rough surface present after solder deposition (see Fig. 7.2.2); a higher temperature therefore works by melting more of the solder, resulting in a thicker conformal layer. Accordingly, 400°C was used as a lower limit for peak temperature for future bonding tests. In addition, it is worth noting that bonding temperatures in excess of 550°C were found to form brittle bonds, due to the complete dissolution of the Ag bulk by the Sn, resulting in the dissolution of the Ni and Ti layers and causing delamination from the silicon chip. Accordingly, 550°C was used as an upper limit for bonding temperatures.

Finally, the effect of clamping pressure was also studied. Standard wafer bonders could not be used for this work, due to the need to bond to 3-D printed parts, which have high roughness, high unevenness, and poor tolerance on overall height, compared to Si



wafers, and would potentially result in a non-uniform bond and damage to the tool. Thus, a custom approach was needed.

While clamping was applied manually for the silicon blank tests, more repeatable and controllable clamping mechanisms were needed. For bonding of header-manifolds to silicon chips, the internal tubing of the manifold can be utilized to clamp the chip to the manifold by applying a vacuum to the manifold. This approach has numerous advantages over the manual application of force: (1) the force is repeatable; (2) the force is uniform; (3) the force is conformal and will cause the chip to deform around a rounded manifold; (4) oxygen is removed from contact with the molten metals, preventing oxidation. Preliminary tests indicated promising results, and so a new bonding apparatus was designed and built to obtain more controllable bonding parameters.

## **7.4 *Bonding Apparatus***

Following the promising results from the preliminary bonding experiments, a new enclosed bonding apparatus was designed to use nitrogen to apply clamping pressure during bonding. There are many advantages of this apparatus over other means:

- (1) The enclosed environment allows supply of neutral environment (nitrogen) or reducing gas supply, to prevent or reverse oxidation, respectively.
- (2) The enclosed environment allows for pressures below and in excess of 1 atm.
- (3) Clamping pressures are controllable and repeatable.
- (4) Gas pressure provides uniform and conformal clamping pressure on the Si chip, allowing it to conform around an unlapped header-manifold (see Fig. 7.4.1).

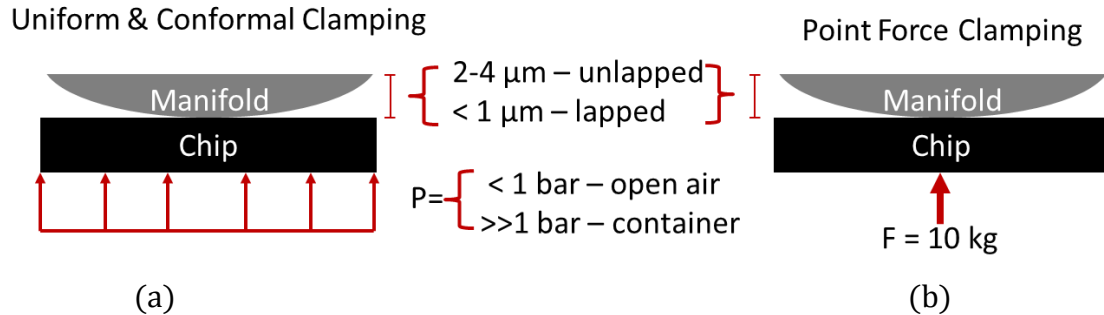
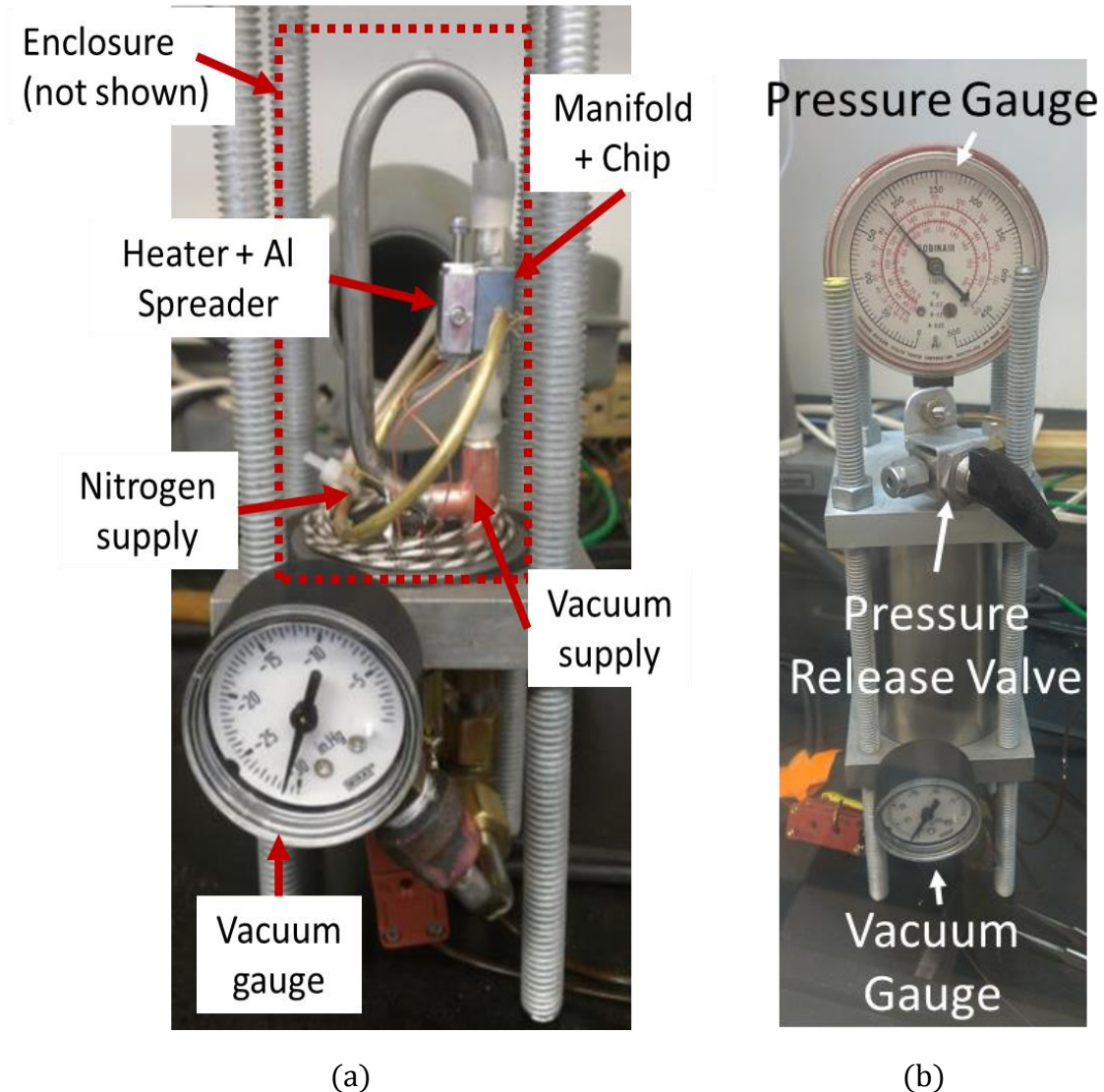


**Fig. 7.4.1: Advantages of uniform clamping pressure: (a) over point force clamping pressure; (b) uniform clamping pressure allows chip to conform around rounded manifold for hermetic bond without need for advanced lapping techniques.**

The bonding apparatus is shown in Fig. 7.4.2. The manifold is attached to a vacuum supply. A second supply releases nitrogen to pressurize the chamber before bonding and rapidly cool the manifold after bonding is complete. An aluminum spreader with an embedded cartridge heater is tied tightly to the manifold and used to heat the manifold to the desired temperature. Three thermocouples—one on the heater, one on the manifold, and one on the chip—are used to measure temperatures during bonding. A vacuum gauge and enclosure pressure gauge are used to assess vacuum strength and enclosure pressure. Power is controlled to the cartridge heater manually via an AC variac power supply.



(a) (b)  
**Fig. 7.4.2: Bonding apparatus: (a) opened and (b) assembled.**

To bond a chip to a manifold, first the chip and manifold were cleaned with nitrogen gun to remove any settled dust particles or Si fragments created during wafer dicing. Then, the heat spreader was tied tightly to the manifold, and the manifold connected to the vacuum supply in the bonding apparatus. Finally, the chip was placed onto the manifold and visually aligned using the trench printed into the manifold for this purpose (see Fig. 7.1.1(c)). The vacuum was then engaged to lock the chip in place during further handling. The thermocouples were attached, and the enclosure was sealed and pressurized to the desired pressure. Low-power ramp tests were first conducted to

ensure thermocouples did not become dislodged during apparatus assembly. Full power was then applied to heat the chip. Upon reaching the desired temperature, the power to the heater was immediately reduced to zero, and the pressure release valve (see Fig. 7.4.2(b)) was opened to allow room temperature nitrogen to convectively cool the manifold.

The bonding apparatus was first tested at elevated clamping pressures, since it was thought that larger clamping pressures were needed to ensure intimate contact between the two soldering surfaces. In particular clamping pressures between 100-300 psig and a peak temperature of 400°C were tested. It was found that those bonded manifolds either failed a routine pressure test well below 75 psig or leaked profusely when submerged underwater. Upon analyzing a whole chip in a microscope and profilometer, 21 microscopic solder bumps were observed (see Fig. 7.4.3), corresponding to the sum of the number of inlets and outlets. In addition, the bumps on the periphery were found to be ten times taller than the sum of the solder layer thicknesses. Accordingly, it was assumed that the high ambient pressure was pushing the semi-molten solder, causing the solder to flow out of the bonding area into the vacant inlets and outlets and resulting in weak bonds and leakage points. Rough calculations of capillary pressure for the expected gap widths suggest surface tension forces capable of withstanding up to 15 psig. Accordingly, clamping pressure was reduced, and further tests conducted.

### 100 psi Bonded Chip



(a)

### Profilometer Scan Results



(b)





**Fig. 7.4.3: (a) 100 psi bonded chip and (b) profilometer scan results for 100 psig bonded chip.**

Four additional pressure tests were conducted at clamping pressures of 3, 5, 7.5, and 15 psig and peak temperatures between 400 and 500°C. It is worth noting that since the pressure difference between the bonding chamber and the internal cavity of the manifold were below one atm, these four test cases could not be performed with a vacuum on the inside of the manifold. Accordingly, the bonding process changed slightly. The steps up to pressurization of the bonding apparatus were the same. At that point, the vacuum was released, and the pressurized environment allowed to clamp the chip onto the manifold. A vacuum was then pulled again to ensure the pressure difference was strong enough to keep the chip attached to the manifold. If a successful vacuum was pulled—indicating the chip remained attached to the manifold—the vacuum would be released again, and the remaining bonding steps followed.

All four bonded manifolds remained intact after a 75 psig leak test, but upon submersion, three of the four leaked, albeit significantly less than those bonded at high clamping pressure. To obtain quantitative results for the bond strengths, the bonded manifolds were tested to bond failure using a hand-cranked liquid piston pump capable of

generating up to 4000 psi. However, before these tests could be conducted, the bonded manifolds needed to be leak tight. To that end, the bonded manifold was sealed with epoxy by attaching it to a vacuum pump, applying epoxy on the perimeter of the bond surface, and engaging the vacuum pump, drawing the epoxy into the leakage points. The epoxy was allowed to cure, and then the sealed and bonded manifolds were tested to failure, and the results are shown in Fig. 7.4.4.

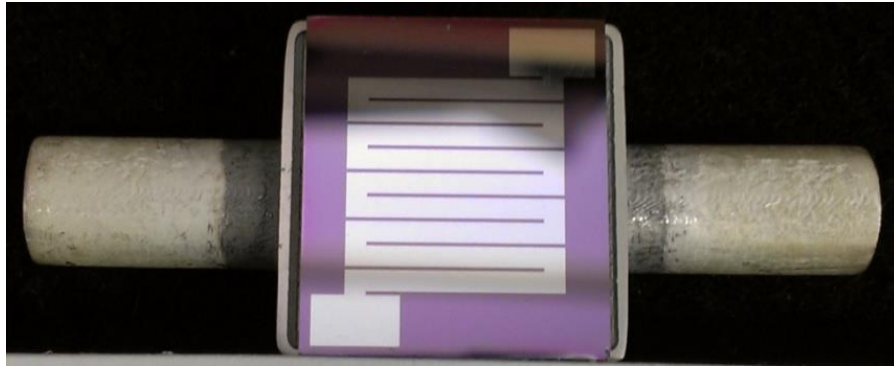
It is clear that clamping pressures near 5-7.5 psig obtain the strongest bond. This is due to the balance between clamping pressure too weak to adequately conform the chip around the unlapped manifold, and clamping pressure being too high, causing the high pressure environment to push the solder out of the bonding area. It is worth noting that while the 5 psig manifold achieved a seal without the need for epoxy, this might not be due to the pressure alone, since peak temperature also spiked up to 480°C due to insufficient cooling. While 480°C isn't above liquidous point for the mixture, a significantly higher volume fraction of solder will be molten (see Fig. 7.2.1(c)), thereby making hermetic sealing more likely, especially when considering the high roughness of the surface after solder deposition (see Fig. 7.2.2).

Clamping Pressure			
15 psig	7.5 psig	5 psig	3 psig
Burst Pressure			
~350 psi	1250 psi	1300 psi	800 psi
			
Sealant			
5 minute epoxy	5 minute epoxy	none	h.t. epoxy
Peak Temperature			
400°C	400°C	480°C	400°C
(a)	(b)	(c)	(d)

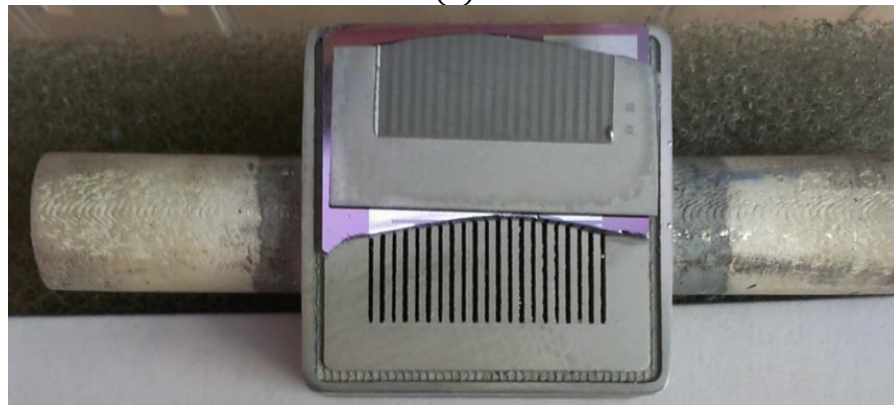
**Fig. 7.4.4: Summary of successful bonding results at various clamping pressures: (a) 15 psig, (b) 7.5 psig, (c) 5 psig, and (d) 3 psig.**

Having established successful bonding with 7.5 psig and 5 psig, working chips were then bonded, mimicking the conditions in Fig. 7.4.4. First, a working chip was bonded at 7.5 psig. Upon pressure testing, half the chip broke off at 30 psig, as shown in Fig. 7.4.5. It is thought that poor contact between the heat spreader and the manifold caused uneven heating, resulting in only one side of the chip bonding to the manifold. To avoid this problem, all manifolds were polished on their backside to ensure proper thermal contact. The chip was then de-soldered and analyzed under a microscope to investigate the possibility of solder clogging of the microchannels. It was observed that solder appears to bridge the gaps between microchannels only in regions where the manifold is bonded to the chip due to the pressure of the chip on the solder. In the inlet and outlet regions, however, there is nothing pressing the solder and solder does not bridge the gaps, indicating that solder plugging of the channels in the inlet and outlet regions of the manifold is less of a concern than previously thought.

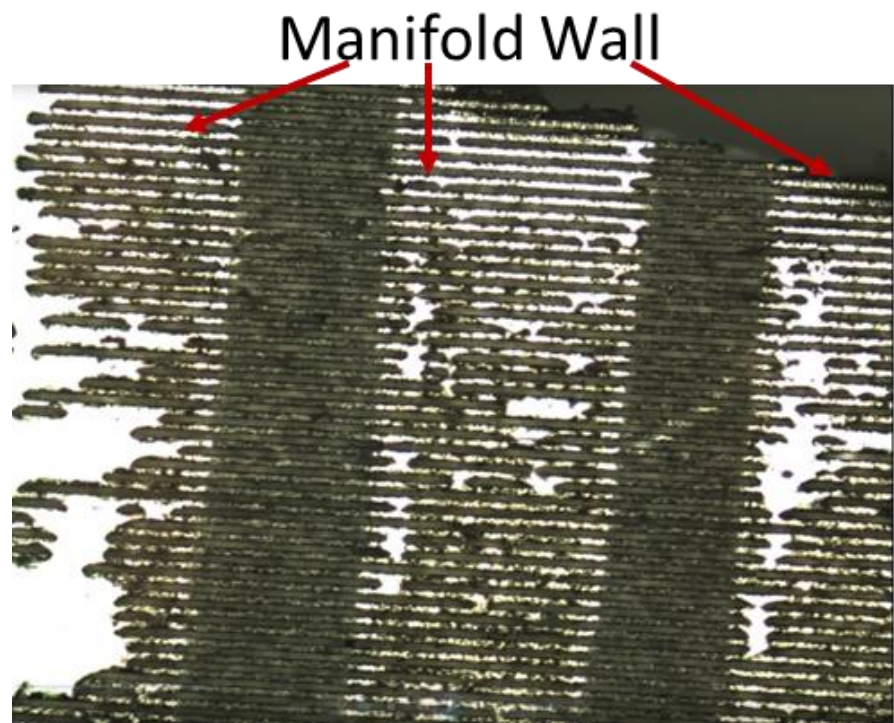




(a)



(b)



(c)

**Fig. 7.4.5: Bonding attempt of working chip at 7.5 psig: (a) before pressure test, (b) after pressure test, and (c) zoomed view of microchannels.**



Next, the conditions matching the 5 psig clamping pressure were used to bond a working chip to a manifold. The bonded manifold was then successfully pressure tested to 75 psig without any leaks. This bonded manifold was then used for experimental testing, which will be detailed in the following section.

## ***7.5 Test Chip 1***

A layer of epoxy was placed around the periphery of the chip to protect the manifold from electrical arcing due to the high voltage. The heater was covered in a thin layer of high temperature Kapton tape, and three thermocouples were placed on the Kapton tape directly over the heater for temperature measurements. The thermocouples were then covered with a thin layer of Teflon, which was clamped down onto the heater to ensure good thermal contact. Next, silver paint was used to connect wires to the heater with minimum contact resistance. The wiring to the test loop—including three thermocouples with a shared reference, positive and negative power supply, and positive and negative voltage measurement—was accomplished using a solderable RS-232 kit. The final wired test section is shown in Fig. 7.5.1.

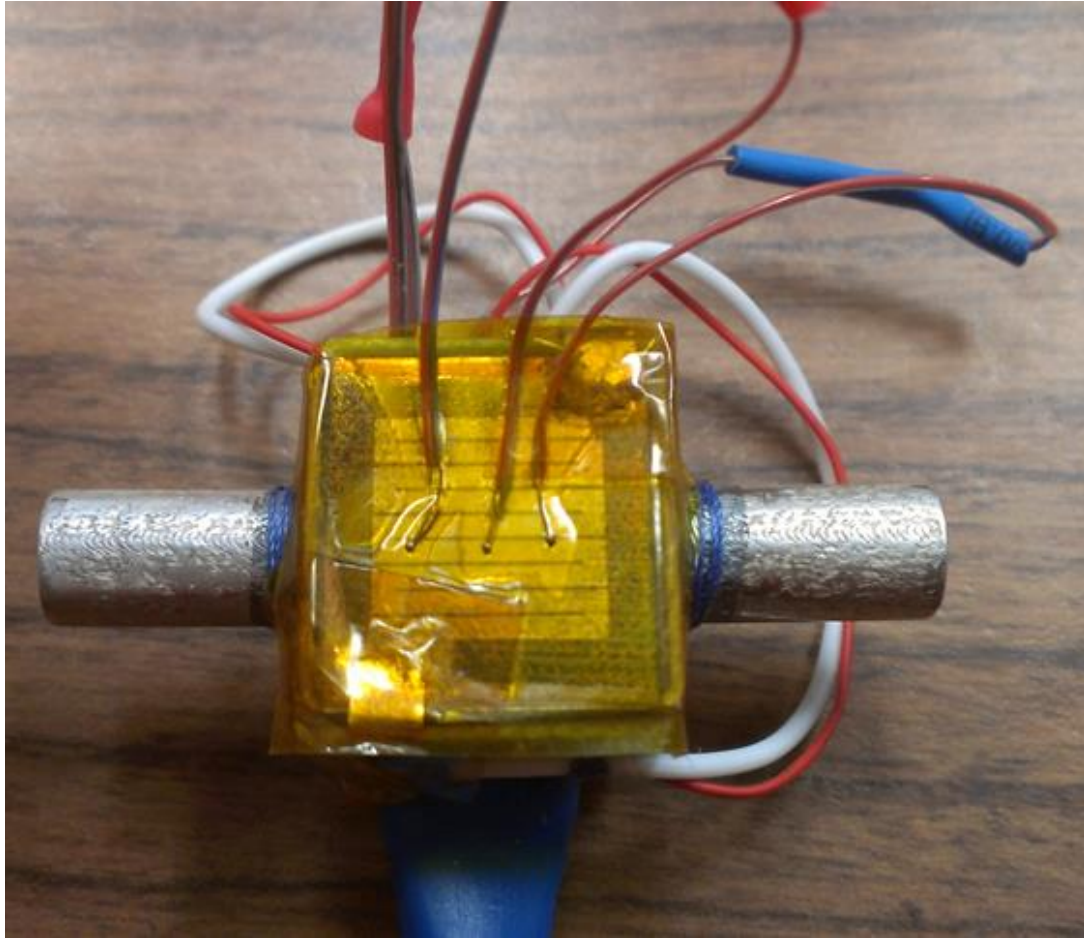
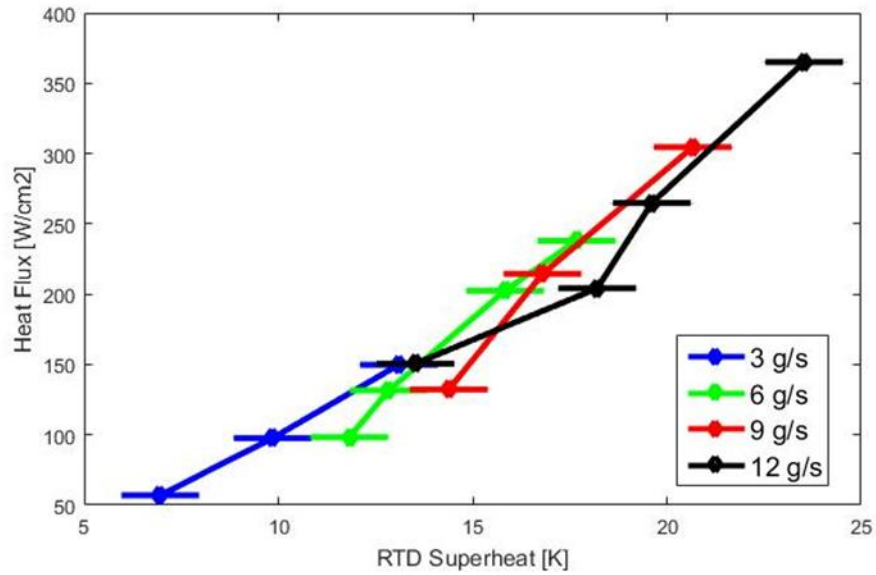
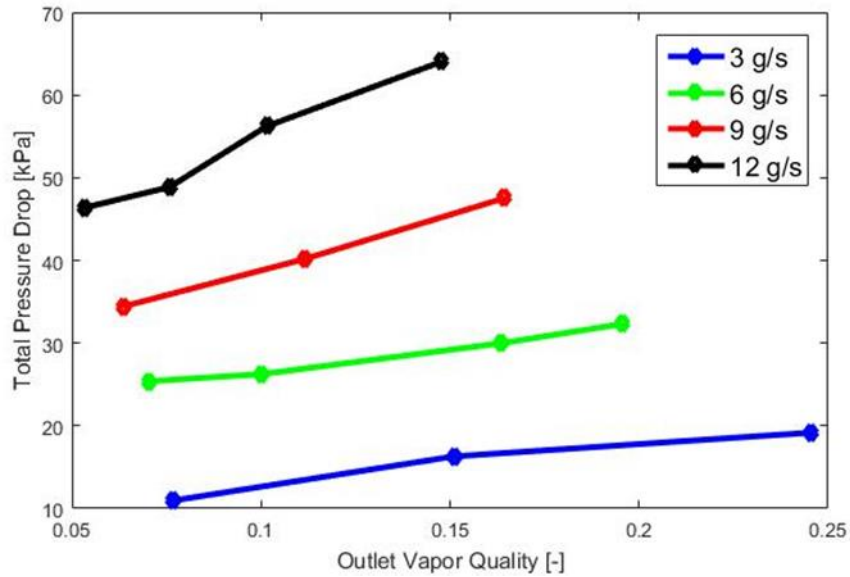


**Fig. 7.5.1: Final wired test section for experimentation.**

The same test loop and data acquisition system used in the modular experiment was used for the bonded manifold as well. The test results for four different refrigerant flow rates are shown in Fig. 7.5.2. For these tests, maximum outlet vapor quality ranged from 25% to 15%, corresponding to heat fluxes of 150 to  $365 \text{ W/cm}^2$  for the lowest and highest flow rates, respectively. Heat fluxes and vapor qualities could not be increased higher due to a sudden and early-onset critical-heat-flux-like event: the loop would be approaching steady-state, with all temperatures and flow rates remaining steady, until suddenly, the heater temperature would start to rise slowly, then faster until the temperature limit would be reached, and the control circuit would turn the power off.



(a)



(b)

**Fig. 7.5.2: Two-phase results with R245fa Chip 1: (a) heat flux vs. RTD superheat and (b) pressure drop vs. outlet vapor quality.**

It was initially suspected that boiling was occurring in the manifold due to the improved thermal contact between the superheated chip and manifold. The outlet valve was constricted to increase the pressure in the test section, thereby increasing the effective sub-cooling. It was noted that while sub-cooling the fluid did delay this early-onset critical-heat-flux-like event, increasing the heat flux would always eventually result

in an early-onset critical-heat-flux-like event. Furthermore, increasing the sub-cooling would only result in an increase in heat flux equal to a fraction of the sensible heat gained. Thus, boiling in the manifold did not seem to be the problem. Next, we considered hot spots resulting from manifold misalignment. An IR camera was used to measure the chip temperature during two-phase operation. A hotspot located near the edge of the chip was observed. Furthermore, the hotspot was observed to increase in temperature as the onset of the critical-heat-flux-like event occurred, implying that the hotspot was linked to this event. Due to the location of the hotspot, a manifold-chip misalignment was assumed.

Two possible misalignments are possible: misalignment in the direction perpendicular to the manifolds and misalignment in the direction parallel to the manifolds. Of these two possibilities, the first is more detrimental, since, if the manifold is misaligned in this direction by more than  $100\text{ }\mu\text{m}$  (half the width of the manifold), then the entire manifold section will be blocked off, resulting in effectively  $500\text{ }\mu\text{m}$  (the pitch of the manifold) of uncooled length (see Fig. 7.5.3(b)). In contrast, if the manifold is misaligned by  $100\text{ }\mu\text{m}$  in the direction parallel to its channels, then approximately five channels, corresponding to  $100\text{ }\mu\text{m}$ , will be without flow (see Fig. 7.5.3(c)). Accordingly, the first possibility (shown in Fig. 7.5.3(b)) is five times worse.

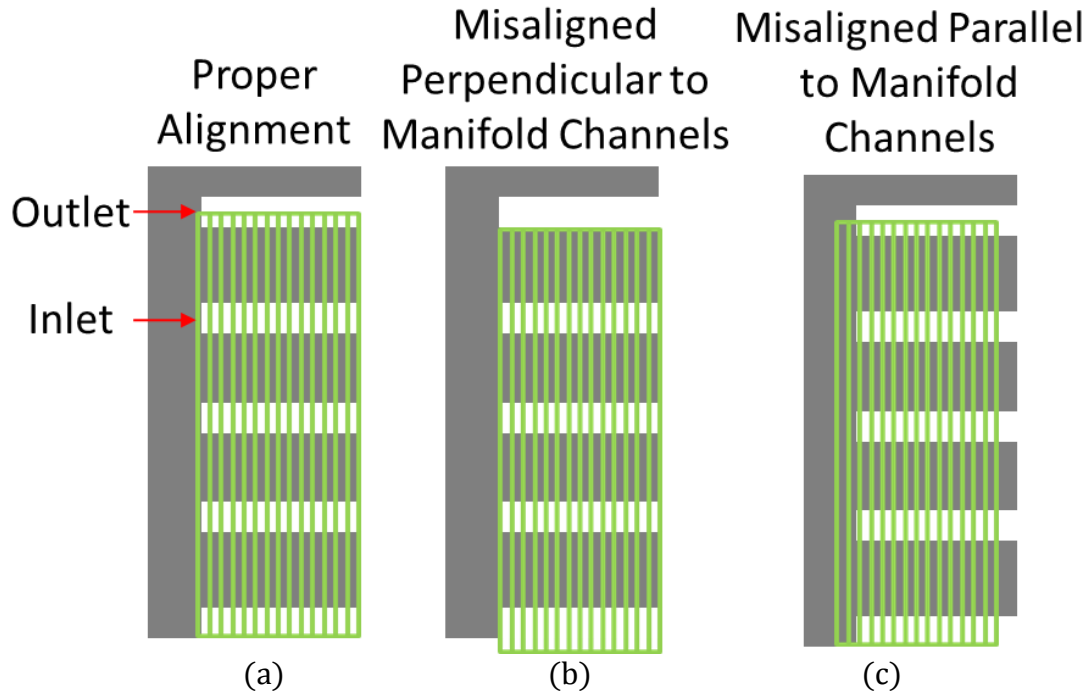


**Fig. 7.5.3: Possible manifold-chip misalignments: (a) properly aligned, (b) direction perpendicular to the manifolds, and (c) direction parallel to the manifolds.**

The bonded manifold was therefore de-bonded to investigate alignment. A careful de-bonding method was needed to ensure the solder remains in place so that information about alignment and microchannel clogging could be inferred. In addition, a controlled environment was preferred so that oxidation of the exposed molten solders could be prevented. The de-bonding was performed as follows: the heat spreader was tied to the bonded manifold, and the bonded manifold was mounted inside the pressure bonder. The pressure bonder was assembled and purged of air. The vacuum supply was then attached to the nitrogen and a small positive pressure ( $\sim 5$  psig) was applied, pushing on the chip from inside the manifold. The heater was then engaged until leakage was heard from the pressure release valve, indicating the chip had de-bonded from the manifold.

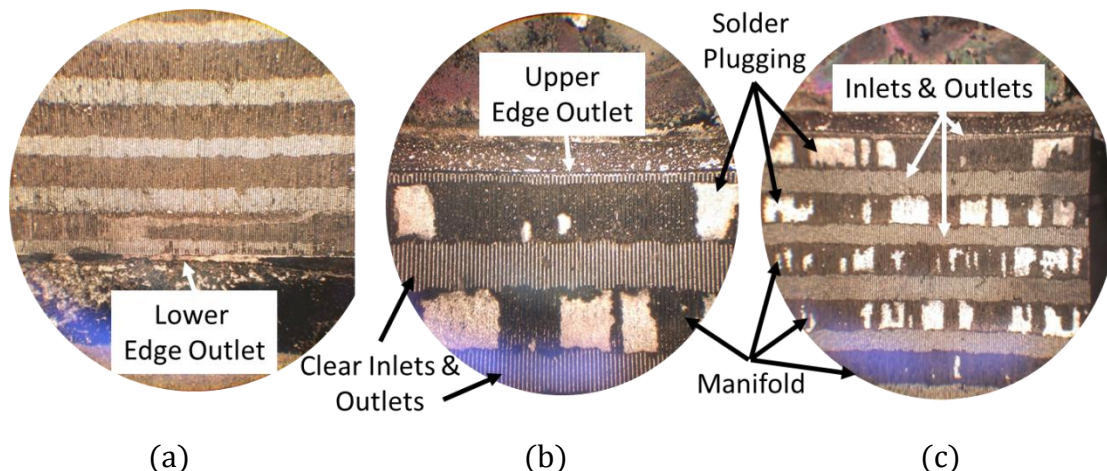


**Fig. 7.5.4: Chip 1 after de-bonding: (a) lower manifold view, (b) upper manifold view, and (c) zoomed-out view near upper manifold.**

The de-bonded chip is shown in Fig. 7.5.4. The lighter portions correspond to the manifold channels, while the darker areas correspond to the manifold walls. Upon examining the de-bonded chip, it became clear that the boundary (lower and upper) manifolds were aligned sufficiently well to obtain some flow, as indicated by the light areas near the edges of the channels. CFD simulations were therefore performed, and for the approximate geometry shown, only a small increase in pressure drop could be expected—not nearly enough to explain the restriction to low heat fluxes and vapor qualities.

Moreover, it is worth noting that here too (see Fig. 7.4.5(c)) solder clogging appeared to be a concern only where the manifold walls bond to the chip, as all of the inlets and outlets appeared free of solder bridges. However, from Fig. 7.5.4(a)-(b), a significant amount of solder adjacent to the microchannels appeared to have been delaminated upon de-bonding, while the remaining area remained untouched. Accordingly, it was suspected that the untouched area was not bonding to the manifold. This is a direct result of the use of gas to apply clamping pressure during bonding. The gas pressure only applies a net force where a lower pressure exists on the opposite side of

the chip. Inside the center of the manifold, where atmospheric pressure is maintained, the gas applies a net force, conforming the chip around the manifold. However, once the chip conforms around the manifold enough to seal it from the elevated chamber pressure, the chip will stop conforming. Accordingly, a pinching force is created at this seal location, and could force solder into the manifold and microchannels near the sealing perimeter. Even though the solder layers were thin, because the bonding perimeter was 2 mm wide, a significant volume was available for clogging. It is worth noting that the presence of solder clogging around the perimeter during bonding was also consistent with the observed hotspot location. Accordingly, this pinching needed to be prevented.

## 7.6 Test Chip 2

A high temperature silica rope was used to apply a relatively uniform and conformal clamping pressure without pinching. A diagram comparing the gas clamping method with the rope clamping method is shown in Fig. 7.6.1. Whereas gas pressure applies zero net force around the perimeter, resulting in a narrow sealing region and subsequent pinching force on the edge of the perimeter, force applied with rope is uniform and allows the chip to evenly conform around the manifold radius, thereby reducing pinching force.

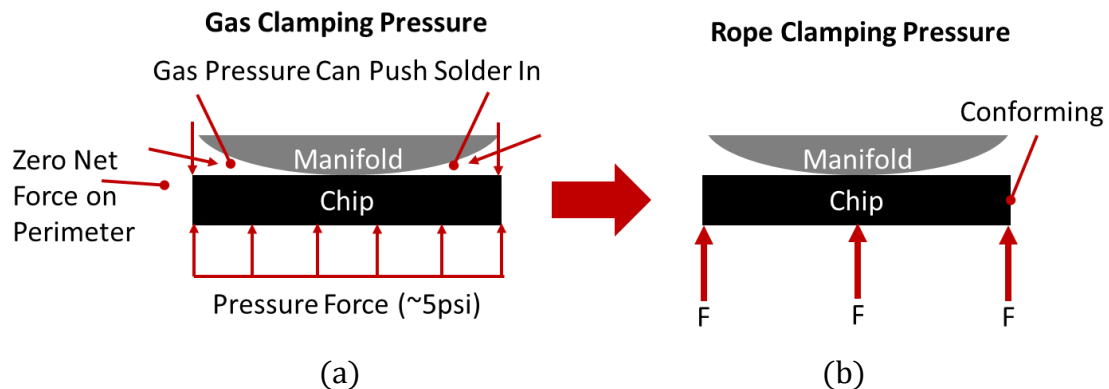


**Fig. 7.6.1: (a) Gas clamping method vs. (b) rope clamping method.**

The use of rope to apply the clamping changed the bonding assembly procedure slightly. The manifold was first sprayed with nitrogen to remove dust and mounted onto a separate device capable of pulling a vacuum. The chip was then placed onto it, and aligned. Once alignment was obtained, a vacuum was pulled, firmly holding the chip in place. The rope was then wrapped around the chip and tied tightly. The vacuum was then released and the manifold placed in the bonding chamber. The vacuum supply line was kept open to air to ensure there was no potential for pressure build-up inside the manifold upon heating of the air inside it. The container was then flushed with nitrogen, and the bonding procedure continued as previously described. First, two blank Si dies were



successfully bonded using this method, leak checked at 160 psig, and tested to failure. A chip was then bonded to a manifold and wired up for testing, as previously described.

SEM images of a chip and manifold after testing and de-bonding are given in Fig. 7.6.2, and a comparison of the nominal, measured, and simulated values is given in Table 7.6.1.

**Table 7.6.1 Comparison between nominal and actual values for microchannel and manifold dimensions of bonded Chip 2**

Dimension [Variable]	Nominal [ $\mu\text{m}$ ]	Measured [ $\mu\text{m}$ ]	Simulated [ $\mu\text{m}$ ]
Microchannel width [ $w_{\text{ch}}$ ]	10	9.5	9.5
Microchannel fin width [ $w_{\text{f}}$ ]	10	10.5	10.5
Microchannel fin height [ $h_{\text{f}}$ ]	100	75	75
Substrate base thickness [ $h_{\text{b}}$ ]	400	285	285
Manifold Inlet [ $L_{\text{in}}$ ]	200	150	150
Manifold Wall [ $L_{\text{man}}$ ]	300	350	350
Manifold Outlet [ $L_{\text{out}}$ ]	200	150	150
Manifold Length [ $L_{\text{ch}}$ ]	500	500	500

From Fig. 7.7.2(a) it is clear that like the press-fit chip, the microchannels here are tapered. However, the tapering appears to be less extreme, and the channel width at the fin tips is  $11\ \mu\text{m}$  while at the base the width reduces to  $8\ \mu\text{m}$ , resulting in an average width of  $9.5\ \mu\text{m}$ . In addition, from Fig. 7.7.2(a), solder is observed to deposit on the sides of the microchannels, resulting in significant constriction which is not present in the press-fit chip due to the lack of the need for solder. The microchannel depth is also measured, and found to be approximately  $75\ \mu\text{m}$  deep, while the base substrate thickness was measured to be approximately  $285\ \mu\text{m}$  thick.

The manifold dimensions were also measured with the SEM, and the results shown in Fig. 7.7.2(c). Due to inaccuracies in the metal 3-D printing process, the manifold channels are extremely rough, wavy, and non-parallel, and the average manifold wall length is larger than the nominal value, resulting in a larger than expected pressure drop. The manifold wall and channel gap size also vary by a significant margin. Due to the relationship between manifold wall length and pressure drop, it is likely that an uneven flow distribution will exist. In turn, this uneven flow distribution might reduce the effective heat transfer coefficient by supplying excess flow where it cannot be used effectively; however, since the effect on pressure drop is linear, no effect on average pressure drop is expected. Furthermore, Fig. 7.7.2(d) shows a far view of the manifold, where the waviness of the channels and variations in gap width and manifold wall length can be observed over a wider area. On average, the manifold inlet and outlet were measured to be 150  $\mu\text{m}$  wide, and the manifold wall was measured to be 350  $\mu\text{m}$  wide.

In addition, it is worth noting that from Fig. 7.7.2(e), it is clear that the solder appears to bridge the gap between channels only directly under the manifold wall. However, unlike previous observations in Section 7.4 and 7.5, this view is angled and indicates that this bridge does not penetrate into the microchannel at all, but rather sits on top of it. Therefore, the potential for solder to clog the microchannels is significantly lower than first expected. Finally, from Fig. 7.7.2(f), it is clear that the manifold imprint on the chip is missing at the center of the chip. This could be due to the use of rope to clamp the perimeter onto the manifold, since the clamping force is almost always applied at the edges. Accordingly, it is possible that a gap exists between the microchannel fin tips and the manifold, allowing fluid to bypass. This fluid bypass could result in reduced

heat transfer coefficient in single-phase mode (see Fig. 6.1.2(b)), and reduced maximum heat flux in two-phase mode.

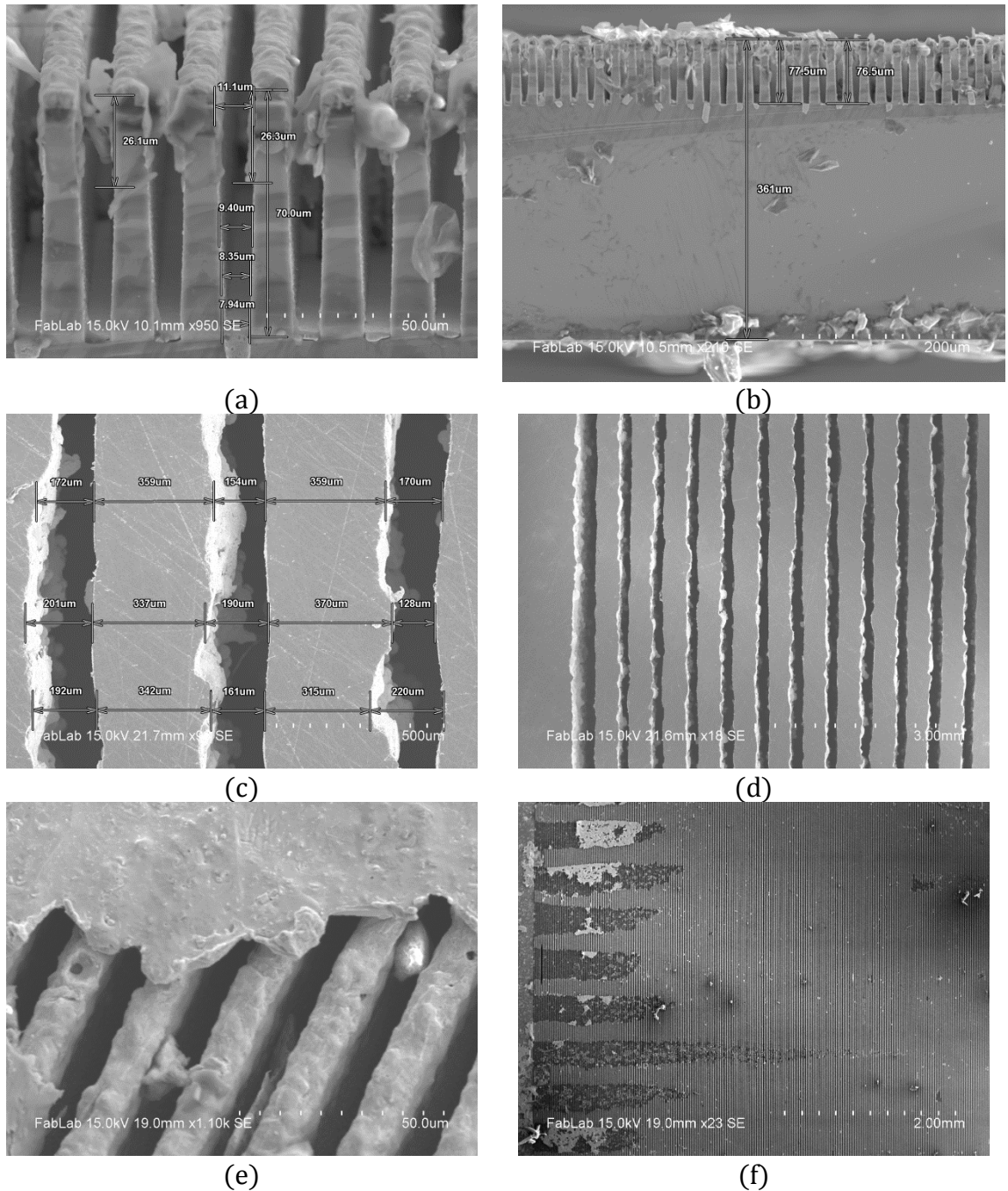


**Fig. 7.6.2: SEM images of chip 2 and its corresponding manifold after testing and de-bonding: (a) cross-section of microchannels, (b) cross-section of chip substrate, (c) manifold measurements, (d) far view of manifold, (e) angled view of microchannel wall, and (f) far view of microchannels.**

To assess repeatability for this chip, the chip was calibrated, tested in single-phase mode, and tested in two-phase mode twice. The chip was first calibrated by supplying a steady flow of refrigerant at the desired temperature. Refrigerant temperature was controlled via the preheater, which, during calibration, was powered by the power supply usually used to control the RTD heater in order to allow automated PID calibration. The RTD was therefore powered by a battery, which supplied a small and noiseless current signal, as well as negligible self-heating (especially when considering the efficient heat sink directly in contact with the RTD). The voltage divider was disconnected during calibration, and a larger ( $\sim 50\ \Omega$ ) calibrated current-sense resistor was used to measure current. Three temperatures between 20-70°C were used to assess linearity. Single-phase tests were then conducted the same way as described in Section 6.8, except that two heat fluxes—in addition to the adiabatic case—were tested as a system check to ensure heat transfer coefficient was not a function of heat flux in single-phase mode. Two-phase tests were then conducted the same way as described in Sections 6.8 and 7.5. Upon completing the two-phase tests, the entire process was repeated, beginning with calibration.

The calibration curve is shown in Fig. 7.6.3. As can be seen, the calibration curve is repeatable, even after single-phase and two-phase testing. Moreover, the change in calibration curve was found to amount to less than 0.2 °C change in temperature, which is acceptable.

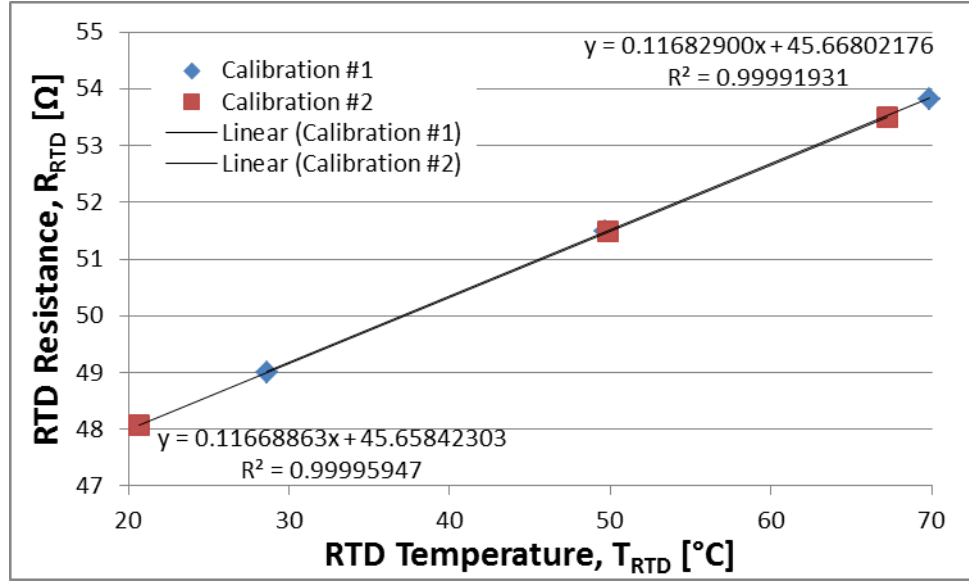


**Fig. 7.6.3: Calibration curve for chip 2.**

Single-phase tests were then conducted in the same way described in Section 6.8, except that two heat fluxes were tested—50 W/cm<sup>2</sup> and 75 W/cm<sup>2</sup>. Two heat fluxes were tested as a system and calibration check to ensure heat transfer coefficient in single-phase mode was independent of heat flux. Besides ensuring that RTD temperature was kept below saturation temperature, single-phase operation was also visually confirmed by installing a transparent Teflon tube between the test section and the outlet valve. The single-phase tests were found to be repeatable to well within the experimental uncertainty for both pressure drop and heat transfer coefficient. However, the pressure drop was observed to be approximately 15% larger, and heat transfer coefficient was observed to be 25% lower than CFD predicts, as shown in Fig. 7.6.4.

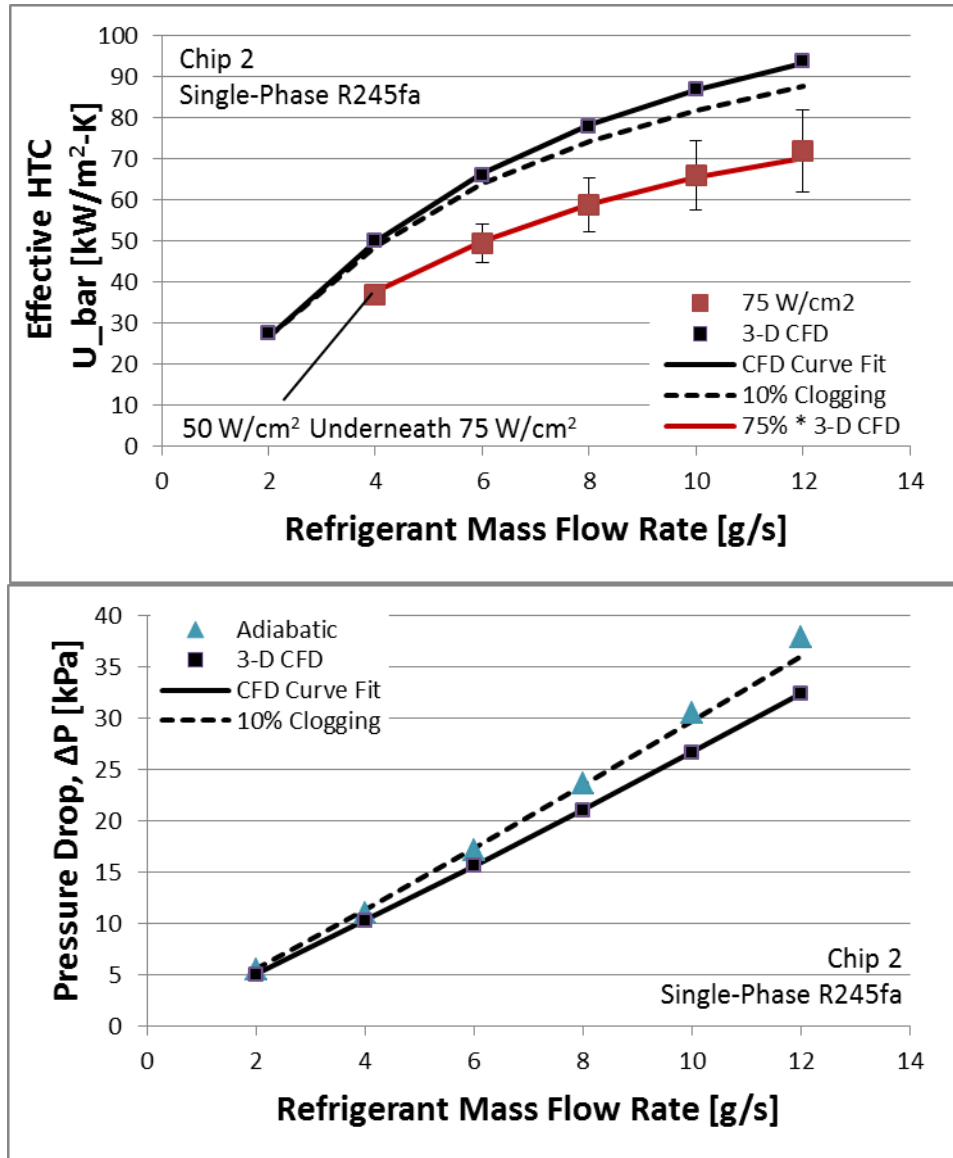


**Fig. 7.6.4: Single-phase results for chip 2.**

A similar analysis to that found in Section 6.8 (see Eqs. (6.8.1)-(6.8.4)) was once again conducted to quantitatively determine the potential for clogging to explain both the increased pressure drop and reduced heat transfer coefficient. Matching the experimental pressure drop values to those predicted by CFD implies approximately 10% clogging; however, 10% clogging is insufficient to explain the 25% reduction in heat transfer coefficient, as shown in Fig. 7.6.4. It is worth noting that for this case, regardless of flow rate, heat transfer coefficient is very closely approximated by 75% of the value predicted

by CFD. This cannot be due to clogging alone, since, at low flow rates, the additional flow in the non-clogged areas increases heat transfer coefficient more than it does at higher flow rates. Accordingly, the ratio between experimental and CFD values for heat transfer coefficient should vary with flow rate. Thus, other factors might be at play.

As noted in the SEM images of this manifold, (see Fig. 7.6.2(c)-(d)), the manifold flow divider thickness varies by a wide margin. This, in turn, could cause flow maldistribution, resulting in reduced overall heat transfer coefficient and no anticipated effect on pressure drop, as described above in this section. In addition, as noted in the SEM images of this chip (see Fig. 7.6.2(f)), the center channel fin tips were not bonded to the manifold flow dividers. This in turn, could result in a gap between the manifold flow dividers and the microchannels, allowing fluid to bypass. Bypassing flow should reduce both pressure drop and heat transfer coefficient, since less flow enters the microchannels. Thus, since the pressure drop was observed to be above CFD value even with bypass, if bypass is occurring, the clogging fraction might be underestimated. Finally, similar to the press-fit chip, the presence of tapered microchannels could result in reduced heat transfer coefficient, and an underestimate of clogging fraction.

Next, the presence of hotspots was investigated in single-phase mode using an IR camera. A hotspot was observed toward the perimeter of the heater, in a similar location as the one found in Chip 1. The presence of a hotspot in single-phase mode—when the RTD temperature is below saturation—further reinforces the idea that nucleate boiling in the manifold is not responsible for the observed hotspot. However, the presence of a hotspot in single-phase mode is not expected to result in reduced heat transfer coefficient, since, for single-phase mode, heat transfer coefficient is independent of heat flux. In

addition, the hotspot location near the perimeter seems to indicate that solder clogging during bonding might be responsible.

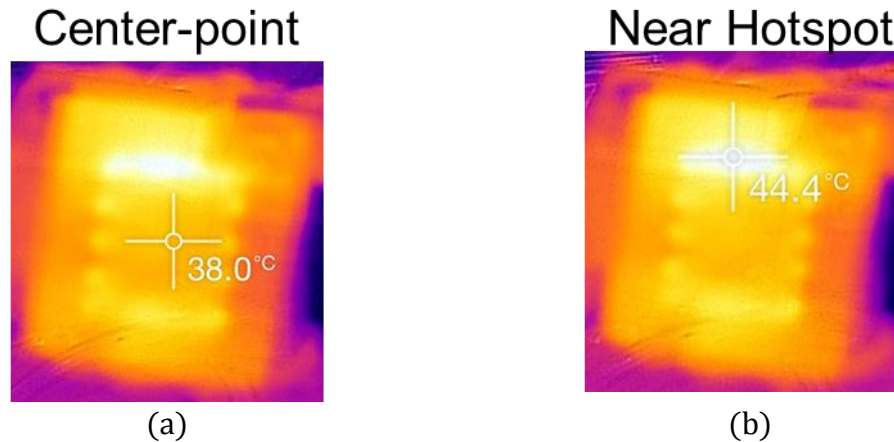


**Fig. 7.6.5: Hot spots on chip 2 in single-phase mode: (a) temperature near center of chip and (b) temperature near hotspot.**

Two-phase tests were then performed with the chip. Four refrigerant flow rates were tested between 3-12 g/s. For all tests, mass flow rate was held constant and heat flux increased until heat flux couldn't be increased anymore due to chip temperature becoming unstable, which will be detailed below. The results are shown in Fig. 7.6.7.

Peak outlet vapor qualities of 35% and 21% were obtained for the lowest and highest flow rates, respectively, corresponding to heat fluxes of  $205 \text{ W/cm}^2$  and  $566 \text{ W/cm}^2$ . If the vapor quality is increased by increasing the heat flux once the vapor quality limits shown have been exceeded, the RTD will continually increasing in temperature until the temperature limit is reached, sometimes at an accelerating rate. The presence of hotspots and the implication of 18% microchannel clogging in single-phase mode could explain this behavior: if a large region of microchannels is partially clogged, less flow will be present in this region, thereby, increasing local vapor quality. Once this vapor quality exceeds unity, the heat can no longer be dissipated by the local fluid supply, and must spread to nearby channels. This, in turn, increases the local vapor quality, which



increases pressure drop, and acts to further reduce flow, thereby once again increasing vapor quality. As heat flux is increased, at some point, the domino effect becomes unstable, and steady-state chip temperature cannot be maintained.

These results are consistent with thermal images taken in two-phase mode, shown in Fig. 7.6.6. Upon exceeding the heat flux limit for a given flow rate, hotspot temperature was observed to steadily increase as the RTD temperature far away remains relatively constant, indicating that hotspot temperature is responsible for the increase in average RTD temperature.

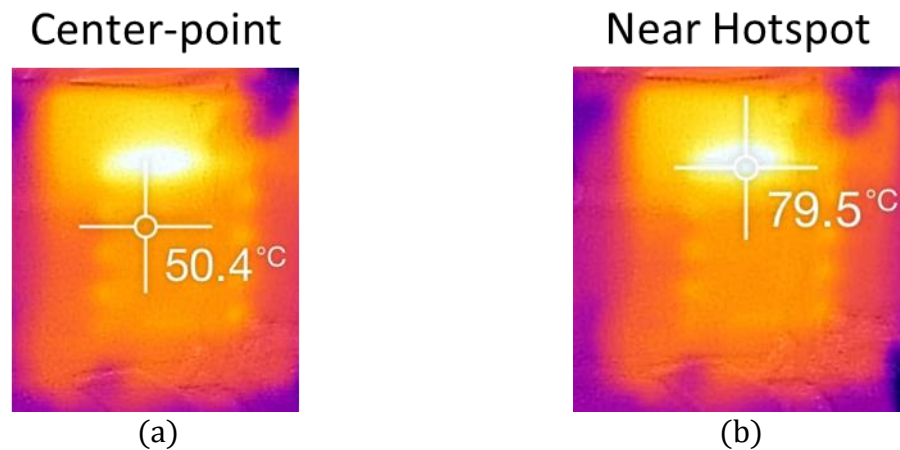


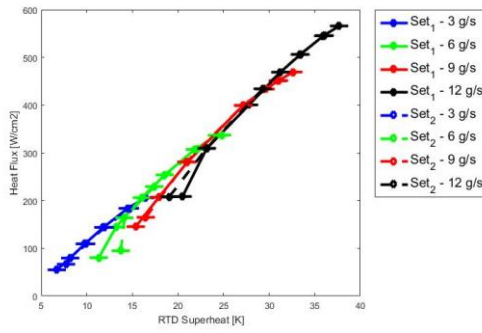
**Fig. 7.6.6: Hot spots on chip 2 in two-phase mode: (a) temperature near center of chip and (b) temperature near hotspot.**

In addition, the stability of hotspots can be explained as follows. It is known from previous two-phase FEEDS experiments that for each flow rate, an optimal vapor quality exists to maximize heat transfer coefficient [10, 42]. This trend is also present in the results presented herein (see Fig. 6.9.1). Below this optimum vapor quality, hotspots are stable, since when the heat flux in the clogged region spreads to nearby unclogged channels, it increases local vapor quality, resulting in increased heat transfer coefficient. The increase in heat transfer coefficient acts as negative feedback to keep hotspot temperature stable. However, above this optimum vapor quality, heat transfer coefficient

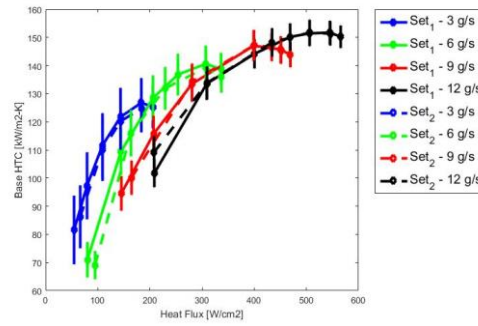
decreases with an increase in quality. Hotspot heat flux spreading would therefore cause a decrease in heat transfer coefficient, which would act to further increase in the temperature of the hotspot. In this region, feedback is positive, and hotspots are therefore unstable. This theory is directly supported by the data presented in Fig. 7.6.7, which shows that for each flow rate, once heat transfer coefficient peaked, vapor quality could not be increased much further before the hotspot was found to become unstable. However, it is worth noting that the presence of a hotspot should decrease optimal vapor quality, and therefore, higher optimal vapor qualities might be possible.

Nevertheless, while peak base thermal conductances between 125 and 150 kW/m<sup>2</sup>-K were obtained, peak fin thermal conductances between 190 kW/m<sup>2</sup>-K and 270 kW/m<sup>2</sup>-K were achieved, indicating that substrate thermal resistance is very important, and contributes up to 33% to overall conductance. In addition, peak vapor qualities between 20-35% were obtained for the highest and lowest flow rates, respectively.

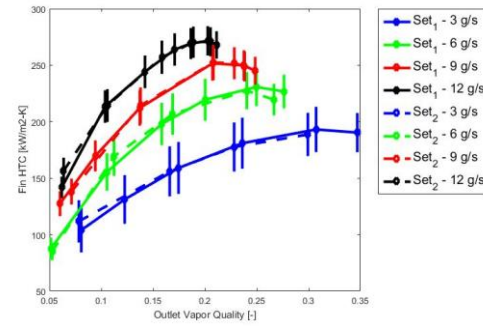
Similar trends to those described in Section 6.9 were observed. For a given vapor quality, heat transfer coefficient increases with increasing flow rate (see Fig. 7.6.7(c)-(d)). Optimal vapor quality is observed to decrease with an increase in flow rate (see Fig. 7.6.7(c)-(d)), and each heat flux is observed to have an optimal flow rate associated with it to produce a maximum heat transfer coefficient (see Fig. 7.6.7(b)). Finally, for a given vapor quality and heat flux, a higher flow rate produces a higher pressure drop, as shown in Fig. 7.6.7(e) and Fig. 7.6.7(f), respectively.



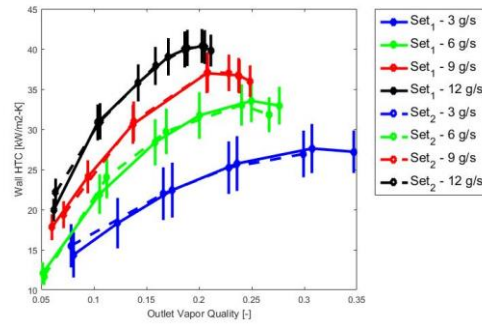
(a)



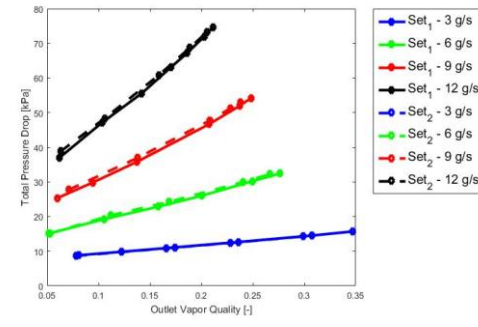
(b)



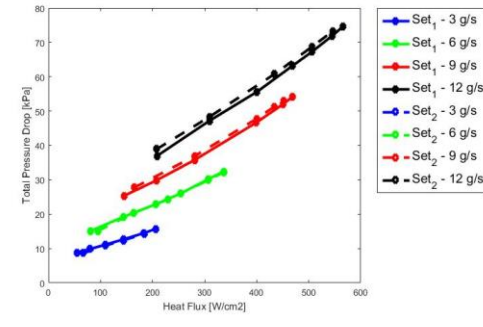
(c)



(d)



(e)



(f)

**Fig. 7.6.7: Two-phase results for chip 2: (a) heat flux vs. RTD superheat, (b) base heat transfer coefficient vs. heat flux, (c) fin heat transfer coefficient vs. outlet vapor quality, (d) wall heat transfer coefficient vs. outlet vapor quality, (e) total pressure drop vs. outlet vapor quality, and (f) total pressure drop vs. heat flux.**

### **7.7 Test Chip 3**

Due to the presence of hotspots located around the perimeter of the chips, it was assumed that solder was still being pushed into the microchannels from the perimeter. Furthermore, from the SEM images, it was also clear that the microchannel fins were not bonding to the manifold, potentially resulting in gaps and flow bypass. To combat this, a hybrid bonding method was attempted. To prevent solder clogging around the perimeter, it is desirable to reduce bonding temperature as much as possible. Reducing bonding temperature is desirable for many reasons and leads to:

- (1) Reduced mass fraction of the solder in the liquid phase, and therefore, the volume of molten solder;
- (2) Increased viscosity of the liquid phase;
- (3) Increased surface tension of the liquid phase;
- (4) Reduced residual thermal stresses.

Accordingly, a hybrid bonding method—wherein rope and gas pressure is used to apply clamping pressure—was developed, in the hope that if the surfaces are in intimate contact, a lower bonding temperature should be possible, since less volume of molten solder will be needed to fill the voids, as shown in Fig. 7.2.2(a). A diagram of the hybrid bonding method is given in Fig. 7.7.1.

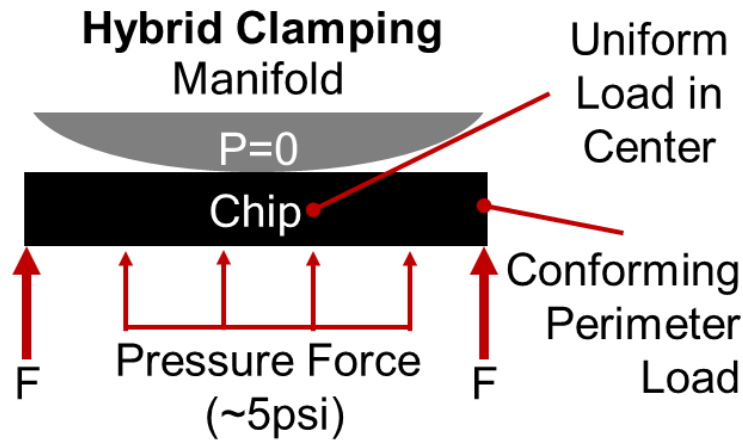


**Fig. 7.7.1: Hybrid clamping method.**

From the diagram, it is apparent that while gas pressure is used to apply a uniform force to the center of the chip, a rope is used to apply a light and conformal load around the perimeter of the chip for sealing. Thus, this hybrid method attempts to utilize these two different clamping mechanisms to obtain a hermetic bond at lower temperature. Using gas pressure to apply a force at the center of the chip also improves the probability that the microchannel fin tips will directly bond to the manifold.

This new bonding method was first attempted on silicon dies with great success. Bonding temperature was reduced from 450°C to 320°C, while still obtaining a hermetic bond up to 160 psig. In addition, the inlet was observed to be sealed from the outlet up to 160 psig, suggesting that the manifold flow-dividers bonded to the silicon die and that upon testing working chips, the manifold flow dividers would bond to the fin tips as well. Furthermore, the tested dies withheld up to 1600 psig before bursting—the highest pressure ever obtained in this work. Accordingly, a working chip was bonded to a manifold using this method and tested.

SEM images of the chip and corresponding manifold were taken after testing and de-bonding. The SEM images are given in Fig. 7.7.2, while the comparison between nominal, measured, and simulated values is given in Table 7.7.1.

**Table 7.7.1: Comparison between nominal and actual values for microchannel and manifold dimensions of bonded chip 3**

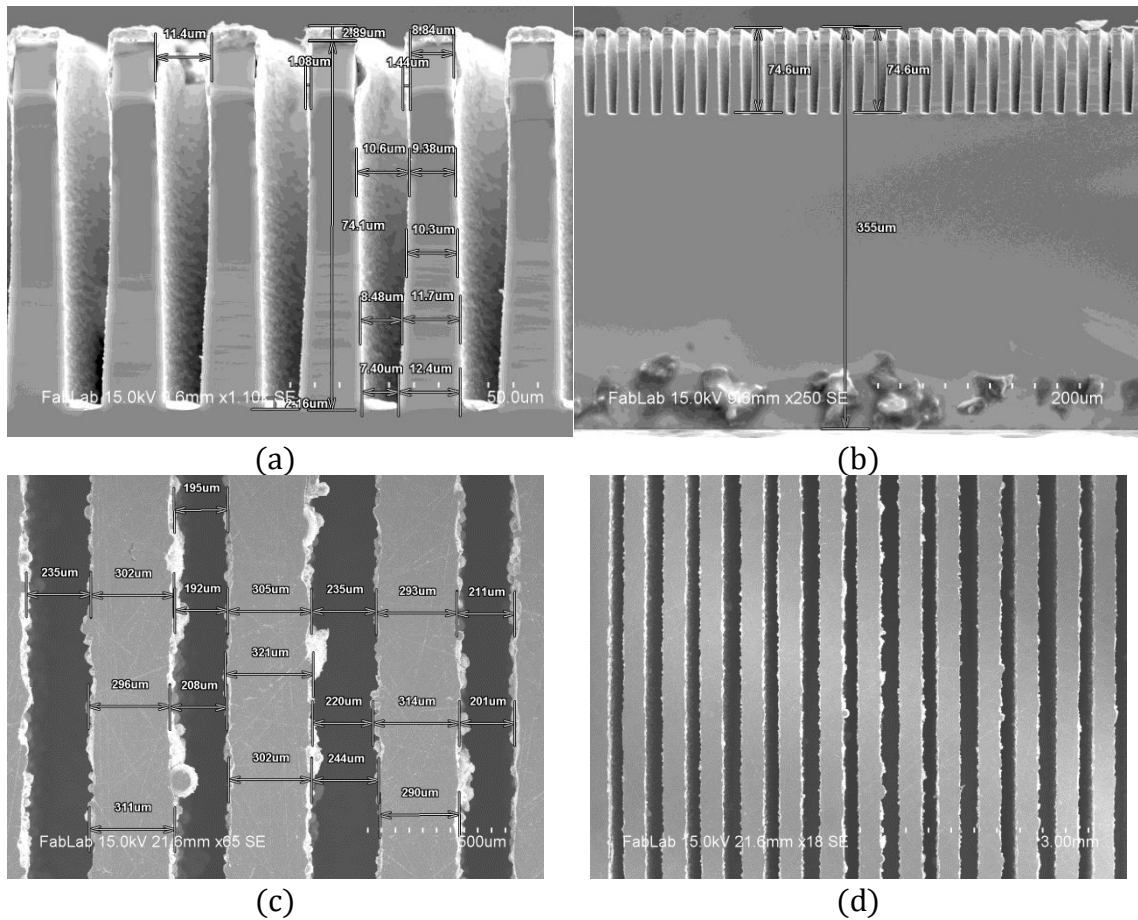
Dimension [Variable]	Nominal [ $\mu\text{m}$ ]	Measured [ $\mu\text{m}$ ]	Simulated [ $\mu\text{m}$ ]
Microchannel width [ $w_{\text{ch}}$ ]	10	9.4	9.4
Microchannel fin width [ $w_{\text{f}}$ ]	10	10.6	10.6
Microchannel fin height [ $h_{\text{f}}$ ]	100	75	75
Substrate base thickness [ $h_{\text{b}}$ ]	400	280	280
Manifold Inlet [ $L_{\text{in}}$ ]	200	200	200
Manifold Wall [ $L_{\text{man}}$ ]	300	300	300
Manifold Outlet [ $L_{\text{out}}$ ]	200	200	200
Manifold Length [ $L_{\text{ch}}$ ]	500	500	500

It is observed that once again, the channel cross-section appears to be tapered (see Fig. 7.7.2(a)), with a microchannel width of  $11.4 \mu\text{m}$  at the tip of the fins down to  $7.4 \mu\text{m}$  at the bottom of the microchannel, resulting in an average channel width of  $9.4 \mu\text{m}$ . The average fin width is measured to be  $10.6 \mu\text{m}$ . From Fig. 7.7.2(b), the average microchannel fin height is measured to be approximately  $75 \mu\text{m}$ , while the substrate base thickness is measured to be approximately  $280 \mu\text{m}$ . These measured values are very close to those of chip 2.

The manifold, on the other hand, is observed to deviate only slightly from the nominal geometry. The nominal inlet and outlet width were observed to match the average width, and the nominal manifold wall and pitch was observed to match average

measured values. Furthermore, the manifold channels are observed to be nearly uniformly spaced and parallel, with reduced roughness compared to the manifold used for chip 2, in Section 7.6. Thus, an improved flow distribution, and resulting improved heat transfer coefficient, can be expected.

In addition, as shown in Fig. 7.7.2(e)-(f), voids are observed on the wall. These voids, if sufficiently deep, could trap fluid, increasing conduction resistance between the wall and the fluid, and result in decreased heat transfer coefficient and increased pressure drop. It worth noting that it is unclear if these voids were also present in Chip 2, since angled SEM images were not taken.



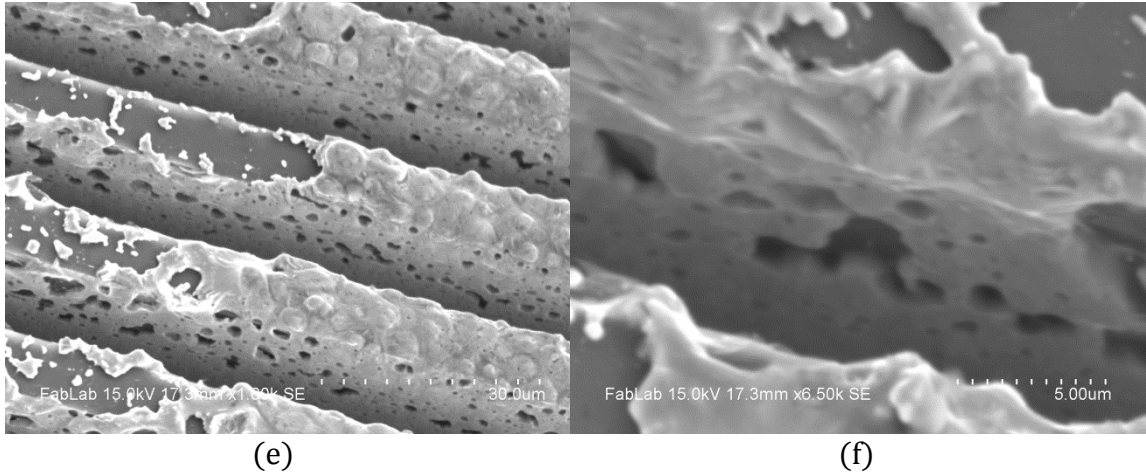


**Fig. 7.7.2: SEM images of chip 3 and its corresponding manifold after testing and de-bonding: (a) microchannels in manifold gap, (b) microchannels bonded to manifold wall, (c) angled view of microchannel wall, (d) close up view of microchannel walls, (e) particulate clogging, and (f) edge of microchannels.**

First, the chip was calibrated, using the same method described in Section 7.7.

The calibration curve is given in Fig. 7.7.3.

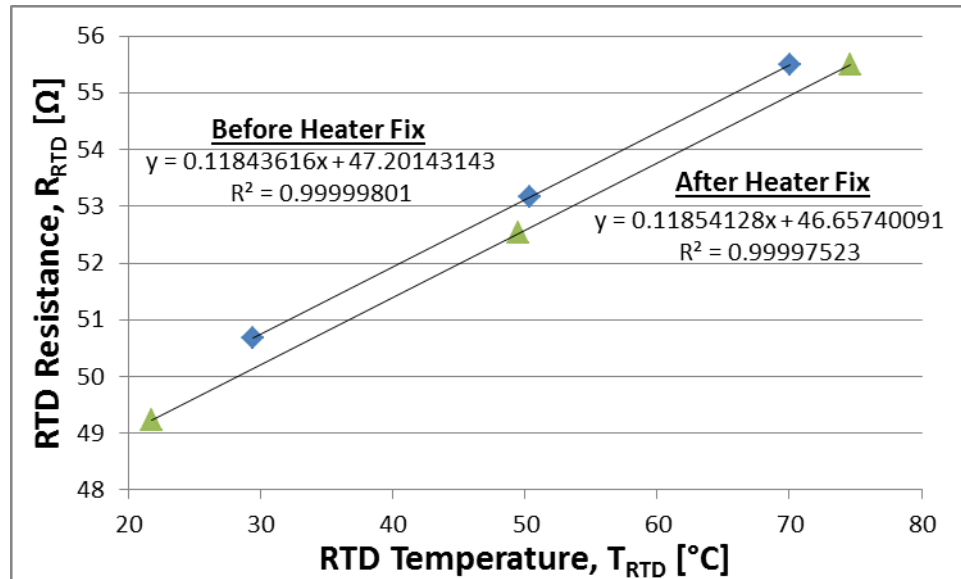


**Fig. 7.7.3: Calibration curve for chip 3.**

Then, single-phase tests were performed, and the results are shown in Fig. 7.7.4.

Once again, pressure drop was observed to be elevated and heat transfer coefficient reduced. The same analysis method was used to quantitatively predict the effect of microchannel clogging on pressure drop and heat transfer, and it was found that



approximately 20% clogging was needed to explain the increased pressure drop—larger than test chip 2. However, as mentioned in Section 7.6, the amount of clogging could be underestimated due to the possibility of fluid bypass resulting from insufficient bonding between the center manifold channels and the microchannel fin tips. Nevertheless, heat transfer coefficient is observed to increase from chip 2 to chip 3, indicating that an improvement was made.

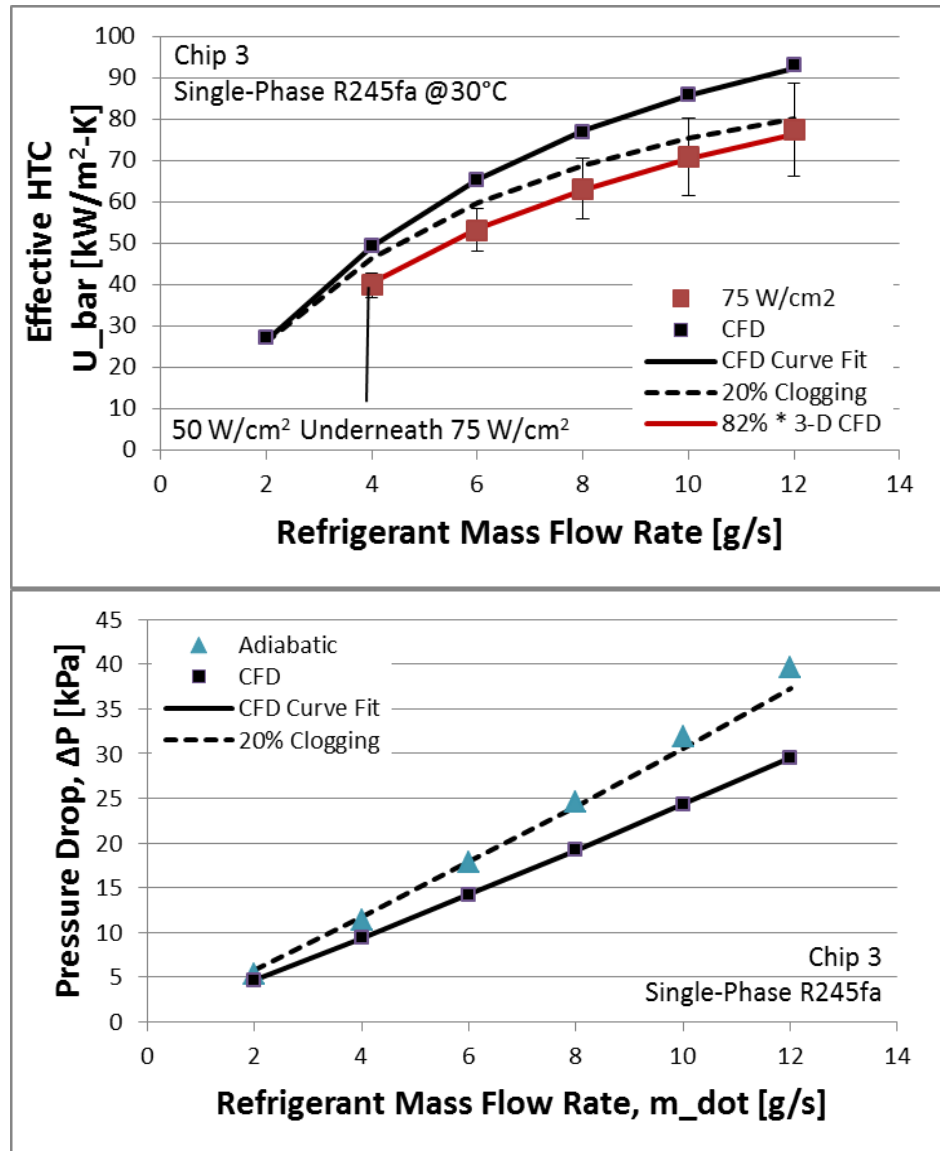
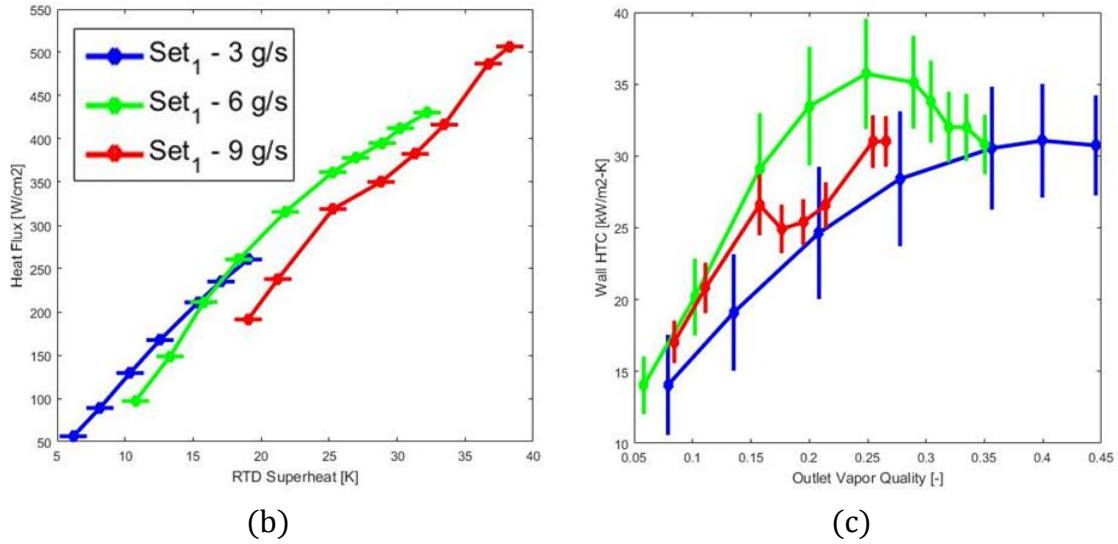


Fig. 7.7.4: Single-phase results for chip 3.

Two-phase testing was then performed. However, when testing at 6 g/s of refrigerant flow and upon exceeding  $350 \text{ W/cm}^2$ , hotspots were visible to the naked eye, as shown in Fig. 7.7.5(a). In order for the hotspots to be visible to the naked eye, local temperatures would have to exceed  $1000^\circ\text{C}$ . Furthermore, upon increasing the flow rate from 6 g/s to 9 g/s, a notable increase in superheat and a reduction in wall heat transfer coefficient at the same vapor quality were observed, as shown in Fig. 7.7.5(c), which is unlike the previous trends obtained with any of the previous chips. Finally, as heat flux exceeded  $500 \text{ W/cm}^2$ , a spark was observed and the current stopped, due to the burning of the heater in this region.



(a)



**Fig. 7.7.5: (a) Hotspots visible to the naked eye; (b) heat flux vs. RTD superheat; and (c) wall heat transfer coefficient vs. outlet vapor quality.**

The cause of this hotspot was then analyzed. Even if the heater were 2x thinner in this region, resulting in a heat flux 2x higher than background, conduction simulations have determined that surface temperatures would not reach the 1000°C required, due to spreading through the silicon substrate. The most likely way to achieve 1000°C temperature would be if the heater strip were locally delaminated from the silicon substrate—either directly from the adhesion layer, or if the adhesion layer and/or oxide layer were delaminated from the silicon substrate—resulting in a toaster-like heating coil (with a heat flux far exceeding that of a toaster). Thus, under these circumstances, even a narrow delaminated strip could exceed 1000°C. It is known from past chips that heater adhesion can be weak in localized areas, making it is easy to lift off sections of the heater with tape. It stands to reason that if the heater adhesion is weak enough that tape could cause delamination, thermal stresses from calibration or testing could cause delamination as well, resulting in the observed effect.

Accordingly, the heater was patched using silver paint, and calibration, single-phase tests, and two-phase tests were performed again. The calibration curve is given in

Fig. 7.7.3. The resistance drops notably, due to the patching of the heater with silver paint, which inevitably short-circuits part of the heater. The chip with the patched heater is shown in Fig. 7.7.6.

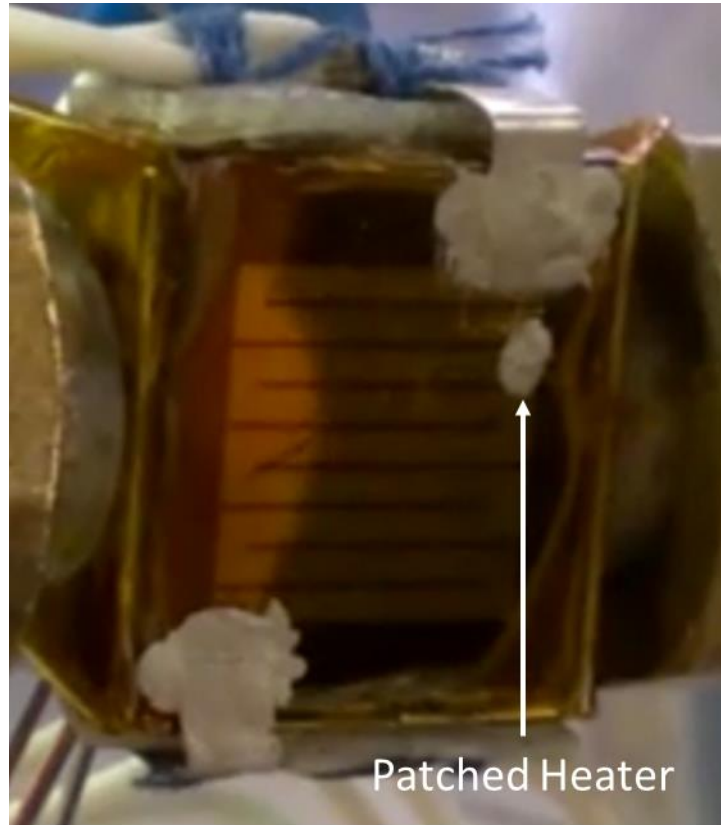


**Fig. 7.7.6: Chip 3 with patched heater.**

The single-phase tests results are shown in Fig. 7.7.7. It is clear that pressure drop increased slightly since the previous test, possibly due to particulate infiltration as the test section was exposed to air. The quantitative clogging analysis was then performed to determine if particulate clogging could explain the increased pressure drop. However, rather than curve-fit CFD to predict the effect of clogging, the experimental results obtained before the fix were curve-fitted instead and used as a reference such that the incremental amount of clogging could be estimated. Matching the experimentally measured pressure drops would imply that there was 14% more clogging than what was

previously observed. However, the heat transfer coefficient is not observed to decrease by the amount predicted. Accordingly, it is possible that the clogging was relatively uniform, resulting only in an increased pressure drop and a reduced or negligible effect on heat transfer coefficient.

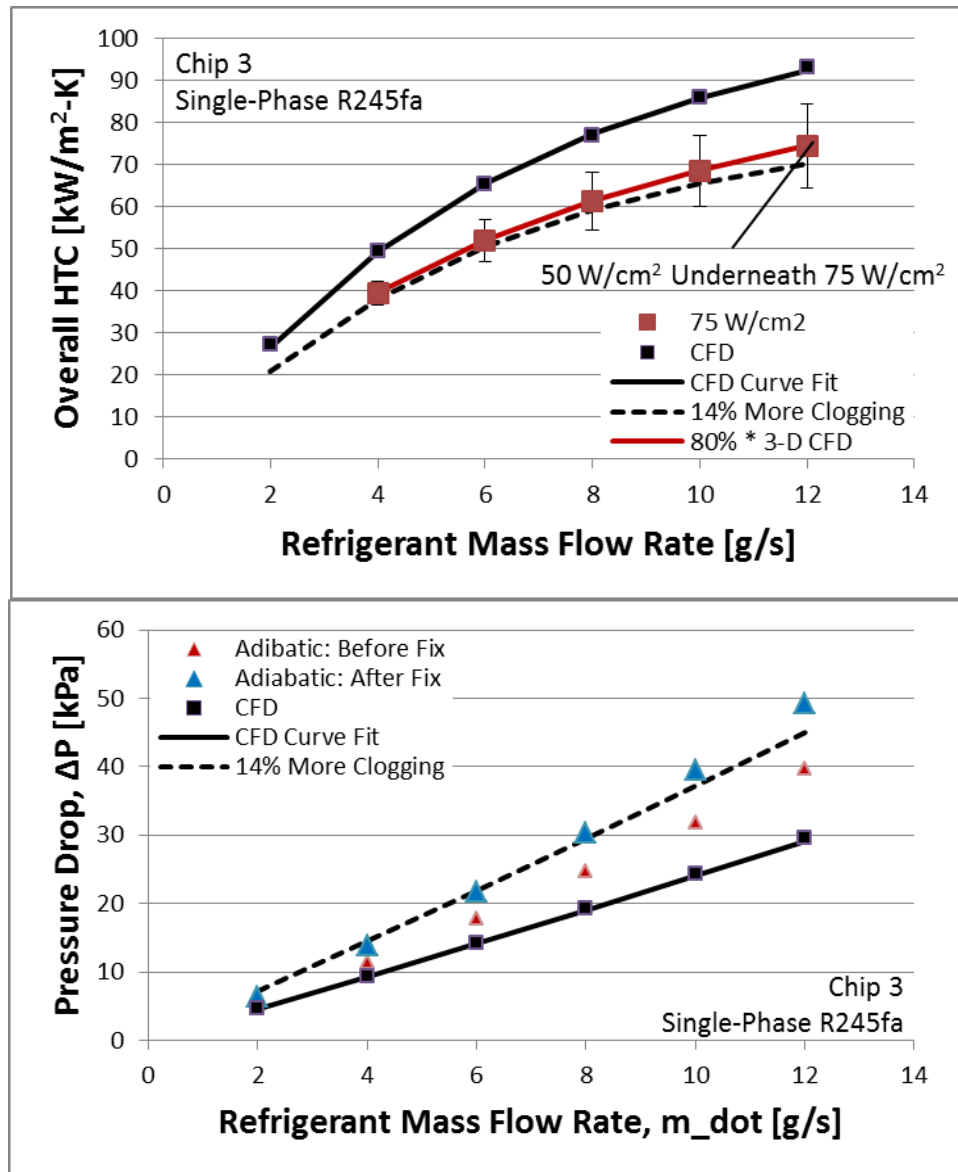
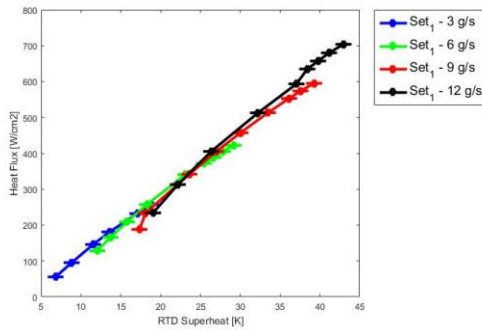


**Fig. 7.7.7: Single-phase results for chip 3 after fixing the heater.**

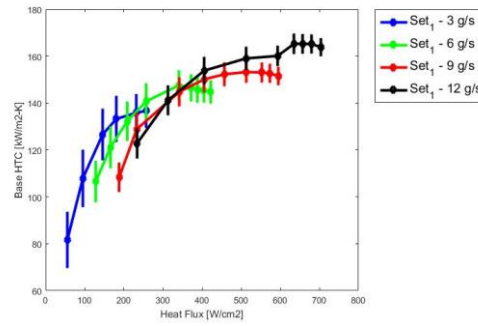
Finally, two-phase tests were conducted, the results of which are shown in Fig. 7.7.8. The two-phase results are very similar to those presented in the previous sections. A peak heat flux of 700 W/cm<sup>2</sup> was obtained at 27% vapor quality and 100 kPa total

pressure drop. However, it is worth noting that after testing the highest flow rate and heat flux ( $> 700 \text{ W/cm}^2$ ), a spark was observed and the oxide-nitride-oxide dielectric insulating layer was broken. Thus, the tests could not be repeated. Furthermore, for the highest flow rate, a sudden change in slope is observed for RTD superheat and heat transfer coefficients. It is thought that this change in slope is the result of the beginnings of dielectric breakdown. Thus, the RTD superheat and heat transfer coefficient measurements for these four data points are not considered to be accurate.

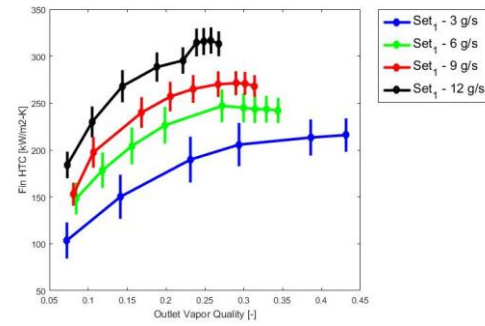
In addition, as before, an optimal flow rate was observed to produce a maximum base heat transfer coefficient for a given heat flux, as shown in Fig. 7.7.8(b). Furthermore, the optimal flow rate was observed to increase with increasing heat flux. An optimal vapor quality was also observed to produce a maximum heat transfer coefficient at vapor qualities ranging from 25-45%, as shown in Fig. 7.7.8(c)-(d), which is higher than that achieved for chip 2. Similarly, optimal vapor quality is observed to decrease with mass flow rate, and heat transfer coefficient for a given vapor quality is observed to increase with mass flow rate. Both of these results are consistent with chip 2. Finally, as shown in Fig. 7.7.8(e)-(f), pressure drop trends for both vapor quality and heat flux are consistent with those observed for chip 2.



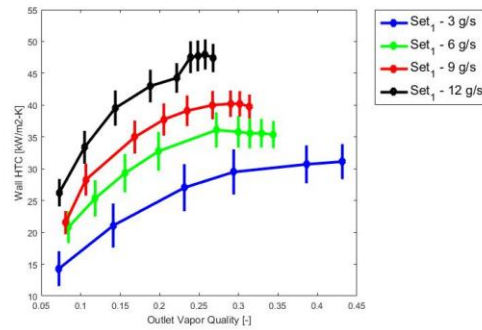
(a)



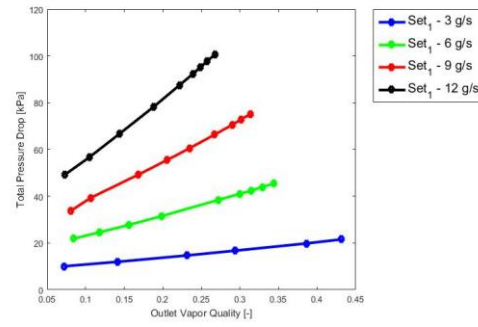
(b)



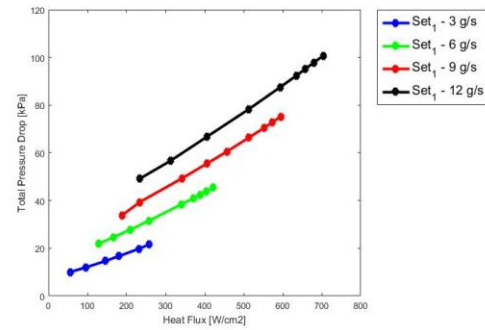
(c)



(d)



(e)



(f)

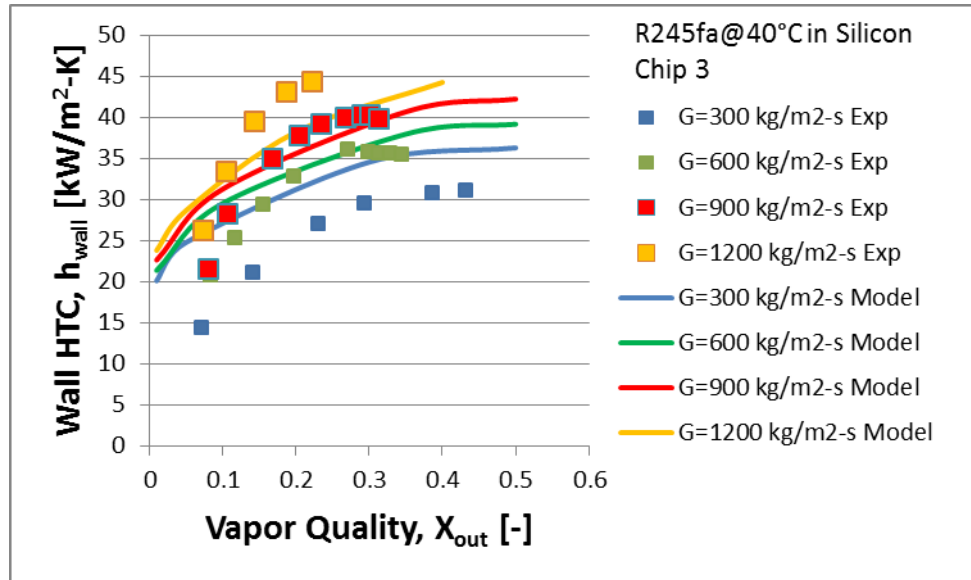
**Fig. 7.7.8: Two-phase results for chip 3: (a) heat flux vs. RTD superheat, (b) base heat transfer coefficient vs. heat flux, (c) fin heat transfer coefficient vs. outlet vapor quality, (d) wall heat transfer coefficient vs. outlet vapor quality, (e) total pressure drop vs. outlet vapor quality, and (f) total pressure drop vs. heat flux.**

## 7.8 *Comparison to Model*

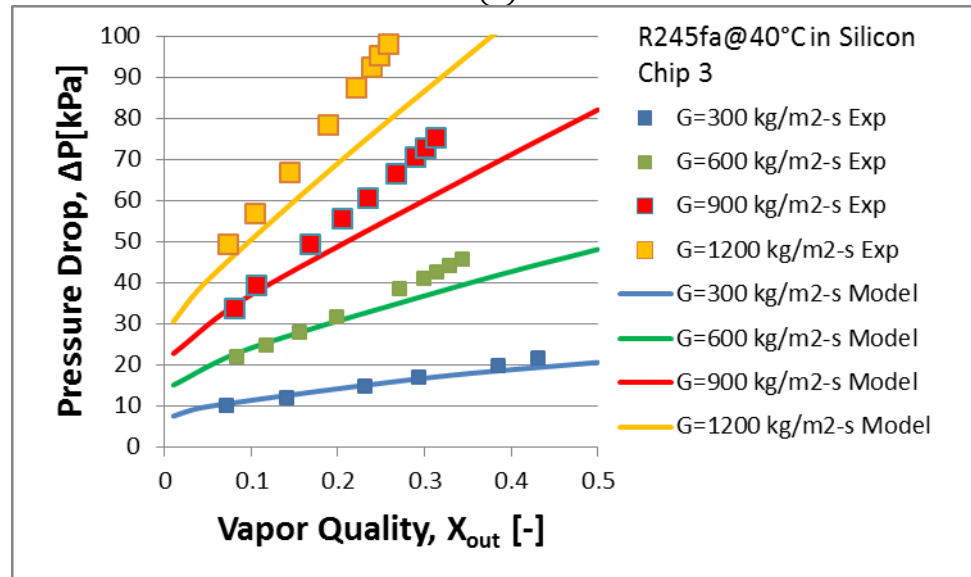
Finally, the results from test chip 3 were compared to the model as well, the results of which are shown in Fig. 7.8.1. Once again, wall heat transfer coefficients are observed to be the correct order of magnitude, and follow the correct trends. In addition, at moderate vapor qualities and mass flow rates, the model matches experimental data. However, as noted in Section 6.10, the model is less sensitive to mass flow rate than experiments.

Similarly, pressure drop predictions are the correct order of magnitude and match experimental trends. Pressure drop predictions are notably more accurate than heat transfer coefficient predictions, and most data points fall within 15% of the value predicted by the model (see Fig. 7.8.1(c)). The experimentally observed curves closely follow the model at low vapor qualities, though some deviation is observed at high vapor qualities, especially for high mass flow rates. Furthermore, it is worth noting that despite the presence of clogging observed during single-phase tests, the tapered channels are expected to have reduced pressure drop, due to the presence of large regions with wider channel width. Thus, the effective channel width might be lower than simulated, resulting in a noticeable difference between experiment and model, which is due to the clogging.

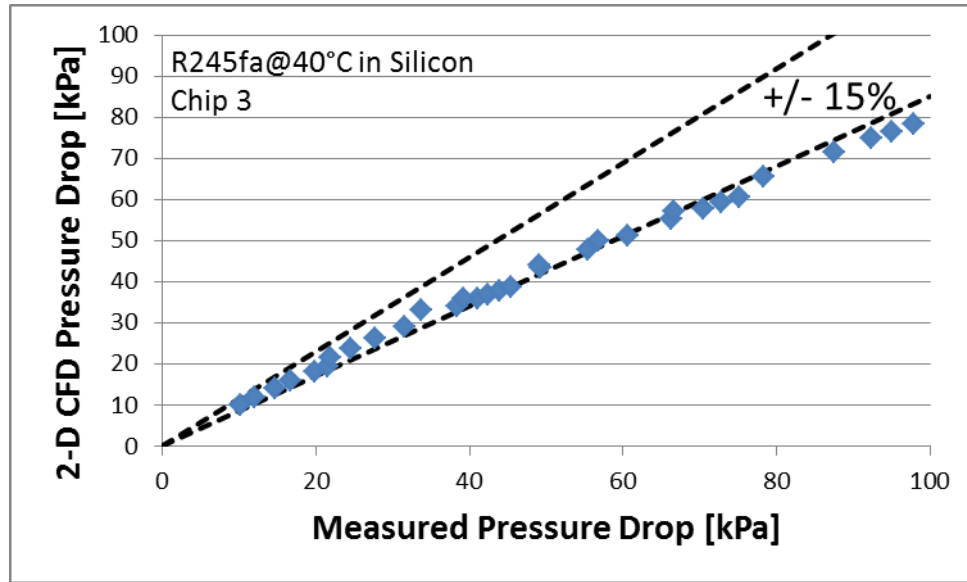




(a)



(b)



(c)

**Fig. 7.8.1: Test chip 3 two-phase results comparison to model: (a) wall heat transfer coefficient vs. vapor quality, (b) total pressure drop vs. vapor quality, and (c) comparison between predicted and measured pressure drop.**

## 7.9 Bonded FEEDS Experiments Summary

A 3-D printed header-manifold was designed to be directly bonded to the embedded Si chip, with the goal of reducing system volume as much as possible. Due to the rough surfaces after 3-D printed, processes for lapping, polishing, metalizing, and bonding the 3-D printed parts to the Si chips had to be developed. Hermetic bonds capable of withstanding up to 1600 psi were obtained. Three such bonded test sections were tested. Solder clogging of the microchannels prevented the first test section from achieving high vapor qualities, while an un-bonded manifold center limited the heat flux of the second test section. A hybrid bonding method was therefore attempted, and resulted in prevention of clogging and excellent bonding of the entire chip. Heat fluxes up to  $700 \text{ W/cm}^2$  were obtained at vapor qualities approaching 30%. However, difficulties with the heater prevented higher heat fluxes from being obtained. Finally, the

thermal and hydrodynamic performance was compared to the model, with correct order-of-magnitude and trends for heat transfer coefficient, and excellent agreement for pressure drop to within 15%.

## 8 Summary and Conclusions

In conclusion, an embedded, two-phase cooler utilizing FEEDS technology was investigated for compact and ultra-low thermal resistance high heat flux removal. Four independent preliminary modeling efforts have shed light on the governing physical phenomena, indicating the importance of nucleate boiling, annular film evaporation, void fraction correlation, single-phase fully developed and developing forced-convection, intra-microchannel flow distribution, and fin conduction. These preliminary models and their governing physics were combined into a 2.5-D master manifold-microchannel model using custom-coded CFD. The master model was first validated using single-phase 3-D CFD, where it was shown that both fully developed and developing flow could be accurately predicted, as long as the flow remains two-dimensional. The model was then validated for two-phase flow by comparing it to past experimental results, with correct orders of magnitude and trends for heat transfer coefficient, and a pressure drop prediction within 30% of experiment. The model was then used to design a geometry capable of meeting the ICECool metrics, during which a parametric study on the effects of various geometric parameters was performed. The working fluid was then selected using a system-level model based on ICECool metrics, and a manifold model was used to evaluate manifold flow configurations. In the end, a novel manifold flow configuration was determined to be necessary to obtain an even flow distribution in two-phase flow, and a manifold was designed to provide an even flow distribution over a wide range of flow rates and working fluids. Focus was then shifted to experiments, where a press-fit test section and a bonded test section were tested. Heat fluxes in excess of  $1 \text{ kW/cm}^2$  and vapor qualities approaching 45% were obtained with the press-fit test section, while heat

fluxes in excess of  $700 \text{ W/cm}^2$  and vapor qualities approaching 30% were obtained with the bonded test section.

## **8.1 *Major Contributions***

- (1) Demonstration of embedded, two-phase cooling concept in Si-based electronics, with ultra-low thermal resistance and operation at moderate vapor qualities. Future versions of this device should easily achieve high exit vapor quality and fully achieve the targeted design metrics.
- (2) Reduction in system volume and form-factor down to the same order of magnitude of the chip for integration into real-world systems without sacrificing flow distribution and performance;
- (3) Direct bonding of a 3-D printed part to an Si-based electronic device, capable of hermetic sealing and withstanding high pressures;
- (4) A deeper understanding of the governing physics from the preliminary modeling, including (a) numerical validation for the Zivi annular flow void fraction correlation; (b) determination that for the range of conditions considered here, void fraction correlation is a function of mass flux and channel width, with wider channel widths and higher mass fluxes resulting in a continuous shift from the annular, fully developed void fraction correlation to the Zivi annular void fraction correlation; (c) determination that film evaporation is dominant in the fully developed flow regime and is the reason why flow boiling correlations provide quantitatively and qualitatively inaccurate predictions, whereas nucleate boiling and forced convection are dominant in the developing flow regime and is the

reason why flow boiling correlations provide improved quantitative accuracy; (d) determination that the asymmetrical liquid feeding and heating causes large regions of dryout on the microchannel wall, which acts to increase heat transfer coefficients at low vapor qualities and reduce them at higher vapor qualities, resulting in a lower optimal heat transfer coefficient than exists for regular microchannels

- (5) Determination that for conditions for which manifold-microchannel flow remains two-dimensional, a simplified 2.5-D model is capable of accurately predicting heat transfer coefficient and pressure drop for single-phase fully developed and developing-flow;
- (6) Development of a novel, simplified 2.5-D model capable of assisting with two-phase design of experiments and parametric analysis, and able to predict correct qualitative trends for heat transfer coefficient, and accurate to within 15% and 30% when predicting two-phase pressure drop for fully developed and developing flow, respectively.

## **8.2 *Opportunities for Future Work***

There are many opportunities for future work for single-phase modeling, two-phase modeling, and experiments.

### **8.2.1 Recommended Single-Phase Modeling Future Work**

- (1) Further testing of the developing flow 2.5-D single-phase model under a wider range of geometries, mass flow rates, and fluids, in order to quantify the robustness of the simplified model;

- (2) Investigation into the dimensionless conditions under which the two-dimensional flow assumption in the 2.5-D single-phase model is valid, such that the accuracy of the model can be known a priori without performing 3-D simulations. This would allow the model can be used more generally without the need for 3-D validation and would enable the model to perform optimization on its own;
- (3) Investigation into potential means of correlating heat transfer coefficient enhancements due to 3-D secondary flows generated in manifold-microchannels, such that the 2.5-D model might still be capable of accurately predicting heat transfer coefficient and pressure drop when flow becomes three-dimensional.

### **8.2.2 Recommended Two-Phase Modeling Future Work**

- (1) Validation of annular film evaporation with physics-based void fraction model using 2-D VOF. The assumptions made in the film evaporation with physics based void fraction model can be put to the test using a 2-D Volume of Fluid (VOF) model. The void fraction, wall shear stress, and heat transfer coefficients can be compared to the simplified model to determine under what conditions the model is accurate.
- (2) Direct incorporation of annular film evaporation with physics-based void fraction equations into 2.5-D CFD microchannel model. The current 2.5-D CFD microchannel model did not directly implement the annular film evaporation with physics-based void fraction equations, but rather relied on the results from the preliminary model to indicate which void fraction correlation should be used. From the preliminary model, a gradual shift from the annular, fully developed void fraction correlation to the Zivi annular flow correlation is observed as mass

flux is increased. Accordingly, direct implementation of the annular film evaporation with physics-based void fraction correlation equations is preferable, and should give more accurate void fraction predictions and resulting heat transfer coefficients.

- (3) A more advanced “2.9-D” approach, wherein the SIMPLE algorithm would be solved separately for the liquid and vapor phases, and the void fraction would be computed by matching the liquid and vapor pressures directly. This suggestion is similar to directly implementing the annular film evaporation with physics-based void fraction equation directly into the 2.5-D model. However, this approach is different in that rather than treat the two phases as a mixture, it treats each phase separately. This allows for the outgoing vapor quality to be different in different directions, which is not possible using the mixture model. Thus, for adiabatic two-phase flow, the previous model would predict a uniform vapor quality everywhere, while the recommended model would allow the phases to separate.

### **8.2.3 Recommended Experimental Future Work**

- (1) Improvement to heater fabrication, to enable more robust heater contact and adhesion, improved dielectric strength, and heater uniformity to improve performance at high heat fluxes;
- (2) Fabrication of chips from thinner substrates and from higher thermal conductivity materials such as SiC to reduce conduction thermal resistance;
- (3) Fabrication of microchannels with more rectangular grooves to prevent intra-microchannel flow maldistribution;



- (4) Wider parametric study on effect of manifold and surface geometry, using a MEMS interposer to precisely control manifold dimensions;
- (5) Testing of additional fluids, such as ethanol and water (and comparing to 2.5-D model);
- (6) Flow visualization study to validate annular film evaporation with physics-based void fraction model and 2.5-D microchannel model.

## 9 Appendix A: Derivations of Equations Used in the Annular Film Evaporation with Physics-Based Void Fraction Model

In this section, length derivations for equations used in the annular film evaporation with physics-based void fraction model will be presented. First, the control volumes with which the continuity and momentum conservation equations can be derived will be presented. Then, the analysis used to arrive at an algebraic friction factor will be presented. Finally, the annular, fully developed void fraction correlation will be derived.

### 9.1 Model Equations

The control volumes for the annular film evaporation with physics-based void fraction model are shown in Fig. 9.1.1.

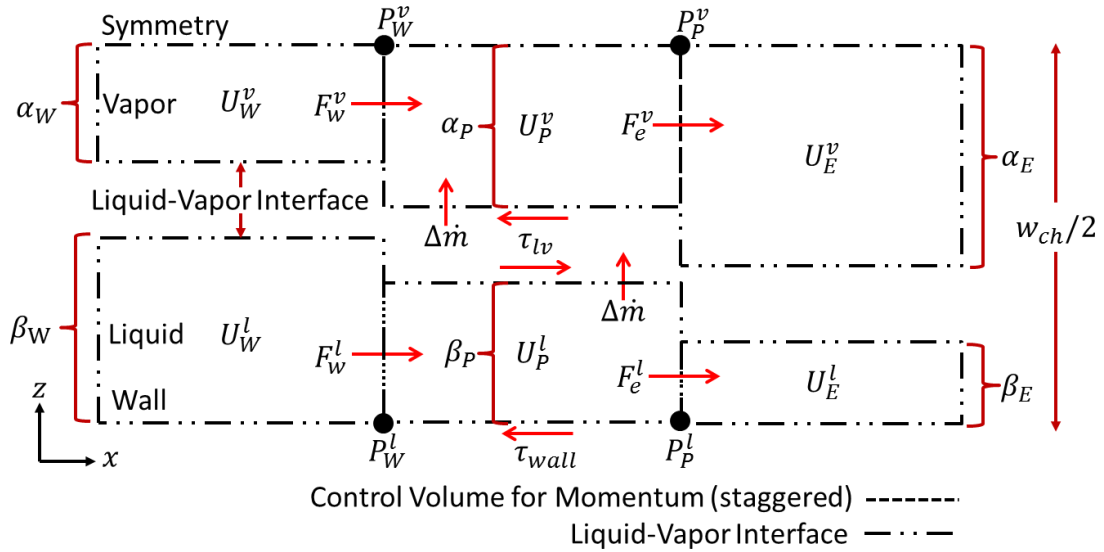


**Fig. 9.1.1: Control volumes used for discretization in the annular film evaporation with physics-based void fraction model.**

### 9.1.1 Continuity Equation for the Liquid Phase

Referring to the control volume shown in Fig. 9.1.1, the continuity equation for the liquid phase is

$$\rho_l \beta_W U_W^l - \rho_l \beta_E U_E^l = F_w^l - F_e^l = \Delta \dot{m} \quad (9.1.1)$$

### 9.1.2 Momentum Equation for the Liquid Phase

Referring to the control volume shown in Fig. 9.1.1, the momentum equation for the liquid phase is

$$\begin{aligned} 2S_p^l U_p^l + \Delta \dot{m} U_p^l + (D_w^l + [-F_w^l, 0])U_p^l + (D_e^l + [F_e^l, 0])U_p^l \\ = (D_w^l + [F_w^l, 0])U_w^l + (D_e^l + [-F_e^l, 0])U_e^l \\ + A^l(P_w^l - P_e^l) + S_p^l U_{lv} \end{aligned} \quad (9.1.2)$$

Multiplying Eq. (9.1.1) by  $U_p^l$ :

$$F_w^l U_p^l - F_e^l U_p^l = \Delta \dot{m} U_p^l \quad (9.1.3)$$

Adding Eq. (9.1.2) and (9.1.3) yields,

$$\begin{aligned} 2S_p^l u_p^l + (D_w^l + F_w^l + [-F_w^l, 0])U_p^l \\ + (D_e^l + [F_e^l, 0] - F_e^l)U_p^l \\ = (D_w^l + [F_w^l, 0])U_w^l + (D_e^l + [-F_e^l, 0])U_e^l \\ + A^l(P_w^l - P_e^l) + S_p^l U_{lv} \end{aligned} \quad (9.1.4)$$

Simplifying Eq. (9.1.4) using the identity:  $[F, 0] - [-F, 0] = F$  yields,

$$2S_p^l U_p^l + (D_w^l + [F_w^l, 0])U_p^l + (D_e^l + [-F_e^l, 0])U_p^l \quad (9.1.5)$$

$$\begin{aligned}
&= (D_w^l + [F_w^l, 0])U_w^l + (D_e^l + [-F_e^l, 0])U_e^l \\
&+ A^l(P_w^l - P_e^l) + S_P^l U_{lv}
\end{aligned}$$

Thus, the momentum equation for the liquid phase can be expressed as

$$a_P^l U_P^l = a_W^l U_W^l + a_E^l U_E^l + b^l + A^l(P_w^l - P_e^l) \quad (9.1.6)$$

where

$$a_P^l = a_W^l + a_E^l + 2S_P^l \quad (9.1.7)$$

$$a_W^l = D_w^l + [F_w^l, 0] \quad (9.1.8)$$

$$a_E^l = D_e^l + [-F_e^l, 0] \quad (9.1.9)$$

$$b^l = S_P^l U_{lv} \quad (9.1.10)$$

### 9.1.3 Continuity Equation for the Vapor Phase

The continuity equation for the secondary phase is:

$$\rho_v \alpha_W U_W^v - \rho_v \alpha_E U_E^v = F_w^v - F_e^v + \Delta \dot{m} = 0 \quad (9.1.11)$$

### 9.1.4 Momentum Equation for the Vapor Phase

The momentum equation for the secondary phase:

$$\begin{aligned}
&S_P^v U_P^v + (D_w^v + [-F_w^v, 0])U_P^v + (D_e^v + [F_e^v, 0])U_P^v \\
&= (D_w^v + [F_w^v, 0])U_W^v + (D_e^v + [-F_e^v, 0])U_E^v \\
&+ A^v(P_w^v - P_e^v) + \Delta \dot{m} U_P^l + S_P^v U_{lv}
\end{aligned} \quad (9.1.12)$$

Multiplying Eq. (9.1.11) by  $U_P^v$ ,

$$F_w^v U_P^v - F_e^v U_P^v + \Delta \dot{m} U_P^v = 0 \quad (9.1.13)$$

Adding Eq. (9.1.12) and (9.1.13) yields

$$\begin{aligned}
& S_P^v U_P^v + (D_W^v + F_W^v + [-F_W^v, 0])U_P^v + (D_e^v + [F_e^v, 0] - F_e^v)U_P^v \\
& \quad + \Delta\dot{m} U_P^v \\
& = (D_W^v + [F_W^v, 0])U_W^v + (D_e^v + [-F_e^v, 0])U_E^v \\
& \quad + A^v(P_W^v - P_e^v) + \Delta\dot{m} U_P^l + S_P^v U_{lv}
\end{aligned} \tag{9.1.14}$$

Simplifying Eq. (9.1.14) using the identity  $[F, 0] - [-F, 0] = F$ ,

$$\begin{aligned}
& S_P^v U_P^v + (D_W^v + [F_W^v, 0])U_P^v + (D_e^v + [-F_e^v, 0])U_P^v + \Delta\dot{m} U_P^v \\
& = \Delta\dot{m} U_P^l + (D_W^v + [F_W^v, 0])U_W^v + (D_e^v + [-F_e^v, 0])U_E^v \\
& \quad + A^v(P_W^v - P_e^v) + S_P^v U_{lv}
\end{aligned} \tag{9.1.15}$$

Thus, the momentum equation for the vapor phase can be expressed as

$$a_P^v U_P^v = a_W^v U_W^v + a_E^v U_E^v + b^v + A^v(P_W^v - P_e^v) \tag{9.1.16}$$

where

$$a_P^v = a_W^v + a_E^v + S_P^v + \Delta\dot{m} \tag{9.1.17}$$

$$a_W^v = D_W^v + [F_W^v, 0] \tag{9.1.18}$$

$$a_E^v = D_e^v + [-F_e^v, 0] \tag{9.1.19}$$

$$b^v = \Delta\dot{m} U_P^l + S_P^v U_{lv} \tag{9.1.20}$$

### 9.1.5 Momentum Equation for the Mixture

Combining Eqs. (9.1.6) and (9.1.16), and using the identity  $A^l + A^v = 1$  results in one momentum equation:

$$\begin{aligned}
& a_P^l U_P^l + a_P^v U_P^v = a_W^l U_W^l + a_W^v U_W^v + a_E^l U_E^l + a_E^v U_E^v + P_w - P_e \\
& \quad - A^l(P_w^c - P_e^c)
\end{aligned} \tag{9.1.21}$$

Defining  $a = a^l + a^v$ , we can rewrite the convective and diffusive neighboring coefficients of Eq. (9.1.21) as

$$a_P^l U_P^l + a_P^v U_P^v = a_P U_P + a_P^l (U_P^l - U_P) + a_P^v (U_P^v - U_P) \quad (9.1.22)$$

$$a_W^l U_W^l + a_W^v U_W^v = a_W U_W + a_W^l (U_W^l - U_W) + a_W^v (U_W^v - U_W) \quad (9.1.23)$$

$$a_E^l U_E^l + a_E^v U_E^v = a_E U_E + a_E^l (U_E^l - U_E) + a_E^v (U_E^v - U_E) \quad (9.1.24)$$

Thus, we can rewrite the mixture momentum equation in the familiar form:

$$a_P U_P = a_W U_W + a_E U_E + b + P_w - P_e \quad (9.1.25)$$

where

$$a_P = a_P^l + a_P^v \quad (9.1.26)$$

$$a_W = a_W^l + a_W^v \quad (9.1.27)$$

$$a_E = a_E^l + a_E^v \quad (9.1.28)$$

$$\begin{aligned} b = & b^l + b^v + a_W^l U_W^l + a_W^v U_W^v - a_W U_W + a_E^l U_E^l + a_E^v U_E^v - a_E U_E \\ & + a_P U_P - a_P^l U_P^l - a_P^v U_P^v - A^l (P_w^c - P_e^c) \end{aligned} \quad (9.1.29)$$

It is worth noting that since, by definition,  $F = F^l + F^v$ , then  $D = D^l + D^v$ . In addition, since,

$$D^l = (1 - \alpha)\mu_l/\Delta x \quad (9.1.30)$$

and

$$D^v = \alpha\mu_v/\Delta x \quad (9.1.31)$$

If we define  $D = \mu/\Delta x$ , then  $\mu$  is the area-averaged (homogenous) viscosity:

$$\mu = (1 - \alpha)\mu_l + \alpha\mu_v \quad (9.1.32)$$

### 9.1.6 Equation for Volume Fraction

An equation for liquid volume fraction can be derived by dividing Eq. (9.1.16) by  $A^v$  and subtracting the result from Eq. (9.1.6) divided by  $A^l$ , yielding

$$\begin{aligned} \frac{a_P^v}{A^v} U_P^v - \frac{a_P^l}{A^l} U_P^l &= \frac{a_W^v}{A^v} U_W^v - \frac{a_W^l}{A^l} U_W^l + \frac{a_E^v}{A^v} U_E^v - \frac{a_E^l}{A^l} U_E^l + \left( \frac{b^v}{A^v} - \frac{b^l}{A^l} \right) + (P_W^v - P_W^l) \\ &\quad - (P_E^v - P_E^l) \end{aligned} \quad (9.1.33)$$

The Young-Laplace equation relates the liquid pressure to the vapor pressure by

$$P^v - P^l = P^c \quad (9.1.34)$$

Substituting (9.1.34) into Eq. (9.1.33) and simplifying results in

$$\begin{aligned} \frac{a_P^v}{A^v} U_P^v - \frac{a_P^l}{A^l} U_P^l &= \frac{a_W^v}{A^v} U_W^v - \frac{a_W^l}{A^l} U_W^l + \frac{a_E^v}{A^v} U_E^v - \frac{a_E^l}{A^l} U_E^l + \left( \frac{b^v}{A^v} - \frac{b^l}{A^l} \right) + P_W^c \\ &\quad - P_E^c \end{aligned} \quad (9.1.35)$$

Since, by definition,  $U^l = \frac{F^l}{\rho_l \beta}$  and  $U^v = \frac{F^v}{\rho_v(1-\beta)}$ , Eq. (9.1.35) can be re-written as

$$\begin{aligned} \frac{a_P^v}{A^v} \frac{F_P^v}{\rho_v(1-\beta_P)} - \frac{a_P^l}{A^l} \frac{F_P^l}{\rho_l \beta_P} \\ &= \frac{a_W^v}{A^v} \frac{F_W^v}{\rho_v(1-\beta_W)} - \frac{a_W^l}{A^l} \frac{F_W^l}{\rho_l \beta_W} + \frac{a_E^v}{A^v} \frac{F_E^v}{\rho_v(1-\beta_E)} - \frac{a_E^l}{A^l} \frac{F_E^l}{\rho_l \beta_E} \\ &\quad + \left( \frac{b^v}{A^v} - \frac{b^l}{A^l} \right) + P_W^c - P_E^c \end{aligned} \quad (9.1.36)$$

Defining  $A_i^l = \frac{a_i^l F_i^l}{A^l \rho_l}$  and  $A_i^v = \frac{a_i^v F_i^v}{A^v \rho_v}$ , Eq. (9.1.36) can be re-written in condensed

form:

$$\begin{aligned} \frac{A_P^v}{(1-\beta_P)} - \frac{A_P^l}{\beta_P} &= \frac{A_W^v}{(1-\beta_W)} - \frac{A_W^l}{\beta_W} + \frac{A_E^v}{(1-\beta_E)} - \frac{A_E^l}{\beta_E} + \left( \frac{b^v}{A^v} - \frac{b^l}{A^l} \right) \\ &\quad + P_W^c - P_E^c \end{aligned} \quad (9.1.37)$$

Since the volume fractions appear in the denominator, they must be linearized:

$$\begin{aligned}\frac{A_P^v}{(1-\beta_P)} &= \frac{A_P^v}{(1-\bar{\beta}_P)} + \frac{A_P^v}{(1-\bar{\beta}_P)^2}(\beta_P - \bar{\beta}_P) \\ &= A_P^v \frac{(1-2\bar{\beta}_P)}{(1-\bar{\beta}_P)^2} + \frac{A_P^v}{(1-\bar{\beta}_P)^2}\beta_P\end{aligned}\tag{9.1.38}$$

$$\begin{aligned}\frac{A_W^v}{(1-\beta_W)} &= \frac{A_W^v}{(1-\bar{\beta}_W)} + \frac{A_W^v}{(1-\bar{\beta}_W)^2}(\beta_W - \bar{\beta}_W) \\ &= A_W^v \frac{(1-2\bar{\beta}_W)}{(1-\bar{\beta}_W)^2} + \frac{A_W^v}{(1-\bar{\beta}_W)^2}\beta_W\end{aligned}\tag{9.1.39}$$

$$\begin{aligned}\frac{A_E^v}{(1-\beta_E)} &= \frac{A_E^v}{(1-\bar{\beta}_E)} + \frac{A_E^v}{(1-\bar{\beta}_E)^2}(\beta_E - \bar{\beta}_E) \\ &= A_E^v \frac{(1-2\bar{\beta}_E)}{(1-\bar{\beta}_E)^2} + \frac{A_E^v}{(1-\bar{\beta}_E)^2}\beta_E\end{aligned}\tag{9.1.40}$$

$$-\frac{A_P^l}{\beta_P} = -\frac{A_P^l}{\bar{\beta}_P} + \frac{A_P^l}{\bar{\beta}_P^2}(\beta_P - \bar{\beta}_P) = -2\frac{A_P^l}{\bar{\beta}_P} + \frac{A_P^l}{\bar{\beta}_P^2}\beta_P\tag{9.1.41}$$

$$-\frac{A_W^l}{\beta_W} = -\frac{A_W^l}{\bar{\beta}_W} + \frac{A_W^l}{\bar{\beta}_W^2}(\beta_W - \bar{\beta}_W) = -2\frac{A_W^l}{\bar{\beta}_W} + \frac{A_W^l}{\bar{\beta}_W^2}\beta_W\tag{9.1.42}$$

$$-\frac{A_E^l}{\beta_E} = -\frac{A_E^l}{\bar{\beta}_E} + \frac{A_E^l}{\bar{\beta}_E^2}(\beta_E - \bar{\beta}_E) = -2\frac{A_E^l}{\bar{\beta}_E} + \frac{A_E^l}{\bar{\beta}_E^2}\beta_E\tag{9.1.43}$$

Substituting Eqs. (9.1.38)-(9.1.43) into Eq. (9.1.37) and combining like terms results in the final form of the volume fraction equation:



$$\begin{aligned}
& \left( \frac{A_P^l}{\overline{\beta_P}^2} + \frac{A_P^v}{(1 - \overline{\beta_P})^2} \right) \beta_P = \\
& \left( \frac{A_W^l}{\overline{\beta_W}^2} + \frac{A_W^v}{(1 - \overline{\beta_W})^2} \right) \beta_W + \\
& \left( \frac{A_E^l}{\overline{\beta_E}^2} + \frac{A_E^v}{(1 - \overline{\beta_E})^2} \right) \beta_E + \\
& P_W^c - P_E^c + 2 \left( \frac{A_P^l}{\overline{\beta_P}} - \frac{A_W^l}{\overline{\beta_W}} - \frac{A_P^l}{\overline{\beta_P}} \right) -
\end{aligned} \tag{9.1.44}$$

$$\left( A_P^v \frac{(1 - 2\overline{\beta_P})}{(1 - \overline{\beta_P})^2} - A_W^v \frac{(1 - 2\overline{\beta_W})}{(1 - \overline{\beta_W})^2} - A_E^v \frac{(1 - 2\overline{\beta_E})}{(1 - \overline{\beta_E})^2} \right) + \left( \frac{b^v}{A^v} - \frac{b^l}{A^l} \right)$$

The capillary pressures,  $P_W^c$  and  $P_E^c$ , can be computed from

$$P_W^c = \sigma \frac{\delta''}{(1 + (\delta')^2)^{1.5}} = \frac{\sigma}{\Delta x^2} \frac{w_{ch}}{2} \frac{\beta_W + \beta_E - 2\beta_P}{\left(1 + \left(\frac{\partial \beta}{\partial x}\right)^2\right)^{\frac{3}{2}}} = s_0(\beta_W + \beta_E - 2\beta_P) \tag{9.1.45}$$

$$P_E^c = \sigma \frac{\delta''}{(1 + (\delta')^2)^{1.5}} = \frac{\sigma}{\Delta x^2} \frac{w_{ch}}{2} \frac{\beta_P + \beta_{EE} - \beta_E}{\left(1 + \left(\frac{\partial \beta}{\partial x}\right)^2\right)^{\frac{3}{2}}} = s_0(\beta_P + \beta_{EE} - 2\beta_E) \tag{9.1.46}$$

$$\begin{aligned}
P_W^c - P_E^c &= s_0(\beta_W + \beta_E - 2\beta_P) - s_0(\beta_P + \beta_{EE} - 2\beta_E) \\
&= s_0(\beta_W - 3\beta_P + 3\beta_E - \beta_{EE})
\end{aligned} \tag{9.1.47}$$

where

$$s_0 = \frac{\frac{\sigma}{\Delta x^2} \frac{w_{ch}}{2}}{\left(1 + \left(\frac{\partial \beta}{\partial x}\right)^2\right)^{\frac{3}{2}}} \tag{9.1.48}$$

$$\frac{\partial \beta}{\partial x} = \frac{\frac{1}{12} \overline{\beta_{WW}} - \frac{2}{3} \overline{\beta_W} + \frac{2}{3} \overline{\beta_E} - \frac{1}{12} \overline{\beta_{EE}}}{\Delta x} \quad (9.1.49)$$

Thus, the volume fraction equation can be expressed as

$$A_P \beta_P = A_W \beta_W + A_E \beta_E + B \quad (9.1.50)$$

where

$$A_P = \left( \frac{A_P^l}{\overline{\beta_P}^2} + \frac{A_P^v}{(1 - \overline{\beta_P})^2} \right) + 3s_0 \quad (9.1.51)$$

$$A_W = \left( \frac{A_W^l}{\overline{\beta_W}^2} + \frac{A_W^v}{(1 - \overline{\beta_W})^2} \right) + s_0 \quad (9.1.52)$$

$$A_E = \left( \frac{A_E^l}{\overline{\beta_E}^2} + \frac{A_E^v}{(1 - \overline{\beta_E})^2} \right) + 3s_0 \quad (9.1.53)$$

$$A_{EE} = -s_0 \quad (9.1.54)$$

$$\begin{aligned} B = 2 \left( \frac{A_P^l}{\overline{\beta_P}} - \frac{A_W^l}{\overline{\beta_W}} - \frac{A_E^l}{\overline{\beta_E}} \right) \\ - \left( A_P^v \frac{(1 - 2\overline{\beta_P})}{(1 - \overline{\beta_P})^2} - A_W^v \frac{(1 - 2\overline{\beta_W})}{(1 - \overline{\beta_W})^2} - A_E^v \frac{(1 - 2\overline{\beta_E})}{(1 - \overline{\beta_E})^2} \right) \\ + \left( \frac{b^v}{A^v} - \frac{b^l}{A^l} \right) \end{aligned} \quad (9.1.55)$$

### 9.1.7 Equation for Liquid Quality

Finally, following the procedure outline in Patankar [57], the conservation of species equation can be written simply as a convection equation. Using the continuity control volumes, the governing equation can be written as follows:

$$a_P^q Y_P = a_W^q Y_W + a_E^q Y_E + b^q \quad (9.1.56)$$

where the neighboring coefficients  $a_W^q$  and  $a_E^q$  are calculated using upwind discretization, as in Patankar [57]:

$$a_W^q = [F_w, 0] \quad (9.1.57)$$

$$a_E^q = [-F_e, 0] \quad (9.1.58)$$

$$a_P^q = a_W^q + a_E^q \quad (9.1.59)$$

The source term,  $b^q$ , is the amount of evaporated liquid per unit length. Since it is assumed that all heat transfer occurs via direct conduction through the thin liquid film, the evaporation rate potential can be calculated as

$$\Delta \dot{m}_{potential} = \frac{k_l}{\delta} \frac{2 \Delta x}{w_{ch} h_{fg}} (T_{wall} - T_{sat}) \quad (9.1.60)$$

where the film thickness,  $\delta$ , is calculated from the geometric relationship between the void fraction and the microchannel geometry:

$$\delta = \beta \frac{w_{ch}}{2} \quad (9.1.61)$$

It is worth noting that for vapor qualities approaching one, the evaporation will approach infinity. Under these conditions, more mass than is entering the control volume will be evaporating, thereby violating conservation of liquid species. For this reason, the evaporation rate must be limited by the amount of liquid entering the cell, which is calculated as

$$\Delta \dot{m}_{max} = a_W^q Y_W + a_E^q Y_E \quad (9.1.62)$$

The final evaporation rate is then equal to the minimum of the evaporation potential,  $\Delta \dot{m}_{potential}$ , and the amount of liquid entering the cell,  $\Delta \dot{m}_{max}$ :

$$\Delta \dot{m}_{evap} = \min[\Delta \dot{m}_{potential}, \Delta \dot{m}_{max}] \quad (9.1.63)$$

The source term,  $b^q$ , is then related to the evaporation rate by:

$$b^q = -\Delta\dot{m}_{evap} \tag{9.1.64}$$

## 9.2 Algebraic Solution for Friction Factor Source Term

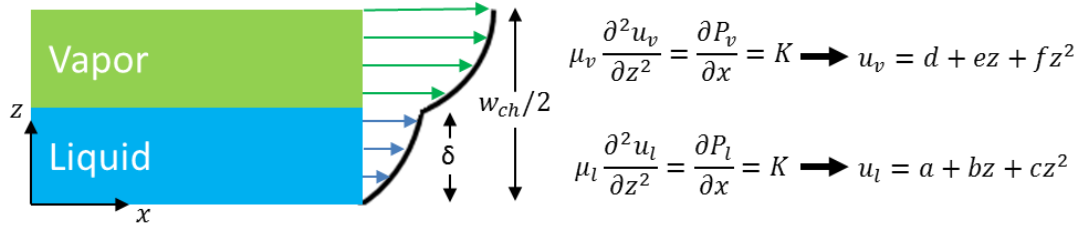


**Fig. 9.2.1: Assumed velocity profiles.**

In this section, an algebraic approach for computing the fully developed friction factor in two-phase, laminar flow will be detailed. The only assumption required for this approach is that the liquid and vapor velocity profiles are quadratic. For the case of fully developed, laminar, annular, adiabatic two-phase flow, the momentum equations reduce to

$$\mu_l \frac{\partial^2 u_l}{\partial z^2} = \frac{\partial P_l}{\partial x} = K = \mu_v \frac{\partial^2 u_v}{\partial z^2} = \frac{\partial P_v}{\partial x} \quad (9.2.1)$$

Accordingly, Eq. (9.2.1) can be integrated to obtain quadratic velocity profiles for the liquid and vapor phases. Thus, the quadratic velocity profile is the exact velocity profile for fully developed condition. However, we can assume quadratic velocity profile even if the flow is not fully developed. The assumed velocity profiles take the form,

$$u_l = a + bz + cz^2 \quad (9.2.2)$$

$$u_v = d + ez + fz^2 \quad (9.2.3)$$

where  $a, b, c, d, e,$  and  $f$  are yet to be determined constants. The following boundary conditions are then applied:

$$u_l(z = 0) = 0 = a \quad (9.2.4)$$

$$U_{lv} = u_l(z = \delta) = a + b\delta + c\delta^2 \quad (9.2.5)$$

$$U_{lv} = u_v(z = \delta) = d + e\delta + f\delta^2 \quad (9.2.6)$$

$$\tau_{lv} = \mu_l \left( \frac{du_l}{dz} \right)_{z=\delta} = \mu_l(b + 2c\delta) \quad (9.2.7)$$

$$\tau_{lv} = \mu_v \left( \frac{du_v}{dz} \right)_{z=\delta} = \mu_v(e + 2f\delta) \quad (9.2.8)$$

$$\left( \frac{du_v}{dz} \right)_{z=w_{ch}/2} = 0 = e + fw_{ch} \quad (9.2.9)$$

$$\tau_{wall} = \mu_l \left( \frac{du_l}{dz} \right)_{z=0} = \mu_l b \quad (9.2.10)$$

where  $U_{lv}$ ,  $t_{wall}$ , and  $\tau_{lv}$  are yet unknown constants. The average liquid and vapor velocities,  $U_l$  and  $U_v$  can be calculated by integrating Eqs. (9.2.2)-(9.2.3):

$$U_l = \frac{1}{\delta} \int_0^\delta u_l dz = \left( \frac{ay + \frac{b}{2}z^2 + \frac{c}{3}z^3}{\delta} \right) \Big|_0^\delta = a + \frac{b}{2}\delta + \frac{c}{3}\delta^2 \quad (9.2.11)$$

$$\begin{aligned} U_v &= \frac{1}{w_{ch}/2 - \delta} \int_\delta^{w_{ch}/2} u_v dz \\ &= d + \frac{e}{2} \left( \frac{w_{ch}}{2} + \delta \right) + \frac{f}{3} \left( \left( \frac{w_{ch}}{2} \right)^2 + \frac{w_{ch}}{2} \delta + \delta^2 \right) \end{aligned} \quad (9.2.12)$$

Thus, we have 12 variables— $a, b, c, d, e, f, \delta, U_{lv}, \tau_{wall}, \tau_{lv}, U_l$  and  $U_v$ —and 9 equations—Eqs. (9.2.4)-(9.2.12). If  $U_l$ ,  $U_v$ , and  $\delta$  are known inputs, then all remaining variables can be determined. After solving the system,  $U_{lv}$  can be expressed as

$$U_{lv} = \frac{6S_1 U_l \alpha + 3U_v \beta}{4S_1 \alpha + 3\beta} \quad (9.2.13)$$

where  $\beta = \frac{2\delta}{w_{ch}}$ ,  $\alpha = 1 - \beta$ , and  $S_1 = \frac{\mu_l}{\mu_v}$ .

In addition, the integral force per volume on the liquid volume,  $F_{vol}^l$ , due to the shear stress at the wall and liquid-vapor interface, is

$$\begin{aligned}
F_{vol}^l &= \frac{2(\tau_{lv} - \tau_{wall})}{w_{ch}} = \frac{2(\mu_l(b + 2c\delta) - \mu_l b)}{w_{ch}} = 2\mu_l \beta c \\
&= \frac{24\mu_l}{\beta w_{ch}^2} (U_{lv} - 2U_l)
\end{aligned} \tag{9.2.14}$$

Similarly, the integral force on the vapor,  $F_{vol}^v$ , due to the shear stress on the liquid vapor interface is

$$F_{vol}^v = \frac{-2\tau_{lv}}{w_{ch}} = \frac{-2\mu_v(e + 2f\delta)}{w_{ch}} = 2\mu_v \alpha f = \frac{12\mu_v}{\alpha w_{ch}^2} (U_{lv} - U_v) \tag{9.2.15}$$

Thus, Eqs. (9.2.15) and (9.2.16) can be used to provide source terms to simulate friction in laminar, two-phase, fully developed flow. It is worth noting that for numerical stability, the source term is broken into two parts: (1)  $S_P$ : an implicit, linearizable component with respect to  $U_l$  and  $U_v$ , and (2)  $S_C$ : an explicit source term proportional to  $U_{lv}$ . Although  $U_{lv}$ , as seen from Eq. (9.2.13), contains linear terms with respect to  $U_l$  and  $U_v$ , one need not substitute in the expression for  $U_{lv}$  in order to linearize its components.

For the liquid phase, the source term takes the form,

$$S^l = S_C^l - S_P^l U_l = \Delta x \Delta y F_{vol}^l \tag{9.2.16}$$

where

$$S_C^l = \frac{24\mu_l \Delta x \Delta y}{\beta w_{ch}^2} U_{lv} \tag{9.2.17}$$

$$S_P^l = \frac{48\mu_l \Delta x \Delta y}{\beta w_{ch}^2} \tag{9.2.18}$$

Similarly, for the vapor phase, the source term takes the form,

$$S^v = S_C^v - S_P^v U_v = \Delta x \Delta y F_{vol}^v \tag{9.2.19}$$

where

$$S_C^v = \frac{12\mu_v \Delta x \Delta y}{\alpha w_{ch}^2} U_{lv} \quad (9.2.20)$$

$$S_P^v = \frac{12\mu_v \Delta x \Delta y}{\alpha w_{ch}^2} \quad (9.2.21)$$

### 9.3 Fully Developed Void Fraction

An analytical solution for fully developed annular flow exists. While the algebraic solution obtained above also assumes a quadratic profile for the liquid and vapor velocities, further simplification can be made if fully developed conditions are assumed. Under fully developed conditions, where the liquid vapor interface is flat and capillary action negligible, the Young-Laplace equation can be differentiated with respect to  $x$  to show that pressure drops in the liquid and vapor must be equal, that is,

$$\frac{\partial P_l^*}{\partial x} = \frac{\partial P_v^*}{\partial x} \quad (9.3.1)$$

where the superscript  $*$  is used to indicate the fully developed value.

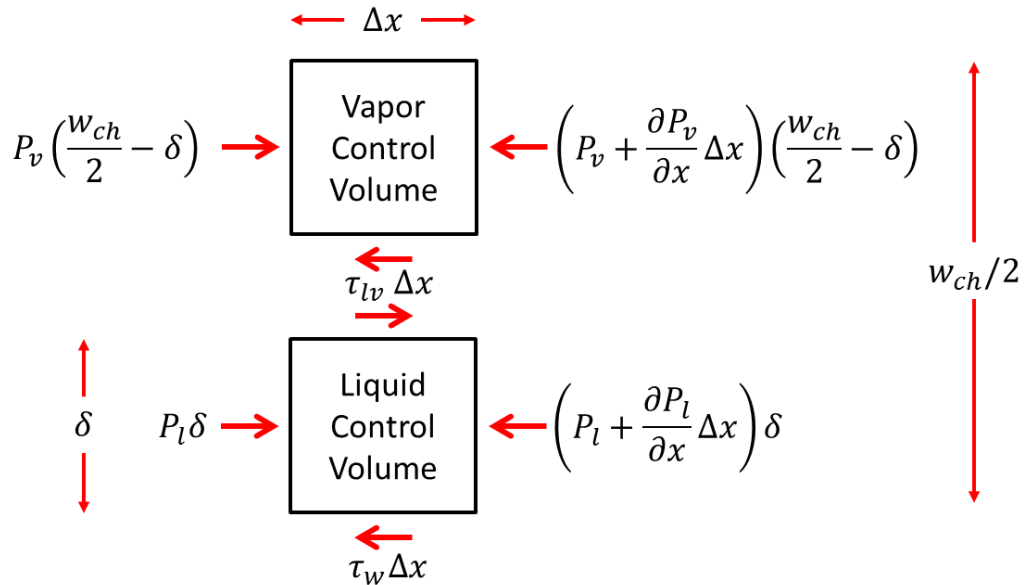


**Fig. 9.3.1: Control volumes to derive pressure drops per unit length for the liquid and vapor phases.**



The relationship between pressure drop and the shear stresses on the wall and liquid vapor interface can be derived by applying a control volume across the liquid and vapor, as shown in Fig. 9.3.1.

For the liquid, the pressure drop is caused by the difference in shear stresses on the wall and the liquid-vapor interface:

$$P_l \delta - \left( P_l + \frac{\partial P_l}{\partial x} \Delta x \right) \delta + (\tau_{lv} - \tau_w) \Delta x = 0 \quad (9.3.2)$$

Eq. (9.2.13) can be simplified to

$$\frac{\partial P_l}{\partial x} \beta = 2(\tau_{lv} - \tau_w) / w_{ch} = F_{vol}^l \quad (9.3.3)$$

Thus, the pressure drop per unit length and the volumetric force are related by:

$$\frac{\partial P_l}{\partial x} = F_{vol}^l / \beta = \frac{24\mu_l}{\beta^2 w_{ch}^2} (U_{lv} - 2U_l) \quad (9.3.4)$$

Similarly, for the vapor phase, the pressure drop is caused by the shear stress on the liquid-vapor interface:

$$P_v \left( \frac{w_{ch}}{2} - \delta \right) - \left( P_v + \frac{\partial P_v}{\partial x} \Delta x \right) \left( \frac{w_{ch}}{2} - \delta \right) - \tau_{lv} \Delta x = 0 \quad (9.3.5)$$

Eq. (9.2.15) can be simplified to

$$\frac{\partial P_v}{\partial x} \alpha = -2\tau_{lv} / w_{ch} = F_{vol}^v \quad (9.3.6)$$

Thus, the pressure drop per unit length and the volumetric force are related by:

$$\frac{\partial P_v}{\partial x} = F_{vol}^v / \alpha = \frac{12\mu_v}{\alpha^2 w_{ch}^2} (U_{lv} - U_v) \quad (9.3.7)$$

Thus, substituting Eqs. (9.2.13), (9.3.4), & (9.3.7) into Eq. (9.3.1) and simplifying yields the following expression for the fully developed slip,  $S^*$ :

$$S^* = \frac{U_v^*}{U_l^*} = \frac{(3 - 2S_1)(\alpha^*)^2 - 3}{\beta^*(3 - \beta^*)} \quad (9.3.8)$$

The equation for slip can then be used to compute the void fraction from the identity:

$$\alpha^* = \frac{1}{1 + \frac{1 - X}{X} \frac{S^*}{S_0}} \quad (9.3.9)$$

where  $S_0 = \frac{\rho_l}{\rho_v}$ . Thus, beginning with an initial guess of the fully developed volume fractions,  $\alpha^*$  and  $\beta^*$ , Eq. (9.3.8) may be evaluated to obtain the fully developed slip,  $S^*$ , and then Eq. (9.3.9) may be evaluated to obtain a new guess of the fully developed volume fraction,  $\alpha^*$ . The guess value for the liquid volume fraction may then be updated, noting that  $\beta^* = 1 - \alpha^*$ . Because Eqs. (9.3.8) and (9.3.9) are non-linear, damping is necessary. An explicit damping factor of 0.5 was found to be sufficient and stable.

#### 9.4 Fully Developed Friction Factor

In addition, the equation for slip can be used to further simplify Eqs. (9.3.4)-(9.3.7) by substitution of Eq. (9.2.13) & (9.3.8), yielding

$$\frac{\partial P}{\partial x} = \frac{\partial P_l}{\partial x} = \frac{\partial P_v}{\partial x} = \frac{24\mu_l}{w_{ch}^2} \frac{U_l^*}{\beta^*(3 - \beta^*)} = \frac{24S_1\mu_v}{w_{ch}^2} \frac{U_v^*}{3 + (2S_1 - 3)(\alpha^*)^2} \quad (9.4.1)$$

where  $\alpha^*, \beta^*, U_l^*$ , and  $U_v^*$  are the annular fully developed void fraction, volume fraction, liquid velocity, and vapor velocity, respectively. It is worth noting here that failure to use the fully developed values will result in incorrect values for pressure drop or slip.

Eq. (9.4.1) should therefore be modified such that arbitrary values of  $\alpha, \beta, U_l$ , and  $U_v$  may be used by noting that via conservation of mass,

$$\begin{aligned}
F_l &= \rho_l \beta U_l = \rho_l \beta^* U_l^*; & U_l^* &= \frac{\beta}{\beta^*} U_l \\
F_v &= \rho_v \alpha U_v = \rho_v \alpha^* U_v^*; & U_v^* &= \frac{\alpha}{\alpha^*} U_v
\end{aligned} \tag{9.4.2}$$

Accordingly, substituting Eq. (9.4.2) into Eq. (9.4.1), yields the following more robust equation for the fully developed pressure drop:

$$\frac{\partial P}{\partial x} = \frac{24\mu_l}{w_{ch}^2} \frac{\beta}{(\beta^*)^2(3-\beta^*)} U_l = \frac{24S_1\mu_v}{w_{ch}^2} \frac{\alpha}{3\alpha^* + (2S_1 - 3)(\alpha^*)^3} U_v \tag{9.4.3}$$

Here, arbitrary mass-conserving values of  $\alpha, \beta, U_l$ , and  $U_v$  may be used, but  $\alpha^*$  and  $\beta^*$  must still be the fully developed values.

The source term is then the integral force on the control volume:

$$S^l = \Delta x \Delta y F_{vol}^l = \Delta x \Delta y \frac{\partial P_l}{\partial x} \beta = \frac{24\mu_l \Delta x \Delta y}{w_{ch}^2} \frac{\beta^2}{(\beta^*)^2(3-\beta^*)} U_l \tag{9.4.4}$$

$$S^v = \Delta x \Delta y F_{vol}^v = \Delta x \Delta y \frac{\partial P_v}{\partial x} \alpha = \frac{24S_1\mu_v \Delta x \Delta y}{w_{ch}^2} \frac{\alpha^2}{3\alpha^* + (2S_1 - 3)(\alpha^*)^3} U_v \tag{9.4.5}$$

Upon linearization with respect to the liquid and vapor velocities, the final form of the source term is obtained:

$$S^l = S_C^l - S_P^l \tag{9.4.6}$$

$$S^v = S_C^v - S_P^v \tag{9.4.7}$$

where

$$S_C^l = 0 \tag{9.4.8}$$

$$S_C^v = 0 \tag{9.4.9}$$

$$S_P^l = \frac{24\mu_l \Delta x \Delta y}{w_{ch}^2} \frac{\beta^2}{(\beta^*)^2(3-\beta^*)} \tag{9.4.10}$$

$$S_P^v = \frac{24S_1\mu_v\Delta x\Delta y}{w_{ch}^2} \frac{\alpha^2}{3\alpha^* + (2S_1 - 3)(\alpha^*)^3} \quad \textbf{(9.4.11)}$$

## 10 Appendix B: Derivations of Equations Used in Microchannel Model

### 10.1 Conservation of Species

The steady-state conservation of species equation for the mixture is given in [54] as

$$\nabla \cdot (\alpha_p \rho_p \vec{v}_m) = -\nabla \cdot (\alpha_p \rho_p \vec{v}_{p,m}) + S \quad (10.1.1)$$

where

$$\vec{v}_{p,m} = \vec{v}_p - \vec{v}_m \quad (10.1.2)$$

$$\vec{v}_m = \frac{\sum_{k=1}^n \alpha_k \rho_k \vec{v}_k}{\rho_m} \quad (10.1.3)$$

$$\rho_m = \sum_{k=1}^n \alpha_k \rho_k \quad (10.1.4)$$

Substituting Eq. (10.1.2) into Eq. (10.1.1) and simplifying yields

$$\nabla \cdot (\alpha_p \rho_p \vec{v}_p) = S \quad (10.1.5)$$

By definition, the volume fraction is related to the mass fraction by

$$Y_p = \frac{\alpha_p \rho_p \vec{v}_p}{\sum_{k=1}^n \alpha_k \rho_k \vec{v}_k} = \frac{\alpha_p \rho_p \vec{v}_p}{\rho_m \vec{v}_m} \quad (10.1.6)$$

Rearranging Eq. (10.1.6) and substituting it back into Eq. (10.1.5), we arrive at the final form of the conservation of species equation employed in the present work

$$\nabla \cdot (Y_p \rho_m \vec{v}_m) = S \quad (10.1.7)$$

## 10.2 Conservation of Energy in the Mixture

The steady-state conservation of energy equation for the mixture is given in [54] as

$$\nabla \cdot \sum_{k=1}^n \alpha_k \rho_k \vec{v}_k C_k T_k = \nabla \cdot (k_{eff} \nabla T_l) + S \quad (10.2.1)$$

where

$$k_{eff} = \sum_{k=1}^n \alpha_k k_k \quad (10.2.2)$$

and  $S$  is a volumetric source term.

Neglecting the heat capacity and heat transfer in the vapor phase, the effective thermal conductivity can be shown to be equal to

$$k_{eff} = \alpha_l k_l \quad (10.2.3)$$

and the convective term reduced to

$$\nabla \cdot \sum_{k=1}^n \alpha_k \rho_k \vec{v}_k C_k T_k = \nabla \cdot \alpha_l \rho_l \vec{v}_l C_l T_l \quad (10.2.4)$$

Using the identity found in Eq. (10.1.6) and substituting Eqs. (10.2.3) and (10.2.4), Eq. (10.2.4) can be simplified to

$$\nabla \cdot (\rho_m \vec{v}_m Y_p C_{p,l} T_l) = \nabla \cdot (\alpha_l k_l \nabla T_l) + S \quad (10.2.5)$$

## References

- [1] DARPA, "Intrachip/Interchip Enhanced Cooling Fundamentals (ICECool Fundamentals)," in *DARPA-BAA-12-50*, ed, 2012.
- [2] Y. Won, J. Cho, D. Agonafer, M. Asheghi, and K. E. Goodson, "Fundamental Cooling Limits for High Power Density Gallium Nitride Electronics," *IEEE Transactions on Components, Packaging, and Manufacturing Technology*, vol. 5, pp. 737-744, 2015.
- [3] Y. A. Cengel and A. J. Ghajar, *Heat and Mass Transfer: Fundamentals and Applications*, Fifth ed. New York, NY, USA: McGraw Hill Education, 2015.
- [4] H. Sutter. (2005) The Free Lunch is Over: A Fundamental Turn Toward Concurrency in Software. *Dr. Dobbs' Journal*. Available: <http://www.gotw.ca/publications/concurrency-ddj.htm>
- [5] V. P. Carey, *Liquid-Vapor Phase Change Phenomena*. New York: Hemisphere Publishing House, 1992.
- [6] A. Bar-Cohen, M. Arik, and M. Ohadi, "Direct Liquid Cooling of High Flux Micro and Nano Electronic Components," *Proceedings of the IEEE*, vol. 94, pp. 1549-1570, 2006.
- [7] A. Faghri, *Heat Pipe Science and Technology*. Washington, DC: Taylor and Francis, 1995.
- [8] R. H. Nilson, S. W. Tchikanda, S. K. Griffiths, and M. J. Martinez, "Steady evaporating flow in rectangular microchannels," *International Journal of Heat and Mass Transfer*, vol. 49, pp. 1603-1618, 2006.
- [9] J. Ha and G. Peterson, "The interline heat transfer of evaporating thin films along a micro grooved surface," *Journal of Heat Transfer-Transactions of the Asme*, vol. 118, pp. 747-755, AUG 1996 1996.
- [10] E. Cetegen, "Force Fed Microchannel High Heat Flux Cooling Utilizing Microgrooved Surfaces," Ph.D., Department of Mechanical Engineering, University of Maryland, College Park, 2010.
- [11] G. M. Harpole and J. E. Eninger, "Micro-channel heat exchanger optimization," presented at the Semiconductor Thermal Measurement and Management Symposium, 1991. SEMI-THERM VII. Proceedings., Seventh Annual IEEE, Phoenix, AZ, USA, 1991.
- [12] D. Copeland, M. Behnia, and W. Nakayama, "Manifold microchannel heat sinks: isothermal analysis," *IEEE Transactions on Components, Packaging, and Manufacturing Technology: Part A*, vol. 20, pp. 96-102, 1997.
- [13] E. Y. K. Ng and S. T. Poh, "Investigative study of manifold microchannel heat sinks for electronic cooling design," *Journal of Electronics Manufacturing*, vol. 9, 1999.
- [14] J. H. Ryu, D. H. Choi, and S. J. Kim, "Three-dimensional numerical optimization of a manifold microchannel heat sink," *International Journal of Heat and Mass Transfer*, vol. 46, pp. 1553-1562, 2003.
- [15] L. Everhart, N. R. Jankowski, B. Geil, A. Bayba, D. Ibitayo, and P. McCluskey, "Manifold Microchannel Cooler for Direct Backside Liquid Cooling of SiC

- Power Devices," presented at the ASME 2007 5th International Conference on Nanochannels, Microchannels, and Minichannels, 2007.
- [16] Y. H. Kim, W. C. Chun, J. T. Kim, B. C. Pak, and B. J. Baek, "Forced air cooling by using manifold microchannel heat sinks," *KSME International Journal*, vol. 12, pp. 709-718, 1998.
  - [17] Y. Yue, S. K. Mohammadian, and Y. Zhang, "Analysis of performances of a manifold microchannel heat sink with nanofluids," *International Journal of Thermal Sciences*, vol. 89, pp. 305-313, 2015.
  - [18] M. Arie, A. Shooshtari, S. Dessiatoun, M. Ohadi, and E. Hajri, "Simulation and Thermal Optimization of a Manifold Microchannel Flat Plate Heat Exchanger," presented at the ASME 2012 International Mechanical Engineering Congress and Exposition, Houston, Texas, USA, 2012.
  - [19] M. Arie, A. Shooshtari, S. Dessiatoun, E. Al-Hajri, and M. Ohadi, "Numerical modeling and thermal optimization of a single-phase flow manifold-microchannel plate heat exchanger," *International Journal of Heat and Mass Transfer*, vol. 81, pp. 478-489, 2015.
  - [20] M. Arie, A. Shooshtari, S. Dessiatoun, and M. Ohadi, "Thermal optimization of an air-cooling heat exchanger utilizing manifold-microchannels," presented at the Proc. Thermal and Thermomechanical Phenomena in Electronic Systems (ITherm), 2014.
  - [21] X. Zhang, M. Arie, D. Deisenroth, A. Shooshtari, S. Dessiatoun, and M. Ohadi, "Impact of Additive Manufacturing on Performance Enhancement of Heat Exchangers: A Case Study on An Air-to-Air Heat Exchanger for High Temperature Applications," presented at the IX Minsk International Seminar on Heat Pipes, Heat Pumps, Refrigerators, Power Sources, Minsk, Belarus, 2015.
  - [22] V. Jha, S. Dessiatoun, M. Ohadi, A. Shooshtari, and E. Al-Hajri, "High performance micro-grooved evaporative heat transfer surface for low grade waste heat recovery applications," *Proc. ASME 2011 Pacific Rim Technical Conference and Exhibition on Packaging and Integration of Electronic and Photonic Systems*, pp. 277-283, 2011.
  - [23] V. Jha, S. Dessiatoun, A. Shooshtari, E. Al-Hajri, and M. Ohadi, "Experimental Characterization of a Nickel Alloy-Based Manifold-Microgroove Evaporator," *Heat Transfer Engineering*, vol. 36, pp. 33-42, 2015.
  - [24] D. Boyea, A. Shooshtari, S. Dessiatoun, and M. Ohadi, "Heat Transfer and Pressure Drop Characteristics of A Liquid Cooled Manifold-Microgroove Condenser," presented at the Proceedings of the ASME 2013 Heat Transfer Summer Conference, Minneapolis, MN, USA, 2013.
  - [25] E. Kermani, "Manifold Micro-Channel Cooling of Photovoltaic Cells for High Efficiency Solar Energy Conversion Systems," Master of Science, Department of Mechanical Engineering, University of Maryland, College Park, MD, USA, 2008.
  - [26] E. Kermani, S. Dessiatoun, A. Shooshtari, and M. Ohadi, "Experimental investigation of heat transfer performance of a manifold microchannel heat sink for cooling of concentrated solar cells," presented at the Proc. IEEE Electronic Components and Technology Conference, San Diego, CA, USA, 2009.



- [27] L. M. Boteler, "Microfabrication and Analysis of Manifold Microchannel Coolers for Power Electronics," Ph.D., Department of Mechanical Engineering, University of Maryland, College Park, 2011.
- [28] L. Boteler, N. Jankowski, P. McCluskey, and B. Morgan, "Numerical investigation and sensitivity analysis of manifold microchannel coolers," *International Journal of Heat and Mass Transfer*, vol. 55, pp. 7698-7708, 2012.
- [29] W. Escher, T. Brunschweiler, B. Michel, and D. Poulikakos, "Experimental Investigation of an Ultrathin Manifold Microchannel Heat Sink for Liquid-Cooled Chips," *Journal of Heat Transfer-Transactions of the Asme*, vol. 132, AUG 2010 2010.
- [30] D. B. Tuckerman and R. F. W. Pease, "High-performance heat sinking for VLSI," *IEEE Electron Device Letters*, vol. 2, pp. 126-129, 1981.
- [31] R. Zhang, M. Hodes, N. Lower, and R. Wilcoxon, "Water-Based Microchannel and Galinstan-Based Minichannel Cooling Beyond 1 kW/cm<sup>2</sup> Heat Flux," *IEEE Transactions on Components, Packaging and Manufacturing Technology*, vol. 5, pp. 762-770, 2015.
- [32] J. Ditri, J. Hahn, R. Cadotte, M. McNulty, and D. Luppia, "Embedded Cooling of High Heat Flux Electronics Utilizing Distributed Microfluidic Impingement Jets," presented at the Proceedings of the ASME 2015 International Technical Conference and Exhibition on Packaging and Integration of Electronic and Photonic Microsystems InterPACK2015 San Francisco, CA, USA, 2015.
- [33] D. H. Altman, A. Gupta, and M. Tyhach, "Development of a Diamond Microfluidics-Based Intra-Chip Cooling Technology for GaN," presented at the Proceedings of the ASME 2015 International Technical Conference and Exhibition on Packaging and Integration of Electronic and Photonic Microsystems InterPACK2015 San Francisco, CA, USA, 2015.
- [34] G. Campbell, H. Eppich, K. Lang, C. Craemer, T. Yurobchak, K. Chu, *et al.*, "Advanced Cooling Designs for GaN-on-Diamond MMICs," presented at the ASME 2015 International Technical Conference and Exhibition on Packaging and Integration of Electronic and Photonic Microsystems and ASME 2015 12th International Conference on Nanochannels, Microchannels, and Minichannels, InterPACKICNMM2015, San Francisco, California, USA, 2015.
- [35] S. Adera, D. Antao, R. Raj, and E. N. Wang, "Hotspot Thermal Management via Thin-Film Evaporation," presented at the iTHERM, Las Vegas, NV, USA, 2016.
- [36] J. W. Palko, H. Lee, D. D. Agonafer, C. Zhang, K. W. Jung, J. Moss, *et al.*, "High Heat Flux Two-Phase Cooling of Electronics with Integrated Diamond/Porous Copper Heat Sinks and Microfluidic Coolant Supply," presented at the iTHERM, Las Vegas, NV, USA, 2016.
- [37] S. G. Kandlikar, T. Widger, A. Kalani, and V. Mejia, "Enhanced Flow Boiling Over Open Microchannels With Uniform and Tapered Gap Manifolds," *Journal of Heat Transfer*, vol. 135, 2013.
- [38] A. Kalani and S. G. Kandlikar, "Combining liquid inertia with pressure recovery from bubble expansion for enhanced flow boiling," *Applied Physics Letters*, vol. 107, 2015.
- [39] F. Houshmand, H. Lee, M. Asheghi, and K. E. Goodson, "High Heat Flux Subcooled Flow Boiling of Methanol in Microtubes," presented at the

- Proceedings of the ASME 2015 International Technical Conference and Exhibition on Packaging and Integration of Electronic and Photonic Microsystems InterPACK2015 San Francisco, CA, USA, 2015.
- [40] Q. Li, P. Tie, and Y. Xuan, "Investigation on heat transfer characteristics of R134a spray cooling," *Experimental Thermal and Fluid Science*, vol. 60, pp. 182-187, 2015.
  - [41] K. P. Drummond, J. A. Weibel, S. V. Garimella, D. Back, D. B. Janes, M. D. Sinanis, *et al.*, "Evaporative Intrachip Hotspot Cooling with a Hierarchical Manifold Microchannel Heat Sink Array," presented at the iTHERM, Las Vegas, NV, USA, 2016.
  - [42] M. M. Ohadi, K. Choo, S. Dessiatoun, and E. Cetegen, *Next Generation Microchannel Heat Exchangers*: Springer Publishing Co., 2012.
  - [43] J. H. Ryu, D. H. Choi, and S. J. Kim, "Three-dimensional numerical optimization of a manifold microchannel heat sink," *International Journal of Heat and Mass Transfer*, vol. 46, pp. 1553-1562, 2003.
  - [44] W. Zhang, T. Hibiki, and K. Mishima, "Correlation for flow boiling heat transfer in mini-channels," *International Journal of Heat and Mass Transfer*, vol. 47, p. 14, 2004.
  - [45] J. C. Chen, "Correlation for boiling heat transfer to saturated fluids in convective flow," *Process Design and Development*, vol. 5, p. 7, 1966.
  - [46] H. K. Forster and N. Zuber, "Dynamics of vapor bubbles and boiling heat transfer," *American Institute of Chemical Engineers*, vol. 4, p. 4, 1955.
  - [47] S. G. Kandlikar, "A General Correlation for Saturated Two-Phase Flow Boiling Heat Transfer Inside Horizontal and Vertical Tubes," *Journal of Heat Transfer*, vol. 112, p. 9, 1990.
  - [48] S. G. Kandlikar and P. Balasubramanian, "An Extension of the Flow Boiling Correlation to Transition, Laminar, and Deep Laminar Flows in Minichannels and Microchannels," *Heat Transfer Engineering*, vol. 25, p. 7, 2004.
  - [49] Y. Taitel and A. E. Dukler, "A model for predicting flow regime transitions in horizontal and near horizontal gas-liquid flow," *American Institute of Chemical Engineers*, vol. 22, pp. 47-55, 1976.
  - [50] T. Harirchian and S. Garimella, "A comprehensive flow regime map for microchannel flow boiling with quantitative transition criteria," *International Journal of Heat and Mass Transfer*, vol. 53, pp. 2694-2702, JUN 2010 2010.
  - [51] J. R. Thome, *Engineering Data Book III*, 2010.
  - [52] H. Wang, S. Garimella, and J. Murthy, "Characteristics of an evaporating thin film in a microchannel," *International Journal of Heat and Mass Transfer*, vol. 50, pp. 3933-3942, SEP 2007 2007.
  - [53] R. Bertossi, Z. Lataoui, V. Ayel, C. Romestant, and Y. Bertin, "Modeling of Thin Liquid Film in Grooved Heat Pipes," *Numerical Heat Transfer Part a-Applications*, vol. 55, pp. 1075-1095, 2009 2009.
  - [54] A. Fluent. (2006). *Fluent 6.3 User's Guide*.
  - [55] Z. Pan, J. A. Weibel, and S. V. Garimella, "A Cost-Effective Modeling Approach for Simulating Phase Change and Flow Boiling in Microchannels " presented at the Proceedings of the ASME 2015 International Technical Conference and

- Exhibition on Packaging and Integration of Electronic and Photonic Microsystems InterPACK 2015, San Francisco, CA, USA, 2015.
- [56] R. Zhuan and W. Wang, "Simulation of subcooled flow boiling in a micro-channel," *International Journal of Refrigeration*, vol. 34, pp. 781-795, 2011.
  - [57] S. V. Patankar, *Numerical Heat Transfer and Fluid Flow*: Hemisphere Publishing Corp., 1980.
  - [58] R. E. Simons. (2016) Estimating Parallel Plate-fin Heat Sink Pressure Drop. *Electronics Cooling*. 10-12.
  - [59] S. A. Klein, "Engineering Equation Solver (EES) Database," ed: F-Chart Software, 2015.
  - [60] B. R. Munson, D. F. Young, and T. H. Okiishi, *Fundamentals of Fluid Mechanics*, Fifth Edition ed. USA: John Wiley & Sons Inc., 2006.
  - [61] T. Obeloer, B. Bolliger, Y. Han, B. L. Lau, G. Tang, and X. Zhang. (2016) Application of Diamond Heat Spreaders for the Thermal Management of GaN Devices. *Electronics Cooling*.
  - [62] C. C. Lee, C. Y. Wang, and G. Matijasevic, "Au-In Bonding Below the Eutectic Temperature," *IEEE Transactions on Components, Hybrids, and Manufacturing Technology*, vol. 16, pp. 311-316, 1993.
  - [63] B. L. Lau, Y. Han, H. Y. Zhang, L. Zhang, and X. W. Zhang, "Development of fluxless bonding using deposited gold-indium multi-layer composite for heterogeneous silicon micro-cooler stacking," presented at the Electronics Packaging Technology Conference (EPTC), 2014 IEEE 16th, Singapore, 2014.
  - [64] P. Wang, J. S. Kim, and C. C. Lee, "Fluxless Wafer Bonding in Vacuum Using Electroplated Sn-Ag Layers," *IEEE Transactions on Electronics Packaging Manufacturing*, vol. 30, pp. 155-159, 2007.
  - [65] I. Karakaya and W. Thomson, "The Ag-Sn (silver-tin) system," *Bulletin of Alloy Phase Diagrams*, vol. 8, pp. 340-347, 1987.